UNIVERSITY OF SOUTHAMPTON
FACULTY OF ENGINEERING AND THE ENVIRONMENT
Engineering Sciences

Direct Numerical Simulation of Hydrogen Fluid Dynamics

by

Mohammad Pezeshki

Thesis for the degree of Doctor of Philosophy

August 2013

Declaration of Authorship

I, Mohammad Pezeshki, declare that this thesis titled, 'Direct Numerical Simulation of Hydrogen Fluid Dynamics' and the work presented in it are my own and has been generated by me as the result of my own original research. I confirm that:

- This work was done wholly or mainly while in candidature for a research degree at this University.
- Where any part of this thesis has previously been submitted for a degree or any other qualification at this University or any other institution, this has been clearly stated.
- Where I have consulted the published work of others, this is always clearly attributed.
- Where I have quoted from the work of others, the source is always given. With the exception of such quotations, this thesis is entirely my own work.
- I have acknowledged all main sources of help.
- Where the thesis is based on work done by myself jointly with others, I have made clear exactly what was done by others and what I have contributed myself.
- None of this work has been published before submission.

Signed: _____

Date: _____

Dedicated to my wife, Maryam,
without whom this work
could have been finished
one year earlier.

UNIVERSITY OF SOUTHAMPTON

ABSTRACT

FACULTY OF ENGINEERING AND THE ENVIRONMENT
Engineering Sciences

Doctor of Philosophy

DIRECT NUMERICAL SIMULATION OF HYDROGEN FLUID DYNAMICS

by Mohammad Pezeshki

Direct numerical simulation of $H_2 - O_2$ in the context of a temporally evolving mixing layer has been performed. Real molecular properties as well as the effects of the species differential diffusion were incorporated into an existing 3D parallel FORTRAN code. The geometry is a box with streamwise and spanwise directions being periodic whereas non-periodic boundaries were set up in transverse (vertical) directions which leads to inhomogeneity for the turbulent field in these directions. Initialisation were performed by error function distributions for streamwise velocity component, scalar mass fraction and temperature along the vertical axis of the domain. Initial pressure is set to be uniform and density was calculated based on ideal-gas law for the mixture. Disturbances were introduced by generating spanwise and streamwise vorticity in the middle of the mixing layer to enable transition from laminar to turbulent.

Simulations started with a binary-species mixing layer undergoing a non-reactive phase followed by a reactive phase using a global one-step reaction mechanism. Results were presented for three sets of simulations in which the only varying quantity was the species Lewis number. Effects of Lewis number on the flow was studied in detail by evaluating the the mixing layer development, mean flow properties and turbulent field. The interaction of the turbulence and scalars was studied by scrutinizing the transport equation for the scalar variance and also by performing a budget analysis for the turbulent scalar flux. DNS studies were expanded by incorporating a 37-step chemical mechanism with 9 species into previous set up. The species transport equations, the energy equation and the boundary conditions were amended accordingly. Simulations were proved to be grid-independent by setting up two cases with the same initial conditions but different number of grid points. In addition, the effects of species Lewis number on multicomponent mixing layer were examined by setting all Lewis numbers equal to 1.0 for one case and using real Lewis number values for the other case. The flow and turbulence interaction were studied by performing budget analysis for scalar variance and turbulent scalar flux of active species for molecules and radicals exist in a reactive multi-component mixture.

Acknowledgements

This research project would not have been possible without the support of the other people in the Energy Technology Research Group of Southampton University. I would like to express my gratitude to my supervisor, Professor Kai H. Luo who was abundantly helpful and offered invaluable support and guidance. I would also like to thank Dr. Jun Xia, former post-doctoral research fellow and Dr. Edward Richardson of Southampton University, for their help and assistance. Computing time on the national high-end computing platform HECToR from the EPSRC grant No. EP/J016381/1 is also gratefully acknowledged.

Last but not the least, I would like to express my special thanks and respect to my family; to my beloved wife Dr. Maryam Talaei and to my beloved mother, father and brother, for their understanding and endless love and support throughout this PhD.

Contents

List of Figures

List of Tables

Symbols

Roman Symbols		
a, b, c	Constants in the Padé scheme, section 2.2	
A	Matrix in appendix A	
A	pre-exponential factor in equation 2.14	
a_1, a_2	Constants in the equation 2.32	
c	Speed of sound	
c	Reaction progress variable, section 4.2.3	
C	Integer coefficient, equation 2.36	
$C_{n,\ell}$	Reaction rate of the species n in the ℓ^{th} reaction	
CFL	Courant-Friedrichs-Lewy number, section 2.33	
Da_ℓ	Damköhler number for the reaction number ℓ	
D_c, D_μ, D_{com}	Terms in equation 2.33	
D_n	Diffusivity of species n	
e	Internal energy	
E_a	Activation energy of the reaction ℓ	KJ/mol
E_T	Total energy	
f	Elemental mixture fraction in equation 4.9	
f_i	Function of independent variable at node i, section 2.2	
F	Flux vector, appendix A	
g	Term in appendix A	
$\Delta h^o_{f_n}$	Standard enthalpy of formation for species n	
k	Term in appendix A	
$k(T)$	Reaction rate constant	
ℓ_i	Amplitude of characteristic waves	
ℓ	Reaction number in equation 2.13	
L_x	Domain length in x-direction, chapter 4	
L_y	Domain length in y-direction, chapter 4	
L_z	Domain length in z-direction, chapter 4	
Le_n	Species Lewis number, chapter 4	

m	Term in appendix A	
M	Matrix in equation A.18	
M_a	Free stream Mach number	
n	Term in appendix A	
N_i	Total number of grid points in the i direction	
	where $i = x, y, orz$	
N_r	Total number of reaction	
N_s	Total number of species	
p	Pressure	
Pr	Prandtl number	
q_i	Heat flux vector	
Q	Solution vector, appendix A	
Q	Storage location in the memory, subsection 2.2.3	
Q_h	Heat release parameter	
Q_w	Storage location in the memory, subsection 2.2.3	
R_u	Universal gas constant	$KJ/mol.K$
Re	Reynolds number	
s	Stoichiometric oxidiser to fuel mass ratio	
Sc	Schmidt number	
S	Sutherland coefficient, equation 2.16	
t	Time	
Δt	Time step, subsection 2.2.3	
T	Temperature	
T	Matrix in appendix A	
T_f	Non-dimensional temperature rise	
	(also shown as α in equation 2.15)	
T_f^*	Temperature rise	K
u, v, w	Velocity components in x,y,z directions	
u_i	Cartesian components of the velocity	
U	Vector of primitive variables, appendix A	
V_i^c	Correction velocity in the i^{th} direction	
V_{ni}	Diffusion velocity for the species n in the i^{th} direction	
W_{mix}	Mixture molecular weight	
W_n	Molecular weight of species n	
x	Coordinate in span-wise direction	
x_i	Cartesian coordinates	
$\Delta x, \Delta y, \Delta z$	Grid spacing in x,y,z directions	
X_n	Mole fraction of species n	
y	Coordinate in stream-wise direction	

Y_{mf}	Mixture fraction	
Y_n	Mass fraction of species n	
z	Coordinate in transverse direction	
Ze	Zeldovich number	
Z_L	Modified mixture fraction, equation 5.1	

Greek Symbols

α, β	Constants in the Padé scheme in section 2.2, or Wave number in chapter 4 and chapter 5	
α_n	Stoichiometric coefficient, table 3.1	
γ	ratio of specific heats	
δ_{ij}	Kronecker delta function	
$\delta^*_{m_0}$	Initial momentum thickness	m
$\delta^*_{\omega_0}$	Initial vorticity thickness	m
ϵ	Dissipation of turbulent kinetic energy	
η	Kolmogorov scale	
θ	Scalar(mass fraction)	
κ	Turbulent kinetic energy	
κ_i	Species 'i' contribution to the differential diffusion, equation 4.10	
λ_i	Velocities of characteristic waves, appendix A	
Λ	Diagonalized matrix of λ_i, appendix A	
μ	Viscosity	
ν_n	Stoichiometric coefficient of species n	
ρ	Density	
τ_{ij}	Shear stress tensor	
ϕ	Equivalence ratio of the mixture	
χ_n	Scalar dissipation for species n, equation 4.3	
ω_n	Reaction rate of species n	
ω_y	Streamwise vorticity component	
ω_T	Overall reaction rate	
$\overrightarrow{\omega}$	Vorticity vector, equation 4.4	
Π_{I_n}	Production by mean velocity gradient for species n, equation 4.4	
Π_{II_n}	Production by fluctuating velocity gradient for species n, equation 4.4	
Π_{var_n}	Scalar production/destruction for species n, equation 4.3	
Φ	Modified mixture fraction, equation 5.1	

Φ_n	Mean pressure gradient term for species n, equation 4.4
Ψ_n	Fluctuating pressure gradient term for species n, equation 4.4
Ω_{var_n}	Reaction-mass fraction correlation for species n, equation 4.3
Ω_n	Reaction-fluctuating velocity correlation for species n, equation 4.4

Superscripts

$''$	Favre fluctuating component
$*$	Dimensional quantity

Subscripts

ref	Represents a reference quantity in dimensional form(SI unit)
ND	Represents a non-dimensional quantity

Abbreviations

CGT/GT	Counter-gradient/gradient transport
DD	Differential diffusion
DNS	Direct numerical simulation
LES	Large eddy simulation
$RANS$	Reynolds-averaged NavierStokes equations
RHS	Right-hand side

Chapter 1

Introduction

1.1 Motivation and Objectives

Hydrogen is a carbon-free fuel, which has a great potential to be an important energy carrier in the future. Hydrogen can be used in a wide range of applications such as fuel cells and internal combustion engines. Due to its high energy density per unit mass, it can be used to power many propulsion systems that currently use hydrocarbons, which lead to global warming and large amount of pollutant formation. Hydrogen can be derived from various sources such as fossil fuels, nuclear power and the most abundant source to get hydrogen is water. In comparison with other fuels especially hydrocarbon fuels, hydrogen combustion produces less pollutant emissions under certain conditions so it is known as a clean fuel. On the other hand, there are some two major issues with hydrogen which must be taken into consideration. One is hydrogen safety, as hydrogen can easily lead to explosion under certain conditions. It has unique properties like low density and high diffusivity, which leads to difficulties in its handling and the other one is hydrogen storage. In its gaseous form, hydrogen diffuses very quickly while in its liquid form, it can easily leak from any container, which causes loss of energy and even compromises safety. Despite the simplicity of its molecular structure, combustion of hydrogen involves up to hundreds of elementary reactions, not all of which are well understood.

The proposed research is to use direct numerical simulations(DNS) to investigate the fluid dynamics of hydrogen. DNS is powerful research tool which provides accurate and detailed description of the flow field without applying any turbulence models. This involves developing a parallel computer program to solve 3D Navier-Stokes equations in a temporally evolving turbulent reacting shear-layer(mixing-layer). Choosing a turbulent mixing-layer is because of the fact that it occurs in many combustion devices such as

internal combustion engines, gas turbine combustors and diffusion flames in industrial furnaces and also jet flames. DNS is one of the best ways to scrutinise the flow field in detail. Everything is resolved throughout the computational domain and the results are reliable and as accurate as the results obtained in experimental investigations.
Incorporation of realistic chemistry of hydrogen combustion and using DNS data will aid us to assess and develop hydrogen combustion models which can have potential to be employed industrial applications as well as research purposes for further developments and will increase hydrogen safety.
According to above description about the importance of DNS study of turbulent reacting shear-layer, the main objectives of this research can be itemised as follows:

- To perform DNS calculations of non-premixed hydrogen-oxygen combustion by implementing one-step $H_2 - O_2$ mechanism.
- To study the effect of species diffusivity on the mixing-layer development and turbulent flow field.
- To study the interaction between turbulence and combustion.
- To study the effect of diffusion combustion on physical properties of the flow such as pressure, temperature, density, viscosity, and so on.
- To expand the code to be able to solve for multi-species Navier-Stokes equations with multi-step reaction mechanisms.
- To study the mixing layer development and the effects of species differential diffusion on that.
- To analyse the interaction of a multi-species mixture and the turbulent field.

1.2 Previous Research

Because of the unique and exceptional properties of hydrogen which was mentioned earlier, there have been many interests until now to study the fluid dynamics of hydrogen as a fuel either in pure condition or as a mixture. When hydrogen reacts with oxidiser in an evolving turbulent shear-layer, the resulting combustion could be one of the most complicated phenomena in fluid dynamics studies. This could be another reason for other researchers to be involved. From numerical and computational point of view, there are three major methods to deal with fluid dynamics studies by simulation or modelling: Reynolds-averaged Navier-Stokes(RANS), large-eddy simulation(LES) and direct numerical simulation(DNS).

In RANS, a time-averaged form of the Navier-Stokes equations are solved to determine the mean velocity field. Reynolds stress terms are unclosed which are needed to be modelled. These terms are obtained from the turbulent viscosity field and the turbulent viscosity can be obtained from different ways which actually determine the type of the modelling used[2]. These models are zero-equation(Baldwin-Lomax), one-equation model(Spalart-Almaras), two-equation models(κ-ϵ or κ-ω) and a seven-equation model which is known as 'Reynolds stress model'. One advantage of this method is to allow using a coarse grid and is extensively used in practical applications.

In LES, as it is inferred from its name, large-scale eddies are calculated and the smaller ones needed to be modelled by a subgrid model. Removing the effect of the small scales, allows to have a grid finer than the one used in RANS but still coarser than the one used in DNS. The effects of the small scales are then modelled using sub-grid scales models.

In DNS, the instantaneous field is solved and this implies that the grid system has to be small enough to resolve the smallest scales, i.e. kolmogorov scales(η). However, in a research by Moin and Mahesh[3], it is claimed that the smallest resolved length scale is required to be of $O(\eta)$, not equal to η, and some cases were presented as a proof of this. This method is still limited to academic topics with simpler geometries and smaller domain size in comparison with the other two. In the context of the LES of hydrogen combustion, work of Mahle et. al.[4] can be referred to. They performed LES of temporal reactive shear layers of diluted hydrogen with the focus on scalar variance and scalar dissipation rate. They computed flamelet database considering multicomponent diffusion the effects of Soret and Dufour. They also performed a simpler version of the computations by ignoring such effects and using Hirschfelder-Curtiss approximations. Research by Knaus and Pantano[5] is a good example of a DNS with one-step global mechanism for hydrogen-oxygen combustion that are explained below in more details.

Several research groups looked into the shear-layer fluid dynamics itself regardless of whether it undergoes a chemical reaction or not[6], while some researchers showed interest to investigate combustion in the turbulent mixing-layer configuration[7, 8, 9]. Rogers and Moser[10] have made fundamental studies on evolution of planar mixing-layer. They started with looking at the Kelvin-Helmholtz roll-up, and then moved on to scrutinize vortex pairing and transition from laminar flow to turbulent flow in a temporally developing mixing-layer[11]. The initial vorticity profile used in the current research is similar to what reported in the work of Rogers and Moser[10].

Dexun et al.[12] presented their results from DNS of transient and turbulent regime in a compressible mixing-layer. They discussed effects of higher convective Mach number on the structure of the mixing-layer. That the flow field becomes turbulent directly

from initial instabilities without any vortex pairing was one of the key findings of their research when the Mach number is close to transonic values. Break up of the large flow structures to the small structures, and formation of $\wedge -$ *shaped* vortices, double horseshoe vortices and mushroom structures, were other aspects of mixing-layer studies they presented as their research work.

Lele[13] worked on simulation of compressible fluid flow for three types of mixing layers with non-reactive scalar mixing. First, for mixing of streams of equal entropy; second, for the mixing of streams of equal stagnation enthalpy, and last, mixing of streams of equal Mach number. To describe compressibility and by specifying the propagation speed of the dominant eddies, a convective Mach number was defined as M_c, which was used in study of the eddy shocklets when the value of M_c increases. Then, the evolution of vorticity field, mixing layer growth rate, and acoustic radiation from vortex evolution were studied.

Steinberger[14] studied the effects of compressibility, reaction exothermicity and non-equilibrium chemical modeling in a two-dimensional mixing layer. The reaction chosen was a second-order general mechanism of the type $'A+B \rightarrow Products+Heat'$ considering both a constant rate and an Arrhenius rate of reaction. Similar to what was done by Lele[13], a convective Mach number has been used to describe compressibility followed by employing a heat release parameter to represent the exothermicity of the reaction as well as Damköhler and Zeldovich numbers to quantify the time scale of the reaction compared to the turbulent time scale of the flow. It was shown that increasing the compressibility, increases stability and reduces turbulence so the rate of growth of the vorticity thickness is remarkably reduced, as well. Increasing the heat release rate also slows down the growth of large scale structures; The fact is that at the initial stages of development of mixing layer, higher heat release, increases the expansion of the core of the layer by enhancing the mixing but since it causes the mixing layer to be less responsive to perturbations, it results in reduction of mixing layer growth rate eventually, and also causes a stabilizing effect by decreasing the extent of reaction afterwards.

Luo[15] had a deeper analysis on the interaction between combustion and turbulence statistical parameters. Full three-dimensional time-dependent compressible Navier-Stokes equations in conjunction with a single-step chemistry which was in the general form were used with a direct numerical simulation method to gain understanding of coupling between combustion phenomenon and fluctuations of flow properties such as velocity, pressure, density and other thermochemical quantities as well as turbulence parameters in the Reynolds stress transport equation specifically the production rate, the strain rate and the viscous diffusion rate. It was stated that combustion-generated waves(in this case, supersonic waves) are the main reason for pressure and density variations

and as the heat release rate increases, these variations increase noticeably. Heat release rate will strongly affect the flow dilatation, as well. The effects of combustion on the growth rate of mixing layer was also studied. The results show that the growth rate is enhanced by heat release. Similar to what attained by Steinberger[14], heat release subsequently results in lowering the mixing layer growth rate principally by increasing the viscosity which has the effect of damping the turbulence and reducing the extent of combustion region. This work was concluded by explaining how combustion and turbulence would affect each other: First, chemical energy is extracted into mechanical form through fluid flow expansion under pressure. This mechanical energy is then fed into the Reynolds stress budget and consequently into the turbulent kinetic energy budget(TKE) via pressure-strain term which contributes to the combustion-generated turbulence. In addition, part of the turbulence energy is again converted back into the thermal energy through increase of viscous dissipation rate. The core of the numerical code which was developed by Luo[15], has been used for the current research. Also, researches by Xia and Luo[16, 17] have utilised the original Luo's code with further modifications.

Echekki and Chen[18], have studied autoignition of hydrogen using a 2-D DNS code coupled with a 9-species 19-step reversible reactions. Their primary scope was to investigate the role of finite-rate chemistry on autoignition in an inhomogeneous turbulent flow field. For this purpose, they considered a non-homogeneous mixture of hydrogen diluted with N_2 by 50% volume which is injected into a heated-air at temperature of $1180K$ and a pressure of 5 atmospheres. Nitrogen has been considered as an inert and does not incorporate in reaction mechanisms. They used an explicit eight-order finite differencing method to deal with spatial derivatives of compressible flow equations and a fourth-order Runge-Kutta scheme to treat temporal derivatives. Similar to what has been in the current research, they implemented a Navier-Stokes characteristics boundary condition which is periodic in stream-wise direction and acts as a non-reflecting boundary in transverse direction. They inserted a reasonable and realistic formulations for the mixture average thermal conductivity(from reference [1]), heat and diffusion coefficients as well as choosing an equation to compute an effective Damköhler number which is related to each species and spatial coordinates. To begin their presentation, first, they started with homogeneous ignition to use it as a reference problem as they stated that study of homogeneous ignition will provide criteria for autoignition based on the balance of chain-branching and chain-termination reactions. It is described in their research that before any significant heat release, concentration of radical pools will be characteristic of autoignition. This radical build-up is a result of competition between chain-branching and chain-termination reactions which occurs in the period of time before autoignition that is known as 'Induction Phase' in which temperature is also has no significant increase. After this phase, kernels, which are discrete localized spatially sites

of mixture, start to ignite resulting in a rapid jump of temperature and heat release. Later on, dissipation of thermal energy causes a shift in the balance between chain-branching and chain-termination reactions, and dissipation of radicals and intermediate species depletes the radical pools. Diffusion also plays an important role in depletion of intermediate species such as HO_2 and H_2O_2 in the radical pools. They, therefore, have associated the location of ignition kernels to the place where the dissipation rate is small, while regions with no sensible autoignition means that higher rates of dissipation governs in those locations that leads to quenching of kernels.

In addition to what is stated above, they added that diffusion of heat and mass fluxes and competition between diffusion of fuel into ignition kernels and diffusion of intermediate species during radical build-up, play an important role in ignition delay time as well as the reasoning for autoignition occurrence in any kernels. This discussion, is accompanied by a detailed investigation of diffusion of important species, like intermediate ones, and their diffusion effects on ignition delay time. They selected four different kernels to scrutinise evolution of important species during induction phase before autoignition starts, and after the autoignition stage when the flame forms with subsequent thermal runaway and heat.They, also, stated that evolution of autoignition depends on two major parameters: the first one, is the number of kernels per unit volume of combustion zone which have a favourable mixture characteristics; and the second one is fraction of these kernels that eventually evolve into thermal runaway, i.e. flame generation.

They concluded their research by focusing to find out how different kernels start to ignite under various conditions. They reported that the ignition or extinction of kernels are associated with 3 items: First, the heat dissipation that reduces the rate of chemical reactions and changes the balance between chain-branching and chain-terminating reactions; second, the destiny of kernel is associated with the mass dissipation which controls the radical pool growth rate; and third, it is strongly connected to the diffusion of H_2 which promotes ignition. Ignition has been the focus of other researchers as well. For example, in the paper published by Xu and Wen[19] ignition of hydrogen in a shock tube with a contracting part has been considered. They utilised a 21-step kinetic scheme for hydrogen in a context of averaged equations. Effects of pressure on the auto-ignition and the combustion were studied. Mastorakos has also performed extensive studies on the autoignition including a recent review paper[20]. Also the work of Doom and Mahesh[21] and Owston and Abraham[22] has been dedicated to ignition of Hydrogen.

Lu et al.[23] presented a direct numerical simulation of premixed and partially premixed Hydrogen-Air jet flame employing CSP method (Computational Singular Perturbation)

which has benefits such as providing a refinement procedure to separate the fast and slow processes as well as two other concepts of radical pointer and participation index that indicate the involvement of species and reactions, respectively, in the fast processes. By definition of an explosion index for explosive mode of the mixture, they effectively detected the radical explosion and thermal runaway, i.e. flame formation particularly the lean flame fronts . They have added that by using CSP method, they could distinguish and capture two premixed flame fronts which are difficult to detect with conventional methods. They used a very fine mesh with 944 million grid points in a 24 by 32 by 6.4 mm domain size to resolve all scales of fluid motion and turbulence, mainly Kolmogorov and flame structure. The boundary condition they applied is non-reflecting in the stream-wise and transverse directions and employed a periodic boundary in span-wise direction. The jet was simulated by injection cold fuel composed of 65 percent of H_2 and 35 percent of N_2 at temperature about 400K into a stream of hot air at 1100K that consequently cause domain to be classified into two types of regions: the non-explosive regions which consists of fuel-lean heated air co-flow outside of central jet, the central jet itself, and a pair of mixing layers just after the lift-off point(or stabilization point where the first parcels of mixture ignites), and an explosive region. The defined the Damköhler number in such a way that let them distinguish between lift-off point affected by auto-ignition and lift-off point affected by flame propagation (species transport). For this purpose they defined the Damköhler number based on time scale of explosive mode which was defined for the purpose of their research, and the scalar dissipation rate as multiplication of the explosive mode by the scalar dissipation rate. By this way, Damköhler numbers much greater than 1 indicate that chemical explosion is much faster than mixing, hence, the mixture is dominated by auto-ignition rather than flame propagation. On the contrary, if the Damköhler number is much less than 1, chemical explosion is strongly governed by mixing and transport of species rather than auto-ignition. Values of 1 for Damköhler number represents the locations where the chemical explosion is balanced by mixing. Furthermore, as their rough measurements showed, the time scale of the explosive mixture is comparable to the time of the flow from nozzle exit to the lift-off point implying that auto-ignition is more likely to be the controlling factor of the lift-off height rather than to be affected by flame propagation. They finish off their work by stating that in addition to the study of lifted flames, the explosive modes can also provide useful information in analysis of other flows such as those involving the competing effects of flame front and ignition front propagation during re-ignitions after local extinctions in highly strained turbulent non-premixed flames.

Knaus and Pantano[5] have studied effect of heat release (from density variation point of view) on inertial and dissipation of Favre-averaged turbulence parameters. They simulated both non-reacting and reacting incompressible shear layers for two global reaction

mechanisms of non-premixed methane-air and hydrogen-air, and compared the effects of combustion heat release on velocity and temperature spectra as well as the mixture fraction spectrum. Their combination, as of velocity and mixture fraction spectra and combination of velocity and temperature spectra were also studied. They accomplished the simulation using DNS of the compressible Navier-Stokes equations with an infinitely-fast-chemistry (equilibrium reaction), and with a high-order spatial and temporal discretization algorithm. For introducing the reactants streams, they considered two opposing streams of fuel and oxidiser diluted with nitrogen to let them have a better resolution of temperature gradient on the fuel-side of the mixing layer, entering into the domain with equal temperatures (for hydrogen-air chemistry, as it is the interest in this research). They initialised the domain with a hyperbolic-tangent velocity and mixture fraction profiles and utilised a model isotropic turbulence spectrum to trigger transition of laminar flow to turbulent regime as quickly as possible. The boundary conditions they applied were periodic in stream-wise and span-wise directions while non-reflective boundaries have been set in transverse directions[24]. To consider the effects of heat release on coupling between chemistry and turbulence solely, they utilised the flame-sheet approximation, assuming an infinitely thin flame sheet to study decay of turbulence spectra. Simulation of incompressible mixing-layer with a convective Mach number of 0.3 is another reason to reduce the effects of compressibility on the flow. Crossing a plane normal to the transverse direction (across the shear layer profile), they used density-weighted(Favre) averaging to obtain statistical quantities of shear layer as well as quantities such as scalar dissipation rate in the context of a passive scalar(that is the mixture fraction Z).
In another DNS study of turbulent shear-layer done by Pantano and Sarkar[25], they presented effects of Mach number on the turbulent field and found out that all turbulence intensity components as well as shear stress are decreased as Mach number is increased. They focused on fluctuations of pressure-strain term in the Reynolds-Stress equation which shows a similar behaviour, that causes an energy transfer to the production term and to the fluctuation in cross-stream direction and to the growth rate of the mixing-layer. They finished their work by looking at the effect of various densities in mixing-layer streams which leads to the substantial decreasing in momentum thickness growth rate and also vorticity thickness growth rate and shear stress term in a smaller value compare to the momentum thickness. In addition, the shear-layer dividing streamlines tend to incline toward the lower-density fluid.

Mason and Rutland[26] looked into the interaction between turbulence and combustion by direct numerical simulation of a single-step second-order irreversible reaction between generic fuel and oxidiser. They focused on the effects of heat release on shear layer growth rate and effects of combustion on the turbulent kinetic energy budgets. They considered

a spatially developing mixing layer with slip wall conditions in the transverse direction far enough from the flow to mimic free-stream condition, periodic condition in span-wise direction to resemble a homogeneous direction for statistical averages, and an inflow and an outflow condition with two separate streams of fuel and oxidiser with different inlet velocities to trigger vortex formation. The velocity profile defined for the streams was a hyperbolic tangent function. To make the flow turbulent, fundamental (Kelvin-Helmholtz) mode of the velocity profile were added as perturbations, excluding 'outer modes' to cause the shear-layer considered as 'forced'. They disregarded the radiation effect as well as neglecting Soret and Dufour effects. The grid size they employed for their domain was chosen in such a way that resolves every structure of the flame and vortices evolving in stream direction. Time step set, was smaller than the flow and reaction timescales, likewise. The post-processing was done by averaging quite a few number of averaging in time as well as in periodic direction to simulate homogeneity in periodic direction.This leads to have turbulent kinetic energy k and other terms in TKE equation stationary and function of two other directions, only. They did their simulations in low Reynolds number to avoid compressibility effects and to help then only evaluate effects of heat release and reaction rate on turbulence. The heat release parameter they used was close to hydrocarbon combustion chemistry. To represent the reaction rate, they introduced the Damköhler number. They analyzed effects of heat release on shear-layer by trying different amount of this factor while keeping Damköhler number unchanged, and likewise, they studied effects of reaction rate on turbulent flow by changing the Damköhler number while heat release parameter is fixed. They found out that as heat release rate increases, vorticity growth rate decreases by suppressing vortex roll-up, as it is expected. Likewise, higher amounts of reaction rate will affect vortex formation, tending to decrease growth rate. They then moved on to analyse how different heat release and reaction rates change the turbulence parameters by look into turbulent kinetic energy budget. Among TKE budgets, turbulent production term is mainly balanced by molecular diffusion, dissipation, turbulent transport, and pressure transport terms in the first quarter of the computational domain where the shear rate is large and initial vortex roll-up occurs. Further downstream, at about half of the domain length and beyond, the molecular diffusion become insignificant and the only quantities which balance the production rate are dissipation, turbulent transport and pressure transport terms. The latter two terms, i.e. pressure transport and turbulent transport behave in a complex manner so that they are negative at the centre of the layer while they are positive towards the edges, helping the growth rate of the mixing layer. Other TKE terms such as dissipation, convection and pressure dilatation are always negative across the shear layer(in transverse direction). They finished their work by comparison the DNS data with standard $k - \epsilon$ model for production and turbulent transport.

Similar to Pantano and Knaus[5], Mahle et. al.[27] studied the effect of heat release rate and compressibility on mixing layers turbulence with focus on Reynolds stress budget as well as turbulent kinetic energy transport equation. Because of existence of reaction in their simulation, they scrutinised pressure-strain correlation in Reynolds stress transport equation. Mathew et. al.[28] also did brief survey on the effects of compressibility and heat release on entrainment process in shear layers. Similarly, results published by Vreman et al.[29] also specifies effects of compressibility on mixing layers growth rate in more details by scrutinising the pressure-strain term in Reynolds stress budget.

Some of the researches were dedicated to study the interaction of two terms with each other in the turbulence field. For example, studies of Swaminathan and Bray[30] deals with the interaction of dilatation on scalar dissipation. In order to achieve this, they expanded the scalar dissipation rate by considering its transport equation and did a thorough analysis to find out how dilatation affects scalar dissipation rate.

Flamelet approach is also a technique which has been widely used by researchers for non-premixed combustion calculations either for hydrogen or other species. The idea behind it is to separate the turbulent flow field solution from the mixture field which is determined by the reaction mechanism[31]. The mixture field is represented by a passive scalar called mixture fraction and therefore, a model for scalar dissipation rate is also needed to be derived in order to account for influence of the flow field on the flame structure[32]. Where differential diffusion is considered, alternative formulations for the mixture fraction, diffusion velocity as well as scalar dissipation rate have to be considered to lead the solution to more accurate results[33]. Dinesh et. al.[34] also combined DNS calculation and flamelet generated manifold(FGM) approach based on a detailed chemistry of hydrogen. They applied the flamelet concept to jet flow impinging on the wall under relatively high Reynolds number. Results from the one-dimensional FGM approach are used as input for the three-dimensional DNS. The variables they obtained from their flamelet calculations are specific heat, viscosity, thermal conductivity, specific heat and constant pressure and enthalpy which are used in the energy and mass transfer equations. Some other publications by Dinesh et. al also focuses on the LES[35] or DNS of hydrogen combustion by FGM modelling to further investigate the effects of non-unity Lewis number(known as preferential diffusion)[36] or the effects of fuel variability(pure hydrogen or hydrogen-syngas mixture) on the species concentration[37].

Most of the researches on shear layers mentioned above, have considered unique properties for the scalars involved in the simulation such as equal molecular weight or equal scalar diffusivity. A comprehensive review by Bilger[38] or results published by

Chakraborty and Cant[39] considered the effect of non-equal diffusion coefficients demonstrated as the different non-unity Lewis number. Both of these researches have considered reactive flows. By a survey through the literatures in this field, it is understood that not many publications have been devoted to the effects of differential diffusion in non-reactive mixing layers considering pure mixing only.

Following some previous researches, in this work, simulation of a turbulent temporally-evolving mixing layers carrying streams of pure hydrogen and pure oxygen or diluted stream of hydrogen with pure oxygen with real species properties (i.e. molecular weight and diffusivity) have been accomplished. Mixing layers are performed in many combustion devices such as burners. In addition, they are also found in jet flows. Knowing such facts which highlight the practical applications in which mixing layers of non-premixed reactants are formed, provides sufficient reasons to perform more research on the mixing layers. In the current research, results are obtained under no-reaction circumstance, a global single-step Arrhenius form reaction mechanism and a more complicated version with 37 elementary reaction steps. Studies have been performed for mean flow variables together with turbulence and scalar statistics analysis under different diffusivity effect. Numerical methods and the results are presented in the next few chapters as follows: Chapter 2 explains the methodology used in the simulation of a binary-species mixing layer, chapter 3 is about the numerical formulations applied for a multi-species mixing layer undergoing finite-rate reaction mechanisms, chapters 4 and 5 have been dedicated to the results obtained from DNS of the equations presented in chapter 2 and chapter 3, respectively, and finally, chapter 6 presents the future work following the achievements in this work for further development of the objectives sought in this research. Appendix A explains the boundary condition formulation used in this work. Appendix B is about expansion of the Navier-Stokes equations used in chapter 4 and chapter 5. Appendix C gives a summary of the amount of work that has been done and CPU time spent in order to develop the 3D compressible multi-species Navier-Stokes equations and to perform the simulations presented in this work.

Chapter 2

Mathematical and numerical formulations for binary-species mixing layers

The methodology used in this part of the work is based on what has been done by Luo[15] but with some modifications and additions to the energy and mass fraction transport equations so that species with different molecular weight and different diffusivity can be simulated correctly. Three-dimensional compressible time-dependent Navier-Stokes equations have been solved in conjunction with transport equations for a single-step hydrogen-oxygen combustion mechanism. Boundaries in the stream-wise and span-wise directions are assumed to be periodic that results in a homogeneous turbulent flow whereas the boundaries in the transverse directions are set to be non-reflecting which permits having an inhomogeneity in this direction. A characteristic non-reflecting boundary condition has been used and tested extensively in previous reacting and non-reacting simulations with similar configurations and was found to be adequately effective for DNS studies[5, 15, 18, 23, 24, 40, 41, 42]. Discretization for spatial derivatives is done using Padé scheme[43] with different order of accuracy for grids located at the boundaries, near the boundaries and interior domain. Temporal derivatives have been treated using a third-order Runge-Kutta method[44]. The flow is subjected to disturbances. The disturbances which are necessary to trigger the turbulence in the flow are determined from a linear stability analysis. Eventually, the flow is initialized and governing equations are solved for the whole domain that has a box-type geometry. Below, are given further explanations about the methodology employed in this work.

2.1 Governing Equations

Full three-dimensional time-dependent compressible Navier-Stokes coupled with chemical species transport equations has been considered for simulation of temporal mixing layer undergoing finite-rate chemical reaction. X, Y and Z axes are considered to be spanwise, streamwise and transverse(cross-streamwise) directions, respectively. The equations are used in their non-dimensional form. Non-dimensionalization has been done with respect to the average initial free-stream properties at fuel and oxidiser sides such as $U^*_{ref} = U^*_1 - U^*_2$, $\rho^*_{ref} = (\rho^*_1 + \rho^*_2)/2$ and $T^*_{ref} = (T^*_1 + T^*_2)/2$. Pressure is non-dimensionalized by $\rho^*_{ref}U^{*2}_{ref}$ and to obtain a non-dimensional length, all dimensions are divided by the $\delta^*_{\omega_0} = \lambda_y/7.29$ in which $\lambda_y = L_y/(initial \quad number \quad of \quad vortices)$ is the wavelength of the initial fundamental spanwise vorticity disturbance(most unstable wave length [45]) and the "initial number of vortices" is 4. The non-dimensionalised equations in tensor form are listed as follows:

$$\frac{\partial \rho}{\partial t} = -\frac{\partial(\rho u_i)}{\partial x_i} \tag{2.1}$$

$$\frac{\partial \rho u_i}{\partial t} = -\frac{\partial(\rho u_i u_j + p\delta_{ij})}{\partial x_j} + \frac{\partial \tau_{ij}}{\partial x_j} \tag{2.2}$$

$$\frac{\partial E_T}{\partial t} = -\frac{\partial[(E_T + p)u_i]}{\partial x_i} - \frac{\partial q_i}{\partial x_i} + \frac{\partial(u_j\tau_{ij})}{\partial x_i} + \sum_{n=1}^{N_s} \Delta h^o_{f_n}\omega_n \tag{2.3}$$

$$\frac{\partial(\rho Y_n)}{\partial t} = -\frac{\partial[\rho Y_n(u_i + V^c_n)]}{\partial x_i} + \frac{\partial}{\partial x_i}(\rho D_n \frac{W_n}{W_{mix}}\frac{\partial X_n}{\partial x_i}) + \omega_n \tag{2.4}$$

where

$$E_T = \rho(e + \frac{1}{2}u_i u_i) \tag{2.5}$$

$$\tau_{ij} = \frac{\mu}{Re}(\frac{\partial u_i}{\partial x_j} + \frac{\partial u_j}{\partial x_i} - \frac{2}{3}\frac{\partial u_k}{\partial x_k}\delta_{ij}) \tag{2.6}$$

$$q_i = \frac{-\mu}{(\gamma - 1)Ma^2 PrRe}\frac{\partial T}{\partial x_i} \tag{2.7}$$

$$V^c_n = \sum_{n=1}^{N_s} D_n \frac{W_n}{W_{mix}}\frac{\partial X_n}{\partial x_i} \tag{2.8}$$

and,

$$D_n = \frac{1}{Re}\frac{\mu}{\rho Sc_n} = \frac{1}{Re}\frac{\mu}{\rho PrLe_n} \tag{2.9}$$

Non-dimensional pressure and internal energy will take the form of:

$$p = (\gamma - 1)\rho e = (\gamma - 1)[E_T - \frac{1}{2}\rho(u_i u_i)] = \frac{\rho T}{\gamma M^2_a}(\sum_{n=1}^{N_s}\frac{Y_n}{W_n}) \tag{2.10}$$

$$e = \frac{T}{\gamma(\gamma-1)M_a^2}\sum_{n=1}^{N_s}\frac{Y_n}{W_n} \tag{2.11}$$

Temperature can then be calculated using ideal-gas law or from the internal energy, e. The code used in this part, can perform combustion calculations for a general single-step chemical reaction. In the present work, one-step realistic chemistry of hydrogen and oxygen has been implemented for the first attempt; then this research will proceed to more accurate multi-step $H_2 - O_2$ mechanism like the mechanisms used and tested in research works of[18, 23, 46, 47], some had an evaluation and comparison between a number of detailed-mechanisms for specific industrial purposes[48]. Among those who have done studies on hydrogen-oxygen combustion mechanism, some researchers used a reduced chemistry model rather than a detailed one[49] while some looked at either of the mechanisms[50]. Some other researchers reduced even more the complexity of the system by employing a one-step hydrogen combustion mechanism and achieved acceptable simulation results in certain flow conditions[51, 52, 53]. The global single-step irreversible reaction that is used in the present work can be written as follows:

$$2H_2 + O_2 \longrightarrow 2H_2O \tag{2.12}$$

The reaction rate for individual species(rate of production or consumption) is defined by Arrhenius Law, which appears in its non-dimensional form as follows:

$$\omega_n = W_n\sum_{\ell=1}^{N_r} Da_\ell(\nu''_{n,\ell} - \nu'_{n,\ell})\prod_{n=1}^{N_s}(\frac{\rho Y_n}{W_n})^{\nu'_n} exp[-Ze(\frac{1}{T}-\frac{1}{T_f})] \tag{2.13}$$

Damkohler number is actually representing the ratio of characteristic fluid time per characteristic reaction time for reaction ℓ and is written in its non-diemnsional form as follows:

$$Da_\ell = t_{ref}(A_\ell T_\ell^\alpha)(\frac{\rho_{ref}}{W_{ref}})^{\sum_{n=1}^{N_s}\nu'_n - 1} exp(-\frac{\beta_\ell}{T_f}) \tag{2.14}$$

T_f is non-dimensional temperature rise (also shown as α) and Ze is Zeldovich number which is a measure of non-dimensional activation energy(also written as β_ℓ):

$$Ze = \beta_\ell \equiv \frac{E_{a,\ell}}{R_u T_f^*}\frac{T_f^*}{T_{ref}} = \frac{E_{a,\ell}}{R_u T_f^*}\alpha \tag{2.15}$$

To calculate viscosity, Sutherland's Law formulation has been employed which produce more accurate results compare to the Power Law formulation especially when the temperature reaches higher values. The non-dimensional viscosity equation has the form:

$$\mu = T^{\frac{3}{2}}\frac{1+S}{T+S} \tag{2.16}$$

with $S = \frac{111}{T_{ref}}$.

2.2 Numerical Algorithms

Compact implicit finite difference scheme introduced by Lele[43] has been used for spatial derivatives that leads to an acceptable and more accurate results compare to other traditional finite difference approximations which are employed in direct simulation techniques. It can be used on range of spatial scales. It is, actually, generalization of Padé or compact finite difference scheme [54, 55]. Two formulations were introduced by Lele for approximation of first-order and second-order derivatives which are explained below.

2.2.1 Approximation of first derivatives

Consider a computational domain with the nodes indexed by i. The independent variable at each nodes is $x_i = h(i-1)$ for $1 \leq i \leq N$ and the value of function at each node is defined $f_i = f(x_i)$ in which N is total number of nodes and h is grid spacing that is considered constatnt. The finite difference approximation of function f at node i is defined as $f'_i = \frac{df}{dx}(x_i)$. In its general form the first derivative are written in the form of:

$$\beta f'_{i-2} + \alpha f'_{i-1} + f'_i + \alpha f'_{i+1} + \beta f'_{i+2} = c\frac{f_{i+3} - f_{i-3}}{6h} + b\frac{f_{i+2} - f_{i-2}}{4h} + a\frac{f_{i+1} - f_{i-1}}{2h} \quad (2.17)$$

To specify the coefficients a,b,c,α and β, this equation must be matched with the Taylor series expansion with various orders of accuracy. More details have been explained in reference[43]. The coefficients in their general form(one-parameter) are as follows:

$$\beta = 0, a = \frac{2}{3}(\alpha + 2), b = \frac{1}{3}(4\alpha - 1), c = 0 \quad (2.18)$$

In the present code, the sixth order of accuracy has been chosen for all grid points which are in periodic directions and internal grid points that are in non-periodic directions. This has been accomplished by choosing $\alpha = \frac{1}{3}$. Rewriting coefficients, one may obtain:

$$\alpha = \frac{1}{3}, \beta = 0, a = \frac{14}{9}, b = \frac{1}{9}, c = 0 \quad (2.19)$$

Applying these coefficients, the maximum stencil size obtained for independent variables in the left-hand side and right-hand side are 3 and 5, respectively, with a truncation error equal to $\frac{4}{5!}h^6 f^{(7)}$. Considering for the whole domain, the equation (2.17) leads to system of linear equations with a tridiagonal matrix for the left-hand side variables (first order derivatives) which can be solved easily by a few lines of programming.

For the grid points which are at the vicinity of non-periodic boundaries, coefficient b is also set to zero by choosing $\alpha = \frac{1}{4}$ that results in a fourth-order conventional Padé scheme with maximum stencil size of 3 in both right hand side and left hand side of equation (2.17). The coefficients are:

$$\alpha = \frac{1}{4}, \beta = 0, a = \frac{3}{2}, b = 0, c = 0 \tag{2.20}$$

And finally, for the grid points which are exactly located at non-periodic boundaries, additional relations must be taken into consideration. At the boundaries, the accuracy of spatial derivatives has to be decreased [40] . Typically, central difference scheme is replaced by one-sided approximation. These points have been treated by equation which has third order of accuracy for boundaries. The relation for the first-order derivative at the boundary is written as:

$$f'_1 + \alpha f'_2 = \frac{1}{h}(af_1 + bf_2 + cf_3 + df_4) \tag{2.21}$$

A third-order accuracy is achieved by coefficients as follows:

$$a = -\frac{11 + 2\alpha}{6}, b = \frac{6 - \alpha}{2}, c = \frac{2\alpha - 3}{2}, d = \frac{2 - \alpha}{6} \tag{2.22}$$

with one parameter α. Choosing $\alpha = 2$, the coefficients which are used in the current work are written as follows:

$$\alpha = 2, a = -\frac{5}{2}, b = 2, c = \frac{1}{2}, d = 0 \tag{2.23}$$

Truncation error will be $\frac{2(\alpha-3)}{4!}h^3 f_1^{(4)}$ for this third order approximation.

2.2.2 Approximation of second derivatives

Analogous to the first-order derivatives, second-order derivatives are discretized using the equation below:

$$\beta f''_{i-2} + \alpha f''_{i-1} + f''_i + \alpha f''_{i+1} + \beta f''_{i+2} = c\frac{f_{i+3} - 2f_i + f_{i-3}}{9h^2} + b\frac{f_{i+2} - 2f_i + f_{i-2}}{4h^2} + a\frac{f_{i+1} - 2f_i + f_{i-1}}{h^2} \tag{2.24}$$

As before, to obtain a family of sixth-order scheme, the coefficients are as follows:

$$a = \frac{6 - 9\alpha - 12\beta}{4}, b = \frac{-3 + 24\alpha - 6\beta}{5}, c = \frac{2 - 11\alpha + 124\beta}{20} \tag{2.25}$$

which are a set of two-parameter coefficients. By selecting $\alpha = \frac{2}{11}$ and $\beta = 0$, the coefficients used in the current work are obtained:

$$\alpha = \frac{2}{11}, \beta = 0, a = \frac{12}{11}, b = \frac{3}{11}, c = 0 \tag{2.26}$$

The maximum stencil size for left-hand side and right-hand side will become 3 and 5, respectively, with a truncation error of $\frac{-8.23}{11.8!}h^6 f^{(8)}$. Points next to the boundary are treated by one-parameter family of fourth-order scheme:

$$\beta = 0, a = \frac{4}{3}(1-\alpha), b = \frac{1}{3}(-1+10\alpha), c = 0 \tag{2.27}$$

α is chosen to be $\frac{1}{10}$ that results in the classical Padé scheme. So, the coefficients which have been used in the current work can be rewritten as:

$$\beta = 0, \alpha = \frac{1}{10}, a = \frac{6}{5}, b = 0, c = 0 \tag{2.28}$$

For the points at the non-periodic borders, similar to what has been done for the first-order derivatives, the equation

$$f_1'' + \alpha f_2'' = \frac{1}{h^2}(af_1 + bf_2 + cf_3 + df_4 + ef_5) \tag{2.29}$$

is used. To have a third order scheme at the boundaries, the one-parameter coefficients are written as follows:

$$a = \frac{11\alpha + 35}{12}, b = -\frac{5\alpha + 26}{3}, c = \frac{\alpha + 19}{2}, d = -\frac{\alpha - 14}{3}, e = \frac{11 - \alpha}{12} \tag{2.30}$$

Choosing $\alpha = 11$, results in:

$$a = 13, b = -27, c = 15, d = -1, e = 0 \tag{2.31}$$

with truncation error equal to $\frac{1}{12}h^3 f^{(5)}$.

2.2.3 Advancement in Time

Time-marching is done by a scheme of explicit third-order Runge-Kutta method introduced by Wray[44]. As also described in reference [41], for each variable of the flow, two storage locations in the memory are considered, say Q and Q_w as shown in equation below:

$$Q^{new} = a_1 \Delta t Q^{old} + Q_w^{old} \qquad , \qquad Q_w^{new} = a_2 \Delta t Q^{old} + Q_w^{old} \tag{2.32}$$

At the beginning, the initialized values for variables are stored in both Q and Q_w; so they are equal. The data in Q is used to compute the right-hand side of the Navier-Stokes equations. Later on, the time-marching will start to be done in three steps; at each step, right-hand side is evaluated, and the new value for Q is used to update both Q and Q_w successively by overwriting the old Q and Q_w. Before the old Q is overwritten, it is stored in another temporary variable to be used for computation of the new Q_w. The coefficients a_1 and a_2 are chosen to be $(\frac{2}{3}, \frac{1}{4})$ for step 1, $(\frac{5}{12}, \frac{3}{20})$ for step 2, and $(\frac{3}{5}, \frac{3}{5})$ for step 3, respectively, and in this manner all three steps of Runge-Kutta time-advancement are accomplished for one time step. To calculate the appropriate time step for the simulation, a model of convection-diffusion-combustion equations has been considered that leads to have the time step as:

$$\Delta t = \frac{CFL}{D_c + D_\mu + D_{com}} \tag{2.33}$$

in which:

$$D_c = \pi c(\frac{1}{\Delta x} + \frac{1}{\Delta y} + \frac{1}{\Delta z}) + \pi(\frac{|u|}{\Delta x} + \frac{|v|}{\Delta y} + \frac{|w|}{\Delta z}) \tag{2.34}$$

$$D_\mu = \frac{\pi^2 \mu}{(\gamma - 1)\rho M_a^2 RePr}(\frac{1}{\Delta x^2} + \frac{1}{\Delta y^2} + \frac{1}{\Delta z^2}) \tag{2.35}$$

where $\Delta x = L_x/N_x$ and similarly for Δy and Δz. D_{com} is chosen to have a linear relation with sum of D_c and D_μ depends on the change of the product mass fraction before and after each computational loop.

$$D_{com} = C.(D_c + D_\mu) \tag{2.36}$$

C is an integer number which depends on the rate of product formation (H_2O in present work). As the difference between product mass fraction before and after each step increases, C becomes larger which results in smaller value for Δt in equation (2.33). In other words, as reaction rate increases, Δt must decrease to capture all time scales of combustion. Δt is computed in all grid points and the worst-case cell is used to fix the time step which actually returns the smallest value for Δt. More explanations have been given in reference [41]. Non-dimensional values of the time step used in the present work varies from O(-4) to O(-2).

2.3 Initial Conditions

Initialization is accomplished by applying an error function variation for streamwise(v) velocity component, mass fraction and temperature distribution. Pressure is set to be uniform all over the computational domain. Spanwise(u) and transverse(w) mean

velocity components initially are set to zero before adding disturbances. Mean density is then initialized using the ideal-gas law for the mixture:

$$\rho = \frac{\gamma M_a^2 p}{T} / (\sum_{n=1}^{N_s} \frac{Y_n}{W_n}) \tag{2.37}$$

Disturbances have been added in the form of velocity fluctuations superimposed on the initial mean velocity profile followed by a procedure used in the work of Miller and Bellan[56] and has been introduced by Moser and Rogers[45]. Both two-dimensional and three-dimensioanl vorticity perturbations are superimposed onto the initial mean velocity profile in spanwise and streamwise directions, respectively:

$$\omega_x(y,z) = F_{2D}(\lambda_x \Delta U_0/\Gamma_x) f(y) f(z) \tag{2.38}$$

$$\omega_y(x,z) = F_{3D}(\lambda_y \Delta U_0/\Gamma_y) f(x) f(z) \tag{2.39}$$

where Γ_x and Γ_y are circulations and,

$$f(x) = A_0 \sin(\frac{2\pi x}{\lambda_x}) + A_1 \sin(\frac{\pi x}{L_x}) \tag{2.40}$$

$$f(y) = B_0 |\sin(\frac{\pi y}{\lambda_y})| + B_1 |\sin(\frac{\pi y}{2\lambda_y})| + B_2 |\sin(\frac{\pi y}{4\lambda_y})| + B_3 |\sin(\frac{\pi y}{8\lambda_y} - \frac{\pi}{2})| \tag{2.41}$$

$$f(z) = exp[-\pi(\frac{z}{\delta_{\omega_0}})^2] \tag{2.42}$$

with indices x for spanwise, y for streamwise and z for transverse directions. Parameters used in the simulations are as follows: $F_{2D} = 0.125$, $F_{3D} = 0.075$, $A_0 = 1$, $A_1 = 0.025$, $B_0 = 1$, $B_1 = 0.5$, and $B_2 = B_3 = 0.35$. The streamwise perturbations' wavelength is $\lambda_y = 7.29\delta_{\omega_0}$ with $\delta_{\omega_0} = 8.57 * 10^{-3} m$. 7.29 is the most unstable wavelength stated in [45]. Spanwise perturbations' wavelength is $0.6\lambda_y$ since the domain length in that direction is 0.6 of the length in streamwise direction.

In addition to initialization of the flow parameters stated above, some reference parameters such as Re, Pr, Sc_n are also needed to be set for the flow simulation. These are listed in chapter 4.

2.4 Boundary Conditions

Thompson's work[42, 57] were among the researches dedicated to boundary treatment. In his first paper[57] a model for 1D and 2D hyperbolic system of equations was developed but only one single formalism for all types of boundary conditions was applied. In

his next paper published[42], the characteristic form of equations for 3D setup was derived and different way of treatment to different boundary types was applied accordibgly. Poinsot and Lele[40] expanded the work of Thompson by applying the method for both Euler and Navier-Stokes equations and presenting more example cases. The method by which boundaries are treated is based on local one-dimensional inviscid(LODI) analysis of the characteristic waves traveling in and out of the computational domain in any particular direction, that's why this method of setting up the boundaries is known as the "Navier-Stokes characteristic boundary condition(NSCBC)" approach. NSCBC approach actually sets both physical and numerical(also known as 'soft') conditions at one or more than one boundary for Euler or Navier-Stokes equations. For Navier-Stokes equations, they add additional relations for the effects of viscosity and diffusivity to the boundary types they studied: supersonic inflow and outflow, subsonic inflow and outflow, and slip and non-slip walls. Some authors did slight modifications to some of the characteristic wave lengths used in the boundary conditions. Among those, one can refer to the paper published by Polifke et. al. [58] which modified the linear relaxation term proposed by Rudy and Strikwerda[59] or the paper by Prosser[60] which proposed a modification to the work of Hedstrom[61] claiming that the new modification either does not generate spurious pressure waves when applied in turbulent flows or allow them to be convected out of the computational domain and the solution reaches to a acoustic transparency state. However, it has been stated that the new modification still has some problems when acoustic waves cross the boundaries at an inclined angle. Lodato et. al.[62] have tested a treatment method for the problem of wave propagation across the corners, edges and waves which do not have normal direction toward the surface. While some researchers study different types boundary conditions for different types of flows, some studies are only devoted to apply modifications to the boundary conditions for a one type of the flow, e.g. boundary condition setup for outflow[63, 64, 65].

For the box-type computational domain used in the present work, boundaries in streamwise and span-wise directions are chosen to be periodic. Choosing this type of boundaries resembles the condition in which a reference frame moves along the upper and lower streams at the mean flow speed and every property of the flow are repeated at the periodic boundaries and because of this, they need not any specific treatment. The boundaries which need special treatment are the ones in the transverse coordinate directions which are placed relatively far from the centre of the mixing-layer to mimic an infinite domain. The method of boundary treatment used in this work, was the one introduced by Thompson[42] which is based on treatment of the waves coming into and going out of the computational domain of hyperbolic systems of equations without any type of modifications proposed by others. It is known that the Navier-Stokes equations are no longer hyperbolic as Re decreases from infinity to finite values [66]. Moreover, addition of viscosity changes the mathematical nature of the system of equations by

increasing its order. However, since Navier-Stokes equations propagate waves in all directions, the first logical approximation is therefore to assume that waves are only associated with the hyperbolic part of the equations and neglect waves associated with the diffusion processes [40].

In the present work of studying a mixing-layer problem, since no physical boundary exists to impose relevant physical conditions on, conservation equations themselves are solved at the boundaries. For each point on the boundary, the characteristic waves are specified; if they behave like an incoming wave, their amplitudes are set to zero otherwise, if they are outgoing waves, they simply just leave the domain and there is no need to take any treatment for them. This kind of treatment, sets non-reflecting boundaries for the computational domain which is inevitable specifically in turbulent shear flows where acoustic waves play an important role in combustion instabilities. When the flow near the boundary can be decomposed into fluctuations with small amplitude about a uniform state, or when the flow cannot be represented as small amplitude disturbances to a nearly uniform state, non-reflecting boundary conditions (NRBCs) are used which have been studied for more than thirty years[67]. As also emphasised by Polifke et al.[58], setting up acoustically non-reflecting boundaries for compressible turbulent flow simulation, especially when the flow undergoes a combustion process and encounters strong instabilities as well as rapid fluctuations in flow properties, is a prerequisite for any CFD applications. These acoustic reflections arise from vortex roll-up, pairing and shedding, shredding, and shape oscillations [13].

Consider the computational domain shown in figure (2.1) in which transverse direction is assumed to be non-periodic and is labeled as x for which NSCBC must be applied. In this figure, characteristic velocity λ_i, are associated with the corresponding ℓ_i's which are the amplitudes of characteristic waves.

The ℓ_i's for three-dimensional equations with one or more scalars (Y_i) are calculated as follows:

$$\ell_1 = \lambda_1(\frac{\partial p}{\partial x} - \rho c\frac{\partial u}{\partial x}) \tag{2.43}$$

$$\ell_2 = \lambda_2(c^2\frac{\partial \rho}{\partial x} - \frac{\partial p}{\partial x}) \tag{2.44}$$

$$\ell_3 = \lambda_3\frac{\partial v}{\partial x} \tag{2.45}$$

$$\ell_4 = \lambda_4\frac{\partial w}{\partial x} \tag{2.46}$$

$$\ell_5 = \lambda_5(\frac{\partial p}{\partial x} + \rho c\frac{\partial u}{\partial x}) \tag{2.47}$$

$$\ell_{i+5} = \lambda_{i+5}\frac{\partial Y_i}{\partial x} \qquad i = 1, N_s \tag{2.48}$$

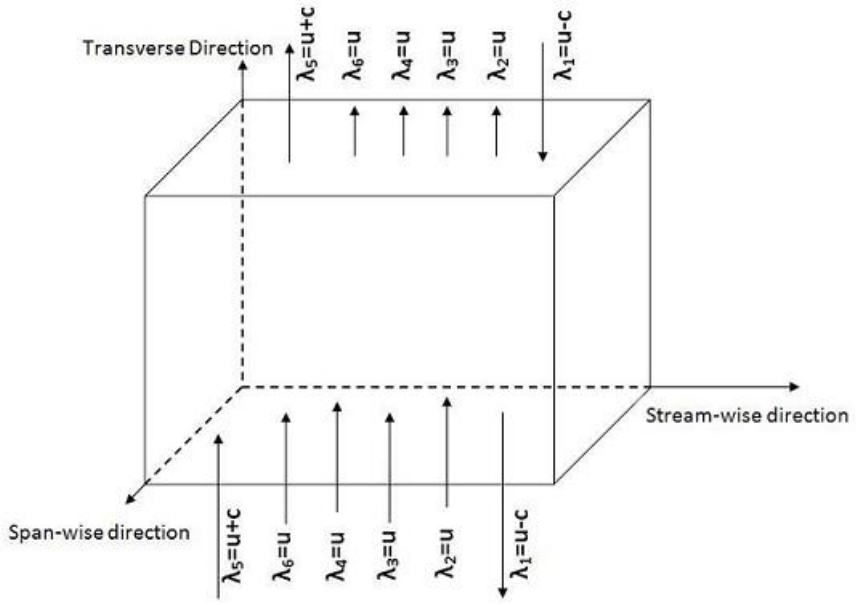

FIGURE 2.1: Characteristic waves traveling in and out of the computational domain for a subsonic flow

in which λ_1 and λ_5 are velocities of sound waves traveling in negative and positive x direction, λ_2 is the convection velocity(the speed at which entropy waves will travel), and finally λ_3, λ_4 and λ_6 are the velocities at which v, w and Y_f are advected in the transverse direction; and are computed as follows:

$$\lambda_1 = u - c, \qquad \lambda_2 = \lambda_3 = \lambda_4 = \lambda_i = u, \qquad \lambda_5 = u + c \tag{2.49}$$

For computation purpose, these characteristic waves' amplitudes are first determined for the points located on the boundaries; then, they are examined to know if they are coming into the computational domain or they are going out of the domain. If the characteristic waves are going out of the domain no action are taken against them, otherwise, if they are coming into the domain, they are set to zero to not to contaminate the solution of the computational domain. The method by which characteristic waves are computed for treatment of the boundaries, has been explained in [57]. The equations obtained at the boundaries are transformed to the conservative form later on, and simulation continues. Following the explanations of Thompson[57], a step by step description for calculation of the wave amplitudes are given in the appendix A.

Chapter 3

Mathematical and numerical formulations for multi-species mixing layers

Three dimensional compressible time dependent Navier-Stokes equations have been solved in conjunction with transport equations for hydrogen-oxygen with 37 elementary steps. The reaction mechanism has been extracted from the work of Stahl and Warnatz[68]. Similar to the technique described in previous chapter, boundaries have been set to be periodic in streamwise and spanwise directions and non-reflecting in transverse (vertical, z in this work) direction but unlike to what explained before, boundaries are treated for a multi-species gas mixture which introduces much more complexity compared to the previous one. Discretization are based on the method which was extensively elucidated in previous chapter: Discretization for spatial derivatives is done using Padé scheme with different order of accuracy for grids located at the boundaries, near the boundaries and interior domain. Temporal derivatives have been treated by employing a third-order Runge-Kutta method explained in previous chapter. Disturbances, however, have been applied according to a method introduced by Roger and Moser[10]. The disturbances which are necessary to trigger the turbulence in the flow are determined from a linear stability analysis. Eventually, the flow is initialized and governing equations are solved for the whole domain that has a box-type geometry. Below, are given further explanations about the methodology employed for multi-species flow.

3.1 Governing Equations

Full three-dimensional time-dependent compressible Navier-Stokes coupled with chemical species transport equations has been considered for simulation of temporal mixing layer undergoing finite-rate chemical reactions. The equations are used in their non-dimensional form. Non-dimensionalization has been done with respect to the average free-stream properties at fuel and oxidiser sides similar to what explained in previous chapter.

The equations are listed in their dimensional form as follows:

$$\frac{\partial \rho}{\partial t} = -\frac{\partial(\rho u_i)}{\partial x_i} \tag{3.1}$$

$$\frac{\partial \rho u_i}{\partial t} = -\frac{\partial(\rho u_i u_j + p\delta_{ij})}{\partial x_j} + \frac{\partial \tau_{ij}}{\partial x_j} \tag{3.2}$$

$$\frac{\partial E_T}{\partial t} = -\frac{\partial[(E_T + p)u_i]}{\partial x_i} - \frac{\partial q_i}{\partial x_i} + \frac{\partial(u_j \tau_{ij})}{\partial x_i} \tag{3.3}$$

$$\frac{\partial(\rho Y_n)}{\partial t} = -\frac{\partial[\rho Y_n(u_i + V_i^c)]}{\partial x_i} + \frac{\partial}{\partial x_i}(\rho D_n \frac{W_n}{W_{mix}} \frac{\partial X_n}{\partial x_i}) + \dot{\omega_n} \tag{3.4}$$

where

$$E_T = \rho(e + \frac{1}{2} u_i u_i) \tag{3.5}$$

$$e = \sum_{n=1}^{N_s} h_n Y_n - \frac{p}{\rho} = \frac{p}{\rho(\gamma_{mix} - 1)} \tag{3.6}$$

$$\tau_{ij} = \mu(\frac{\partial u_i}{\partial x_j} + \frac{\partial u_j}{\partial x_i} - \frac{2}{3}\frac{\partial u_k}{\partial x_k}\delta_{ij}) \tag{3.7}$$

$$q_i = \lambda_{mix}\frac{\partial T}{\partial x_i} + \rho \sum_{n=1}^{N_s} h_n Y_n V_{ni} \tag{3.8}$$

$$h_n = \Delta h_{f_n}^0 + \int_{T_0}^{T} C_{p_n}(T) dT \tag{3.9}$$

V_{ni} is the diffusion velocity and consists of a diffusion term and a correction velocity term and may be written in the form of:

$$V_{ni} = -\frac{D_n}{X_n}\frac{\partial X_n}{\partial x_i} + \sum_{n=1}^{N_s} Y_\beta (\frac{D_\beta}{X_\beta})\frac{\partial X_\beta}{\partial x_i} \tag{3.10}$$

with D_n which is written as,

$$D_n = \frac{1}{Re}\frac{\mu}{\rho Sc_n} \tag{3.11}$$

in non-dimensional form. In the simulations, Schmidt number is calculated by the alternative relation which is expressed in terms of Lewis number and Prandtl number($Sc =$

$Le * Pr$). Prandtl number is constant and so is Lewis number but it takes different values for each individual species. Other forms of diffusivity which is based on the species binary diffusion coefficient and species mole/mass fraction have also been use by others[1][69, 70]. Non-dimensional thermal conductivity of the mixture also takes the form of,

$$\lambda_{mix} = \frac{1}{Re}\frac{\mu Cp_{mix}}{Pr} \tag{3.12}$$

Temperature is calculated assuming that the the mixture follows ideal-gas law and is presented in its non-dimensional form:

$$T = \frac{e(\gamma_{mix} - 1)W_{mix}}{R_u} \tag{3.13}$$

with $W_{mix} = 1/\sum_{n=1}^{N_s} \frac{Y_i}{W_i}$ as the mixture average molecular weight.

To calculate viscosity, Sutherland's Law formulation has been employed which produce more accurate results compare to the Power Law formulation especially when the temperature reaches higher values. Similar to what explained in previous chapter, the non-dimensional viscosity equation takes the form of:

$$\mu = T^{\frac{3}{2}}\frac{1+S}{T+S} \tag{3.14}$$

with $S = \frac{111}{T_{ref}}$.

3.2 Chemistry and reaction mechanisms

A reduced mechanism consist of 37 elementary reaction steps has been used. Table 3.1 shows the $H_2 - O_2$ reduced mechanism in detail. The mechanism has been extracted from the work of Stahl and Warnatz[68]. This reduced mechanism had already been used by other research groups such as the work of Tabejamaat et. al.[71] Specific reaction rate constant is calculated based on the Arrhenius Law and is in the form of:

$$k(T) = AT^{\beta}exp(\frac{-E_a}{R_u T}) \tag{3.15}$$

In general, a reaction mechanism for multi-step reversible reactions is written as

$$\sum_{n=1}^{N_s} \nu'_{n,l} C_n = \sum_{n=1}^{N_s} \nu''_{n,l} C_n \tag{3.16}$$

[1] $D_n = \frac{1-Y_n}{\sum_{m=1,m\neq n}^{N_s} X_m/D_{nm}}$.

		Reaction	A_ℓ (cm/mol/s)	β_ℓ	E_{a_ℓ} KJ/mol
1	1f	$O_2 + H = OH + O$	2.20E14	0.00	70.30
2	1b	$OH + O = O_2 + H$	1.72E13	0.00	3.52
3	2f	$H_2 + O = OH + H$	5.06E04	2.67	26.30
4	2b	$OH + H = H_2 + O$	2.22E04	2.67	18.29
5	3f	$H_2 + OH = H_2O + H$	1.00E08	1.60	13.80
6	3b	$H_2O + H = H_2 + OH$	4.31E08	1.60	76.46
7	4f	$OH + OH = H_2O + O$	1.50E09	1.14	0.42
8	4b	$H_2 + O = OH + OH$	1.47E10	1.14	71.09
9	5f	$H + H + M = H_2 + M$	1.80E18	-1.00	0.00
10	5b	$H_2 + M = H + H + M$	7.26E18	-1.00	436.82
11	6f	$H + OH + M = H_2O + M$	2.20E22	-2.00	0.00
12	6b	$H_2O + M = H + OH + M$	3.83E23	-2.00	499.48
13	7f	$O + O + M = O_2 + M$	2.90E17	-1.00	0.00
14	7b	$O_2 + M = O + O + M$	6.55E18	-1.00	495.58
15	8f	$H + O_2 + M = HO_2 + M$	2.30E18	-0.80	0.00
16	8b	$HO_2 + M = H + O_2 + M$	3.19E18	-0.80	195.39
17	9f	$HO_2 + H = OH + OH$	1.50E14	0.00	4.20
18	9b	$OH + OH = HO_2 + H$	1.50E13	0.00	170.84
19	10f	$HO_2 + H = H_2 + O_2$	2.50E13	0.00	2.90
20	10b	$H_2 + O_2 = HO_2 + H$	7.27E13	0.00	244.33
21	11f	$HO_2 + H = H_2O + O$	3.00E13	0.00	7.20
22	11b	$H_2O + O = HO_2 + H$	2.95E13	0.00	244.51
23	12f	$HO_2 + O = OH + O_2$	1.80E13	0.00	-1.70
24	12b	$OH + O_2 = HO_2 + O$	2.30E13	0.00	231.71
25	13f	$HO_2 + OH = H_2O + O_2$	6.00E13	0.00	0.00
26	13b	$H_2O + O_2 = HO_2 + OH$	7.52E14	0.00	304.09
27	14	$HO_2 + HO_2 = H_2O_2 + O_2$	2.50E11	0.00	-5.20
28	15f	$OH + OH + M = H_2O_2 + M$	3.25E22	-2.00	0.00
29	15b	$H_2O_2 + M = OH + OH + M$	1.69E24	-2.00	202.29
30	16f	$H_2O_2 + H = H_2 + HO_2$	1.70E12	0.00	15.70
31	16b	$H_2 + HO_2 = H_2O_2 + H$	1.32E12	0.00	83.59
32	17f	$H_2O_2 + H = H_2O + OH$	1.00E13	0.00	15.00
33	17b	$H_2O + OH = H_2O_2 + H$	3.34E12	0.00	312.19
34	18f	$H_2O_2 + O = OH + HO_2$	2.80E13	0.00	26.80
35	18b	$OH + HO_2 = H_2O_2 + O$	9.51E12	0.00	86.68
36	19f	$H_2O_2 + OH = H_2O_2 + HO_2$	5.40E12	0.00	4.20
37	19b	$H_2O_2 + HO_2 = H_2O_2 + OH$	1.80E13	0.00	134.75

$C_M = \sum_{n=1}^{N_s} \alpha_n C_n = 1.0[H_2] + 6.50[H_2O] + 0.40[O_2] + 0.40[N_2]$

TABLE 3.1: Reaction mechanism for $H_2 - O_2$ system

The net rate of change in mole concentration of species n by reaction l is:

$$C_{n,l} = (\nu''_{n,l} - \nu'_{n,l})(k_{f,l} \prod_{n=1}^{N_s} C_n^{\nu'_{n,l}} - k_{b,l} \prod_{n=1}^{N_s} C_n^{\nu''_{n,l}}) \tag{3.17}$$

in which $\nu_{n,l}$ is the stoichiometric coefficient of species n for the reaction step l , with the prime and double primes representing the reactant and product, respectively. The overall production or consumption of species n can then be obtained:

$$\dot{\omega_n} = W_n \sum_{l=1}^{N_l} C_{n,l} \tag{3.18}$$

3.3 Numerical Algorithms

Numerical algorithm is in accordance with what used in chapter 2 except for time integration which is explained here.

3.3.1 Advancement in Time

Similar to the previous chapter, an explicit third-order Runge-Kutta method has been used but unlike the method used in previous chapter, a simple constant time step has been used for each simulation. The value of Δt is a factor of the reference time scale which is obtained by dividing the reference length scale(initial vorticity thickness) by the reference velocity. The largest non-dimensional time step used in multi-step multi-species simulations is order of O(-3) and used for non-reactive simulations whereas the reactive cases employed an order of magnitude smaller Δt.

3.4 Initial Conditions

Similar to section 2.3, domain initialisation is done by applying an error function profile for velocity, temperature, species' mass fraction(which are hydrogen, oxygen and an inert in this work). Pressure is applied as uniform and equal to 1 atm. Initial density was calculated using ideal gas law formulation(2.37).
Initial vorticity distribution is based on the work of Miller and Bellan[56] which was explained in previous chapter.

3.5 Boundary Conditions

Setting a correct boundary condition is the key for the successful simulation of a multi-species system of equations and is not a trivial task. Among the researches which are dedicated to boundary condition set up for a multi-species Navier-Stokes equations, one can refer to the work of Baum et. al.[72] which was taken into account the effect of different species and their thermodynamic properties. The Navier-Stokes Characteristic Boundary Condition (NSCBC) method presented in their work, was later reported that can result to an ill-posed simulation as reported by[73] because of employing $5+N_s$ variables but one more equation which is actually summation of the mass fraction or partial densities which lead to 1 or total mixture density, respectively. Therefore, Moureau et. al.[73] used one equation less. Okong'o and Bellan[74] derived characteristic boundary condition equations for a real gas mixture but unlike Baum at al. who took temperature(T) as the primitive variable, they considered pressure(P) to calculate the waves' amplitude. Considering pressure as primitive variable also make the final form of the characteristic equations much simpler. This was seen in the work of Moureau et. al.[73] as well. Pakdee and Mahalingam[75] also presented the characteristic boundary condition formulation for a mixture of ideal gas with or without reaction. They particularly focused on the impact of the choice of primitive variables vector without one species(inert species in their work). Sutherland and Kennedy[76] included the source terms in the relevant equations and therefore, respective characteristic waves' amplitudes for treatment of the boundaries. They actually made an extension to the work of Dutt[77] and considered only N-1 species equations. Poinsot and Veynante[78] wrote a comprehensive overview of the methods used for characteristic boundary condition treatment.

In this work, similar to the method applied in previous chapter for binary-species mixing layer, the NSCBC strategy for Euler equations has been employed considering the effect of multicomponent mixture. As there are no physical inflow/outflow boundaries for the set up used in the present work, only the treatment proposed for Euler equations used here. Perfectly non-reflecting boundary condition was set up to make sure no reflected wave will contaminate the solution i.e. setting the amplitude of all incoming waves to zero. Mixture properties were included in the computation of the wave amplitudes [2]. This is in compliance with the 'subsonic outflow' boundary condition expressed in the work of Thompson[42]. Although in some of the papers mentioned above, it is claimed that setting the incoming wave to zero(perfectly non-reflecting) will delay determination or of the average value of the pressure in the computational domain[72] and one should follow the suggestion initially proposed by Rudy and Strikwerda[59] which allows some

[2]Ratio of specific heats as well as speed of sound and all other quantities, are computed for mixture of n species at the flow temperature and pressure. More details are found in reference [75]

reflection inside the domain through the outlet to bring the mean pressure back to a value around preset pressure at infinity[40]. This method was also followed for one case and the results are found to be very close to the results obtained following the method of Thompson[42] (Results are not shown in here).

Even the modification to the Euler equations for the purpose of solving the Navier-Stokes equations at the boundaries, i.e. setting the viscous and diffusion fluxes normal to the boundary to zero was reported to be unstable[76]. In addition, setting the gradient of normal fluxes to zero is also not ideal although is not as severe as setting the fluxes themselves to zero[76]. Where there is no real and physical inflow or outflow exists in the current research, there is no need to apply extra condition used for Navier-Stokes equations as this can cause discontinuities depending on the problem. Therefore, selecting a right type of boundary suitable for the set up one considered is a problem-dependent choice[67].

Chapter 4

Results and discussions for binary-species mixing layers

This chapter covers the results obtained by simulation of 2D and 3D turbulent non-reactive and reactive shear-layers. As it was stated in chapter 1 the parallel 3D code initially started with, is the one used in reference[15] with further modifications. Before starting 3D simulation and implementation of hydrogen combustion mechanism, it was necessary to get some preliminary results from an easier version and compare with the results obtained by another research work. This will also help better understanding of the results which will be obtained from the 3D hydrogen-oxygen combustion simulation. Also, behaviour of a mixing layer in terms of the vortex pairing and evolution is better understood. Moreover, the numerical code and the Navier-Stokes equations will be found easier to deal with and facilitates implementing the new changes and modifications. This will boost the ability for controlling the run-time behaviour of the code and manipulating simulation parameters. To achieve this objective, this work is first started by setting up a 2D case based on a serial code for simulation of compressible mixing-layer with a scalar in order to qualitatively compare the preliminary results with the result of reference[41]. The next stage is moving on to the 3D parallel code. New case has been set up and new parts were added to the existing code responsible for more realistic binary-species simulation. Diffusion term was modified by introducing Lewis number effects in the equations. In addition, diffusion correction velocity was added to the convection term to satisfy the species' mass conservation. Also, real molecular weigh has been considered which enables more realistic simulation of mixing and combustion for hydrogen-oxygen mixture. Moreover, various subroutines have been added to the code for extracting data from turbulence field and evaluation of scalar statistics.
More descriptions about the approach stated above, are given in following sections.

Mach number	$L_y \cdot L_x$	Time(from table 4.1 of ref. [41])
0.2	7.48*10	15.0
0.4	8.06*10	17.6
0.6	9.52*10	24.0
0.8	13.37*10	37.2

TABLE 4.1: Initial non-dimensional parameters.

4.1 Two dimensional mixing-layers

In this section, results are compared with the results of Sandham and Reynolds[41]. Simulations have been done for two purposes; firstly, to observe the effect of Mach number on vortex formation, and secondly to observe the development of vortex pairing in the mixing-layers with time considering a non-reactive scalar.

4.1.1 Mach number effects

Domain size, Mach number and the times in which the flow snapshots have been taken are given in Table 4.1. Domain size is in accordance with the work presented in [41]. In this work, L_y is considered to be the streamwise length and L_x is spanwise length. This is not conventional in numerical simulation but the code started with was originally developed in this way. Changes in the length of the domain with Mach number, is because of the fact that it is selected equal to the most amplified wavelength to start transition from laminar to turbulence sooner. Transverse(cross-streamwise) dimension has been kept constant. Number of grid points for all Mach numbers is equal (64*81), with $Pr = Sc = 1.0$ and specific heat ratio of $\gamma = 1.4$ and a fixed $Re = 400$ for all simulations. Wave amplitude is set to 0.05. Free stream input parameters and reference quantities used for non-dimensionalisation are all equal to the values considered in [41]. Reference velocity is equal to the upper and lower free stream velocities(which are equal themselves). Initial velocity profile is distributed using an error function profile with non-dimensional value of 1.0 for both streams but in opposite directions. Temperature profile was distributed using Crocco-Busemann relation and the inverse of it, makes the initial density profile. Initial scalar distribution was accomplished by applying a hyperbolic tangent profile. Details on the equations solved and the methods applied are found in [41] and is not necessary to be repeated in here. Contours of scalar and pressure are chosen to be shown in this work. Other contours such as vorticity and density are not shown in this section but the trend of those contours are also match with the data obtained in the reference work. Results shown in figure 4.1 are for the conserved scalar (called mixture fraction in the reference work) for four Mach numbers given in Table 4.1. The trend of the scalar contours in this work matches quite well with the original

work. The original plots are not reprinted in here but reader is referred to sketch (a) of figures 4.10 to 4.13 in [41]. Dashed lines represent negative values while solid lines correspond to positive scalars. As seen in these figures, the flow structure is elongated as Mach number increases. This is in agreement with the plots shown in the reference work. The values shown in the contours are f-0.5 to match with the data in the reference work.

Contours of pressure distribution at different Mach numbers are shown in figure 4.2.

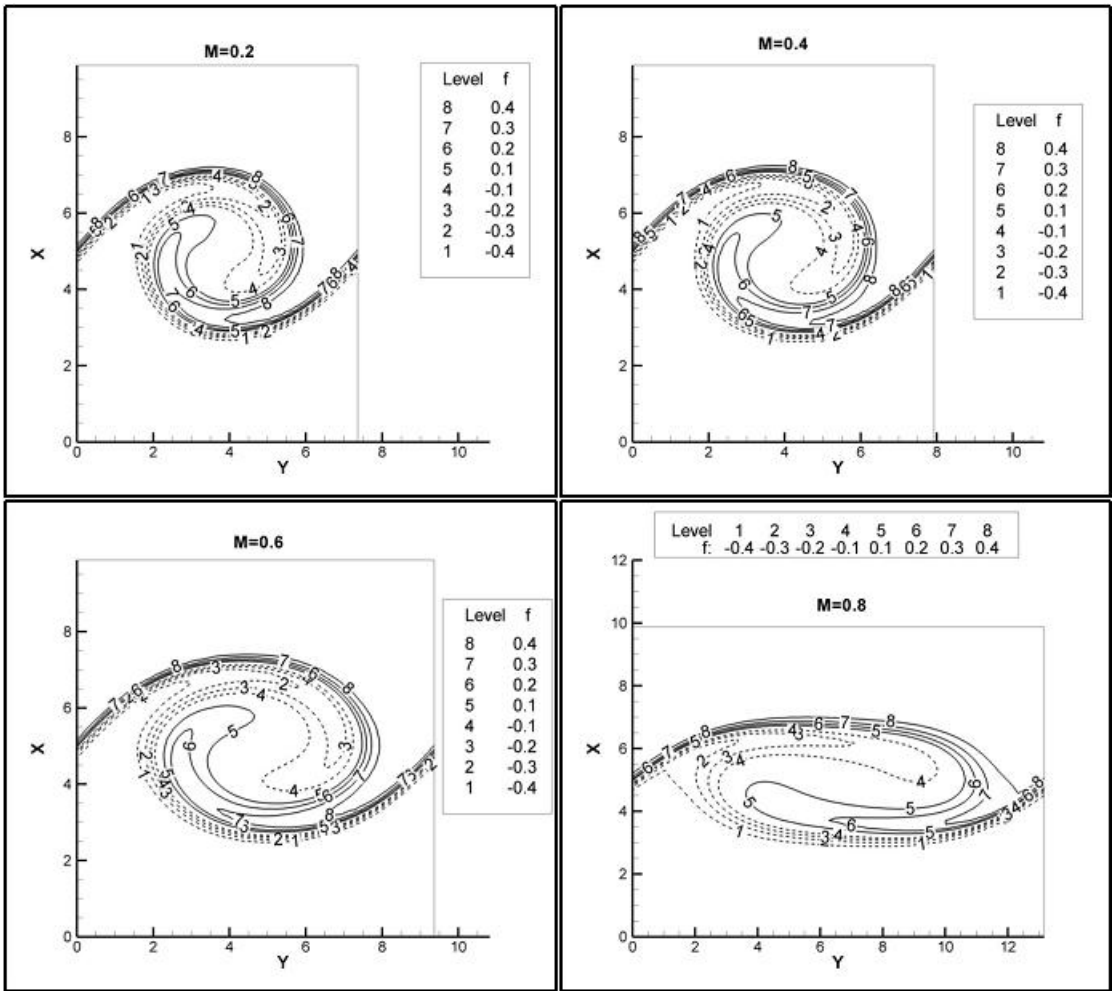

FIGURE 4.1: Developed structure for the scalar at different Mach numbers.

The contours shown in this figure comply completely with the contours in the reference work and show a reduction in the vortex core and an increase at the saddle point[41]. The only difference seen in these two figures with the ones produced by Sandham and Reynolds[41], is that the simulation times do not exactly match each other which is because of the differences between perturbations added in this work and in the reference work as their value were not available. The only parameter which matches in both works is the amplitude of the disturbances which is set to 0.05. So, for example, at time t=15

in the reference work, part of the scalar structure has been passed from the left boundary whereas at this time, the scalar braid is in the middle of computational domain. This the same for pressure contour but the values and the shape of the contours are in very close agreement. It is like there is a small delay in the mixing layer evolution in the current work compared to that of the reference work chosen.

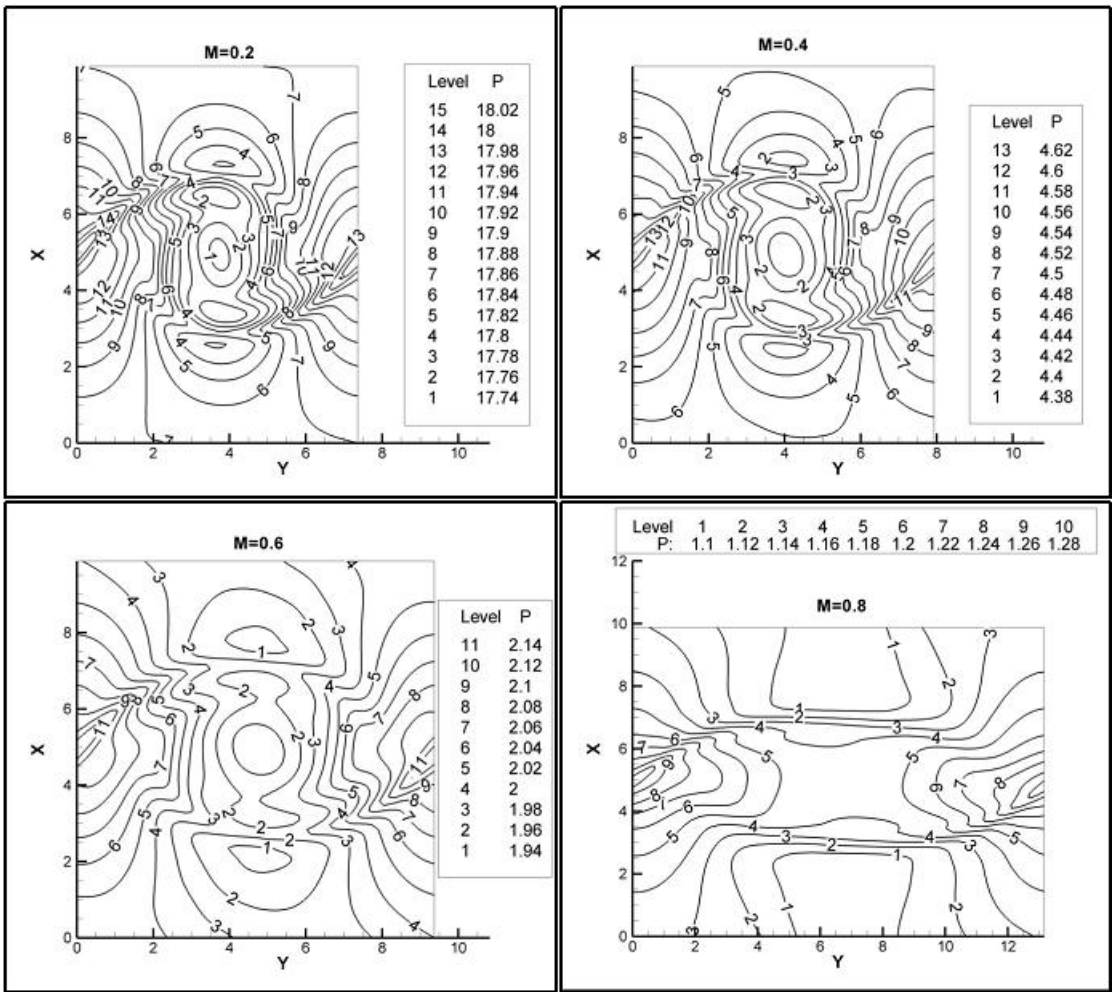

FIGURE 4.2: Developed structure for the pressure at different Mach numbers.

4.1.2 Vortex pairing

In this section, developing mixing layers with initial conditions stated in the previous section convecting with M=0.2, is considered at different time stages. Results are shown in figures 4.3 and 4.4. Similar to previous section, only contours of the pressure and scalar are selected to be illustrated. Main points about the flow development with time can be explained as follows: Fundamental mode and subharmonic mode of instabilities start

to grow [1] during vortex roll-up and saturate(figure 4.3, top). Rotation continues and maximum vorticity thickness is reached when one vortex lies above the other one. In this case, the upper vortex tends to rotate toward down while the lower vortex is inclined upward(figure 4.3, middle). Later on, vortices are still located one above the other while having rotated about 180° and rotation continues(figure 4.3, bottom). At later times, vortices are still rotating around each other having completed half way around each other and vorticity thickness is reduced compared to the previous state(figure 4.4, top). Finally, both vortices have completed rotation and if simulation continues, it will be observed that the vorticity thickness will be reducing as time proceeds(figure 4.4, bottom). In general, the results obtained in this part are in very good agreement with the results of previous research. Despite differences in some initial disturbance parameters, the development of mixing-layers looks reasonable and in close agreement with the results published in reference work. This was taken as an introductory stage before moving on to the next stage which is dealing with the 3D parallel code with active and passive scalars. The above piece of work that was briefly presented, is only the very first step into DNS of mixing layer before involving into more complex simulations.

4.2 Three dimensional mixing-layers

In this section, results for DNS of three dimensional non-reactive and reactive hydrogen and oxygen temporally evolving mixing layers are presented. No dilution has been applied to any of the streams. Hydrogen molecule is known as the lightest fuel with molecular weight of 2 while oxygen's molecular weight is 16 times larger than hydrogen and is equal to 32. Direct numerical simulation of the governing equations for such system of pure species is not a trivial task. In addition, hydrogen has much larger diffusivity compared to oxygen so this large difference will add additional difficulty to the system of equations. In the literatures published so far regarding DNS of H_2-O_2 mixing layer, not many of them have considered pure scalars/reactants. Among those, researches published by Bellan's group[79, 80] have been devoted to pure scalars (and only for non-reactive case) whereas the majority of the publications in this field have utilised diluted streams. Therefore, DNS of non-diluted reactants/scalars would be a positive contribution toward understanding the complex dynamics of turbulent pure hydrogen-oxygen mixing and turbulent combustion. The main focus of this study is on the effects of different diffusion coefficients on the flow field as well as turbulence analysis. A parametric study of H_2-O_2 mixing layers is compared with a different case in which the diffusion coefficient of species are equal. For the sake of isolating the diffusivity effects, all other input parameters are chosen to be equal to enable us to achieve

[1] More details about fundamental and subharmonic modes of instabilities are found in [41].

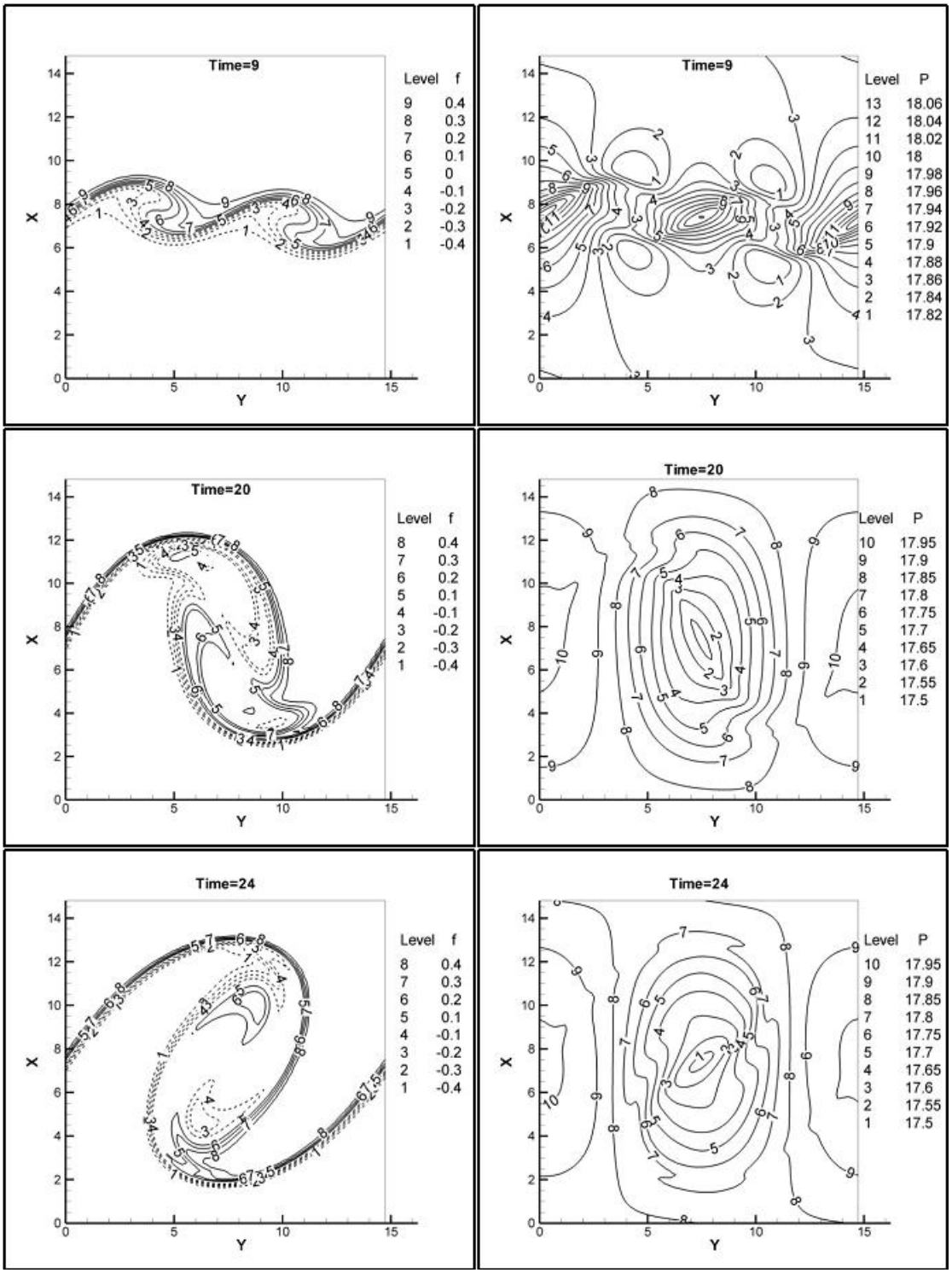

FIGURE 4.3: Pairing process at M=0.2 at time=9, 20 and 24.

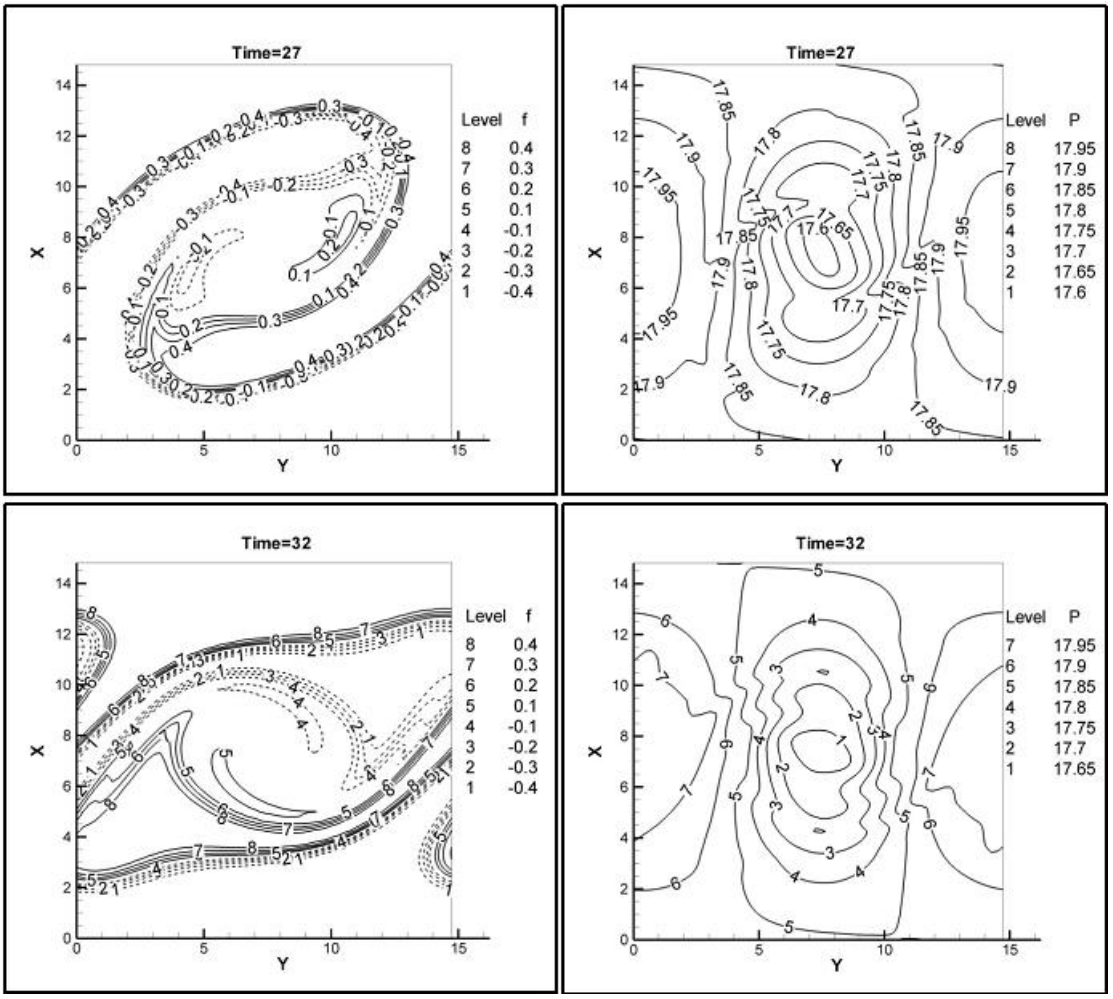

FIGURE 4.4: Pairing process at M=0.2 at time=27 and 32.

a quantitative measurement of the mixing layers flow under different species' diffusivity. Diffusivity effect has been applied to a series of simulations via introducing the Lewis number($Le_n = Sc_n/Pr$). Three cases have been studied: Case 1 with $Le_{H_2} = 0.3$ and $Le_{O_2} = 1.0$, Case 2 with $Le_{H_2} = Le_{O_2} = 0.3$ and case 3 with $Le_{H_2} = Le_{O_2} = 1.0$. To study the effect of combustion on the flow field and turbulence, a global single-step reaction with a rate calculated from the Arrhenius Law, between H_2 and O_2 is introduced that leads to formation of gaseous H_2O. The reaction mechanism was explained in chapter 2. Results are presented for non-reactive and for reactive cases. Input data for non-reactive and reactive simulations are listed in Table 4.2: Reference values for the molecular weight, density and temperature are obtained by taking the average of the corresponding initial values in both streams. Given the assumed Mach number and initial temperature, free stream velocity can readily be calculated. In this work, however, free stream velocity for hydrogen has been calculated by this method and the same value was set for the oxygen stream but in different direction. Reference velocity is then

the difference between these two values which is twice the velocity magnitude for either of the flows. These reference values are then used for non-dimensioanlisation. All the quantities stated in the following sections are all in their non-dimensional form unless explicitly stated and accompanied by a unit. All quantities including figure captions and axes titles are either specified mathematically in their non-dimensional form or simply accompanied by subscript ND. For example, non-dimensional time is written as $tU_{ref}/\delta_{\omega_0}$ or simply t_{ND}. All lengths are divided by δ_{ω_0} and are shown in fraction form. Simulation started with an error function distribution for streamwise velocity, temperature and scalar mass fraction. Other mean velocity components are considered to be zero. Velocity disturbances are then superimposed according to the method explained in chapter 2 on the mean velocity profile. Mixing layer geometry together with the initial distribution profile in transverse direction for temperature, density, velocity and mass fraction in the middle of the domain are shown in figures 4.5 through 4.6. The mass fraction profile at t_{ND}=80 is also included which shows the mixing status even without presence of reaction. Initial pressure is uniform throughout the domain. Grid size is $N_x * N_y * N_z = 208 * 352 * 352$ in x,y,and z directions, respectively. Simulation continued without reaction to let the flow entrains and both streams reach to a level of mixedness. Difference in the mass fraction profile shows the effect of species' diffusivity on binary mixing. Density profile is calculated based on the ideal-gas law which was explained earlier in chapter 2. Choice of high temperature for oxygen is in order to have a closer density ratio between two streams so that the numerical simulation will not be as stiff as the case where both reactants have close temperatures. This also helps to have more stable solution for the system of the equations solved in this study. Preheating of reactants is also used in practical cases to have better combustion efficiency and pollutant reduction so the use of heated oxidiser is sensible in this simulation. For the reactive case, simulations have been done for two different rates by changing the Damkohler number, Da=10 and Da=50. Other combustion parameters such as Ze and T_f are selected to be 3.0 and 1.42, respectively which gives a value of 35 KJ/mol for the activation energy. This section are followed by the following subsections:

- Effect of diffusivity on flow development and turbulence analysis,
- Scalar variance budget analysis,
- Quantification of differential diffusion,
- Study on local counter gradient transport in diffusion flames.

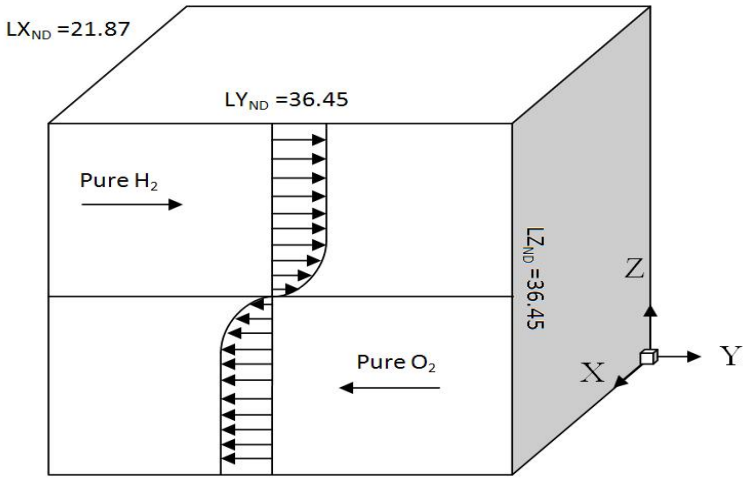

FIGURE 4.5: Mixing layer geometry. Periodic directions are x(spanwise) and y(streamwise); Non-periodic direction is z(transverse). Initial velocity components are only in y-direction and are equal +v for hydrogen stream and -v for oxygen stream.

Parameter	Value	Description	Unit
γ	1.4	Ratio of specific heats	
Pr	1.0	Prandtl number	
Re	750	Reynolds number	
M_a	0.4	Mach number	
$Y^0_{H_2}$	1.0	H_2 mass fraction in fuel stream	
$Y^0_{O_2}$	1.0	O_2 mass fraction in oxidiser stream	
$\phi_{L_z/2}$	7.83	Equivalence ratio at the interface of both streams	
s	8	Mass stoichiometric ratio	
f_{st}	0.11	Stoichiometric mixture fraction	
T_{H_2}	300	Hydrogen initial temperature	K
T_{O_2}	2500	Oxygen initial temperature	K
U_{H_2}	+529.47	Initial velocity of Hydrogen stream	m/s
U_{O_2}	-529.47	Initial velocity of Oxygen stream	m/s
P_{ref}	101325	Reference Pressure	Pa
T_{ref}	1400	Reference temperature	K
U_{ref}	1058.9	Reference velocity	m/s
W_{ref}	17.0	Reference Molecular weight	Kg/Kmol
ρ_{ref}	0.118	Reference Density	Kg/m^3
t_{ref}	8.06	Reference Time	μs
δ_{ω_0}	8.57	Reference Length	mm

TABLE 4.2: Reference data and input parameters

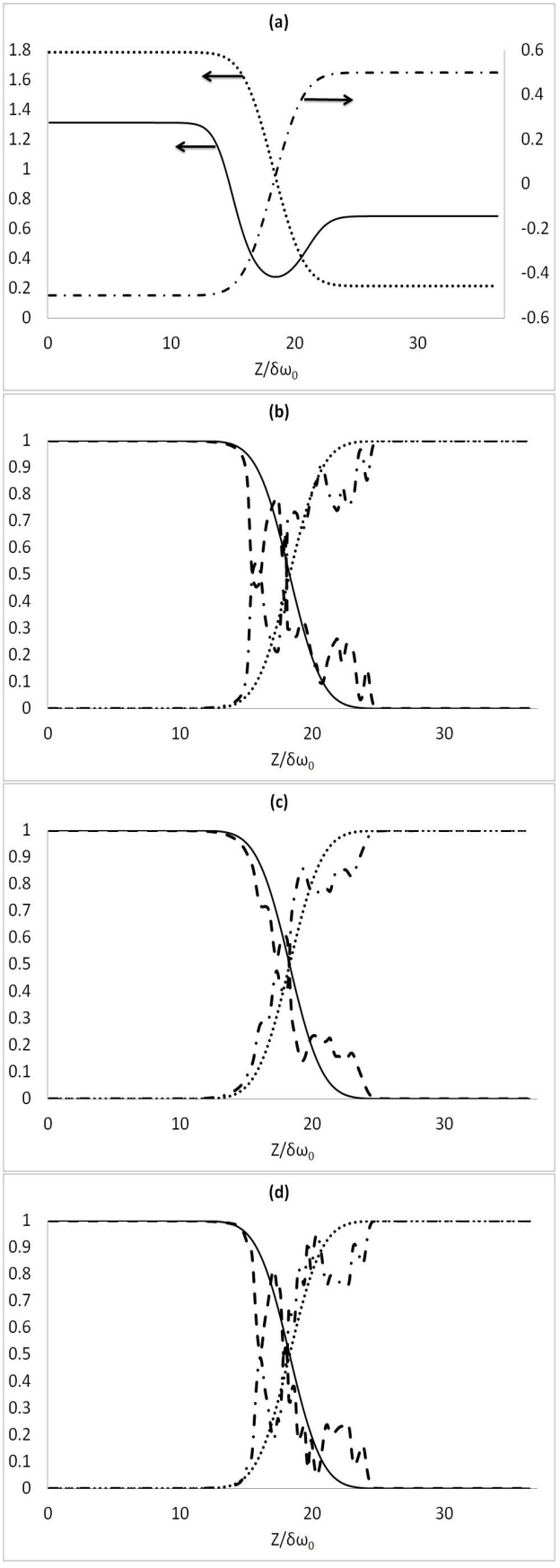

FIGURE 4.6: Initial profile for instantaneous non-dimensional quantities: (a) temperature($\cdots$), density(———) and streamwise velocity($- \cdot - \cdot$); and Species' mass fraction at $y = L_y/2$ at t_{ND}=0 and t_{ND}=80 for (b) case 1; (c) case 2; (d) case 3. O_2 at t_{ND}=0(———), O_2 at t_{ND}=80($- - -$), H_2 at t_{ND}=0($\cdots$) and H_2 at t_{ND}=80($- \cdot - \cdot$). The data are for the middle line along the transverse direction.

4.2.1 Effects of species diffusivity

4.2.1.1 Non-reactive mixing layer

As stated earlier, simulation started without reaction. All three cases progressed until time t_{ND}=80. To get an overview of flow development and to examine the effect of the Lewis number on this process, it is useful to first, have a look at some macroscopic properties in the flow. Figure 4.7 shows a snapshot of the instantaneous distribution of density of the flow in the mid-plane in streamwise direction comparing results of a mixing layer with different Lewis number(case 1), mixing layer with Lewis number equal to 0.3 for both scalars(case 2) and finally, mixing layer with unity Lewis numbers for the mixing scalars (case 3). It can be seen that density minimum and maximum values for case 1 is different from the other two cases. Having a higher upper limit for cases 2 and 3 is a result of more layer compression at the interface of both flows. In addition, case 2 with the least value for Lewis number shows a lesser extent of mixing and diffusion of one stream into another. However, case 3 with unity Lewis number shows a pattern similar to case 1 with different Lewis number and both mixing layers have more convoluted density contour specially above the interface inside the hydrogen stream compared to that of case 2. The larger extent of the lower stream into upper stream is because of the density stratification exist; upper stream with smaller molecular weight and lower density, can be easily surrounded by the large rolling structures in the mixing layer and that's why, the flow penetration into higher stream is more pronounced. Mass fraction contours are also similar to density contours in terms of the structure and extent to which the streams penetrate into one another and there is no point of showing another set of contours in here with similar pattern. Instead, figure 4.6(b d) shows a general picture of the scalars' mixing at the end of the simulation time. Similar to what stated for the density, case 2 shows the minimum penetration of the streams into each other as species' mass fraction profile do not overlap compared to the ones for the other two cases. As will be shown later, the vorticity structure and growth rate for all cases are very similar which represents similar flow evolution for all the cases and the extent of the Lewis number effect on this quantity. therefore, the major reason (and perhaps the only reason) for such difference in mass fraction or density profiles will be the difference in the species' diffusivity.

Figure 4.8 shows the time advancement for the vorticity and momentum thickness together with spanwise and streamwise vorticity extrema. Vorticity thickness is written as $\delta_\omega = \Delta U/max|(\partial\overline{v}/\partial z)|$ and momentum thickness is defined as follows[6, 81]:

$$\delta_m = \frac{\int_{z_{min}}^{z_{max}} [\overline{(\rho v)}_{z_{max}} - \overline{(\rho v)}][\overline{(\rho v)} - \overline{(\rho v)}_{z_{min}}]dz}{((\overline{\rho v})_{z_{max}} - (\overline{\rho v})_{z_{min}})^2} \tag{4.1}$$

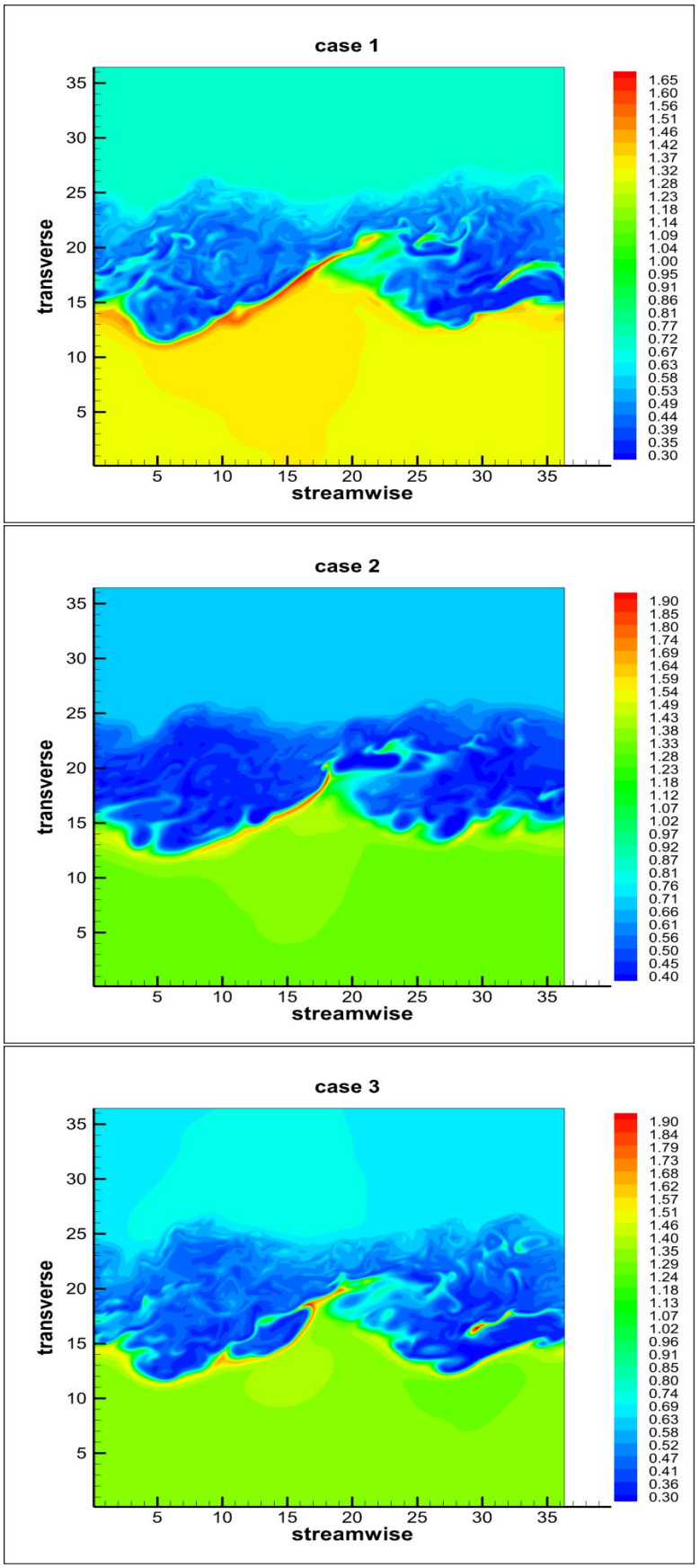

FIGURE 4.7: Snapshots of the mixing layer density distribution at $tU_{ref}/\delta_{\omega_0}$=80 in the streamwise mid-plane. 30 contours are shown for each plot. Initial density distribution for all cases was the same.

Other forms of the momentum thickness can also be used such as the definition proposed by Schlichting and Gersten[82] or the one used by Hadjadj et. al.[83]. As seen in this figure, momentum thickness which is a measure of the mixing layer growth rate, increases monotonically except a slight variation at about $tU_{ref}/\delta_{\omega_0}$=14. Vorticity thickness can also be used as a quantity for assessment of mixing layer growth rate. This is also shown in plot (b) of this figure. Change of the Lewis number does not change the trend of the momentum thickness and has negligible effect on its magnitude. As for vorticity thickness, species' Lewis number does not have a substantial effect on the magnitude and also its trend. δ_ω for case 1 with different Lewis numbers(0.3 and 1.0) is located between case 2(Le=0.3) and case 3(Le=1.0) with constant Lewis number throughout the mixing layer evolution except a small region around $tU_{ref}/\delta_{\omega_0}$=55. Basically, since the vorticity thickness growth rate has more fluctuations compared to that of the momentum thickness(because of the fact that the vorticity thickness is actually the derivative of the mean velocity which has fluctuations throughout the domain), it is affected by species' diffusivity although in small percentages. Momentum thickness, however, is more stable since it is an integral quantity and is not considerably affected by Lewis number variations. The monotonically increasing trend proves that the flow has reached to a self-similar state which in the present work happens from $tU_{ref}/\delta_{\omega_0}$=20 onward. This is in agreement with other turbulent flow studies published so far such as[27, 28, 84, 85] in which momentum thickness trend was a sign for achievement of self-similarity in mixing layer.

To depict the evolution of streamwise and spanwise vortices in the mixing layer, a series of three-dimensional contour plots of both quantities have been shown in figure 4.9. These plots are all for case 1 at different times during the flow evolution. Initial vorticity field in the spanwise and streamwise directions follows the one used in the work of Rogers and Moser[10]. Although spanwise vorticity contour would be an ideal quantity to assess the pairing process, the spanwise vorticity contours in this set of simulations did not seem to have a clear depiction of such happening. Majority of the iso-contours are close to zero except very few patches with positive or negative values not close to zero(whose extrema was shown in figure 4.8(c)). From the 3D snapshots shown in the figure 4.9, it is difficult to understand if there is complete vortex pairing. The sign of the vortex pairing can be deducted with the aid of spanwise vorticity extrema which has already been shown in figure 4.8. At time $tU_{ref}/\delta_{\omega_0}$=40 where the trace lines have been diverged, first pairing happens. The process continues until the second extrema occurs for spanwise vorticity that is sign for start of the second stage in vortex pairing. Time of this occurrence is different for each case studied here. For case 1, the second ω_x^+ extremum is at $tU_{ref}/\delta_{\omega_0}$=60 whereas for case 2, this occurs at earlier stage at around $tU_{ref}/\delta_{\omega_0}$=57 and slightly earlier at $tU_{ref}/\delta_{\omega_0}$=55 for case 1. The negative spanwise vorticity, ω_x^-, also shows extremum values very close to the positive extrema. Only case

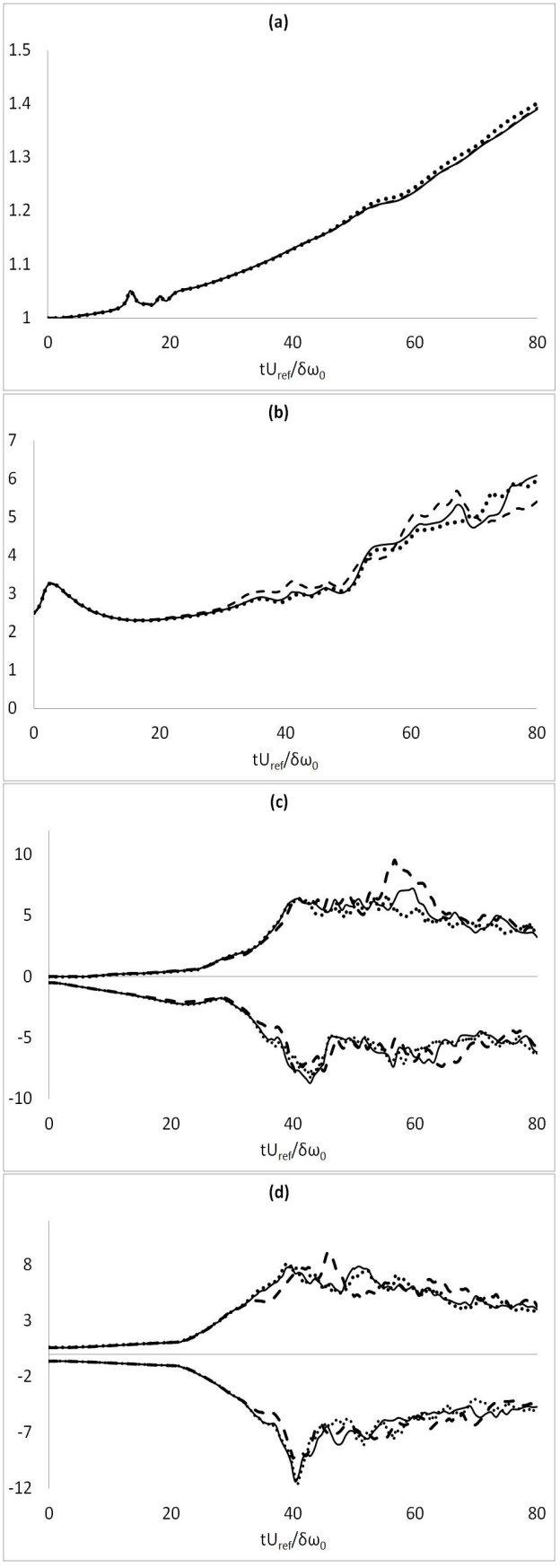

FIGURE 4.8: (a)Time evolution of momentum thickness normalised by its initial value(δ_m/δ_{m_0}), (b)Time evolution of vorticity thickness, (c)Time evolution of spanwise vorticity extrema, and (d)Time evolution of streamwise vorticity extrema. case 1(———), case 2(– – –) and case 3(· · · ·).

2 has shown a predominant peak compared to case 1 or case 3. Overall, the rate of the growth rate for all three mixing layers are slow and this can be concluded by looking at the slope by which vorticity thickness or momentum thickness grows. Also comparison between their initial and final value during the simulation does not shows a very large difference which is responsible for small percentage of the mixing layer growth. For example, momentum thickness only shows 40 percent growth compared to its initial thickness value whereas this can reach to a few hundred percent depending on the flow and the simulation condition(for example in the work of Balaras et. al.[85], normalised momentum thickness increased to even 5 times of the initial value and Okong'o, Harstad and Bellan[6] showed an increase of up to 9 times of the beginning value.). Since the main goal of this work is not to focus on vortex pairing and vorticity transport or vorticity budget analysis but the turbulence analysis, scalar transport as well as combustion, this does not affect the aims sought in this work.

Examining of pressure iso-surfaces is also an alternative way to look at this phenomenon. As known, they are usually formed as a tube around vortex axis and this indicates the trace of vortices[86]. Moreover, pressure surfaces with minimal values represent core of the vortices and maximal values are indications of the space between the vortices[87, 88]. Iso-contours of the pressure for case 1 have been shown in the figure 4.10 for $tU_{ref}/\delta_{\omega_0}$=10,20,40 and 80 together with pressure iso-surface for case 2 and case 3 at the end of the simulation(just for the purpose of comparison of the Lewis number effect on pressure field). At $tU_{ref}/\delta_{\omega_0}$=40, in line with the depiction of the spanwise vorticity extrema, pressure iso-contours also show the evidence of vortex merging by forming a zone of low pressure field and an adjacent zone with higher pressure magnitude. At $tU_{ref}/\delta_{\omega_0}$=60 when the flow starts its second pairing, iso-contours of pressure will form larger zones with bulker low-pressure cores as well as larger surrounding ring of high pressure field compared to earlier time when 1st pairing started. As pairing process is completed, these zones are isolated from each other until they completely depart at the the end of the simulation time i.e. $tU_{ref}/\delta_{\omega_0}$=60.

To find out the effects of Lewis number on the vorticity, the snapshots of streamwise vorticity contours at the end of the simulation ($tU_{ref}/\delta_{\omega_0}$=80) have been shown in figure 4.11 for all three cases. For the sake of comparison, equal number of contours are shown in each plot. There are differences in the final maximum and minimum values but apart from this difference, there is not a noticeable change in the patterns of the contours shown which means vorticity field have very similar evolution and Lewis number that is a measure of species' diffusivity does not strongly affect the vortex entrainment. This is sensible as vorticity and vortex dynamics are largely affected by the velocity field rather than the species properties. It also worth checking the suitability of the size of the computational domain as well as grid resolution to find out firstly, the domain size does not suppress the structure of the turbulence and let it develop and secondly, the

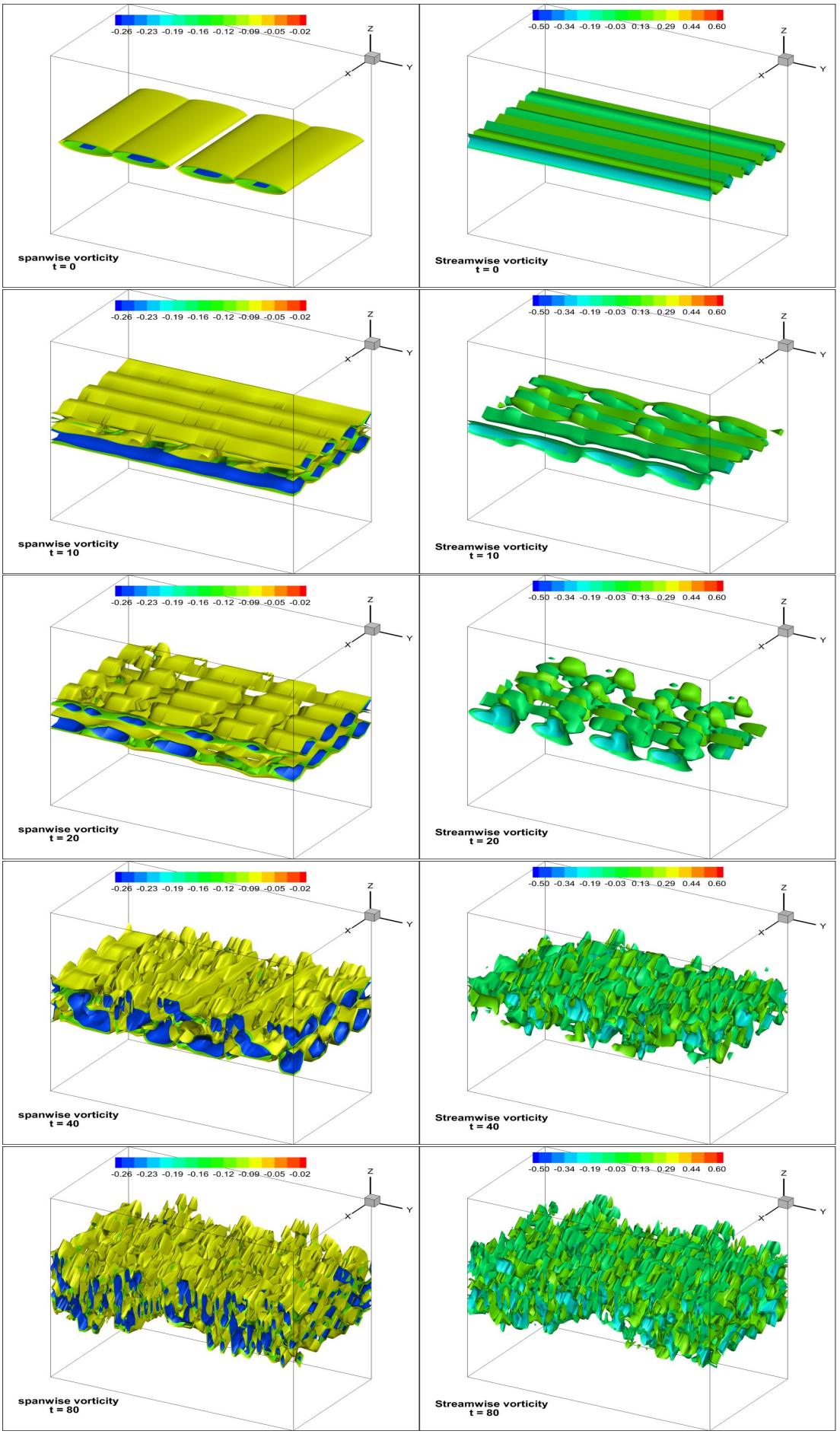

FIGURE 4.9: 3D iso-contours of spanwise(left) and streamwise(right) vorticity for case 1 at various times starting from t_{ND}=0 to t_{ND}=80. Three iso-surfaces are shown in each plot: $\omega_x\delta_{\omega_0}/U_{ref}$= -0.244, -0.12, and -0.08; $\omega_y\delta_{\omega_0}/U_{ref}$= -0.204, -0.079, and +0.168.

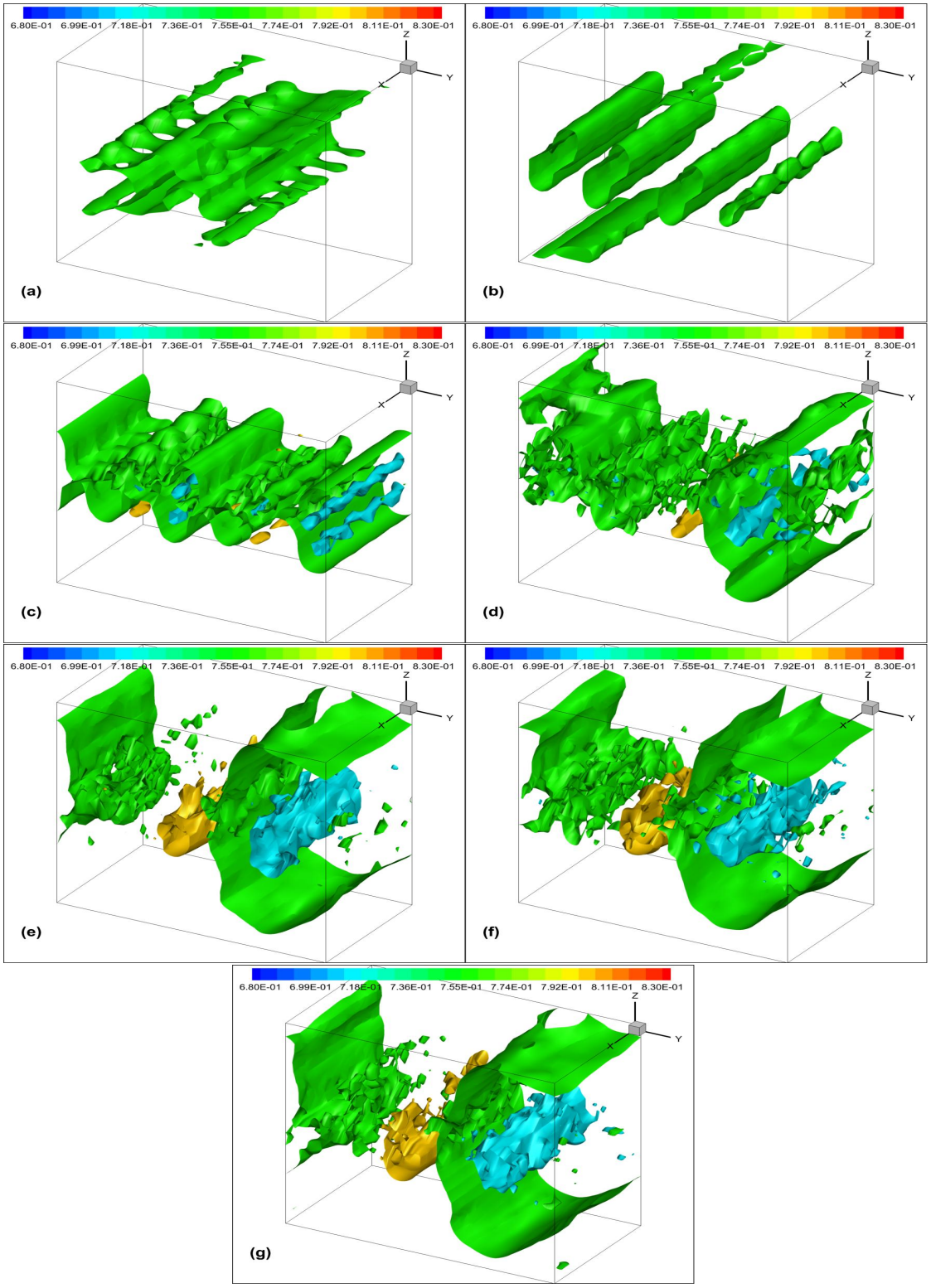

FIGURE 4.10: Pressure iso-contours for case 1 at various simulation time: (a)t_{ND}=10, (b)t_{ND}=20, (c)t_{ND}=40, (d)t_{ND}=60, (e)t_{ND}=80. Also shown pressure iso-contours at t_{ND}=80 for case 2(f) and case 3(g). Three pressure iso-contours are shown in each plot: $p/\rho U_{ref}^2$= 0.71, 0.76, and 0.80. Initial non-dimensional pressure is 0.76 and is uniform throughout the domain.

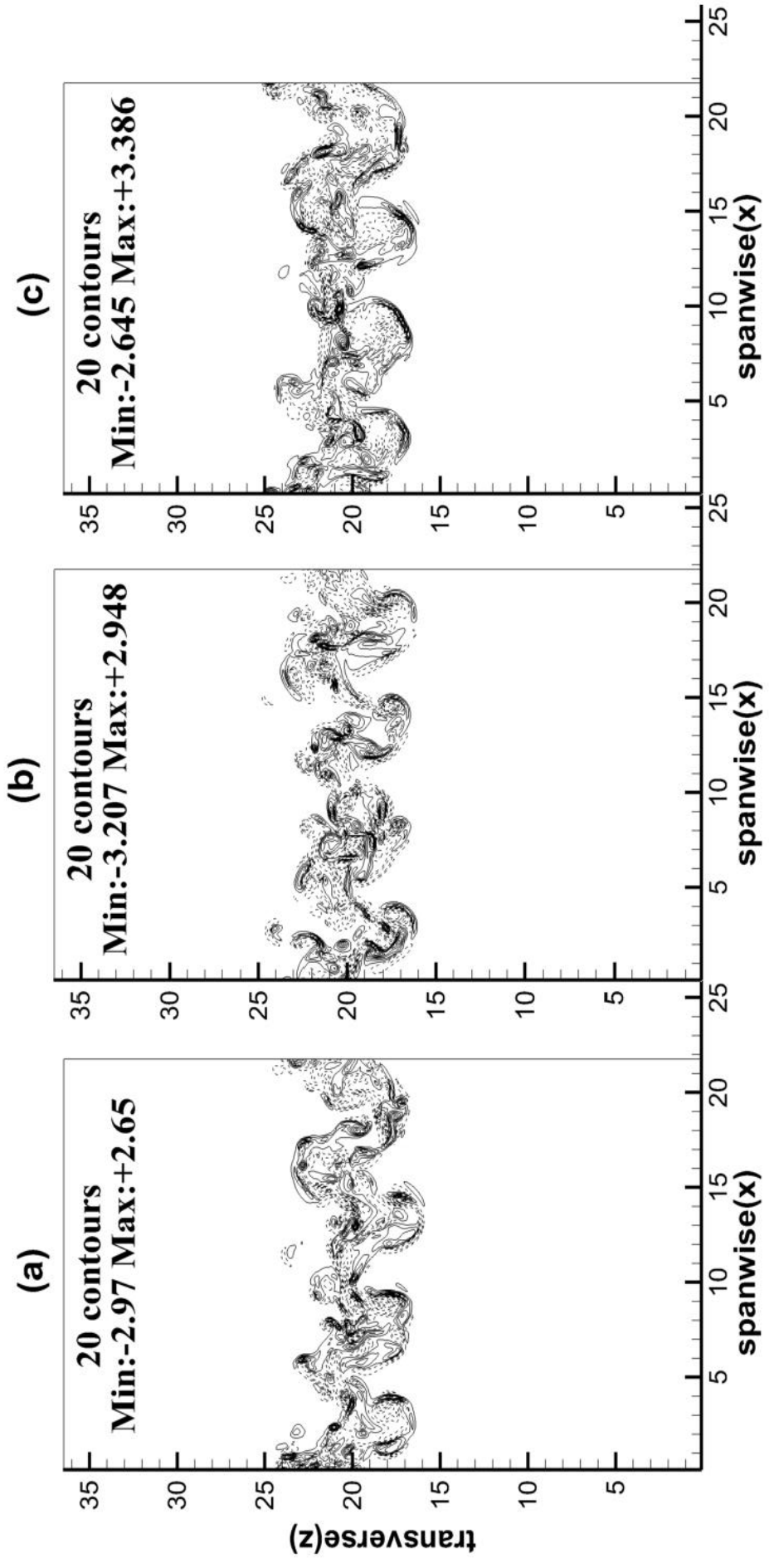

FIGURE 4.11: Streamwise vorticity($\omega_y \delta_{\omega_0}/U_{ref}$) at t_{ND}=80 and in middle of mixing layer ($y = L_y/2$) for non-reactive case. Cases 1 to 3 are shown in plots (a) to (c), respectively. Dashed lines show negative values. Values of both axes are non-dimensional.

mesh is capable of resolving as much scales as possible. The statistics which contains information on the spatial structure of the turbulence field is the two-point one-time autocovariance function which is known as two-point correlation[2]. Since the domain initialisation and disturbance introduction to the mean flow field is the same for all three cases, only case 1 is considered for this purpose. Two-point correlation function is written as follows[83]:

$$R_{\varphi\varphi}(r) = \sum_{k=1}^{N-k_r} \overline{\varphi_k^{'} \varphi_{k+k_r}^{'}} \qquad k_r = 0, 1, 2, ..., N-1 \tag{4.2}$$

in which N is the number of grid points in the i^{th} direction.

Two-point correlation function for fluctuating velocity components and pressure fluctuation in X and Y directions are shown in figure (4.12). Three different planes across the domain(in transverse direction) have been considered. The choice of the planes are according to the length in transverse direction which is covered by the entraining mixing layers to make sure all the selected planes passes through the locations where the flow shows more entrainment and hence, larger gradients in the fluctuating quantities can be observed. Values are normalised by their $R_{\varphi\varphi}(0)$. Both parts of this figure at each level across the domain illustrates that the flow major fluctuating quantities (i.e. u', v', w' and p') are decorrelated over the distances L_x and L_y. This shows that the extent of the domain is large enough so it does not have preventing effect on turbulence dynamics and also can accommodate the largest scales of turbulence. Spanwise correlation, however, shows more correlation across the x-direction but eventually approaches to zero over the entire length in that direction. Pressure fluctuation correlation in the spanwise direction is the only variable which has a completely different trend compared to the trends observed for the velocity fluctuating components along the spanwise direction. A wider domain could have solved this issue. In contrast to the pressure correlation in spanwise direction, two-point correlation function for the p' along the streamwise direction shows a more reasonable trend that proves the suitable size of the domain in that direction. From the contour plots in x-z plane (e.g figure 4.11), it is clear that the extent of the domain in the transverse direction is also sufficient and is not suppressing turbulence as the flow entrainment is far from the lower and upper boundaries.

To ensure the grid resolution is also adequate for the DNS study, turbulent kinetic energy spectra(κ) for cases 1 to 3 and over three x-y homogeneous planes have been plotted in figure 4.13. The larger the difference in the extrema of energy density spectrum is, the better the grid resolution would be. The range between low wave number with high energy density and high wave number with low energy density represents the scales exist in the turbulent flow and the degree to which these have been resolved[89]. At each x-y

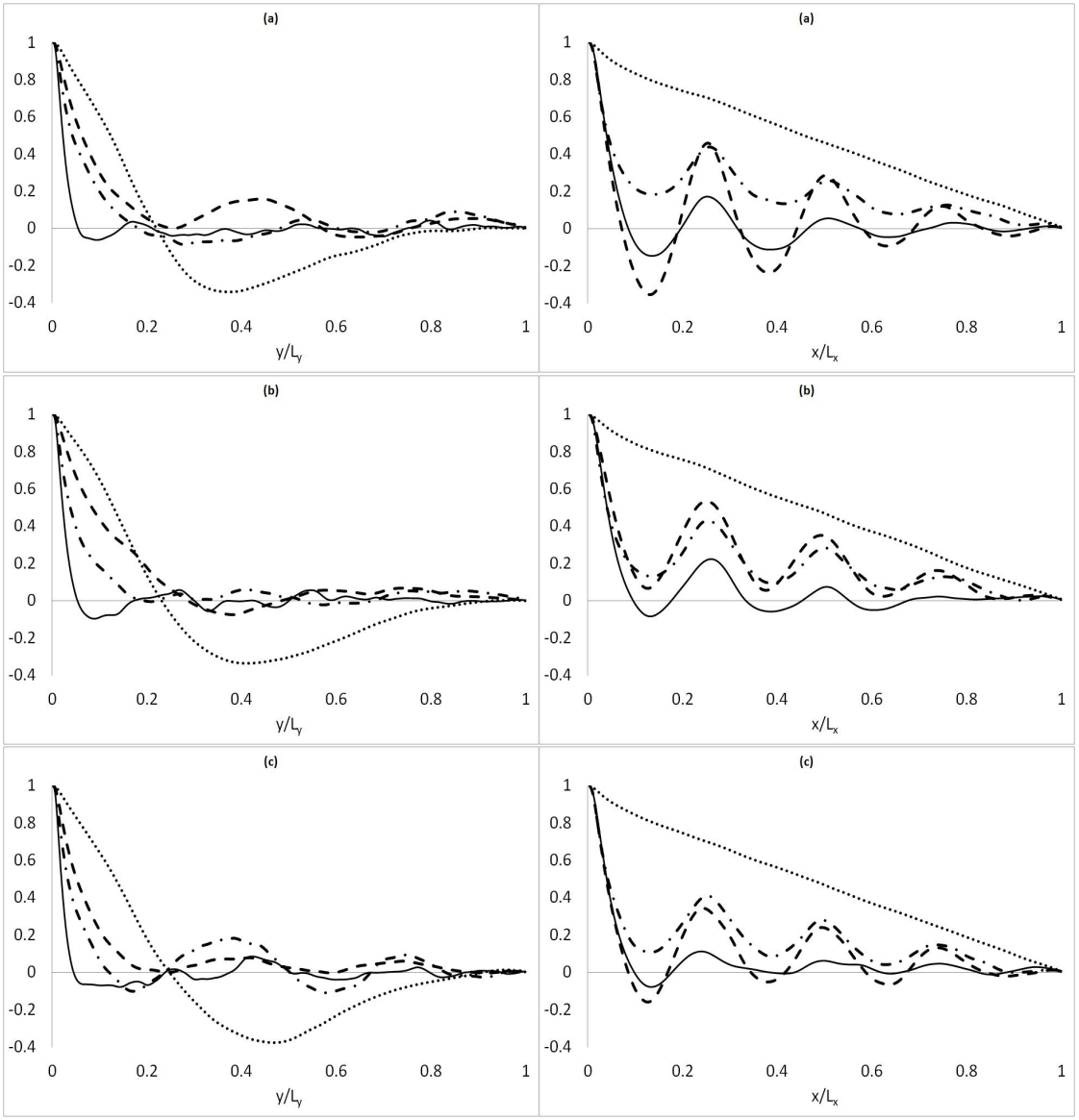

FIGURE 4.12: Two-point correlation function normalised by $R_{\varphi\varphi}(0)$ in streamwise(left) and spanwise(right) directions for case 1 at t_{ND}=80 and three different transverse locations: (a) N_z=176 where $z = 0.5 * L_z$; (b) N_z=195 where $z = 0.55 * L_z$; and (c) N_z=214 where $z = 0.6 * L_z$. (———)$R_{u'u'}(r)/R_{u'u'}(0)$, (– – –)$R_{v'v'}(r)/R_{v'v'}(0)$, (– · – ·)$R_{w'w'}(r)/R_{w'w'}(0)$, and (· · · ·)$R_{p'p'}(r)/R_{p'p'}(0)$

plane, a number of 88 equally spaced lines have been chosen for this purpose. The spectra are shown in the figure, are actually the average of the 88 turbulent kinetic energy spectra over that particular homogeneous plane for each case. As shown in this figure, energy spectrum covers a range of the magnitude of several decades from higher-energy contents corresponding to larger scales down to lower-energy contents corresponding to smaller scales with no energy pile-up at high wavenumbers that proves a satisfactory cascade across different scales. Scalar spectrum has been illustrated in figure 4.14 for all the cases at three different cross-stream locations. In figure 4.14(a), the range of the spectra are much larger than the other two planes. All three spectra follow the

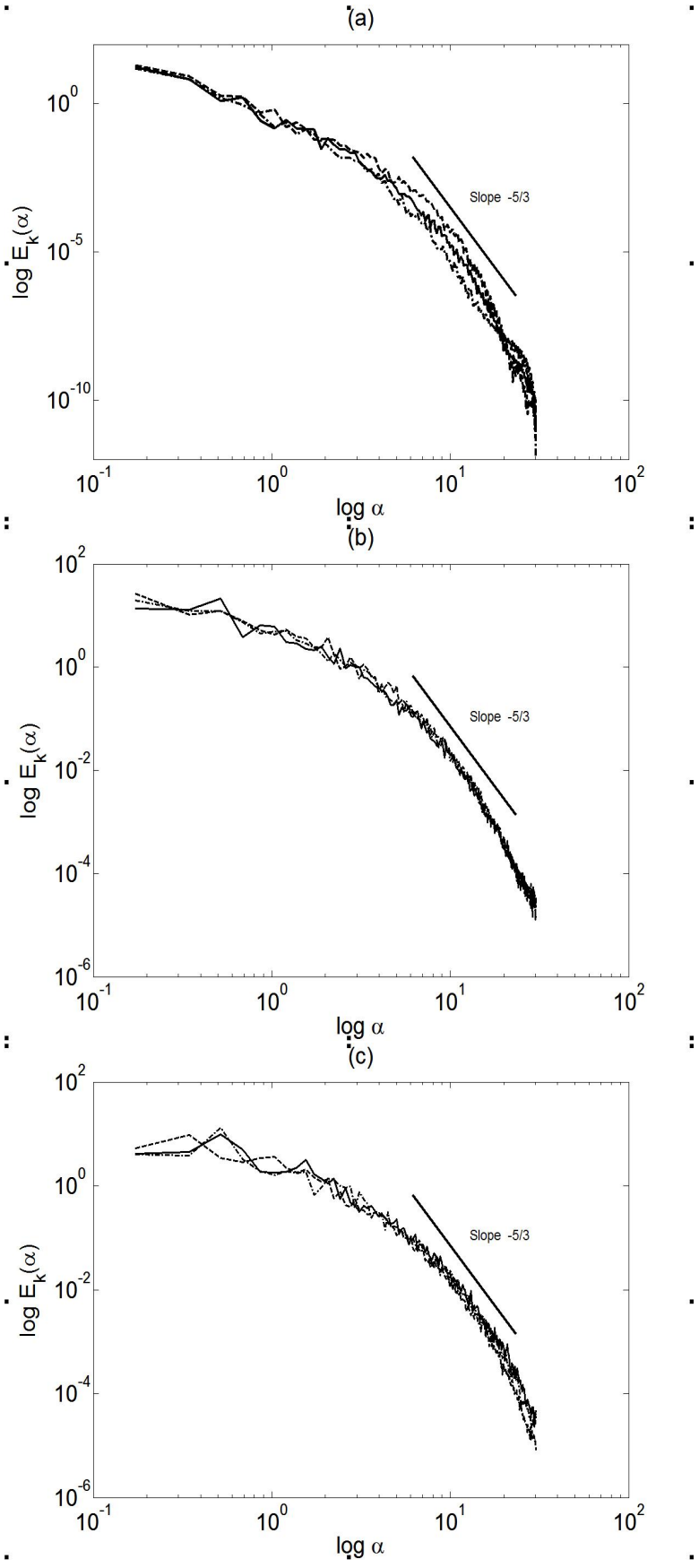

FIGURE 4.13: Energy spectrum illustration of the turbulent kinetic energy(κ) for the three cases at t_{ND}=80 in logarithmic scale; (a) x-y plane at $z = L_z/3$, (b) x-y plane at $z = L_z/2$ and (c) x-y plane at $z = 2L_z/3$. (———)case 1; (– – –)case 2; and (– · – ·)case 3.

Kolmogorov's energy cascade with the slope of -5/3 for the mid-range wavenumbers. As seen in this figure, it can be concluded that the resolution is adequate to resolve the scalar statistics as well. However, figure 4.14(b) which shows the same statistics but in a x-y plane located at the middle of the mixing layer (which was interface of two streams at the beginning of the simulation), shows not very good resolved mass fraction spectra. There are evidences of energy pile-up for all three cases specially for the case 3 compared to the other two. Overall trend of the spectra, however, follows the -5/3 slope in the inertial subrange. Homogeneous x-y plane located at $z = 2L_z/3$, shows a promising trace of spectra as shown in figure 4.14(c): no energy pile-up at smallest scales range as well as conformity to the Kolmogorov's -5/3 power law in the inertial subrange.

In overall, it can be deducted that all three cases follow the Kolmogorov's theory regarding energy cascade but at the locations with the highest interaction between the turbulent layers, energy of the smallest scales cannot be dissipated in accordance with the Kolmogorov's theory which result in some energy accumulation. Compressing the grid system across the centre planes of the mixing layer , can possibly solve the problem. Using a much finer mesh is also another way to tackle this issue provided the computational costs have the second degree of importance. These plots together with the ones shown in the figure 4.13 show a balance between the capability of the simulation in resolving the smallest scales and the computational costs. Moreover, the effect of the scalar's Lewis number is also more evident in the scalars' spectra plots as this is the factor which directly affects the mass fraction transport in the flow. Although the largest scales in the energy containing range have almost identical energy level(because of the fact that all three cases are initialised the same and therefore, energy generation at the largest scales always remains at the same range), when arrives to inertial subrange with mid-size scales or dissipation range containing the smallest scales, their mass fraction spectra begin to depart which highlights the effect Lewis number on the smaller scales. This is more evident for the Case 2 with both scalars' Lewis number equal to 0.3, from wavenumber equal to 2 or 3 within the inertial subrange through dissipation range. Cases 1 and 3 show close energy content throughout the different scales although at the lower x-y plane some differences in the energy level could be seen.

Time evolution for the dissipation rate of turbulent kinetic energy and turbulent kinetic energy have been plotted in figure 4.15. Dissipation rate of turbulent kinetic energy is written in its non-dimensional tensor form as $\epsilon_{ii} = -\overline{\frac{\partial u_i''}{\partial x_k}\tau_{ki}}$. Figure 4.15(a) shows the time history for variation of this quantity for all the cases considered here, integrated along the non-homogeneous direction, z. Cases 1 and 3 show very close values especially before t_{ND}=40 with overlapping values. Only after this time (when the first vortex pairing occurs), they start to depart but the difference is so small. Case 2 with Lewis number equal to 0.3, however, shows a different trace compared to the other two slightly

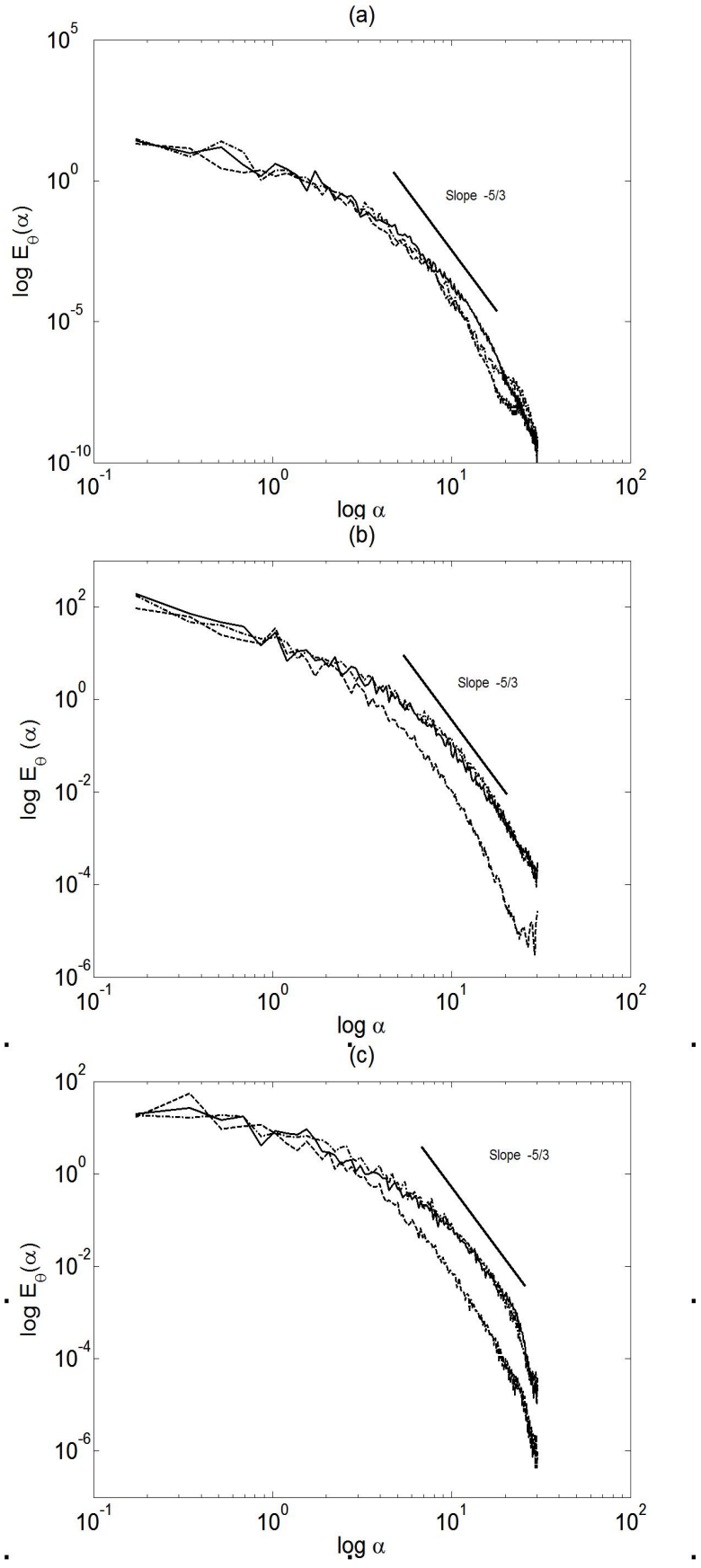

FIGURE 4.14: Scalar spectrum illustration: Hydrogen mass fraction for three cases at t_{ND}=80 in logarithmic scale; (a) x-y plane at $z = L_z/3$, (b) x-y plane at $z = L_z/2$ and (c) x-y plane at $z = 2L_z/3$. (———)case 1; (– – –)case 2; and (– · – ·)case 3.

after t_{ND}=20. Similar behaviour is also observed in the trend of turbulent kinetic energy (figure 4.15(b)) with case 2 having the largest difference in comparison with case 1 and case 3. Therefore, applying different diffusivity for scalars will change the trend of of turbulence dissipation as well as turbulent kinetic energy which cannot be easily neglected. A budget analysis is needed to understand the source of the difference and how Lewis number affect that. This has been done but for the reactive case where the Lewis number effect is supposed to be more prominent in the presence of a chemical reaction.

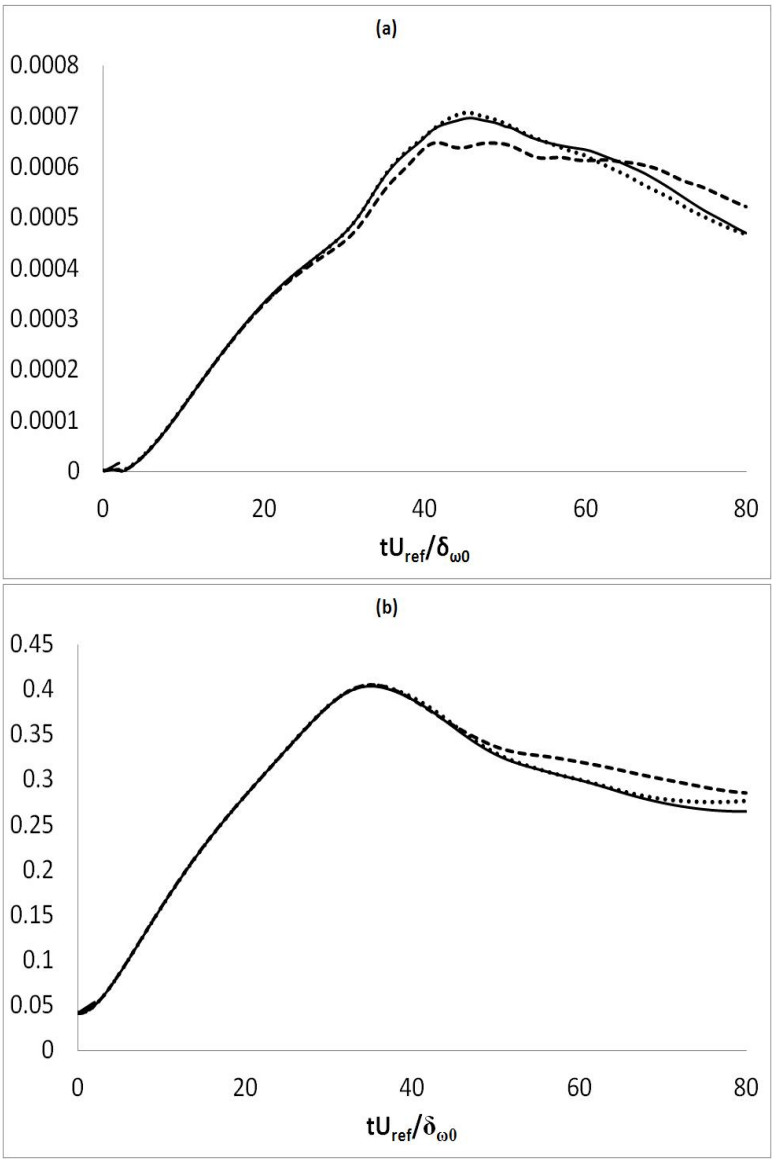

FIGURE 4.15: (a) Time variation of (a) Integrated mean turbulent energy dissipation rate ($-\overline{\frac{\partial u_i''}{\partial x_k}\tau_{ki}}\frac{\delta\omega_0}{\rho U_{ref}^3}$), and (b) Integrated Favre-averaged turbulent kinetic energy ($\frac{1}{2}\widetilde{u_k''u_k''}/U_{ref}^2$). (———)case 1, (– – –)case 2, and (· · ·)case 3.

4.2.1.2 Reactive mixing layer: Flow structure and turbulence analysis

To avoid early relaminarisation effect of the reaction heat release, reaction was delayed until $tU_{ref}/\delta_{\omega_0}$=40 after the mixing layers has had enough entrainment and the first peak in the vorticity extrema(first pairing) happens. Simulation continued up to the time $tU_{ref}/\delta_{\omega_0}$=60 with Damkohler number set to 10.
Vorticity thickness growth rate have been plotted in figure 4.16(a). The plots cover the time bound from the start of reaction at $tU_{ref}/\delta_{\omega_0}$=40 until the end of simulation. For comparison, the trace of non-reacting mixing layer has also been superimposed. also shown in that figure, evolution of the turbulent kinetic energy(k), and dissipation of k in plots (b) and (c), respectively. Similar to the plot for vorticity thickness growth rate, non-reactive traces are also superimposed for comparison. Immediately after start of the reaction, there is jump in the graphs due to reaction-generated pressure waves. After the peak, vorticity thickness continues its growth rate almost monotonically except case 3 with unity Lewis number which shows a temporary decrease in the growth rate at about $tU_{ref}/\delta_{\omega_0}$=50 before starts the second stage of growth. Turbulent kinetic energy and turbulent dissipation rate, however, start to decline after the sudden rise after the reaction was started. As seen in plots (b) and (c), Lewis number does not have a noticeable effect on these quantities and they are mainly controlled by the variations in the velocity field(which was initialised the same for all three cases). Since the Lewis number represents diffusivity of individual species, it is expected that the effect of this parameter on the mixing layer properties is mainly appeared on the mean or fluctuating scalar field. Before starting to evaluate such potential effects, it worths looking into the data relating to scalar transport to get overall picture about the domain and the combustion. In order to do this, contour plots of product mass fraction(H_2O) has been shown in figure 4.17 at the end of the simulation i.e. $tU_{ref}/\delta_{\omega_0}$=60. It is observed that the Lewis number do not substantially change the flame structure but there are local differences in the product formation throughout the domain.

Mean pressure and temperature distribution would also generate a picture of the changes that reaction has made to the flow and also highlights the differences that the Lewis number applies to the solution. These are shown in figure 4.18 at different times just before the reaction starts at $tU_{ref}/\delta_{\omega_0}$=40, and in some intervals during reaction progress at $tU_{ref}/\delta_{\omega_0}$=40, 45, 50, 55 and 60. As seen in this series of plots, initial pressure has got a uniform distribution across the domain just before combustion starts(plot (a)). All three cases have equal mean pressure. As previously shown, the Lewis number's effect on quantities such as pressure, temperature and density is negligible in non-reactive flows. In plot (b), as a result of combustion and because of generation of positive pressure waves spreading across the domain, the effects of Lewis number start to show themselves although the difference is very small for pressure. However, the differences

for mean temperature is considerably larger than pressure especially at the interface of both streams when peak temperature occurs. The difference in pressure and temperature grows until further time(plot (c)) during combustion and after this stage, when the reaction rate experience a dramatic decrease(this is shown in section 4.2.3), the pressure field is stabilized gradually. this is shown in plots (d) and (e). Mean pressure increases monotonically until the end of the simulation as there is a constant heat release parameter which has been defined for the one-step global mechanism used. One point worth noting and that is the performance of the non-reflecting boundary conditions utilised in this work. In plot(b), there are two locations in the mean pressure profile that are generated due to combustion(combustion-generated pressure waves). These two waves are moving toward lower and upper boundaries. the same scenario for the temperature but in one direction(toward the lower boundary). In plot(c), the pressure and temperature waves become closer to the lower boundary whereas the other pressure wave has left the domain from the upper boundary. In plot(d), both pressure and temperature wave have left the lower boundary and there is no evidence of reflection of these waves toward the boundary during the rest of the simulation(plot (d)). Regarding the mean temperature profile across the mixing layer, it has been shown that the case 2 with the smallest Lewis number for both species, over-predicts the temperature compared to case 1 with unity Lewis number which under-predicts it. Case 1 with different Lewis number, reads values in between. The same happens for mean pressure as well where case 1 has values between case 2 and case 3 that has been shown in plot (b) and plot (c) during earlier stages of combustion in which reaction rates are high. There is a positive shift in mean pressure at later stages of combustion (plots (d) and (e))compared to the mean pressure before combustion (plot (a)), although at the end of the simulation, pressure decreases due to reduction in the reaction rate as well as heat release rate(plot (d) vs. plot (e)).

4.2.2 Scalar variance budget: non-reactive and reactive flow

To study the effect of diffusivity on scalar statistics, the transport equation for scalar variance $\widetilde{\theta''\theta''}$ is analysed in which θ is the scalar's mass fraction with the Favre fluctuations denoted by $\tilde{\theta''}$. Scalar variance transport equation is written in the non-dimensional

form as follows:

$$\frac{\partial}{\partial t}(\rho\widetilde{\theta''^2}) = \underbrace{-\frac{\partial}{\partial x_i}(\overline{\rho}\tilde{u}_i\widetilde{\theta''^2})}_{convection} + \underbrace{\frac{\partial}{\partial x_i}\overline{(\frac{\mu}{RePrLe_\theta}\frac{\partial\theta''^2}{\partial x_i})} + \overline{2\theta''\frac{\partial}{\partial x_i}(\frac{\mu}{RePrLe_\theta}\frac{\partial\tilde{\theta}}{\partial x_i})}}_{molecular\ diffusion}$$
$$\underbrace{-\frac{\partial}{\partial x_i}\overline{(\rho u_i''\theta''^2)}}_{turbulent\ transport} - \underbrace{2\overline{\rho u_i''\theta''}\frac{\partial\tilde{\theta}}{\partial x_i}}_{production/destruction} \underbrace{-\overline{2\frac{\mu}{RePrLe_\theta}\frac{\partial\theta''}{\partial x_i}\frac{\partial\theta''}{\partial x_i}}}_{dissipation} + \underbrace{\overline{2\theta''\dot{\omega}_\theta}}_{reaction} \tag{4.3}$$

In this work, x_i is the coordinate in z direction which contains non-homogeneity in turbulence field.

Some other researches have also done a budget analysis for the scalar variance transport performing a DNS study[90, 91] or both DNS and LES[92] simulations. Some literatures, however, have only focused on the scalar dissipation rather than dealing the whole transport equation using either DNS[93, 94, 95], LES by proposing and testing a model for scalar dissipation rate term in order to utilise it in combustion modellings[96, 97], RANS for hydrogen-air non-premixed flame[98] or even taking an analytical approach[99]. Some of the research works have a more fundamental approach and looked into this quantity further by deriving the transport equation for the scalar dissipation term using DNS[100, 101] or LES[102]. All of these works have analysed passive scalar which is the mixture fraction in the flame. In this work, however, reactive scalars are chosen for evaluation of their variance transport although for the first stage of the simulations and xbefore combustion starts, they also act as an passive scalars. Therefore, non-reactive non-premixed mixing layer is considered first and then the analysis is shifted toward the reactive mixing layer.

4.2.2.1 Non-reactive mixing layer

Among the terms in the scalar variance transport equation, production/destruction and dissipation by the mean scalar gradient are known to have the most contribution into the scalar variance transport by increasing or decreasing its value. Although other terms have their own local contributions to increase or decrease the scalar variance, some of the terms are known to be redistributive terms as their integration across the domain is zero or close to zero which means minimum contribution in the scalar variance budget. These terms are actually the ones that usually appear in the form of derivative of a mean quantity. By looking at the equation 4.3 it can be deducted that the convection term, first part of the molecular diffusion term and turbulent transport term are the terms that have such specification. Case 2 with Le=0.3 is chosen to assess this in more detail. Variation of the terms across the domain as well as integration of the terms in equation

4.3 along the transverse direction have been shown in figure 4.19. Molecular diffusion is almost zero as seen in th figure. Moreover, Since convection and turbulent transport have several sign changes across the mixing layers(which implies locally increasing or decreasing the scalar variance), a clear conclusion of their role in the budget analysis is hard to be understood. Based on this, the concentration in here is only on production and dissipation terms as the major contributing quantities to scalar variance. Particularly, there have always been interests on the scalar dissipation rate in the studies on turbulent flow with or without reaction and literatures that have focused on this topic. Figure (4.20) depicts the variance for H_2 and O_2 mass fractions across the mixing layer at time $tU_{ref}/\delta_{\omega_0}$=80 for three cases. As shown in this figure, variance of hydrogen in the flow with Le=0.3 has the least amount compared to the other two cases. Two other cases, however, show a closer trend although case 3 with unity Lewis number has an offset(either toward a larger value or a smaller value) from case 1 with different(and realistic) Lewis number values. Similar results have also been found in the literatures published by Jaberi et. al [103] and Yeung and Pope [104]. They studied differential diffusion effects under homogeneous turbulence and showed that the variance of a scalar with higher diffusivity (smaller Schmidt or Lewis number) is less than the variance of a scalar with lower diffusivity (higher Lewis number). Variance of O_2 has not shown because of the fact that all three cases are just a binary mixing problem (when no reaction exists at this stage), and the variance of hydrogen and oxygen becomes identical.

Variations of the dissipation rate term and production term have been shown in figure 4.21. For cases 2 and 3 with equal species' Lewis number, the trace of dissipation term and production term of H_2 and O_2 are overlapping. For case 1, however, dissipation term shows considerable differences that clearly highlights the effect of different diffusivity on each of the species dissipation rate. Production rate for case 1 also shows an overlapping variations for both species because the mixing layer has only gone through a binary mixing process without any reaction. From the mathematical expression for the production term, such similarity is also expected as there is no evidence of the diffusivity term appearing in that expression. Dissipation term, contains the species diffusivity parameter and therefore show differences between different species with non equal diffusivity (as shown in figure 4.21). The effect of species diffusivity can be seen from the difference in the trend of the scalar(species' mass fraction) dissipation rate among three cases. While the magnitude of the dissipation increases as Lewis number decreases, dissipation rate of O_2 for case 1 has an offset in comparison with case 3(where the dissipation for H_2 and O_2 overlaps). In both cases Lewis number of O_2 is equal to 1 but O_2 in the case with different Lewis number shows a smaller value for dissipation compared to case 3. Also dissipation of H_2 in case 1 shows a difference in dissipation rate that cannot be ignored in comparison with that of the case 3 although both cases share the same value for Lewis number, i.e. 0.3. Production rate terms of all three cases show smaller

differences compared to their dissipation rate term since the diffusivity does not directly appear in the formulation. Also it shows more fluctuations(although it is an averaged quantity) and this is because of the existence of 'turbulent scalar flux' term which makes the production term inherit the turbulence field fluctuations by means of the velocity fluctuations component in transverse/non-homogeneous direction.

4.2.2.2 Scalars variance budget analysis in reactive mixing layer

Scalar variance budget analysis has been repeated for the reactive mixing layer. Reaction starts at $tU_{ref}/\delta_{\omega_0}$=40 and continues until $tU_{ref}/\delta_{\omega_0}$=60. Similar to what stated for the non-reactive mixing layer, the terms which do not contribute to overall change in the variance are convection, molecular diffusion, and turbulent transport term. In the reactive case, their fluctuation across the domain is even much more compared to the non-reactive case and hence, these terms are excluded from the budget analysis. Instead, the reaction term(scalar-reaction rate correlation) will be shown to play a major role in the variance of the reacting scalars.

Variance of the reactive mixing layer has been shown in figure 4.22 for all three cases and for both reactants, i.e. hydrogen and oxygen. Data are extracted across the mixing layer. Toward the upper and lower boundaries, there are no changes in the variance or the changes can be ignored as they are tiny; so the z axis has been truncated and only a region that has accommodated large changes is of interest. As shown in this figure, variance of hydrogen or oxygen in case 1 where different Lewis number has been applied, lies between the variance of the same species in the other two cases. While both hydrogen molecules share equal Lewis number in case 1 and case 2, but the outcome of their variances do not match. Similarly, oxygen molecule in case 1 and case 3 both have Le=1.0 whereas their variance differ at the peak. However, since all the graphs follow almost similar trace and the differences are only in the magnitude of the variance, it can be concluded that the variance of a scalar(whether undergoing a reaction or not) is mainly affected by the overall structure of the mixing layer and the role of the scalar's diffusivity is only to shift the variations up or down. Therefore, equal Lewis number can only cause underestimation or over-estimation of the scalar variance in comparison with the non-equal Lewis number and other than that, no considerable changes will be applied by this quantity.

To further investigate the effects of the Lewis number on the scalar variance, those terms of the transport equation which do not integrate to zero, have been selected for the budget analysis. These terms are production rate, dissipation rate and the reaction rate. Figure 4.23 shows these three terms across the mixing layer in the transverse direction. Budget analysis has been done for both hydrogen and oxygen molecules

and for all three cases. Production terms for either hydrogen or oxygen are very close for all three cases. This was also the case for non-reactive mixing layer. One thing worths noting is that different sign of the production rate term for hydrogen and its counterpart, oxygen. Production term is multiplication of the turbulent scalar flux term by the mean scalar gradient. As known, when the turbulent scalar flux moves in the same direction as the mean scalar gradient. Therefore, when the production term($-\overline{\rho u_i'' \theta''} \frac{\partial \tilde{\theta}}{\partial x_i}$) is positive, turbulent scalar flux($\overline{\rho u_i'' \theta''}$) and mean scalar gradient($\frac{\partial \tilde{\theta}}{\partial x_i}$) have opposite sign that means gradient transport for the scalar. In contrast, when $-\overline{\rho u_i'' \theta''} \frac{\partial \tilde{\theta}}{\partial x_i} < 0$, the scalar θ contributes to counter-gradient transport. By looking at the figure 4.23(a), it can be deducted that the oxygen molecule undergoes a counter-gradient transport as its total value is negative whereas hydrogen molecule shows a gradient transport. Such behaviour is the same for all three cases. Further more, the difference in the sign of the production rate for hydrogen and oxygen implies that for the oxygen molecule, this term is actually acting as an destruction term rather than production as the variations are negative. For Oxygen molecule, convection, diffusion and turbulent transport increase the variance locally(not shown).

As for scalar dissipation rate, the variations are different from non-reactive case presented before. Cases 1 and 2 show close values for the hydrogen mass fraction dissipating rate whereas case 3 with Lewis number equal to 0.3 has a considerable offset from the other two. The conditions for oxygen is completely different so that the oxygen mass fraction for case 3 has the maximum dissipation rate and cases 1 and 2 vary close to each other. Finally, reaction rate term for the scalars has been shown in figure 4.23(c) with hydrogen having positive values and oxygen showing negative values because of θ'' being positive or negative in oxygen or hydrogen side($\dot{\omega}_\theta$ for oxygen and hydrogen is negative as these species undergo a one-sided global reaction). Case 3 with unity Lewis number shows the highest and the lowest peaks of the curves for reaction rate term and case 1 with more realistic Lewis numbers shows values between case 2 and case 3. Unity Lewis number cause an overestimation of this terms whereas the equal Lewis number of 0.3 underestimates the variation compared to the more realistic case with different Lewis number. Since this term is large in terms of the magnitude, its contribution to the scalar variance cannot be ignored and the effect of diffusivity on this term and therefore, on the transport of the scalar variance is more pronounced.

Spectrum of the scalar energy(which is actually the spectrum of the scalar variance and it is analogous to the spectrum of turbulent kinetic energy k) has been shown in figure 4.24 for all three cases at three homogeneous planes across the domain. similar to previous section, the planes are located along the z direction at distances of $L_z/3$, $L_z/2$ and $2L_z/3$ from the lower boundary. The overall scalar energy cascade gets smaller from lower plane toward upper plane. Also, at the lower plane, the scalars all have closer spectra whereas the spectra start to get separated toward to upper planes. This

shows that the upper stream(hydrogen) has diffused/penetrated more into the lower stream(oxygen) so that the scalars energy, gets closer values. For the uppermost plane at $z = 2L_z/3$, as observed in plot (c), the energy spectra for hydrogen and oxygen is completely separate proving the least amount of diffusion from the lower stream into the upper stream. This is even valid for cases 2 and 3 in which Lewis numbers are equal. The reason for this happening is their difference in molecular weight as well as density difference between two stream. Upper stream is much lighter than the lower one and during the mixing layer evolution, upper stream penetrates easier into the lower, heavier stream.

To compare the scalars' energy spectra (variance spectra) among individual species with difference in Lewis number, two things worths noting. Firstly, in pure hydrogen stream(upper) or oxygen stream(lower), the energy of the corresponding scalar to that stream are higher than the other scalar. For example, in plot(a), hydrogen spectra are more energetic than the oxygen. On the other hand, in plot (c) which is located in the oxygen stream, oxygen mass fraction spectra has more energy compared to that of hydrogen. At the interface plane which has been shown in plot (b), hydrogen variance has more energy than its counterpart. Moreover, higher Lewis number results in higher energy spectrum. Case 3 with unity Lewis number has been shown to have the highest value for the scalar energy spectrum at the planes shown in figure 4.24(a-c) and case 2 with smaller Lewis number own the lowest values. This difference has been augmented in the middle plane where both streams interact.

4.2.3 Gradient and Counter-gradient transport

Study the gradient or counter gradient transport phenomenon has attracted the combustion and fluid dynamics researchers for more than a decade. Majority of the researches which have been devoted to this topic, were concentrated on the premixed flame[39, 105, 106, 107, 108, 109, 110, 111, 112]. Only a limited number have been devoted to study a non-premixed or partially premixed flame[7, 38, 113, 114]. The reason could be because of the fact that such phenomenon is more likely to happen in premixed combustion where the reaction rate is very high. For a non-premixed or partially premixed flames, it is always believed that the transport of scalars are from higher concentration to lower concentration by diffusion process. Counter-gradient diffusion takes place when the flow field adjacent to the flame brush is dominated by the dilatation due to reactions whereas gradient diffusion occurs when the turbulent motion of the flow field governs [105]. For turbulent premixed flames, transport equation for reaction progress variable(c) has been of interest to researchers. Bailly et. al.[106] introduced a new model for the mean reaction rate appears in transport for the reaction

progress variable and compared it with the experimental results of Shepard et. al.[115] and found the prediction of their model from counter-gradient diffusion and associated combustion-induced production are in close agreement with the experimental results. Chakraborty and Cant[39, 110] studied the effects of species Lewis number on scalar transport in turbulent premixed flames. They also performed the simulations for the reaction progress variable and considered constant but different Lewis number for each series of simulations. They performed a budget analysis for the the transport term and assessed the behaviour of each individual term in promoting or inhibiting counter-gradient or gradient transport. They found that the flames with smaller Lewis number show counter-gradient transport of the reaction progress variable whereas for higher Lewis number cases, this will be changed to normal gradient transport. Moreover, they proposed a model for the turbulent flux of the reaction progress variable and compared it with DNS database. Malkeson and Chakraborty [107], performed DNS in order to evaluate the models exist for turbulent flux of the fuel mass fraction(active species) and mixture fraction(passive scalar) in a premixed flame. However, they used a simplified one-step chemistry with unity Lewis number, similar to case 3 presented in the current work. They started to validate different models proposed for turbulent scalar flux at flows with low Damkohler number(i.e. Da <1), qualitatively as well as quantitatively. They have reported that some models predicts the turbulent scalar flux not satisfactorily and therefore, proposed an alternative modelling for this term. Since they have not considered differential diffusion for their DNS and also used a global one-step chemical mechanism, they have admitted that the existing models for $\overline{\rho u_j'' \theta''}$ are still needed to be verified more. Lipatnikov and Sabelnikov[108] tested a model for turbulent scalar flux in premixed flame which was developed by themselves. They have reported that in a frozen turbulence, scalar flux can show CGT at an earlier stage of the combustion(in the case if the peak mean rate of product generation moves toward the trailing edge of the flame brush) followed by transition to GT at later stages of the reaction. In contrast, in a decaying turbulence, the condition is reversed i.e. initially GT governs the turbulent flux of scalars and then it moves toward being CGT at later stages of flame development. A similar study on transition from gradient transport to counter-gradient transport or vice versa, has already been done by Zimont and Biagioli[109] in which they assessed the phenomenon theoretically and numerically by proposing a gasdynamic model for counter-gradient transport and incorporating the effects of the pressure across the flame brush. They split the turbulent scalar flux into two terms: one term accounts for turbulent diffusion which controls the increment of the flame brush and is described by the normal gradient behaviour of the flux, and a second term which accounts for pressure-driven transport of the scalar flux term and is generated by the pressure drop across the turbulent flame brush. Yoshizawa et. al[112] also have done researched to propose a model for counter-gradient diffusion. They started to theoretically find a

mechanism which causes CGT, and to apply that in the context of Reynolds-averaged model towards the application to the practical cases where counter-gradient diffusion exists. Some of the literatures studied the relationship between the turbulent scalar flux and the flame structure rather than propose a model for that. Among those, it can be referred to the work published by Swaminathan et. al.[111] in which they used a two-dimensional DNS with complex chemistry for hydrogen-air flame (and also methane-air flame) in order to assess the direct relationship between the turbulent scalar flux and the instantaneous flame structure. To do this, they analyzed conditional reaction rate, diffusion of reaction progress variable and dilatation due to combustion heat release from their DNS database and found the correlation between each of these terms and the turbulent scalar fluctuations in a premixed-flame context.

For diffusion flames, there are not as many publications as in the premixed flames. Richardson et. al.[113] used DNS to analyse the gradient diffusion model used in conditional turbulent flux term in CMC equation and found out that the existing first-order model is not appropriate to be applied at the edge flame. Also, by analysing the major terms in the conditional scalar flux equation, they reported that the pressure fluctuation is the term that contributes more into the counter-gradient transport; a finding which had been reported earlier by Luo and Bray[7] and later on with more details as a combustion symposium paper presented by Luo[114].

In this part, a qualitative approach has been taken to perform a budget analysis for the turbulent scalar flux equation in a partially premixed flame. Turbulent scalar flux equation is written in the non-dimensional form as follows:

$$\begin{aligned}\frac{\partial}{\partial t}\overline{(\rho\theta'' u_j'')} = &- \underbrace{\frac{\partial}{\partial x_k}\overline{(\rho\theta'' u_j'' \tilde{u}_k)}}_{convection} - \underbrace{\overline{(\rho\theta'' u_k'')}\frac{\partial \tilde{u}_j}{\partial x_k}}_{production\ I} - \underbrace{\overline{(\rho u_j'' u_k'')}\frac{\partial \tilde{\theta}}{\partial x_k}}_{production\ II} - \underbrace{\frac{\partial}{\partial x_k}\overline{(\rho\theta'' u_j'' u_k'')}}_{triple\ correlation} \\ &\underbrace{- \overline{\theta''}\frac{\partial \overline{p}}{\partial x_j} - \overline{\theta''\frac{\partial p'}{\partial x_j}}}_{pressure\ gradient} + \underbrace{\frac{\partial}{\partial x_k}\overline{\theta'' \tau_{kj}} + \frac{1}{RePrLe_\theta}\frac{\partial}{\partial x_k}\overline{\mu\frac{\partial \theta}{\partial x_k}u_j''}}_{viscous\ diffusion} \\ &\underbrace{- \overline{\frac{\partial \theta''}{\partial x_k}\tau_{kj}} - \frac{1}{RePrLe_\theta}\overline{\mu\frac{\partial \theta}{\partial x_k}\frac{\partial u_j''}{\partial x_k}}}_{viscous\ dissipation} + \underbrace{\overline{u_j''\dot{\omega}_\theta}}_{reaction}\end{aligned} \tag{4.4}$$

in which *production I* is production by mean the mean velocity gradient and *production II* is production by mean scalar gradient. Pressure gradient is also consist of a mean gradient term and a fluctuation gradient term. Because turbulence field is inhomogeneous in the transverse direction, equation 4.4 has been solved in this direction so j^{th} component of velocity is the velocity in normal direction(z). Simulation was carried out using the set of combustion parameters stated earlier in this section(4.2) with Damkohler number chosen to be 50 so that a stronger reaction (compared to the case presented

before where Da=10 was applied) is taken place for the purpose sought in this part. Damkohler number effect will appear in the final heat release value(source term in the energy equation which is equal to $\omega_T * Q_h$) where ω_T is the overall reaction rate and is written as follows:

$$\omega_T = Da_\ell \prod_{n=1}^{N_s} (\frac{\rho Y_n}{W_n})^{\nu'_n} exp[-Ze(\frac{1}{T} - \frac{1}{T_f})] \tag{4.5}$$

Combustion heat release is considered to be a constant value of 25.37 which is indeed, equal to the enthalpy of formation of the water and is non-dimensionalised by the reference velocity.

Results are chosen at the time when reaction rate reaches to its peak value where the maximum counter-gradient transport is expected. These times are actually different for each case. For the flow with different Lewis number or for the case with unity Lewis number (cases 1 and 3), the maximum reaction rate occurs at the non-dimensional time $tU_{ref}/\delta_{\omega_0}$=40.9 whereas for case 2 with Le=0.3, the maximum reaction rate will be at $tU_{ref}/\delta_{\omega_0}$=41.2. For the sake of comparison, the data are extracted at the non-dimensional time $tU_{ref}/\delta_{\omega_0}$=41 when the reaction rate for all the cases has reached to 90 percent of the peak value. The trend of the maximum reaction rate from $tU_{ref}/\delta_{\omega_0}$=40 until $tU_{ref}/\delta_{\omega_0}$=45 when has been shown in figure 4.25. Effect of Lewis number on the scalar mass fraction and therefore, reaction rate is clear in this plot. Case 2 with $Le_{H2} = Le_{O2} = 0.3$ has the least value as well as a delay in the peak reaction rate compared to two other cases. Similar to the case 2, applying unity Lewis number for both fuel and oxidiser will result in an under-estimation of the reaction rate but to a lesser extent. Mean reactants' mass fraction distribution has been plotted in figure 4.26. This figure shows the fuel and oxidiser mean mass fraction across the domain at the initial stage of the combustion, i.e. $tU_{ref}/\delta_{\omega_0}$=40 and also while maximum reaction rate occurs. As seen in this figure, both cases have monotonically decrease or increase the mean mass fraction which lead to negative or positive mean scalar gradient, respectively. In this section, occurrence of the local counter-gradient transport(LCGT) for fuel and oxidiser is shown first. Then, all the terms in the turbulent scalar flux has been analysed individually and the most dominant terms are chosen for discussion. Gradient/Counter-gradient transport for both reactants have been shown first shown but only turbulent flux of hydrogen molecule is chosen to be analysed further in this study.

Figure 4.27 shows turbulent scalar flux and mean scalar gradient (H_2 and O_2 mass fraction) across the mixing layers for all cases. All cases show counter-gradient transport(turbulent scalar flux changes in the direction as the mean mass fraction gradient) for hydrogen and oxygen at about z/δ_{ω_0}=19 and z/δ_{ω_0}=13-14, respectively. Case 1 is the realistic one where real molecular diffusion coefficients have been applied. For case 2 with all Lewis numbers equal to 0.3, an over-prediction for the LCGT of O_2 can be

observed although it is small. For H_2, apart from one LCGT at z/δ_{ω_0}=19, it is observed that this phenomenon for the case 1 is extended further and covers a region from z/δ_{ω_0}=19 to z/δ_{ω_0}=21. In addition, hydrogen scalar flux transport has higher peaks compared to that of the case 2. Case 3 with unity Lewis number for both reactants shows a different behaviour in turbulent flux of either of the species especially for the O_2. It has the most severe state for counter-gradient transport of the O_2 as the non-dimensional value for this term is 0.2 whereas for case 2 this is just under 0.1 and for the case 1 with realistic diffusion coefficients is around 0.5. Hydrogen's mean mass fraction gradient and its turbulent flux shows a similar trend in terms of the magnitude and the extent of the LCGT compared to the case 1. Luo [114] has done a study on the occurrence of LCGT due to combustion and proposed a criterion for that. Based on his criterion, the most important terms which contribute to counter-gradient transport are production and pressure gradient term. In this study, it is aimed to assess the effect all terms in the turbulent scalar flux transport considering real molecular weight and different diffusion coefficients and compare it with the cases in which equal species' diffusivity are applied. In addition, the focus in this study is on the active scalars rather than passive scalar considered in the earlier study. For this purpose, it is necessary to do a budget analysis for all the terms. Similar to the earlier study, terms on the right hand side of turbulent scalar flux equation are categorised as conservative (convection, transport by turbulent flow field also known as triple correlation and viscous diffusion), non-conservative(production by the mean velocity gradient, production by the mean scalar gradient, mean and fluctuating pressure gradients and viscous dissipation) and finally, velocity-reaction rate correlation term. All the terms locally promote gradient or counter-gradient transport. For a quantitative study, one needs to do an integration of all the terms across the domain but since our aim is a budget analysis, a qualitative approach has been taken to study the effect of each term separately.

Figure 4.28 shows the conservative terms which are normalised by the mean scalar mass fraction gradient, $\frac{\partial \tilde{Y}_f}{\partial z}$. Therefore, when a fluctuating quantity is positive it means that its variation is in the same direction of mean scalar mass fraction gradient and hence, it promotes counter-gradient transport. As can be seen in this figure, convection has promoting and inhibiting contribution toward occurrence of LCGT whereas triple correlation term locally promotes counter gradient transport. For all three cases at z/δ_{ω_0} ≈19, where the scalar flux has the first positive peak, convection term has a positive contribution in occurrence of CGT but at further distance from the centre of the flow (Z/δ_{ω_0} ≈19.5) it behaves differently. For cases 1 and 2 it has an inhibiting effect on CGT (therefore, promotes gradient transport) but for case 3 it still shows a positive value which is counted toward counter-gradient transport boost although the turbulent scalar flux term solely varies toward a gradient transport as its normalised value is negative which means moving in the opposite direction of the mean mass fraction gradient.

Transport by turbulent flow field or triple correlation term varies in accordance with turbulent scalar flux term so wherever there is counter-gradient transport exists in the flow, triple correlation has promoting effect. Viscous diffusion is another conservative term which is considered here but since its magnitude is negligible compared to the convection and triple correlation terms, it has no key role in promotion or inhibition of CGT or GT. This term together with viscous dissipation term can be assessed together as both have the same order of magnitude and their local behaviour in the turbulent flow field and negligible contribution can be analysed. The effect of Lewis number on the trend of these quantities and the difference in the three cases studied here is evident.

Figure 4.29 illustrates the non-conservative terms contribution in promoting the counter-gradient or gradient transport. Similar to previous figure, all the quantities are normalised by the mean scalar mass fraction gradient so that any positive trend is counted toward promoting CGT and a negative value shows promoting GT. As can be seen, mean and fluctuating pressure gradient have the highest positive contribution when CGT occurs followed by the production II (production by mean scalar gradient) and production I(production by mean velocity gradient) terms. Viscous dissipation has the least contribution on promoting or inhibiting counter-gradient transport. All the plots are truncated from a point in the vertical axis in order to show the smaller variations of the non-conservative terms as well. The magnitude of mean and fluctuating pressure gradient terms are a few times larger than that of the production terms and an order of magnitude larger than the dissipation term. The fact that these quantities have a lot of fluctuations even when they are averaged and normalised makes it really difficult to express their effect as a general rule but it can be clearly observed that they play a key role in promoting CGT or GT as their magnitude is relatively larger than other terms. Since the conservative terms are known to act as redistributive quantities for the turbulent scalar flux [114], pressure gradient terms become the most dominant term to be a source or sink for the occurrence of counter-gradient or gradient transport. As can be seen in all three cases, both mean and fluctuating pressure terms promote or inhibit CGT in local sense. Where they are positive they promote CGT and where they are negative they inhibit CGT. This is in contrast with findings reported in [114] where the pressure terms are always found to locally promote CGT. The fact is that for the non-premixed flame, the pressure gradient across the shear layer has positive and negative values due to combustion and this generates both favourable and adverse pressure gradient. It has been found that for a premixed flame, favourable pressure gradient induces counter-gradient transport whereas the adverse pressure gradient enhances the gradient transport[78]. If a diffusion flame is treated as a number of small patches of premixed or partially-premixed reactants along the flame interface, then this fact can be extended to this type of flow as well. Therefore, it may not be true to generalise the idea that the mean and fluctuating pressure terms in scalar flux transport equation

promote counter-gradient transport as this may not always be the case. It is also evident from this figure that both production terms have smaller magnitudes compared to that of the pressure terms so they cannot play a key role in gradient or counter-gradient transport when pressure terms exist. However, for case 1 and case 2 at Z/δ_{ω_0} ≈19.5, production I and II show a positive contribution in occurrence of CGT whereas for case 3 at the same location the flow does not have this feature which again proves the fact that such terms are highly behave locally and their effect cannot be generalised under different flow conditions. Figure 4.30 shows the mean fluctuating velocity-reaction rate correlation for all three cases. It has an order of magnitude smaller value compared to the pressure terms but actually the combustion generated waves are the main source for generation of the pressure gradient terms. As can be seen, reaction-velocity correlation term has a sheer local effect on promoting or inhibiting CGT. For cases 1 and 3 at z/δ_{ω_0} ≈19, term $\overline{w''\dot{\omega}_f}$ has positive value which means a positive contribution toward occurrence of CGT whereas for case 2 it has inhibiting effect on CGT. At z/δ_{ω_0}=19.5, velocity-reaction correlation for case 2 and case 3 tends to promote CGT as they are positive in that region whereas for case 1, this term is negative so acts as a sink despite the fact that the flow shows counter-gradient transport behaviour as the turbulent scalar flux term is positive. This difference in the behaviour of the velocity-reaction correlation term makes it difficult to assess the way it affect the gradient transport. Such complicated trend was also reported in the work of Luo[114]. So far, all the terms in the right hand side of the turbulent scalar flux equation has been expressed and their variations across the mixing layers has been briefly illustrated. One question that may arise is that: Is there any possibility to decrease the complexity of the right-hand side and approximate sum of the all terms by a simpler expression. Is it possible to estimate the value of the turbulent scalar flux without having to solve for all the terms on the right-hand side. For this purpose, variations of the following quantities are plotted in figure 4.31: sum of terms on the right-hand side of the equation 4.4, which is referred as RHS in here, right-hand side minus the pressure gradient terms(both mean and fluctuating), RHS minus $[-\overline{\theta''}\frac{\partial\overline{p}}{\partial x_j} - \overline{\theta''\frac{\partial p'}{\partial x_j}}]$, and sum of the mean and fluctuating pressure gradient term, $-\overline{\theta''}\frac{\partial\overline{p}}{\partial x_j} - \overline{\theta''\frac{\partial p'}{\partial x_j}}$, along with turbulent scalar flux term, $\overline{(\rho\theta''u_j'')}$. To be consistent with other figures presented earlier, all the quantities are normalised by the mean scalar(H_2) mass fraction gradient. As discussed earlier, the pressure gradient terms (either the fluctuating term or the mean term) are the main source or sink for local counter-gradient or gradient transport of the species in a reacting shear-layer. By looking at all three plots it is deducted that when the mean and fluctuating pressure gradient are deducted from the RHS, the rest of the terms vary almost along with the turbulent scalar flux and follow the same trend as the scalar flux term (solid lines vs. dashed lines). So it can be immediately concluded that summation of the pressure terms

has the governing role on the outcome of the right-hand side of the turbulent scalar flux equation. While the rest of the RHS terms vary along with the turbulent scalar flux term, mean and fluctuating pressure gradient can cause a change in the trend which results in either gradient or counter-gradient occurrence. Another point worths noting is that the trend of sum of the mean and fluctuating pressure gradient terms follows that of the RHS terms(summation of all the quantities including the pressure gradient terms) but with an offset from each other(dotted lines vs. dashed-dotted lines). So if the whole right-hand side of the turbulent scalar flux equation is replaced with the sum of the mean and fluctuating pressure gradient terms, it still predicts a reasonably good estimation of the right-hand side magnitude as well as its trend. Luo[114] proposed a relation to estimate the summation of the mean and fluctuating pressure gradient called as "effective pressure gradient":

$$\frac{\partial p_e}{\partial x_j} = -\frac{1}{\sqrt{\widetilde{\theta''\theta''}}}(\overline{\theta''\frac{\partial p'}{\partial x_j}} + \overline{\theta''}\frac{\partial \overline{p}}{\partial x_j}) \tag{4.6}$$

Therefore, perhaps this can be a fairly accurate estimation to be replaced with the right-hand side of the turbulent scalar flux when there is no interest in analysing all the terms individually or when only an estimation of the turbulent scalar flux value is of interest. In addition, if this relation is found to be very close to the summation of the RHS terms(so that the offset between the corresponding plots are minimised), it can be a good alternate for predicting the counter-gradient or gradient transport. Summation of the RHS terms in all three plots show a positive value at the locations where counter-gradient transport have occurred. By bringing the value of the "effective pressure gradient" as close as possible to that of the sum of the RHS terms, prediction of the counter-gradient transport seems to be possible by just using this quantity. More simulations under different conditions are still needed to bring this hypothesis into practice. Also, the expression for the "effective pressure gradient" may need some alterations to be reasonably accurate under different flow conditions.

4.2.4 Quantification of differential diffusion

A mixture fraction in the conventional sense cannot be defined for a binary-fluid mixing layer with different Lewis numbers. This is one manifestation of differential diffusion. Linan[116, 117] was among the first persons who introduced an alternative definition for mixture fraction in the presence of differential diffusion. The definition proposed by him, later studied in more detail by Cuenot and Poinsot[118] and Veynante and Vervisch[119]. Sutherland et. al.[120] proposed a definition to be able to quantify differential diffusion. According to them, differential diffusion can be quantified as the difference between

diffusion term of the mixture fraction's transport equation with real properties and diffusion term of the mixture fraction's transport equation with the assumption of equal diffusivity. This can be written in the form of:

$$DD \equiv \frac{-1}{\beta_1 - \beta_0} \sum_{\ell=1}^{N_e} \gamma_\ell \left(\sum_{i=1}^{N_s} \frac{a_{\ell i} W_\ell}{W_i} \nabla \boldsymbol{j}_i \right) - \nabla(\rho D_{mix} \nabla f) = \gamma_{exact} - \gamma_{approx.} \tag{4.7}$$

in which $\boldsymbol{j}_i$ is the diffusion flux for the species i, γ_l is weighting factor, $a_{\ell i}$ is number of atoms of element ℓ in species i, W_ℓ is the molecular weight of element ℓ, W_i is species molecular weight, D_i is the diffusivity of species i, Y_i is mass fraction of species i, ρ is the mixture density,γ_{exact} is the diffusion term with real diffusivity of species, γ_{approx} is the diffusion term with equal diffusivity of species, D_{mix} is the mixture fraction diffusivity and is a constant and taken to be the average of species diffusivity[121] and finally, β and f are coupling function and mixture fraction based on coupling function, respectively, which are defined as:

$$\beta = \sum_{\ell=1}^{N_e} \gamma_\ell \left(\sum_{i=1}^{N_s} \frac{a_{\ell i} W_\ell Y_i}{W_i} \right) \tag{4.8}$$

and:

$$f = \frac{\beta - \beta_o^0}{\beta_f^0 - \beta_o^0} \tag{4.9}$$

with f_{st} being 0.11 in the current study as both streams carry pure single reactant. Differential diffusion (DD) shows the difference between the exact diffusion term γ_{exact} (first term on the RHS) and that assuming equal diffusivity $\gamma_{approx.}$ (second term on the RHS). This is essentially the error caused by the equal-diffusivity assumption in the form of unity Lewis number.

Individual species also has a contribution to DD which is defined as follows[120]:

$$\kappa_i = \frac{-1}{\beta_1 - \beta_0} \sum_{\ell=1}^{N_e} \frac{\gamma_\ell W_\ell a_{\ell i}}{W_i} (\nabla \boldsymbol{j}_i + \nabla(\rho D_{mix} \nabla f)) \tag{4.10}$$

To quantify this parameter in mixing layer flows, case 1 with different Lewis number and case 3 with equal(unity) Lewis number are chosen. Results are presented for the non-reactive mixing layer at $tU_{ref}/\delta_{\omega_0}$=40 and for reactive mixing layer at $tU_{ref}/\delta_{\omega_0}$=60 considering the simulation with Da=10. It must be noted that the value of DD is equal to zero for the flows with equal Lewis number as both terms of equation 4.7 are equivalent. Figure (4.32) shows the DD, γ_{exact} and $\gamma_{approx.}$ terms, hydrogen mass fraction and oxygen mass fraction contribution to DD, all normalised by γ_{exact} across the mixing layer for case 1 with different Lewis number. Quantities are averaged in the x-y homogeneous planes and plotted along the vertical coordinate(z). In figure 4.32(a), all the quantities are constant across the domain when there is no reaction. DD/γ_{exact} shows a value of

0.295 which is actually the difference between normalised γ_{exact} and γ_{approx} which means equal Lewis number assumption to the H_2-O_2 mixture, introduce an error of about 30 percent compared to the case where the real Lewis number values are used. Each of the two species contribute to this error. As shown in the same plot, H_2 contributes the most as its normalised value is very close to the normalised DD and combining this with the oxygen's contribution gives the number of 0.295 for DD. The DD can be also represented as the summation of all the species' contribution[120]. When combustion is started, these figures show a dramatic increase. Figure 4.32(b,c) show the reactive case where the DD and $\gamma_{approx.}$ show a peak(in different direction) around the stoichiometric mixture fraction (f=0.11 at $z/\delta\omega_0 \approx 13$). Species contribution has also been increased compared to the non-reactive case since the species are more rigorously interacting with hydrogen still shows a larger quantity except at the region where DD/γ_{exact} is negative.

4.2.5 Summary and Conclusions

Direct numerical Simulation for binary-species mixing layer has been conducted. The results have been presented for non-reactive mixing layer as well as reactive mixing layer with two different reaction rates. Reaction rate is determined based on the Arrhenius Law with two different values for Damkohler number. For comparison, only Lewis number has been changed in the flows. Three cases were studied. Case 1 with different Lewis number of 0.3 and 1.0 for hydrogen and oxygen, respectively. Case 2 with equal Lewis number of 0.3 for both species and case 3 with unity Lewis number. The effects of species Lewis number have been studied on mixing layer development together with a turbulent field analysis. It was shown that the Lewis number does not have a substantial effect on the properties such as growth rate, vorticity field and turbulent kinetic energy or dissipation rate. Also for non-reactive mixing layer, quantities such as density and scalar mass fraction have only small differences. For reactive mixing layer, however, properties of the flow which are linked more to the species transport, show more variations compared to other quantities. Product mass fraction and scalar energy(represented as a spectrum or transport of variance) are among these quantities which were presented in the text. Next stage in this research, was scrutinising the interaction between the scalar field and the turbulence field. Scalar variance budget and turbulent scalar flux transport analysed for both non-reacting and reacting mixing layer to achieve to this aim. The effects of difference in the species diffusivity became more prominent. It was shown that applying unity Lewis number for both species makes them to get more energy due to turbulence as their variance is the highest among the two other cases. Scalars with smallest Lewis number were shown to have the minimum amount of

scalar energy. In contrast, scalars with higher Lewis number values, were shown to have the minimum dissipation rate which further supports the reason why they have larger variance. The flow in case 3 with different species Lewis number showed values between case 1 with unity Lewis number and case 2 with Le=0.3. Therefore, unity Lewis number over-predicts such variations compared to the case with different(and yet more realistic) species Lewis number. Differences in flow properties and turbulence data become more pronounced when reaction is in progress.

Turbulent scalar flux has been studied to evaluate the importance of each term in its transport equation. It was shown that the pressure terms(fluctuating and mean parts) as well as convection term play the major role where counter-gradient transport exist in the flame. Among the pressure terms, fluctuating term shows the most contribution to this. It was shown that the net amount of the other terms can be neglected in predicting the gradient or counter-gradient transport since the summation of the pressure terms are in close agreement with the variation of counter-gradient transport and it is suggested that a combination of these two terms can be replaced to the RHS of the scalar transport equation.

Quantification of the differential diffusion has also been performed. This shows the amount of error which exists when the equal Lewis number assumption is employed. The error increases when reaction is started.

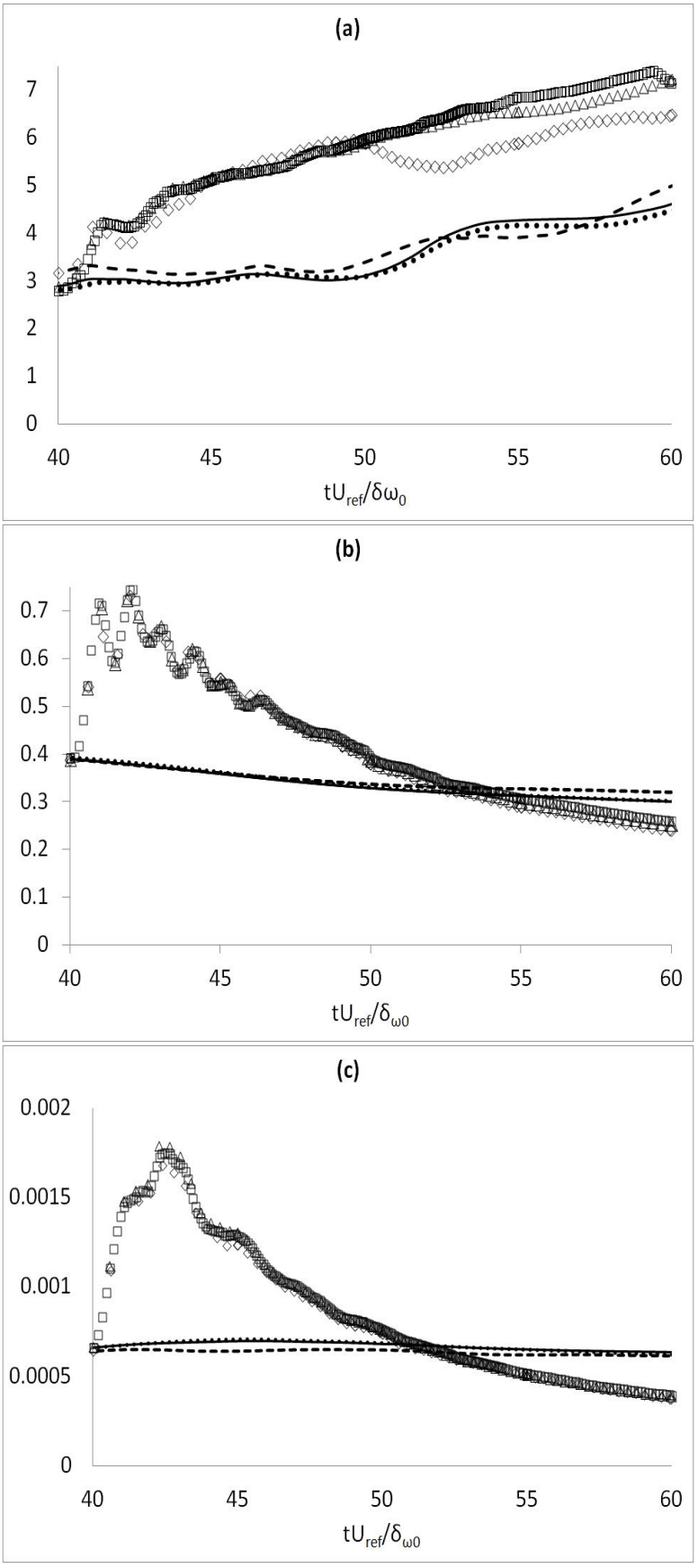

FIGURE 4.16: (a) Vorticity thickness growth rate. (b) Time history of turbulent kinetic energy κ evolution. (c) Time history of turbulent dissipation rate ϵ evolution. Lines represent quantities in non-reactive simulation and symbols represent quantities in reactive simulation. For the non-reactive mixing layer (———) case 1, (– – –) case 2, and (· · · ·) case 3. For the reactive mixing layer: (△) case 1, (◊) case 2, and (□) case 3.

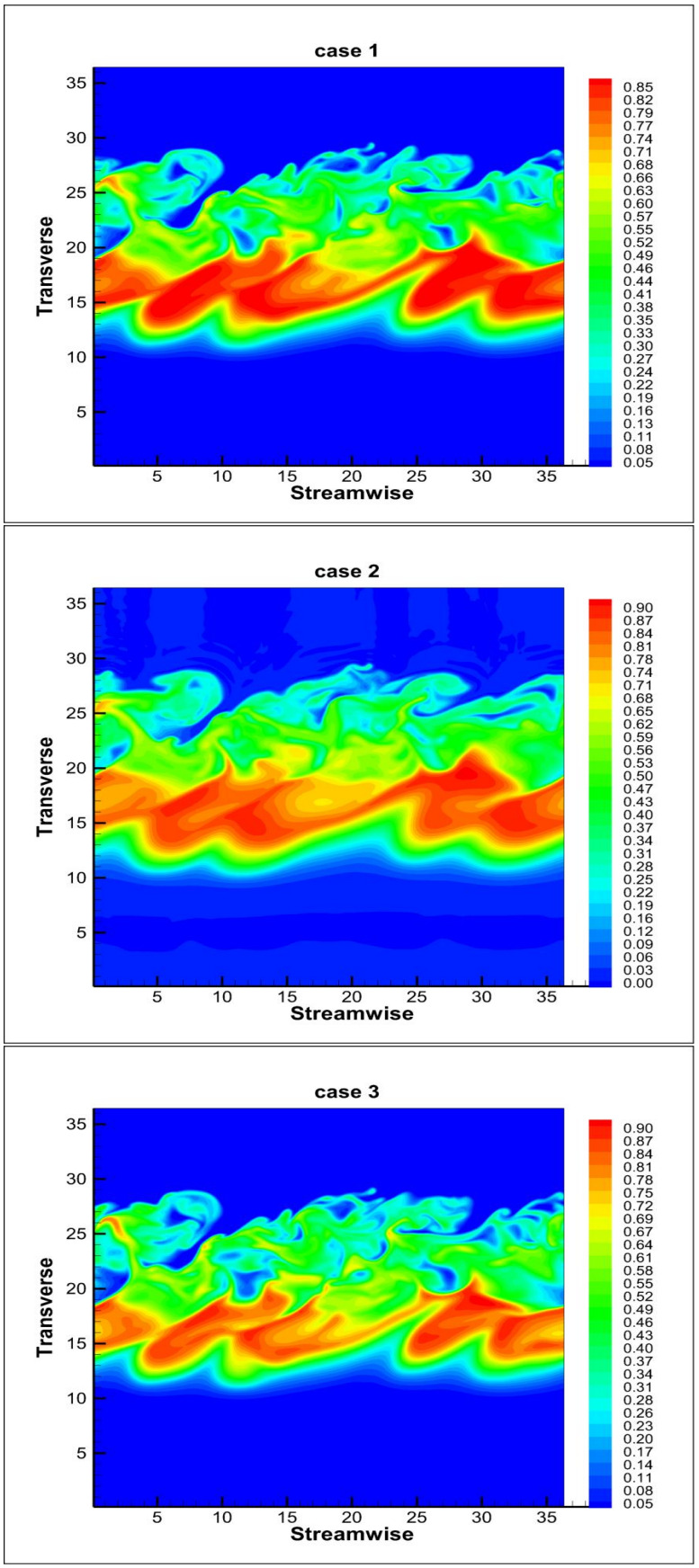

FIGURE 4.17: Snapshots of product mass fraction contour (Y_{H_2O}) at $tU_{ref}/\delta_{\omega_0}$=60 and at y-z non-homogeneous plane in the middle of the mixing layer for cases 1 to 3. Each plot shows 30 contours.

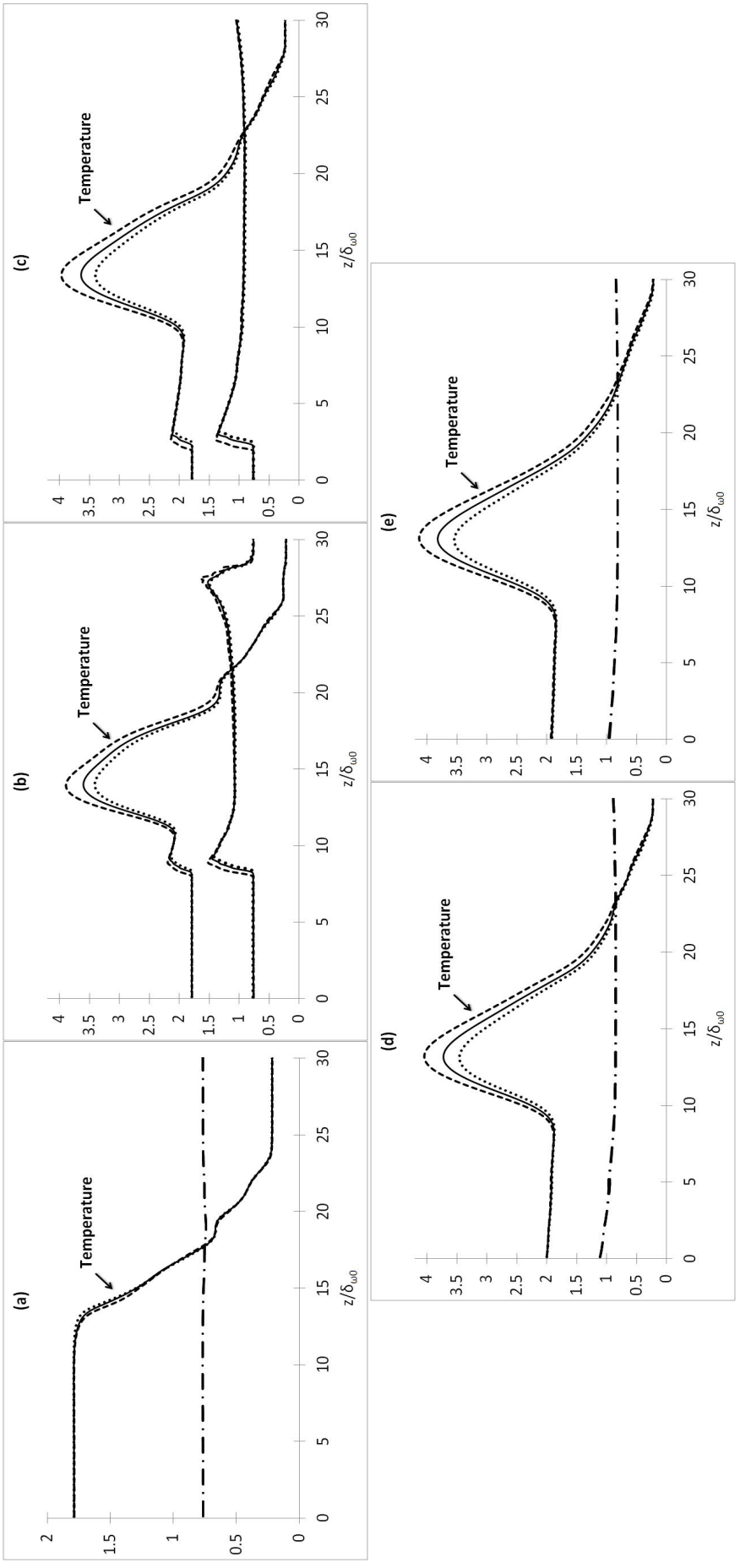

FIGURE 4.18: Mean pressure and temperature across the mixing layer for all three cases at different simulation times before reaction, during reaction and at the end of simulation: (a) $tU_{ref}/\delta_{\omega_0}$=40, (b) $tU_{ref}/\delta_{\omega_0}$=45, (c) $tU_{ref}/\delta_{\omega_0}$=50, (d) $tU_{ref}/\delta_{\omega_0}$=55, (e) $tU_{ref}/\delta_{\omega_0}$=60. (———) case 1, (– – –) case 2, (· · · ·) case 3, (– · – ·) overlapped pressure profile in (a,d and e) for all the cases.

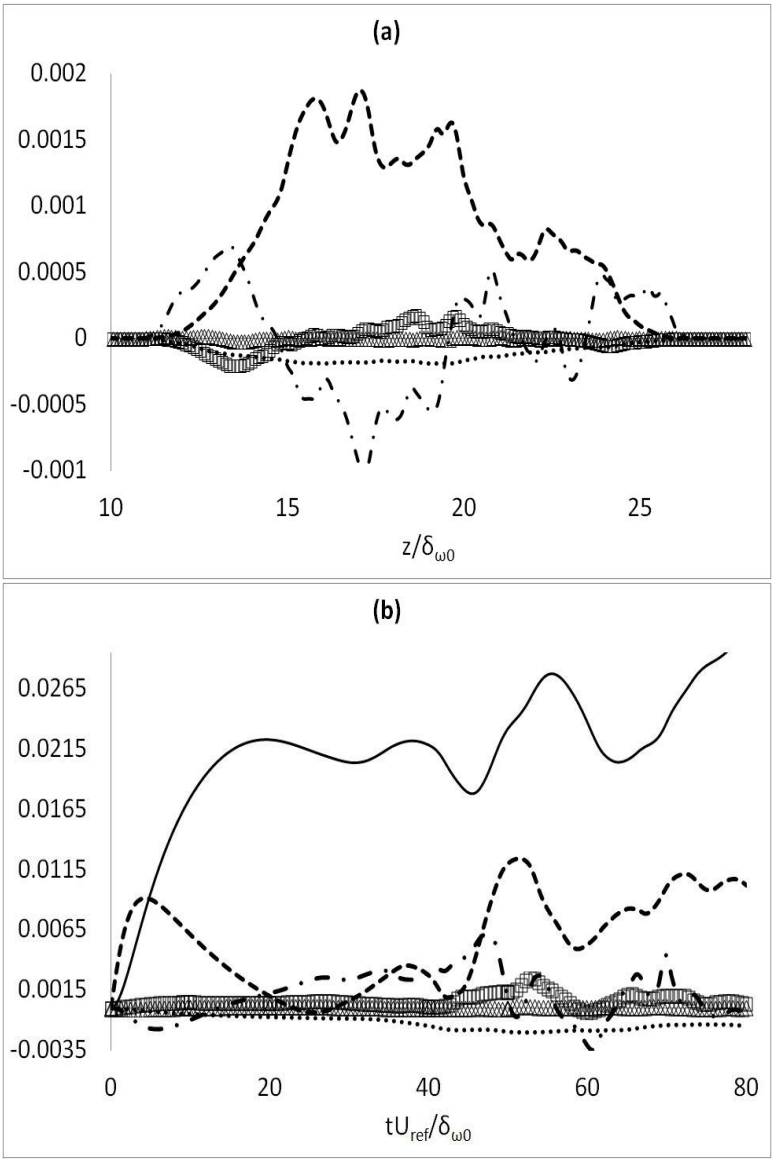

FIGURE 4.19: Hydrogen mass fraction variance budget($\widetilde{Y''^2_{H_2}}$) for case 2 with equal Lewis number of 0.3. (a)Scalar variance budget across the domain at time $tU_{ref}/\delta_{\omega_0}$=80, (b) Time history of the integrated terms in the equation 4.3 across the domain. (□)Convection, (△)Molecular diffusion, (– · – ·)Turbulent transport,(– – –)Production by mean scalar gradient, (· · · ·)Scalar dissipation, and (———)Integral of hydrogen mass fraction variance$\widetilde{Y''_{H_2}}$/10(only in (b)).

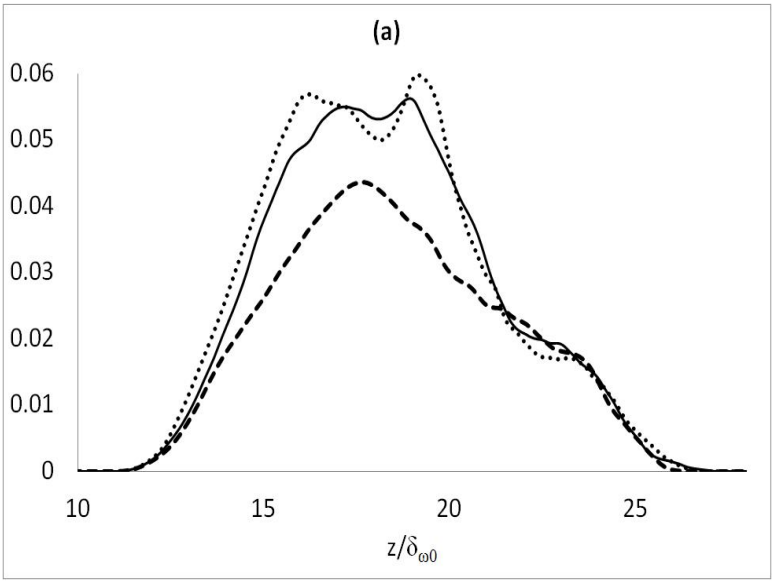

FIGURE 4.20: Variance of the hydrogen mass fraction($\widetilde{Y''_{H_2}Y''_{H_2}}$) at time $tU_{ref}/\delta_{\omega_0}$=80. (———) case 1, (– – –) case 2, and ($\cdots$) case 3.

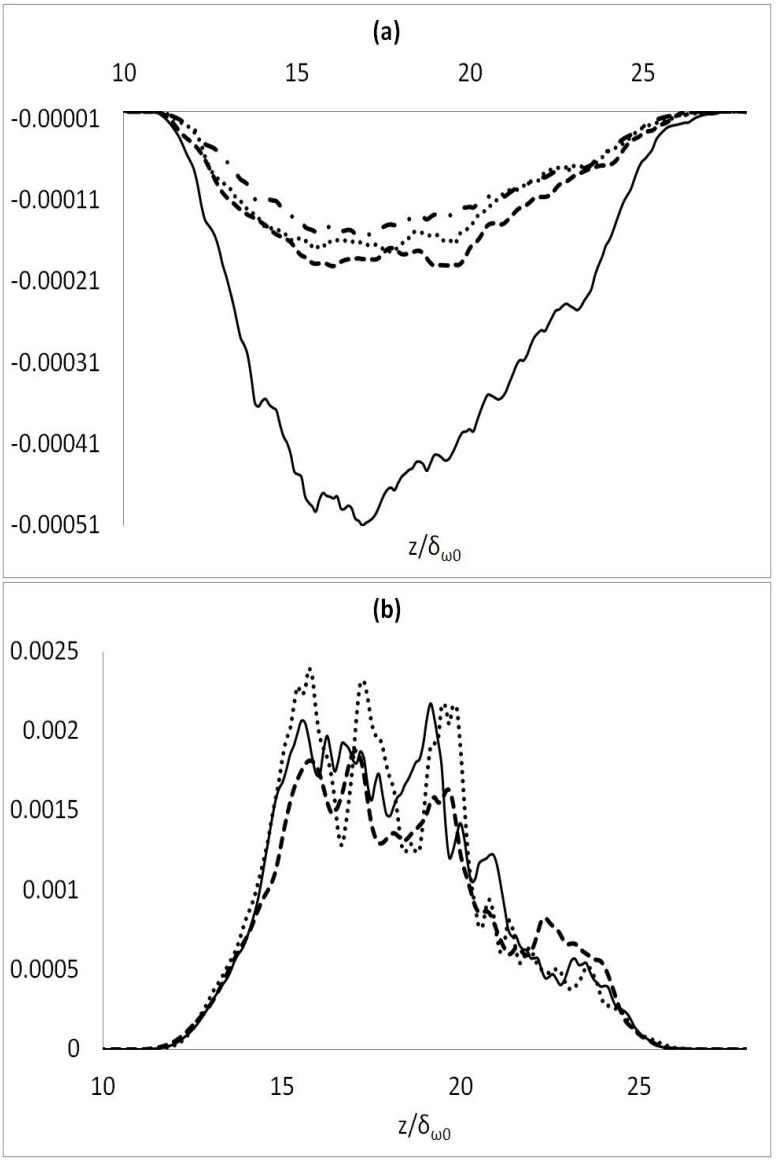

FIGURE 4.21: (a)Scalar dissipation, (b)Production by mean scalar gradient.(———)case 1 for H_2, (– – –)case 2 for H_2, (· · · ·)case 3 for H_2, and (– · – ·)case 1 for O_2.

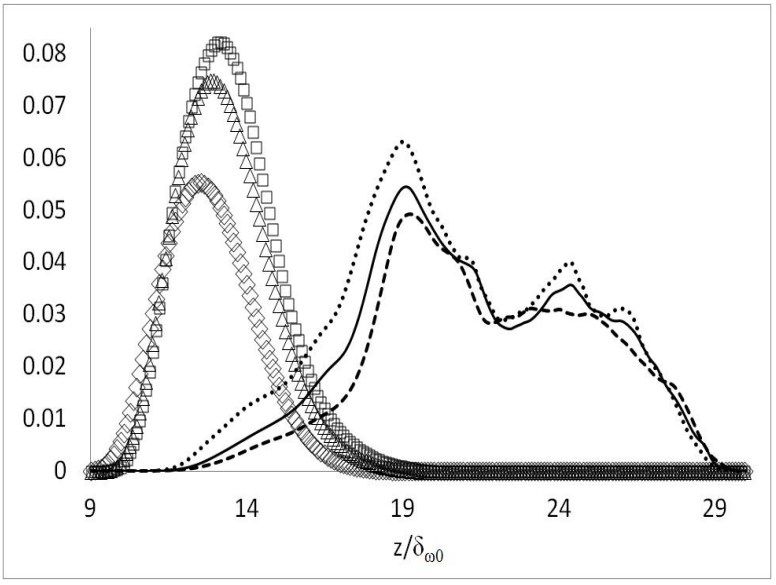

FIGURE 4.22: Variance of the scalar mass fraction($\widetilde{Y''_{H_2}Y''_{H_2}}$ and $\widetilde{Y''_{O_2}Y''_{O_2}}$) at time $tU_{ref}/\delta_{\omega_0}$=60 in reactive mixing layer. Lines represent hydrogen variance and symbols represent oxygen variance. $\widetilde{Y''_{H_2}Y''_{H_2}}$: (———) case 1, (– – –) case 2, and ($\cdots$) case 3. $\widetilde{Y''_{O_2}Y''_{O_2}}$: ($\triangle$) case 1, ($\Diamond$) case 2, and ($\square$) case 3.

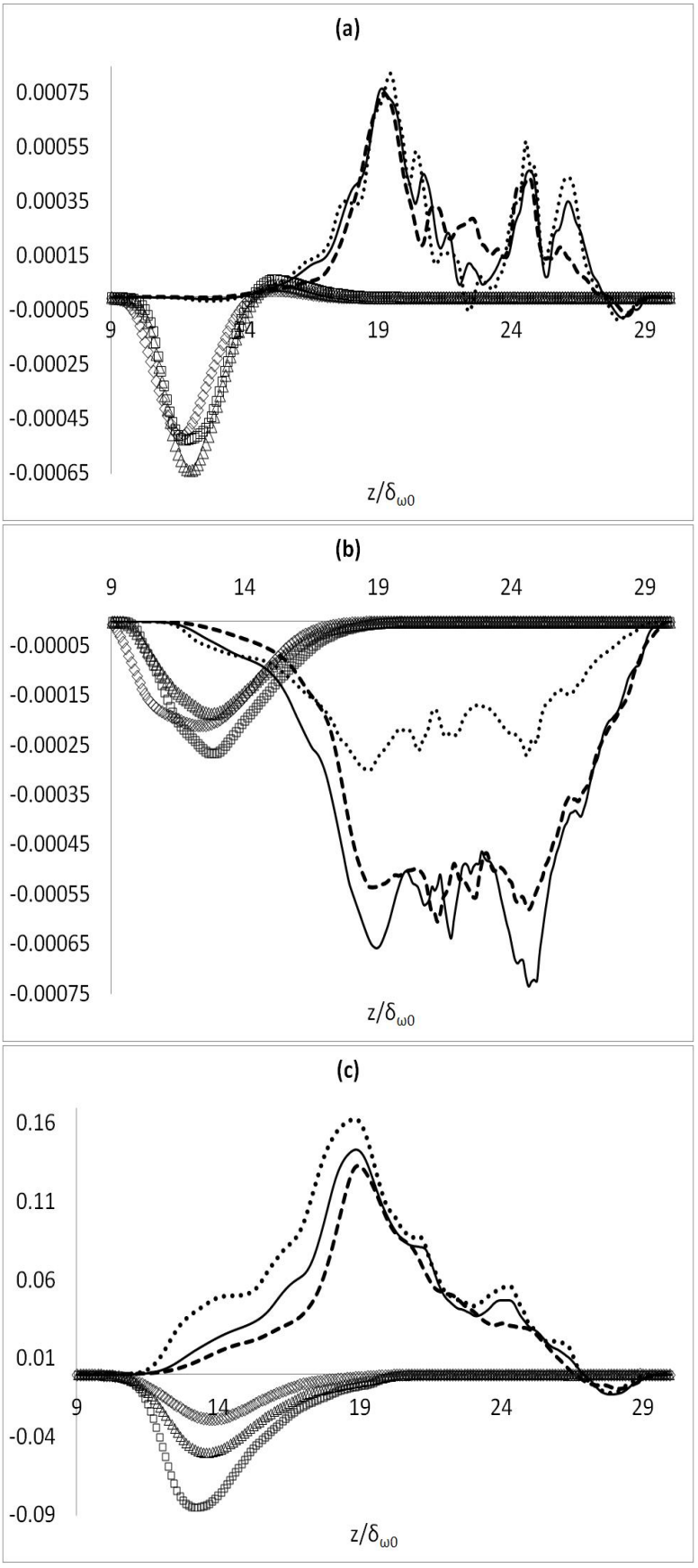

FIGURE 4.23: Major contributing terms in the scalar variance budget at time $tU_{ref}/\delta_{\omega_0}$=60 in reactive mixing layer. (a) Production term, (b) Dissipation term, and (c) Reaction term. For the variance of hydrogen mass fraction: (———) case 1, (– – –) case 2, and (· · ·) case 3. For the variance of oxygen mass fraction: (△) case 1, (◊) case 2, and (□) case 3.

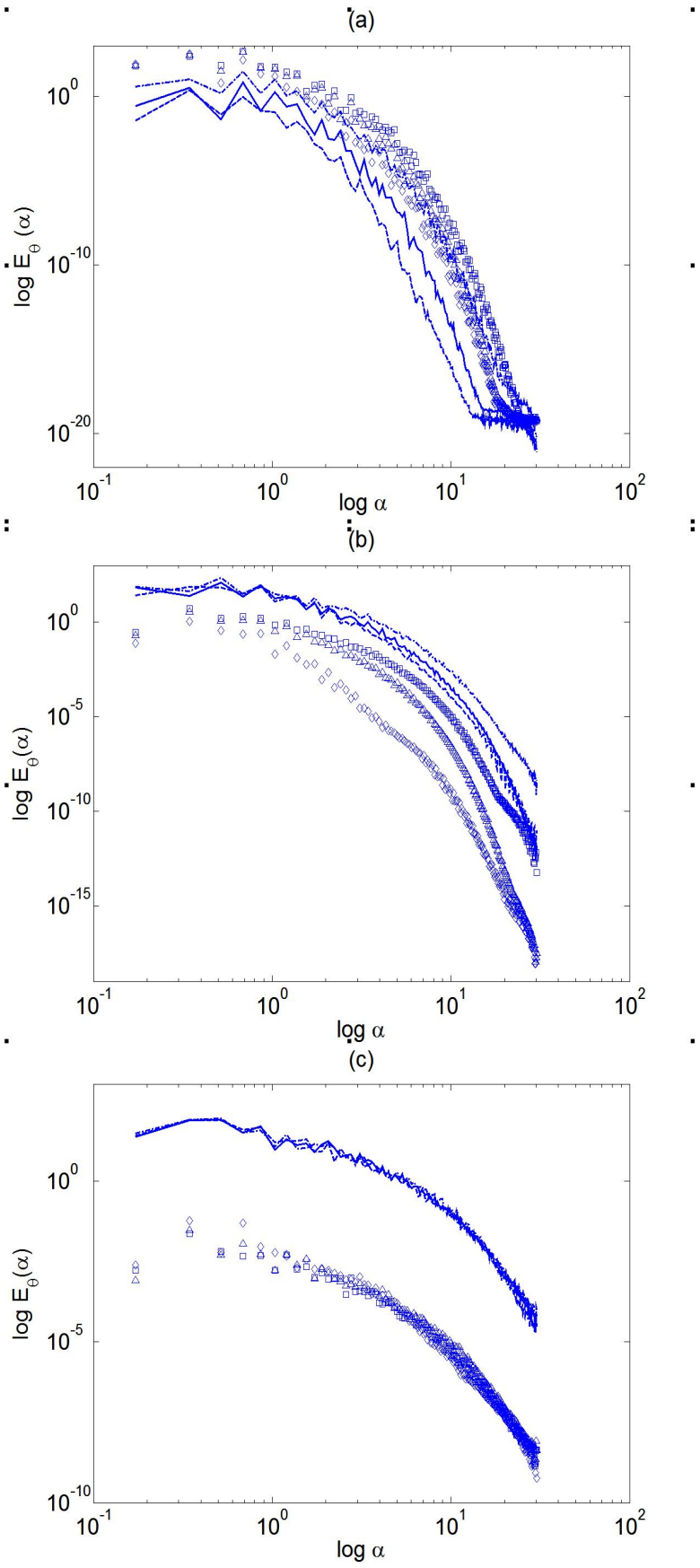

FIGURE 4.24: Scalar energy spectra at time $tU_{ref}/\delta_{\omega_0}$=60 in reactive mixing layer at three different planes in the transverse direction. (a) at $z = L_z/3$, (b) at $z = L_z/2$, and (c) at $z = 2L_z/3$. For the spectra of hydrogen variance: (———) case 1, (– – –) case 2, and (· · · ·) case 3. For the spectra of oxygen variance: (△) case 1, (◊) case 2, and (□) case 3.

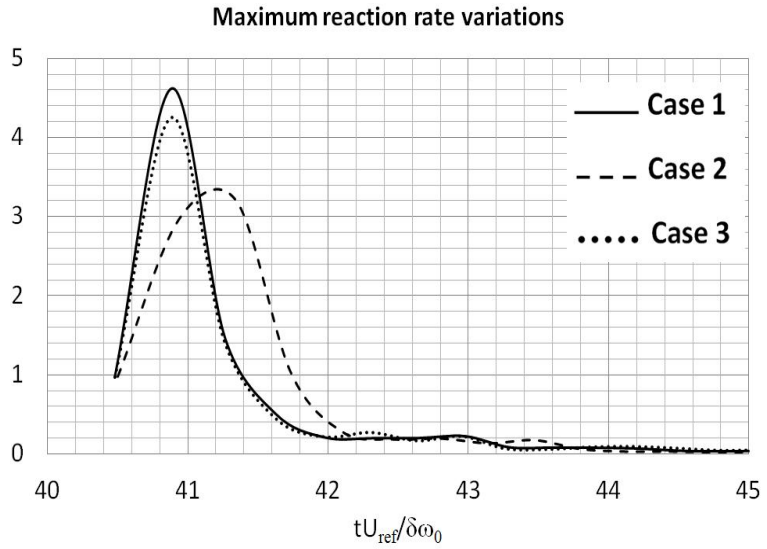

FIGURE 4.25: Variation of the maximum reaction rate with time.

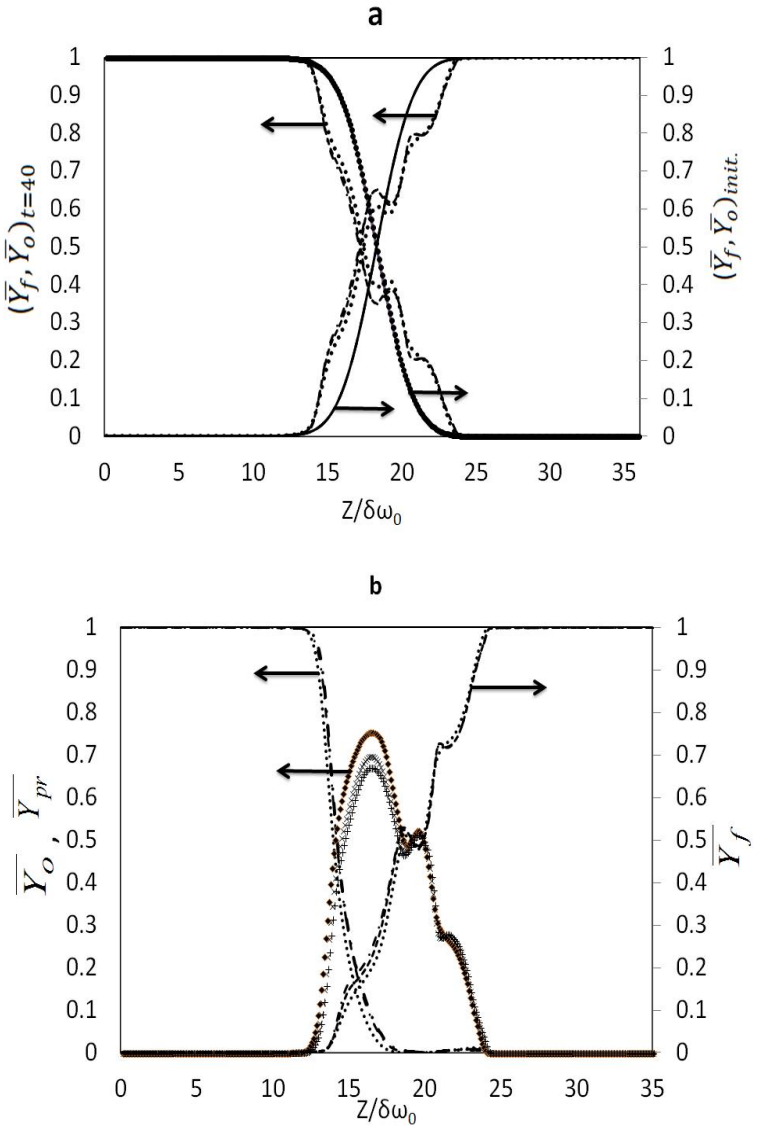

FIGURE 4.26: Mean scalar mass fraction distribution across the mixing layer. (a): Right axis shows $\overline{Y_{H_2}}$ at initialisation stage(with overlapping graphs as all cases are initialised the same) and at $tU_{ref}/\delta_{\omega_0}$=40(just before reaction starts) and left axis shows $\overline{Y_{O_2}}$ at initialisation stage(with overlapping graphs which shows unique mass fraction distribution) and at $tU_{ref}/\delta_{\omega_0}$=40; (b): At $tU_{ref}/\delta_{\omega_0}$=41 when maximum reaction rate occurs. Right axis shows $\overline{Y_{H_2}}$ and left axis shows $\overline{Y_{O_2}}$ and $\overline{Y_{H_2O}}$. (– – –) case 1, (· · · ·) case 2,(– · – ·) Case 3. For the plot(b) where combustion exist, symbols are: (X) $\overline{Y_{H_2O}}$ for case 1, (ffl)(◇) $\overline{Y_{H_2O}}$ for case 2, and (+) $\overline{Y_{H_2O}}$ for case 3.

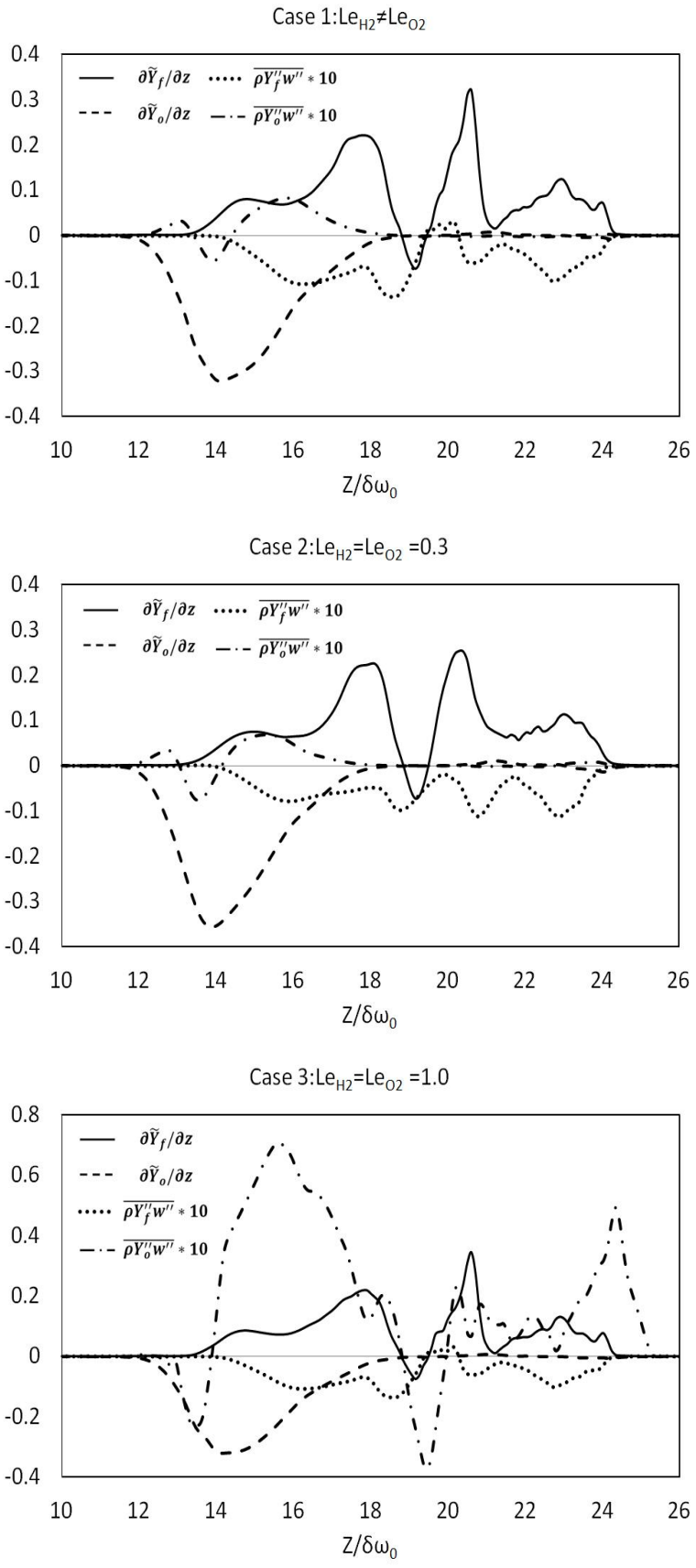

FIGURE 4.27: Turbulent scalar flux and mean scalar gradient at $tU_{ref}/\delta_{\omega_0} = 41$.

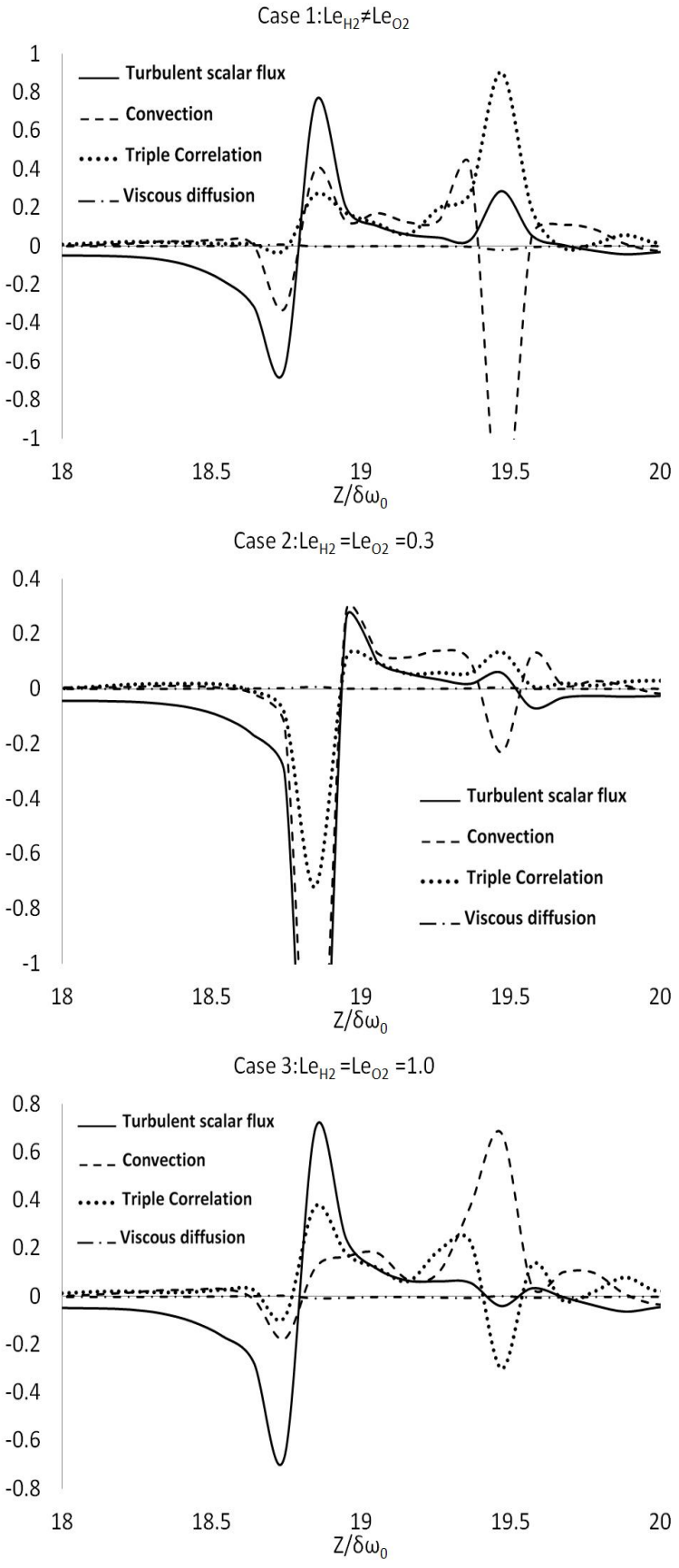

FIGURE 4.28: Contribution of conservative terms in the LCGT. All fluctuating quantities are normalised by $\frac{\partial \tilde{Y}_f}{\partial z}$.

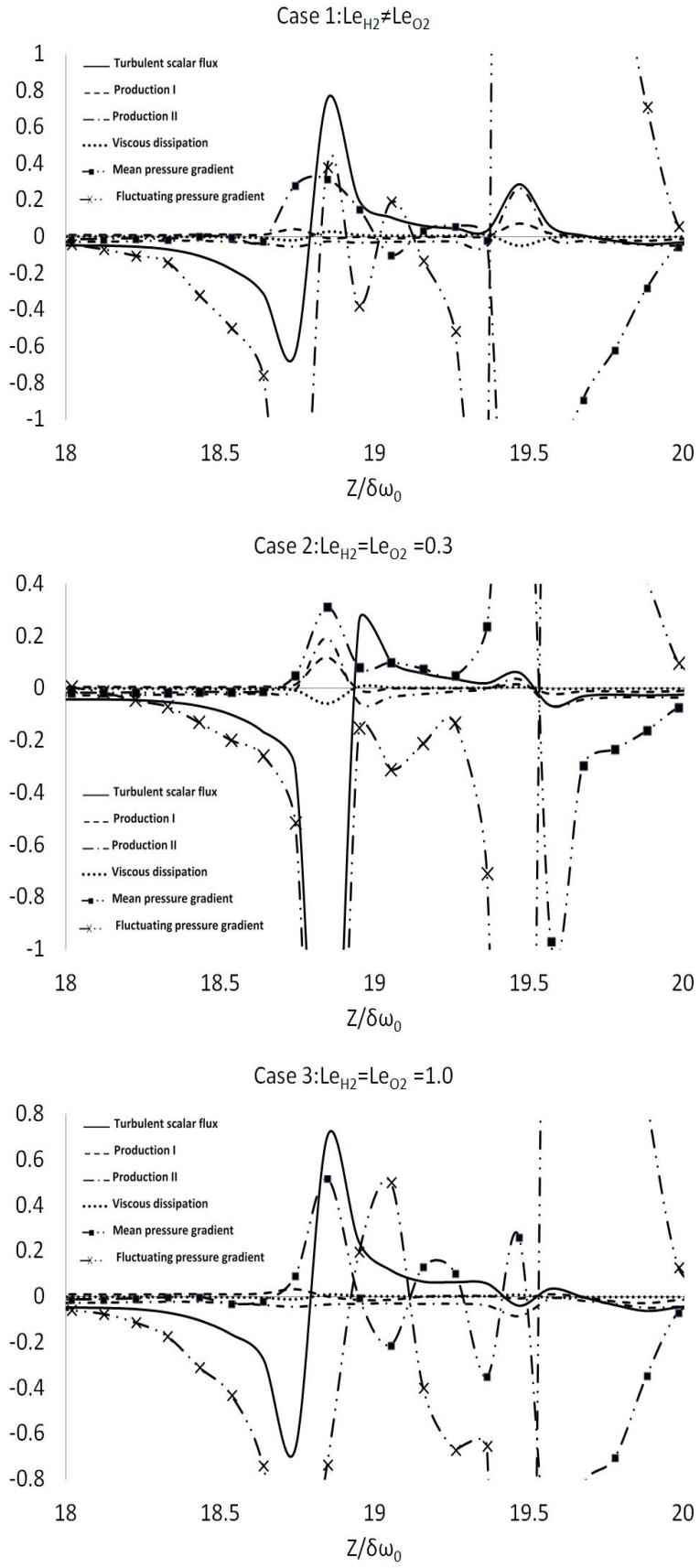

FIGURE 4.29: Contribution of non-conservative terms in the LCGT. All fluctuating quantities are normalised by $\frac{\partial \tilde{Y}_f}{\partial z}$.

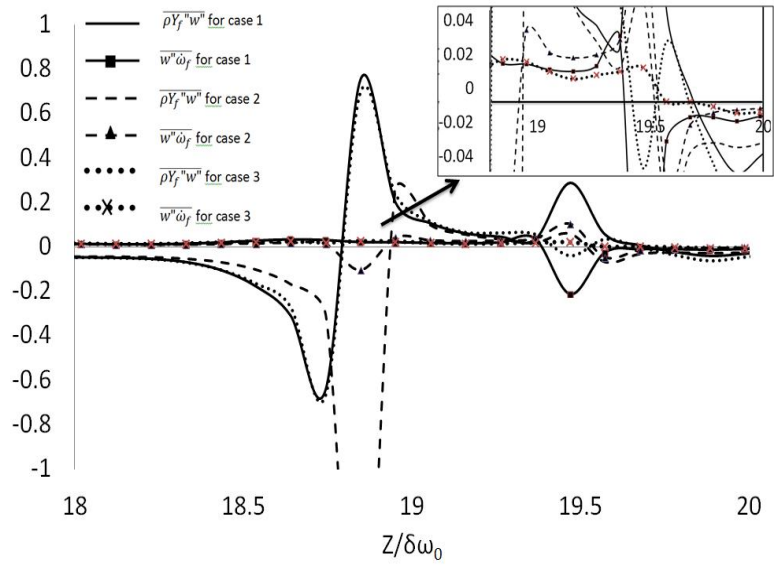

FIGURE 4.30: Contribution of velocity-reaction correlation term in the LCGT. All fluctuating quantities are normalised by $\frac{\partial \tilde{Y}_f}{\partial z}$.

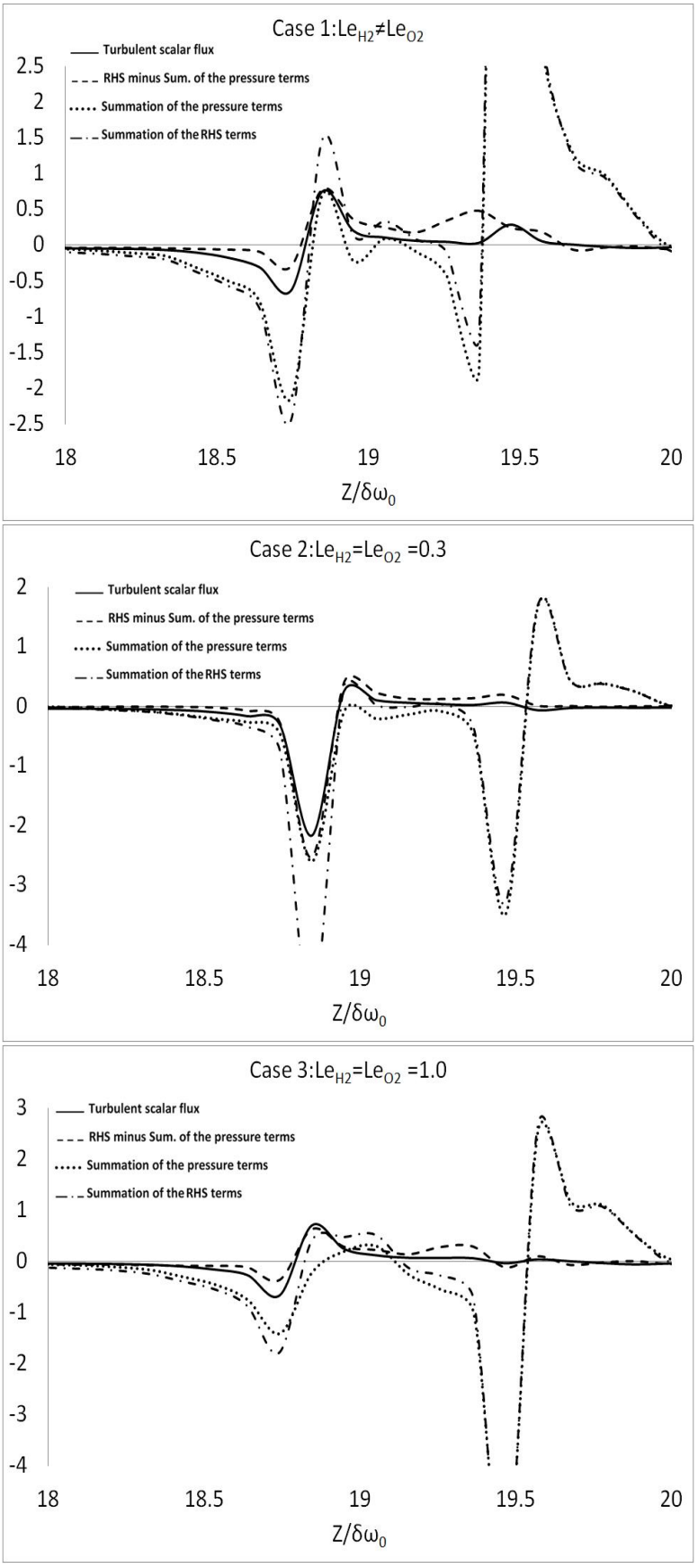

FIGURE 4.31: Comparison of the major contributing terms in GT or CGT for all three cases. Solid line: $\overline{\rho Y_f'' u_j''}$, Dashed line: RHS of equation 4.4 minus $[-\overline{\theta''}\frac{\partial \overline{p}}{\partial x_j} - \overline{\theta''\frac{\partial p'}{\partial x_j}}]$, Dotted line: $-\overline{\theta''}\frac{\partial \overline{p}}{\partial x_j} - \overline{\theta''\frac{\partial p'}{\partial x_j}}$, Dashed-dotted line: RHS of equation 4.4. All fluctuating quantities are normalised by $\frac{\partial \tilde{Y}_f}{\partial z}$.

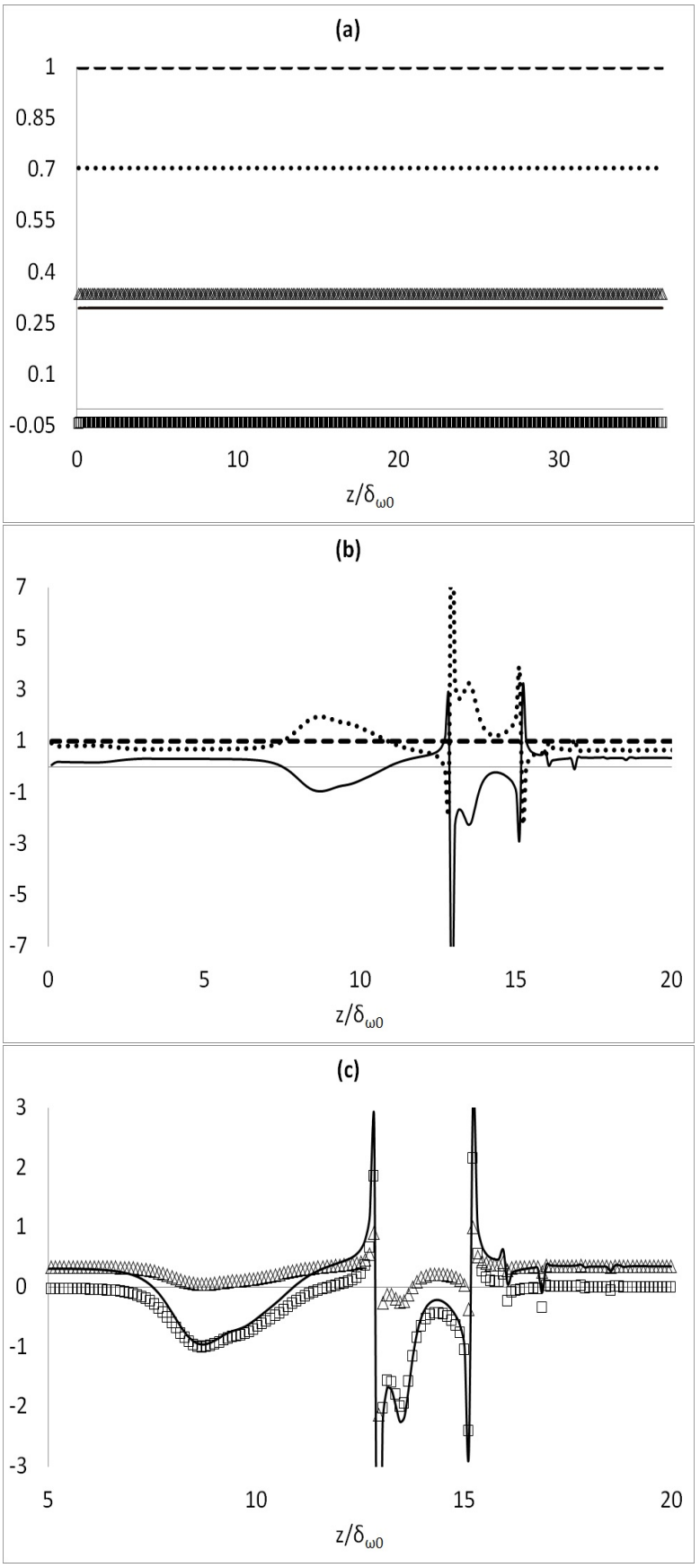

FIGURE 4.32: (a) Non-reactive mixing layer representing: (———) DD, (– – –) γ_{exact}, ($\cdots$) γ_{approx}, (△) κ_{H_2}, (□) κ_{O_2}. (b and c) Reactive mixing layer representing the same quantities as in (a). All quantities are normalised by γ_{exact}.

Chapter 5

Results and discussions for multi-species mixing layers

Direct numerical simulation of fluid flow carrying species with real properties is among the most accurate ways to study the physics of such flows. In this chapter, the results of the DNS simulation for a $H_2 - O_2$ temporal mixing layer with real molecular properties have been presented. The chemistry is based on a 18-step finite-rate reversible reactions which is based on the reduced mechanism of hydrocarbon combustion. Total number of 9 species form reactants and products. The geometry is a three-dimensional box with periodic boundary conditions in stremwise and spanwise directions and non-periodic as well as non-reflecting boundary conditions for upper and lower boundary in the transverse direction. Reactants which are two separate streams of hydrogen and oxygen occupy the upper-half and the lower-half of the domain, respectively. Hydrogen stream has been diluted with nitrogen with the ratio of 60% to 40%. Dilution of hydrogen with nitrogen has been also seen in the works of Grinstein and Kailasanath[51], Echekki and Chen[18], Lu et. al.[23], Im et. al.[9] and Knaus and Pantano[5]. Simulation was started with distribution of diluted hydrogen and pure oxygen in the upper and lower streams, respectively. Initial temperature, velocity and mass fraction were applied using an error function profile. For oxidiser a higher temperature was chosen to bring the density ratio of two streams closer. This will also facilitates the study of auto-ignition in mixing layers. Choosing such a high temperature was also reported in the work of Zheng et. al.[122]. Moreover, error function applies some degree of premixing to the scalar field at the interface of both streams. Velocity disturbances were added as spanwise and streamwise vorticity field whose velocity components were superimposed to the initial mean velocity field. The main goal in this chapter is to highlight the effects that multiple species will have on the turbulent flow in comparison with a turbulent flow carrying only two or three species which was discussed in previous chapter.

In this chapter, five series of DNS have been performed. Three of them utilise smaller domain compared to the latter two which comprise a larger domain with streamwise and spanwise length are doubled. DNS of smaller cases are presented first. Results are presented in a way to show the grid independency of the simulations and in parallel, show the differences between unity Lewis number assumption and real Lewis number to the mean flow properties. For the two larger domains, two cases have been set up. One with real Lewis number and one with unity Lewis number assumption for the species. The topics that are covered in this section are as follows:

- Mixing layer development and flame structure: effects of species Lewis number
- Scalar variance budget analysis for multi-species mixture
- Study on the gradient and counter-gradient transport process for multi-species mixture
- Quantification of differential diffusion for multi-species mixture

5.1 Mixing layers development and flame structure

5.1.1 Part A: Small Geometry

Three cases with the smaller geometry are considered in this section. Two cases utilise different Lewis number for the mixture (real value of the species' Lewis number from [1] which is shown in table 5.2) and the other one comprises the species with unity Lewis number (whether as reactants or combustion products). Hereafter, these three cases are shown as cases 1 and 1-HR both with real Lewis number and the latter with a higher resolution grid system in order to check the grid independency of the simulations; case 2 with the same grid numbers as in case 1 but with unity Lewis number for species. Initial parameters and reference quantities are listed in table 5.1. Domain size is a box with the same configuration presented previously in chapter 4 with the non-dimensional size equal to 8.75∗14.58∗29.158 in x(spanwise), y(streamwise) and z(transverse) directions, respectively. The grid system comprises of ≈6.5M nodes($nx*ny*nz = 104*176*352$) for cases 1 and 2 whereas case 1-HR employs ≈26M nodes($nx*ny*nz = 208*352*352$). Simulation is started without chemical reaction and continues until time $tU_{ref}/\delta_{\omega_0}$=150 after which, combustion is started. The reactive flow simulation continues until $tU_{ref}/\delta_{\omega_0}$=160 undergoing the finite-rate chemistry mechanism presented in chapter 3. Time history of vorticity and momentum thickness which show the mixing layer growth together with vorticity extrema have been shown in figure 5.1. The trends for case 1 and case 1-HR are

Parameter	Value	Description	Unit
Pr	1.0	Prandtl number	
Re	1500	Reynolds number	
M_a	0.4	Mach number	
$Y^0_{H_2}$	0.6	H_2 mass fraction in fuel stream	
$Y^0_{O_2}$	1.0	O_2 mass fraction in oxidiser stream	
$\phi_{L_z/2}$	4.7	Equivalence ratio at the interface of both streams	
s	8	Mass stoichiometric ratio	
f_{st}	0.17	Stoichiometric mixture fraction	
T_{H_2}	300	Hydrogen initial temperature	K
T_{O_2}	2000	Oxygen initial temperature	K
U_{H_2}	+529.49	Initial velocity of Hydrogen stream	m/s
U_{O_2}	-529.49	Initial velocity of Oxygen stream	m/s
P_{ref}	101325	Reference Pressure	Pa
T_{ref}	1150	Reference temperature	K
U_{ref}	1058.9	Reference velocity	m/s
W_{ref}	17.0	Reference Molecular weight	Kg/Kmol
ρ_{ref}	0.138	Reference Density	Kg/m^3
t_{ref}	6.48	Reference Time	μs
δ_{ω_0}	6.85	Reference Length	mm

TABLE 5.1: Reference quantities and initial parameters

in good agreement which proves a similar state of development when two different mesh size have been applied. Also the approximately constant slope of momentum thickness shows that all the flows have reached to a degree of self-similarity. At $tU_{ref}/\delta_{\omega_0}$=150 when reactions are activated, both momentum thickness and vorticity thickness experience a sharp drop. This shows the inhibiting effect of the reactions on the mixing layer growth. There is no big difference in the trends due to Lewis number difference and only a small offset are observed at some location between case 2 and two other cases. Also shown in figure 5.2, contours of spanwise vorticity at $tU_{ref}/\delta_{\omega_0}$=160 in the middle plane. It is clear that the species' diffusivity do not have noticeable effects on the evolution of the mixing layer. These results are in agreement with the results presented in chapter 4. To study the flame structure, mean quantities such as species mean mass fraction has to be analysed. As this is a multicomponent medium with different diffusion coefficient, a modified mixture fraction needs to be defined[116, 117, 118, 119]. This definition is also applicable for case 2 where all species diffusivity are equal:

$$Z_L = \frac{\Phi \frac{Y_{H_2}}{Y^0_{H_2}} - \frac{Y_{O_2}}{Y^0_{O_2}} + 1}{\Phi + 1} \tag{5.1}$$

with $\phi = s\frac{m_{H_2}}{m_{O_2}}$ being equivalence ratio, $s = \frac{\nu_{O_2} W_{O_2}}{\nu_{H_2} W_{H_2}}$ being the oxygen to hydrogen stoichiometric mass ratio and $\Phi = (Le_{O_2}/Le_{H_2})\phi$.

Mean mixture fraction are shown in figure 5.3 across the mixing layer(z coordinate)

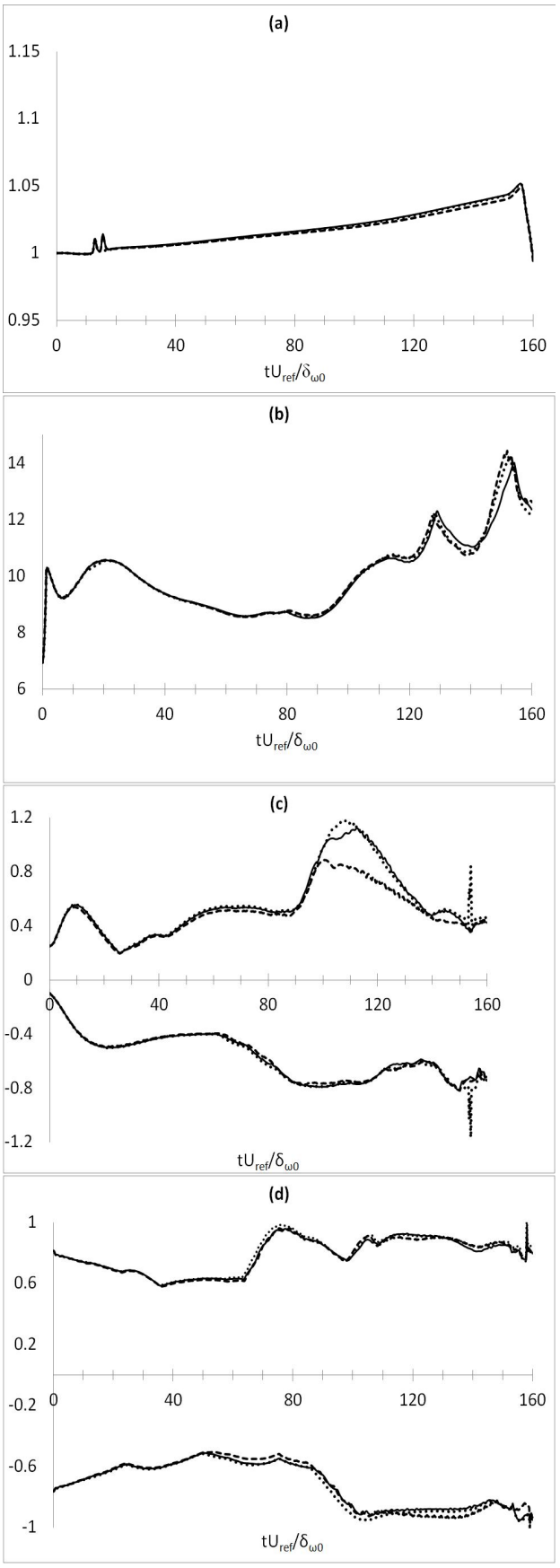

FIGURE 5.1: (a) Momentum thickness growth rate(normalised by δ_{m_0}), (b) Vorticity thickness growth rate, (c) Spanwise vorticity extrema, (d) Streamwise vorticity extrema. (———) case 1, (– – –) case 2, (· · · ·) case 1-HR.

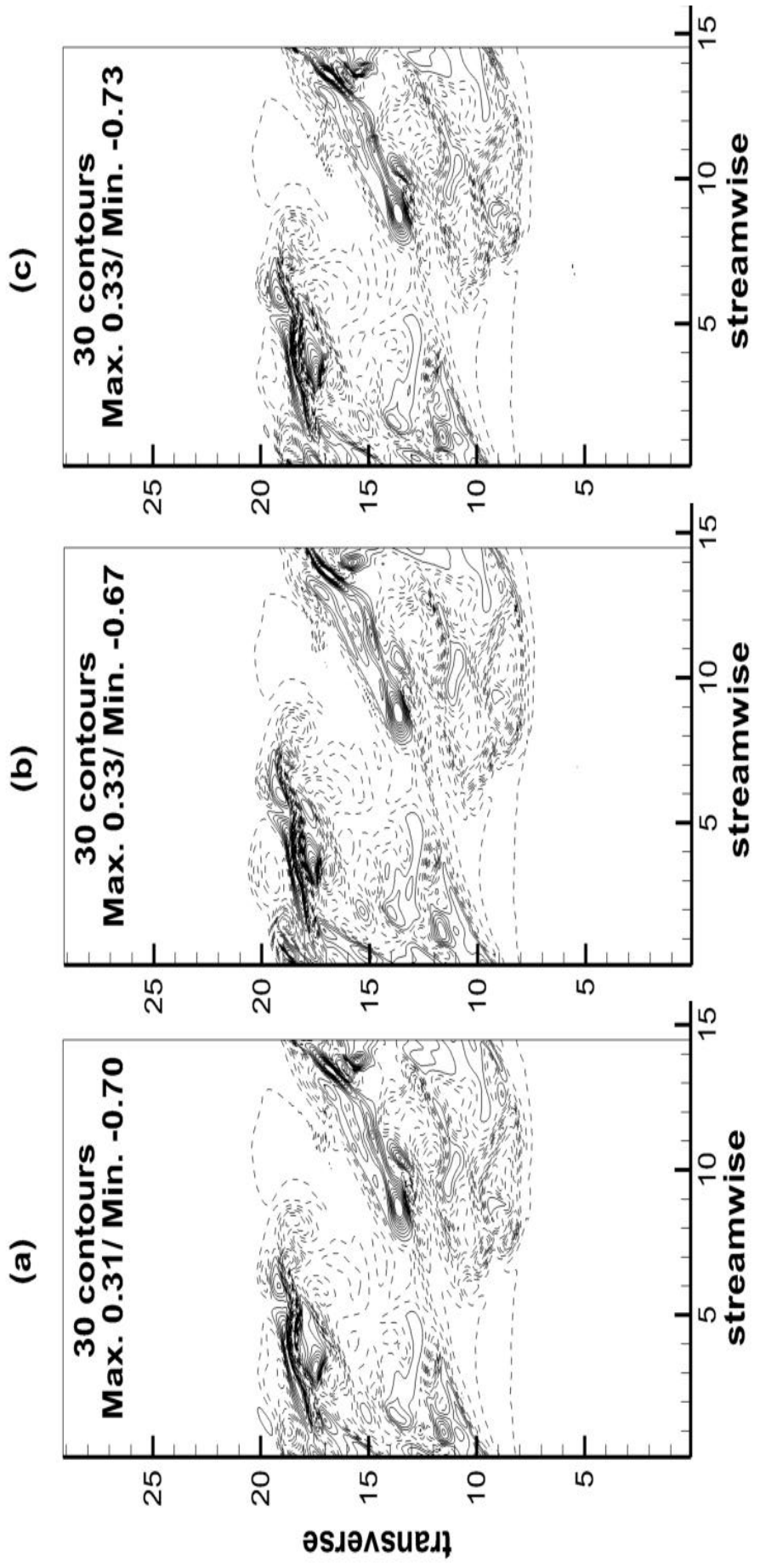

FIGURE 5.2: Spanwise vorticity contour in the middle-plane at $tU_{ref}/\delta_{\omega_0}$=160. (a) case 1, (b) case 2, (c) case 1-HR.

at three different times: Start of the simulation($tU_{ref}/\delta_{\omega_0}$=0), start of the reaction ($tU_{ref}/\delta_{\omega_0}$=150) and end of the simulation($tU_{ref}/\delta_{\omega_0}$=160) when combustion has had enough time to progress and form the products. At the beginning of the simulation,

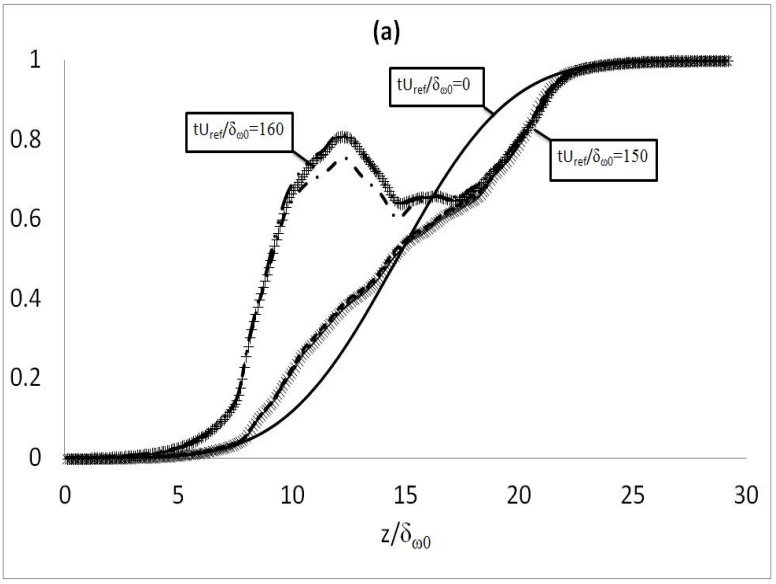

FIGURE 5.3: (a) Modified mean mixture fraction across the mixing layer in transverse direction. At $tU_{ref}/\delta_{\omega_0}$=0: (———) for all three cases(overlapping); At $tU_{ref}/\delta_{\omega_0}$=150: ($\times$) case 1, ($-\ -\ -$) case 2, ($\cdot\cdot\cdot$) case 1-HR (all trends are either overlapped or very close); At $tU_{ref}/\delta_{\omega_0}$=160: ($+$) case 1, ($-\cdot-\cdot$) case 2, ($-\cdot\cdot-$) case 1-HR (trends for case 1 and case 1-HR are either overlapped or very close).

mixture fraction for all three cases are overlapped since the domain has been initialised equally. Even during the flow entrainment without combustion, the mixing process are governed by the vorticity and turbulence field rather than species' diffusion coefficient which results in quite similar mixture fraction distribution. Also the grid independency of the current set of simulations is clear since the results of case 1 and case 1-HR are quite close or even overlapped at some location across the domain. For reactive mixing layer, however, the effects of diffusion coefficient becomes more prominent. At $tU_{ref}/\delta_{\omega_0}$=160, mixture fraction for case 2 shows a lower peak compared to that of case 1 or case 1-HR. These peaks happens at about z/δ_{ω_0}=12 for all three cases where the maximum change in the mixture composition exists(which also shows the location where the maximum mixing between upper and lower streams occurs). It is also worth noting that the location of the peak in mean mixture fraction is the same for all three cases confirming the fact that the flow structure and the mixing layer evolution are not considerably affected by changes in the species' diffusivity. What will be affected is the composition of the mixture which appears as the magnitude of the mixture fraction.

Mean mass fraction of the reactants and the combustion products are shown along the z axis. Data have been extracted for $tU_{ref}/\delta_{\omega_0}$=150 and $tU_{ref}/\delta_{\omega_0}$=160 and are plotted in figure 5.4. Before reactions are started the mass fraction distribution for all three cases

are equal because all the cases have been initialised the same(plot (a)). However when reactions start, the effects of Lewis numbers on the species' distribution will increase. In plot(b) the mass fraction of the H_2, O_2 and H_2O have been presented. For the case 2 with unity Lewis number, there is an over-prediction for the mass fraction of oxygen molecule and to a lesser extent for the hydrogen molecule which is appeared as an offset in the trends between case 1 (in which real species diffusivity has been applied) and case 2. In contrast, for H_2O as the main product, this offset shows an under-prediction for the mean mass fraction. In plot (c) mass fraction of three radicals (H, O and OH) have been chosen to be shown since their amount is an order of magnitude higher than the other radical species exist in the mixture(i.e. HO_2 and H_2O_2). Where mean mass fraction of oxygen atoms are in good agreement in all three cases, H and OH mass fraction profiles show differences between the unity Lewis number case (case 2) and the real Lewis number case (case 1). For the sake of checking the grid-independency similar to what stated in figure 5.3, it is seen that the mean mass fraction profiles in case 1-HR are in very good agreement with case 1. Another point worths noting is that the penetration of the higher stream into the lower stream is much higher. Along the vertical axis, stoichiometric modified mixture fraction lies in the oxygen side and therefore, the majority of the combustion products are formed around this stoichiometric value(f=0.17).

5.1.2 Part B: Large Geometry

So far, it is shown that the performed simulation is grid-independent. The ultimate goal sought in this chapter, is to conduct the analysis for DNS of turbulent mixing layer with a larger domain so that a larger vortex structure in the mixing layer can be captured within the domain frame. Therefore, a larger domain has been set up whose length in streamwise and spanwise is double the length of the smaller domain used earlier in this chapter. The only parameters which are different in the simulations done in this part, are the species' Lewis number that follows the routine presented in previous part(5.1.1). Two cases are considered: case 1L with real Lewis number for nine species and case 2L with unity Lewis number for all of species. Table 5.2 lists the values for Lewis numbers. Case 1L comprises 86M grid points and case 2L accommodates 24M grids. There would be a qualitative comparison between the two cases since they don't share equal number of grid points. On the other hand, this can be a further proof of being grid-independent since the method of the initialisation as well all the input data are the same for both cases. Therefore, the effect of the species' diffusivity on the flow evolution is studied and in parallel, the grid independency of the simulations are tested. As stated earlier, the initialisation(for mean and fluctuating quantities) for case 1L and 2L are the same as in

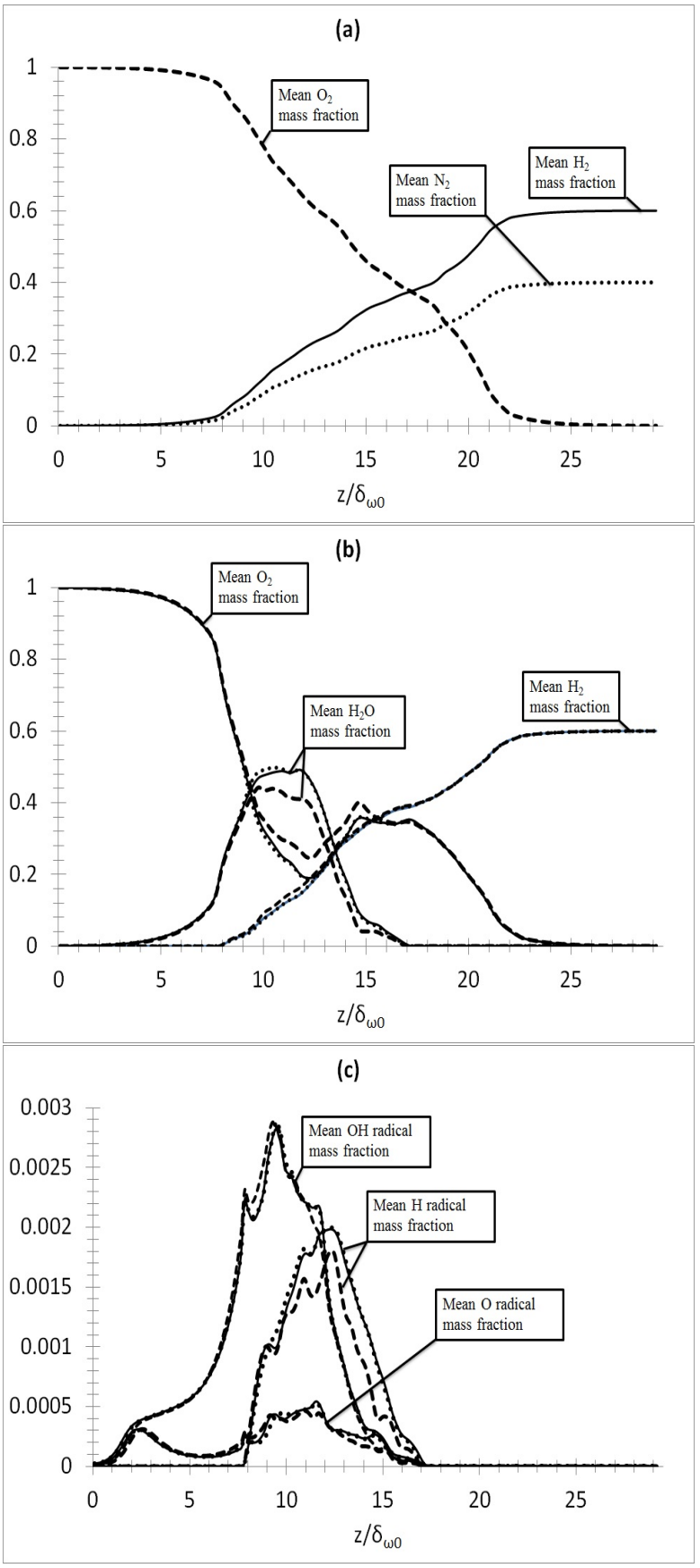

FIGURE 5.4: (a) Mean scalar mass fraction across mixing layer in transverse direction. (a) At $tU_{ref}/\delta_{\omega_0}$=150: (———) $\overline{Y_{H_2}}$, (– – –) $\overline{Y_{O_2}}$, (· · · ·) $\overline{Y_{N_2}}$ - overlapping lines. (b) At $tU_{ref}/\delta_{\omega_0}$=160 for $\overline{Y_{H_2}}$, $\overline{Y_{O_2}}$ and $\overline{Y_{H_2O}}$ and (c) At $tU_{ref}/\delta_{\omega_0}$=160 for $\overline{Y_H}$, $\overline{Y_O}$ and $\overline{Y_{OH}}$: (———) case 1, (– – –) case 2, (· · · ·) case 1-HR.

case 1L								
Le_{N_2}	Le_{O_2}	Le_{H_2}	Le_{H_2O}	Le_H	Le_{HO_2}	Le_{OH}	Le_O	$Le_{H_2O_2}$
1.00	1.11	0.30	0.83	0.18	1.10	0.73	0.70	1.12
case 2L								
Le_{N_2}	Le_{O_2}	Le_{H_2}	Le_{H_2O}	Le_H	Le_{HO_2}	Le_{OH}	Le_O	$Le_{H_2O_2}$
1.0	1.0	1.0	1.0	1.0	1.0	1.0	1.0	1.0

TABLE 5.2: Species Lewis number from reference [1]

cases 1,2 and 1-HR with smaller domain and therefore, there is no need to be repeated in here(table 5.1 shows input parameters). The size of the domain and the number of grid points at each direction are as follows: Case 1L with $nx * ny * nz = 312 * 528 * 528$ and case 2L with $nx * ny * nz = 208 * 352 * 352$ grid points, both of which share the same geometry with the size of $21.82 * 36.36 * 36.36$ [1] in x,y and z directions, respectively. Hereafter, only the DNS results of cases 1L and 2L are discussed.
In this section, the following topics are presented and analysed:

- Mixing layer growth
- Scalar distribution and flame structure

Simulation started without reaction and proceed until $tU_{ref}/\delta_{\omega_0}$=150 until the initial vortices have had roll-up and pairing which results in the development of the mixing layer as well as showing self-similarity with a coherent structure of the components of interest in the flow field. Explanations about these, appear next.

5.1.2.1 Mixing layer growth

Mixing layer growth is understood by examining at the vorticity field and time rate of change of momentum thickness. These has been shown in figure 5.5 for momentum and vorticity thickness growth rate as well as spanwise and streamwise vorticity extrema for both cases. In addition, the overall structure of the flow can be known through vorticity contours. Spanwise and streamwise vorticity contours are shown in figures 5.1.2.1 and 5.7. The initial spanwise vorticity is positive everywhere in the flow and generation of negative values shows the development of different length scales and smaller structures within the flow field. The vorticity field, as seen in these figures, are not considerably affected by the scalar diffusivity and also, both cases show a similar trend in the momentum and vorticity thickness growth rate and a very similar pattern in the vorticity contours. The main differences are only in the maximum and minimum values as shown in figure 5.5 (c) and (d). Since the contours are for the time when the reactions were

[1] Numbers are in non-dimensional form.

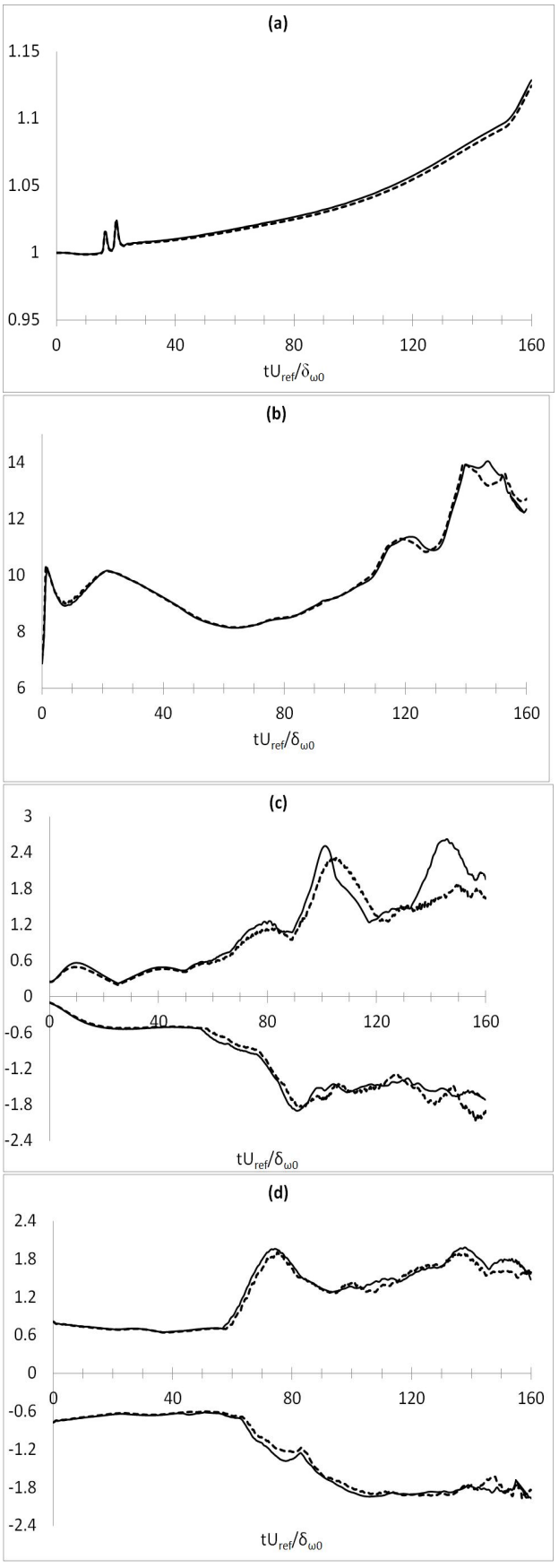

FIGURE 5.5: (a) Momentum thickness growth rate(normalised by δ_{m_0}), (b) Vorticity thickness growth rate, (c) Spanwise vorticity extrema, (d) Streamwise vorticity extrema. (———) case 1L with real Lewis number, (– – –) case 2L with unity Lewis number.

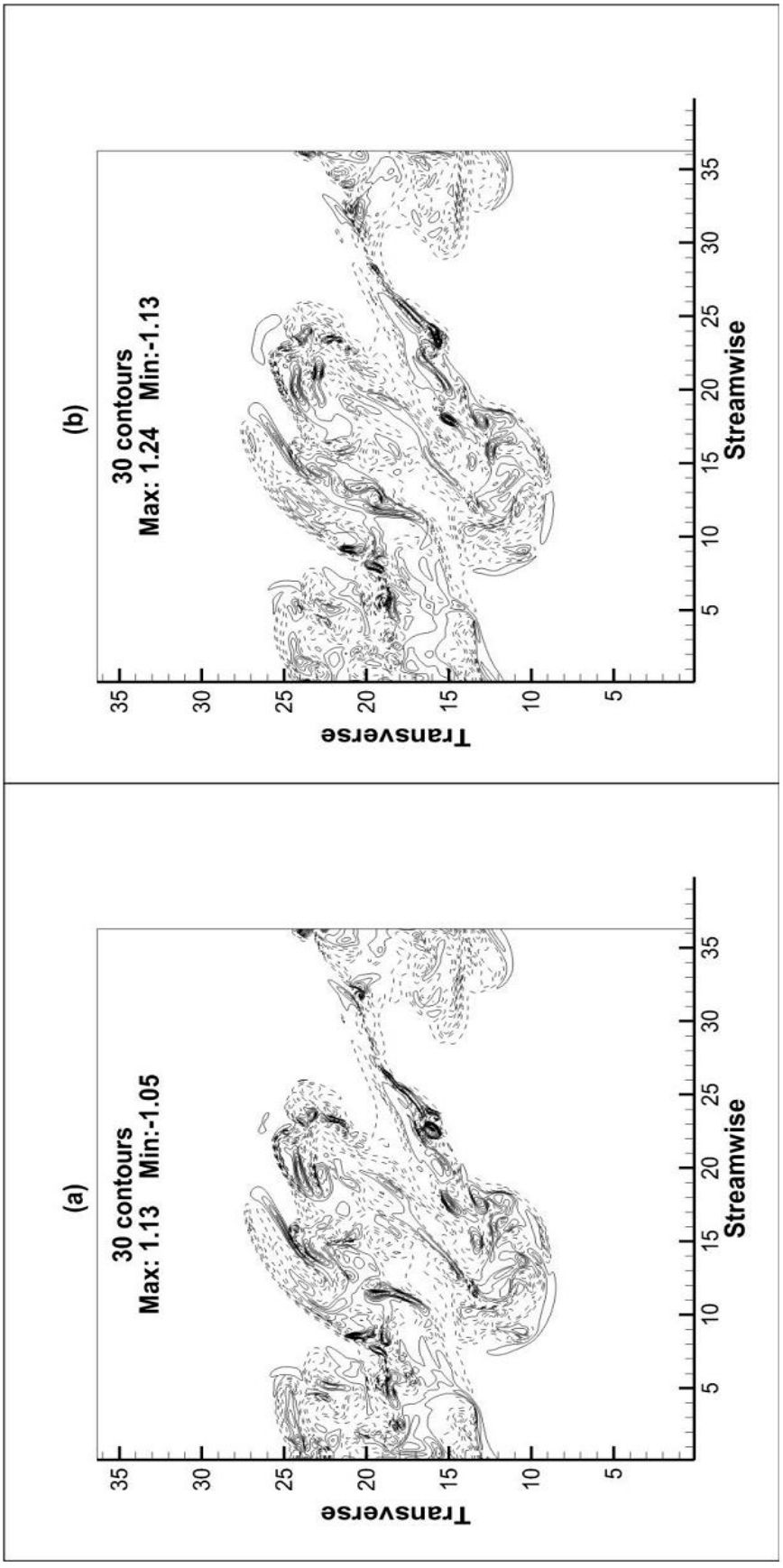

FIGURE 5.6: Spanwise vorticity contours in the middle-plane at $tU_{ref}/\delta_{\omega_0}$=160. (a) ω_x for case 1L, (b) ω_x for case 2L. Dashed lines show negative values.

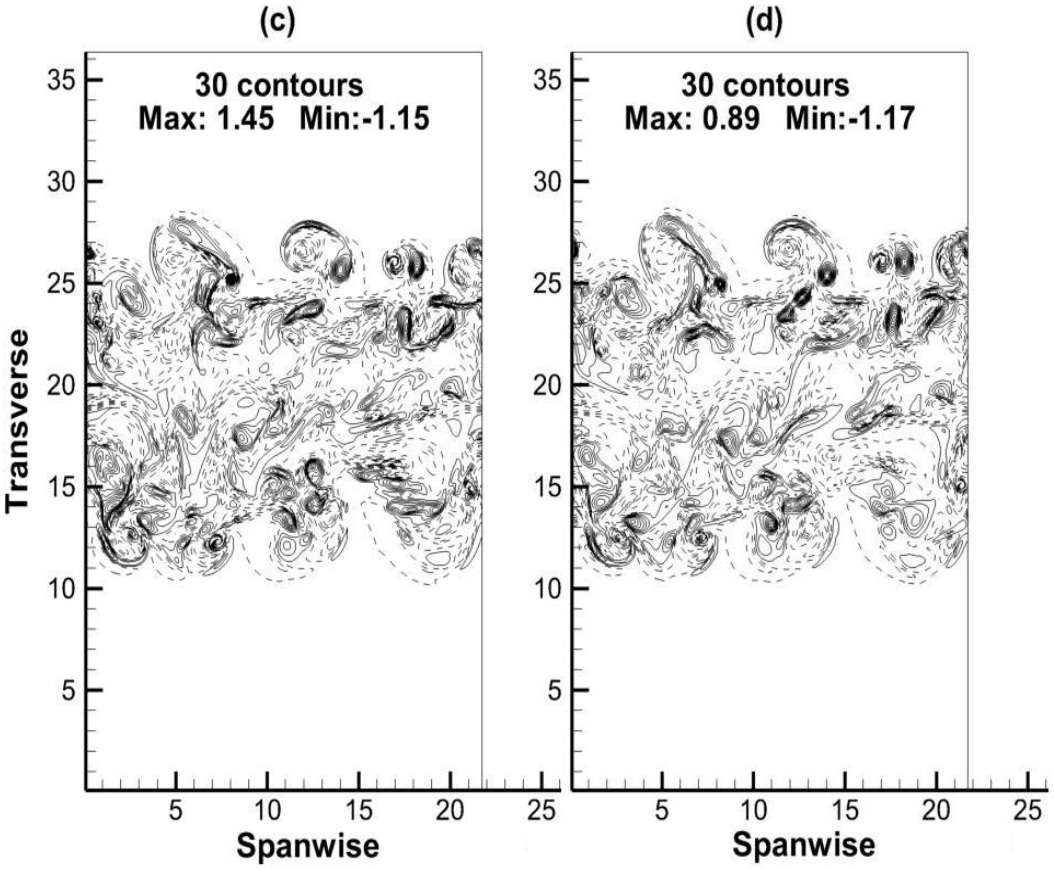

FIGURE 5.7: Streamwise vorticity contours in the middle-plane at $tU_{ref}/\delta_{\omega_0}$=160. (c) ω_y for case 1L, (d) ω_y for case 2L. Dashed lines show negative values.

active, obtaining such results highlights the negligible effects of species diffusivity on the velocity field as well as the vorticity structure. Meanwhile, grid independency of the simulations are proved since the number of grid points for both cases differs by almost three times. Moreover, the spanwise vorticity extrema in figure 5.5 and spanwise vorticity contours in figure 5.6 shows that the flow has completed roll-up and two pairings(two peaks for the spanwise vorticity extrema) which shows a high level of entrainment and also coherency in the structure. To control that the domain has suitable size and do not suppress the turbulent field as well as the vorticity structure, it is useful to calculate two-point correlation function.

Figure 5.8 shows the two-point correlation function for case 1L. Similar to chapter 4, the correlation function are calculated in three different planes across the domain. The planes were chosen from locations close to the centre of the domain where both streams are supposed to have the maximum interaction so that the flow variables show maximum fluctuations. As shown in these figures, all the quantities are decorrelated along the

desired distance. For streamwise direction, the results are better compared to those obtained in spanwise direction. However, spanwise direction is also proved to have suitable dimension as the quantities have been decorrelated and the final values converge to zero. Dilatation of flow is a quantity which is a measure of expansion or contraction of fluid.

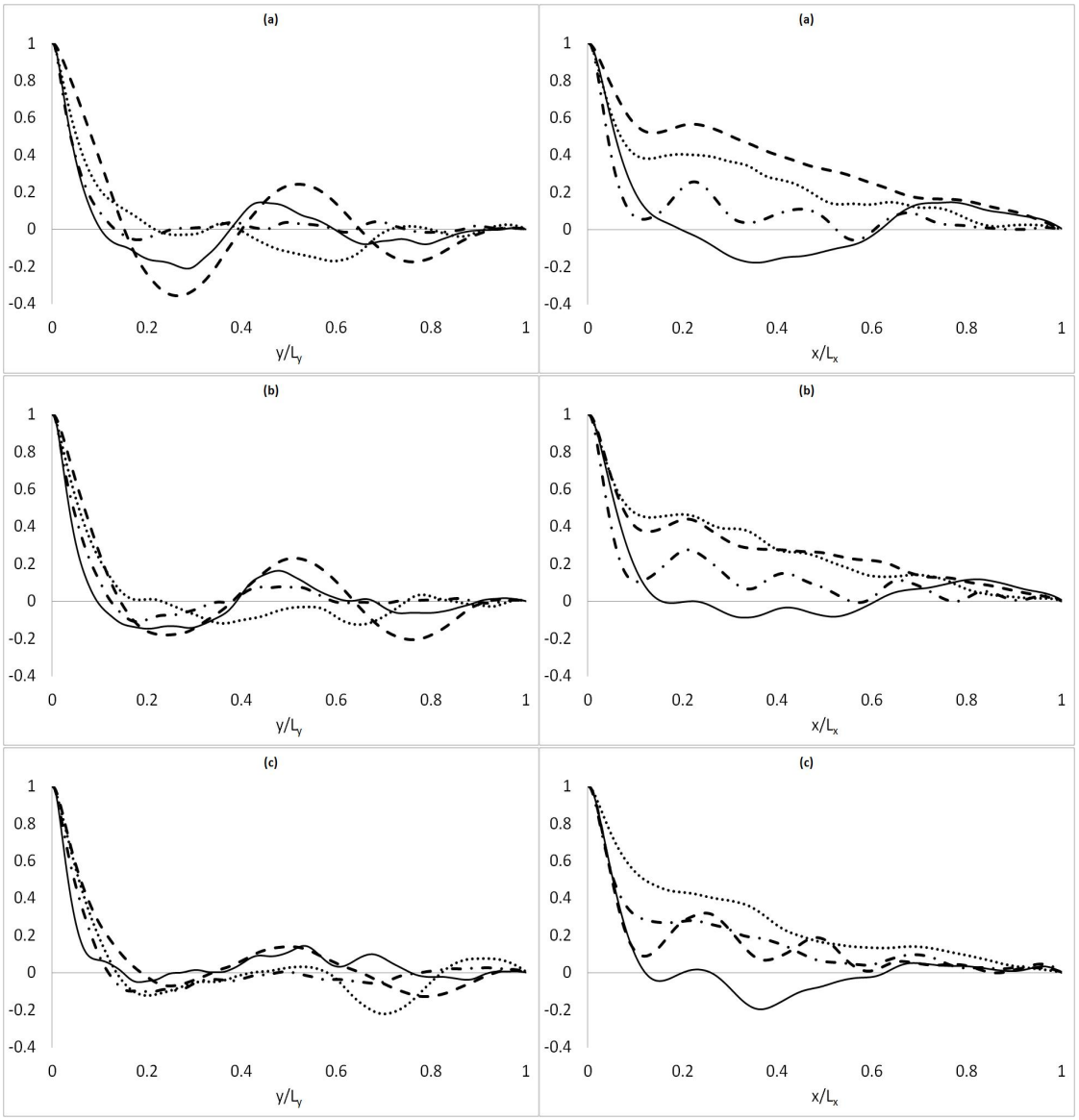

FIGURE 5.8: Two-point correlation function normalised by $R_{\varphi\varphi}(0)$ in streamwise(left) and spanwise(right) directions for case 1L at t_{ND}=80 and three different transverse locations: (a) N_z=264 where $z = 0.5 * L_z$; (b) N_z=283 where $z = 0.55 * L_z$; and (c) N_z=302 where $z = 0.6 * L_z$. (———)$R_{u'u'}(r)/R_{u'u'}(0)$, (– – –)$R_{v'v'}(r)/R_{v'v'}(0)$, (– · – ·)$R_{w'w'}(r)/R_{w'w'}(0)$, and (· · · ·)$R_{p'p'}(r)/R_{p'p'}(0)$.

For a compressible flow, positive values show expansion whereas negative ones indicate contraction. Dilatation is defined as divergence of velocity ($\nabla.V$). This quantity have been shown in figure 5.9 for both cases at three different times: $tU_{ref}/\delta_{\omega_0}$=150 before reactions are started, $tU_{ref}/\delta_{\omega_0}$=150.5 when species reaction rates reach to maximum or minimum values (this is shown in section 5.1.2.2) and $tU_{ref}/\delta_{\omega_0}$=160 which is the end of

the simulation. As shown in this figure, both cases have an increase in the range of the maximum and minimum values for dilation as time proceeds. This is a sign of increase in the degree to which the fluid is compressed or expanded. In addition, as time proceeds, the extent of the changes is spread across the domain. Comparing the contour plots (a) and (b) which are flow dilatation at $tU_{ref}/\delta_{\omega_0}$=150 with the contour plots (e) and (f) which represent the same quantity at $tU_{ref}/\delta_{\omega_0}$=160, shows that a wider region along the z direction is affected by the divergence of the velocity, $\nabla.V$. This is mostly toward the lower stream which shows that the hydrogen stream has penetrated more into the oxygen stream. Initially, the dilatation covers the area from z/δ_{ω_0}=10 to z/δ_{ω_0}=25 as shown in plots (a) and (b); when reactions start, the values begin to change as a sign of changes in the velocity and pressure in the flow and at the end of simulation these changes reach close to the lower boundary whereas the extension of these changes into the hydrogen side is to $z/\delta_{\omega_0} \approx 30$ for case 1L (plot(e)) and slightly more for case 2L.

5.1.2.2 Scalar distribution and flame structure

Scalar mass fraction together with species reaction rates give an understanding from the flame structure and kinetic of the reactive system. Figures 5.10 and 5.11 show the integrated mean reaction rate for each species across the mixing layer. Figure 5.10 shows the $\dot{\omega}_n$ for molecules of O_2, H_2, and H_2O and figure 5.11 shows the reaction rate of the radicals H, HO_2, OH, O and H_2O_2. The integration time is from $tU_{ref}/\delta_{\omega_0}$=150, just before reaction, to $tU_{ref}/\delta_{\omega_0}$=160, when simulation finishes. The figures actually shows the net rate of consumption or production for each individual species. Molecule of N_2 acts as inert so the net rate of production and consumption of this species is zero. Positive values mean species production and negative values means species consumption. Hydrogen and oxygen molecules as the main reactant are continuously consumed and convert to H_2O as the main product plus five other radicals. As seen in figure 5.10, oxygen is consumed at a much higher rate than hydrogen as a result of the chemistry mechanism used. In addition, case 2L in which unity Lewis number has been applied, shows a delay of around half a non-dimensional time unit to start the reactions so that the $\dot{\omega}_n$ begins to change. Mean mass fraction of the scalars are plotted along the transverse direction. Data are chosen at two different times: when reaction rate is maximum i.e. $tU_{ref}/\delta_{\omega_0}$=150.5, and at the end of the simulation that is $tU_{ref}/\delta_{\omega_0}$=160. Figure 5.12 shows the mean mass fraction values for all reactive species (H_2, O_2, H_2O, H, HO_2, OH, O and H_2O_2) at $tU_{ref}/\delta_{\omega_0}$=150.5 for case 1L. Values for case 2L at this time that is early stage after reaction starts, are very close to that of case 1L and therefore, are not shown. Figure 5.13 shows the mean mass fraction for the reactants and the products at $tU_{ref}/\delta_{\omega_0}$=160 for both cases. As seen in these pictures, when the

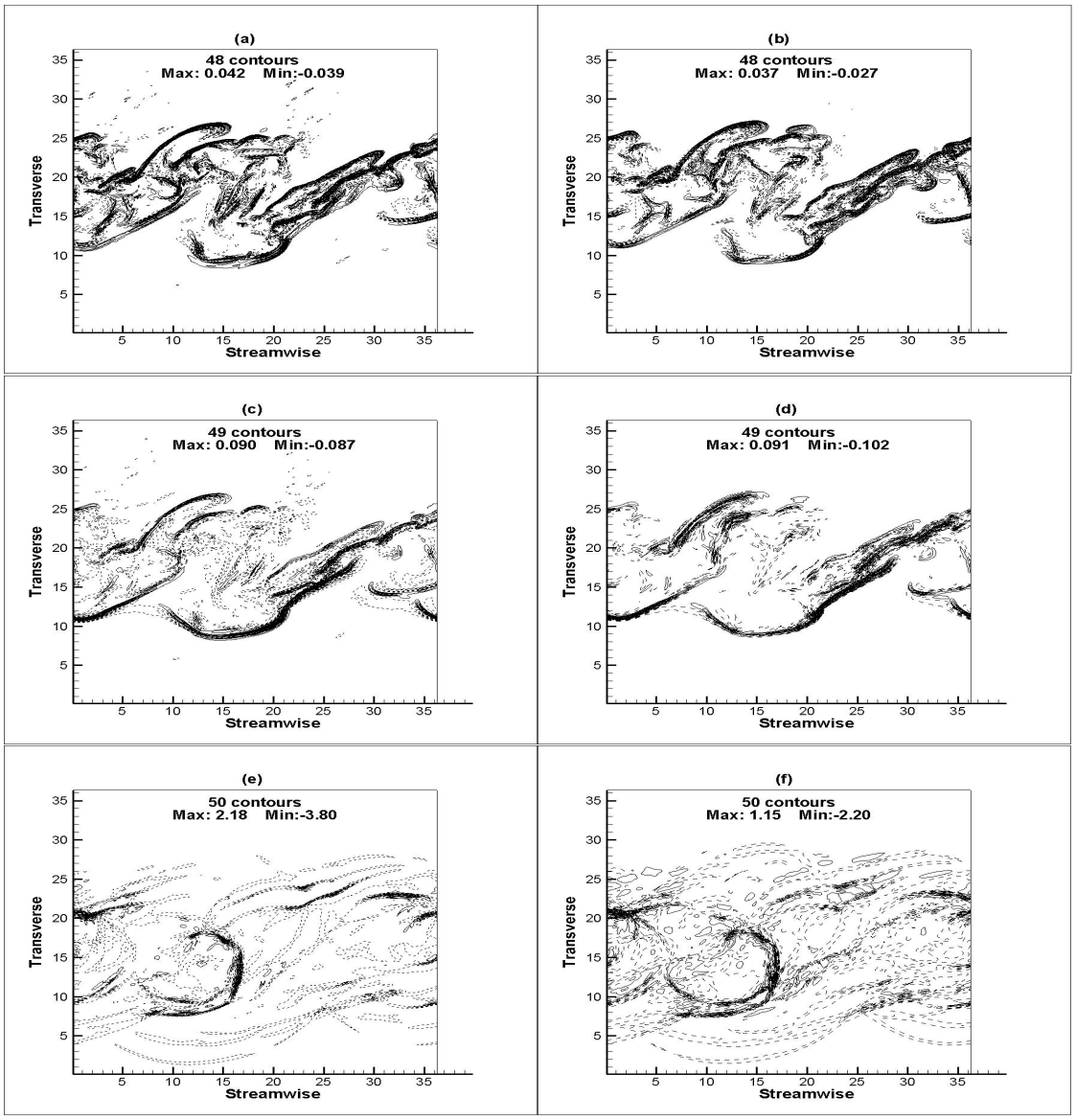

FIGURE 5.9: Dilatation contours in the middle plane. Left plots are for case 1L and right plots are for case 2L. (a,b) $tU_{ref}/\delta_{\omega_0}$=150, (c,d) $tU_{ref}/\delta_{\omega_0}$=150.5, (e,f) $tU_{ref}/\delta_{\omega_0}$=160. Dashed lines show negative values and solid lines show positive contours.

reaction rates are high, mass fraction of the radicals are maximum and at later stages, radical pool decreases but mass fraction of the molecular products which is H_2O in the current chemical mechanism, increases.

Snapshots of species mass fraction contours for both cases at $tU_{ref}/\delta_{\omega_0}$=160 which is the final stage in the current simulation also gives us an overall picture of distribution of the scalars as well as the extent of the reaction zone. The contours represent the values in the mixing layer's middle plane and are shown in figures 5.14 to 5.21. N_2 mass fraction contours are not shown as it is inert and its changes are similar to H_2 mass fraction contours in terms of the pattern but its magnitude varies from 0 to 0.4.

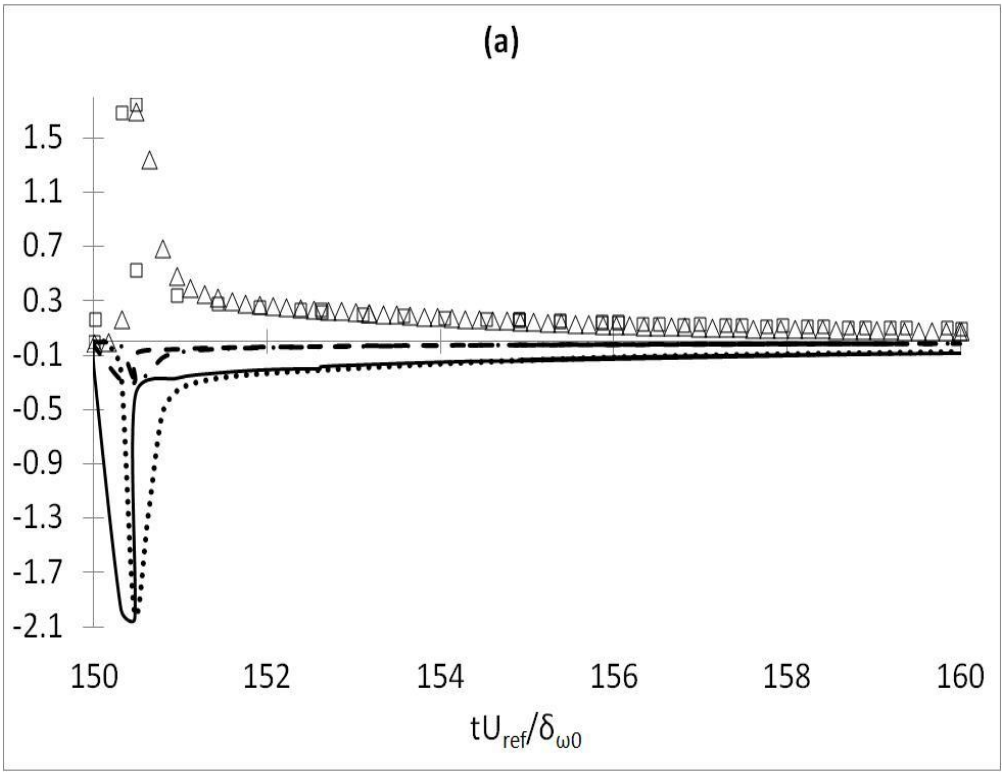

FIGURE 5.10: Integrated mean reaction rate for molecules: (———) $\dot{\omega}_{O_2}$ case 1L, $(\cdots)$ $\dot{\omega}_{O_2}$ case 2L, $(- - -)$ $\dot{\omega}_{H_2}$ case 1L, $(- \cdot - \cdot)$ $\dot{\omega}_{H_2}$ case 2L, (□) $\dot{\omega}_{H_2O}$ case 1L, (△) $\dot{\omega}_{H_2O}$ case 2L. Quantities are in non-dimensional form and all are multiplied by $W_n * t_{ref}/\rho_{ref}$ in which W_n is the molecular weight of the species.

To have a better comparison between the two cases and to understand how Lewis number affects the mass fraction transport, there are 30 contours shown in each plot. Therefore, apart from potential difference in the pattern of the contours, the maximum and minimum values also reveal the differences originated from the Lewis number effect. The main reactants, i.e. H_2 and O_2, show small differences in the contours as seen in figures 5.14 and 5.15 between case 1L and 2L. Also both cases have equal maximum and minimum values. The mass fraction of the products, however, show differences among the two cases. H_2O mass fraction contour in figure 5.16 shows the difference mainly in the minimum value. Although the maximum mass fractions are very close between case 1L and case 2L, this difference in the minimum value shows that the overall production of H_2O is more in case 1L where real Lewis numbers have been applied. This also proves the fact that differential diffusion increases the molecular mixing which is appeared as species mass fraction. This is common in all figures from 5.16 to 5.21. All the contours for species mass fraction in case 1L show larger values for the peak mass fraction. The minimum values for some species such as H_2O(as stated above), H, OH and O in case 1L also are larger that those in case 2L.

Contours of the reaction rate of the species in the middle plane have been shown for case 1L in figures 5.22 to 5.25. Each figure is split into a lower plot and an upper

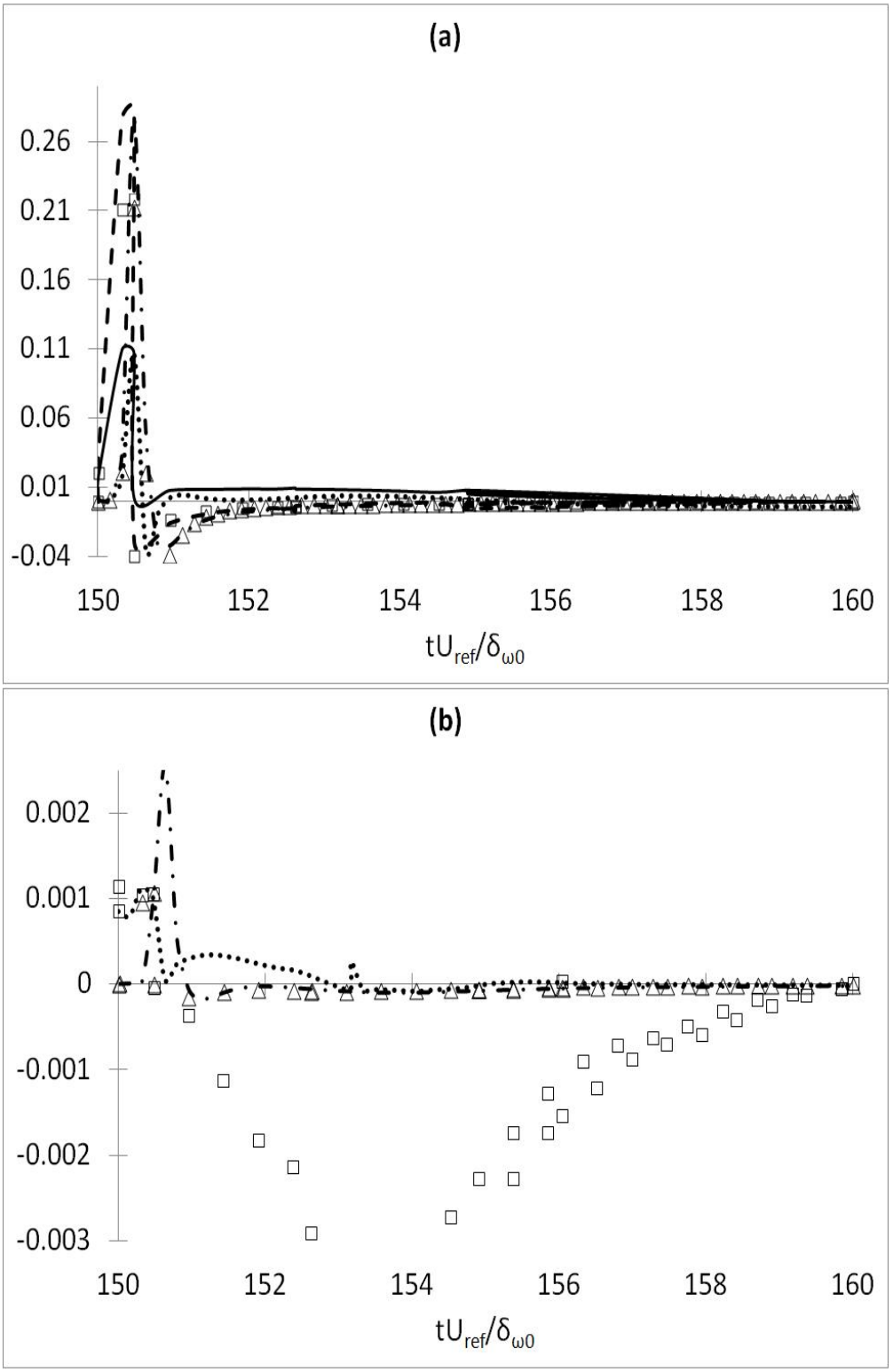

FIGURE 5.11: Integrated mean reaction rate for radicals: (a): (———) $\dot{\omega}_H$*10 case 1L, $(\cdots)$ $\dot{\omega}_H$*10 case 2L, $(--)$ $\dot{\omega}_{OH}$ case 1L, $(-\cdot-\cdot)$ $\dot{\omega}_{OH}$ case 2L, (□) $\dot{\omega}_O$ case 1L, (△) $\dot{\omega}_O$ case 2L. (b): (□) $\dot{\omega}_{HO_2}$ case 1L, $(\cdots)$ $\dot{\omega}_{HO_2}$ case 2L, (△) $\dot{\omega}_{H_2O_2}$ case 1L, $(-\cdot-\cdot)$ $\dot{\omega}_{H_2O_2}$ case 2L. Quantities are in non-dimensional form and all are multiplied by $W_n * t_{ref}/\rho_{ref}$ in which W_n is the molecular weight of the species.

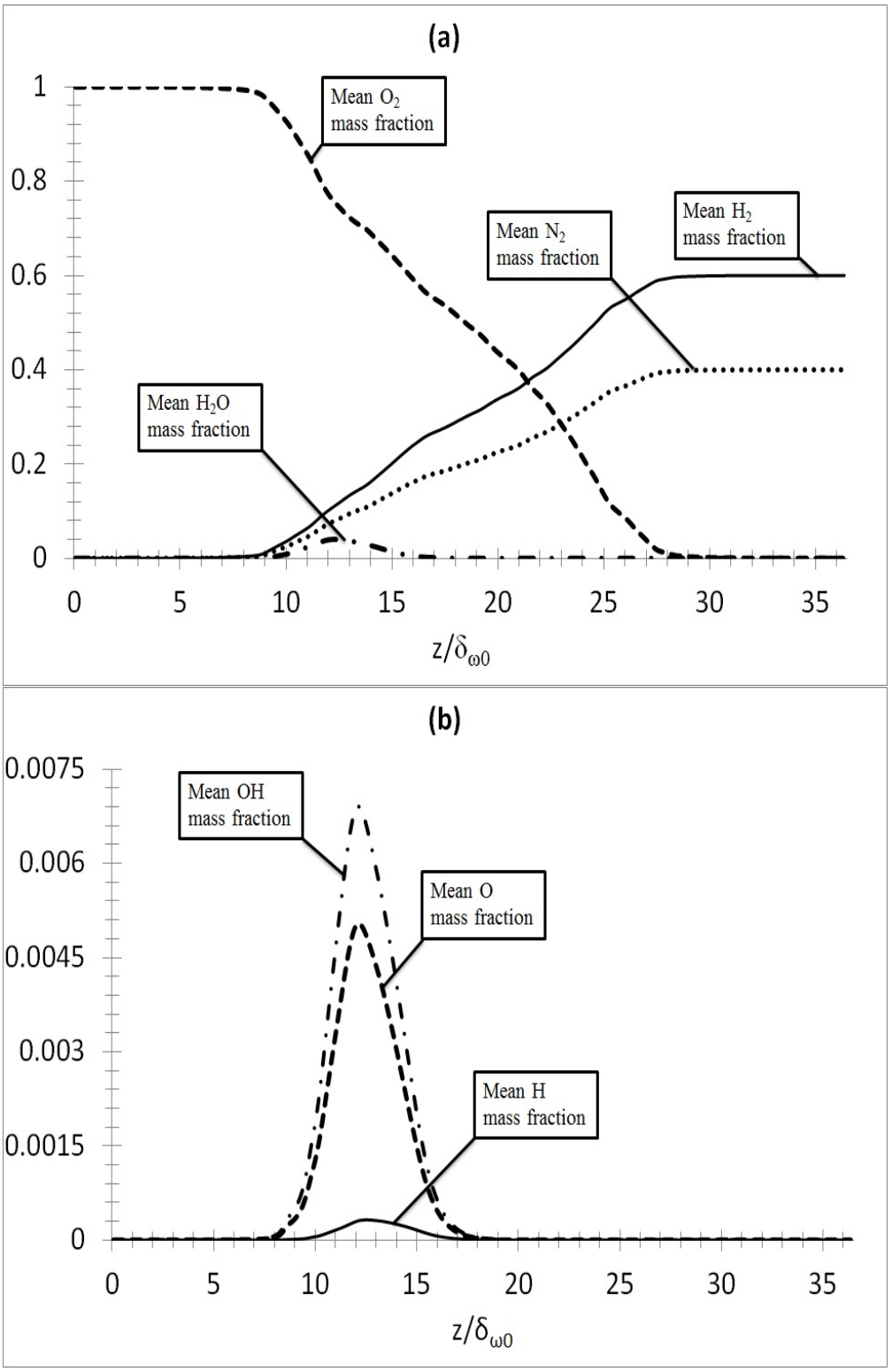

FIGURE 5.12: Mean scalar mass fraction across the mixing layer for case 1L at $tU_{ref}/\delta_{\omega_0}$=150.5. (a) $\overline{Y_n}$ for molecules H_2, O_2 and H_2O; (b) $\overline{Y_n}$ for radicals H, O and OH. n represents different species.

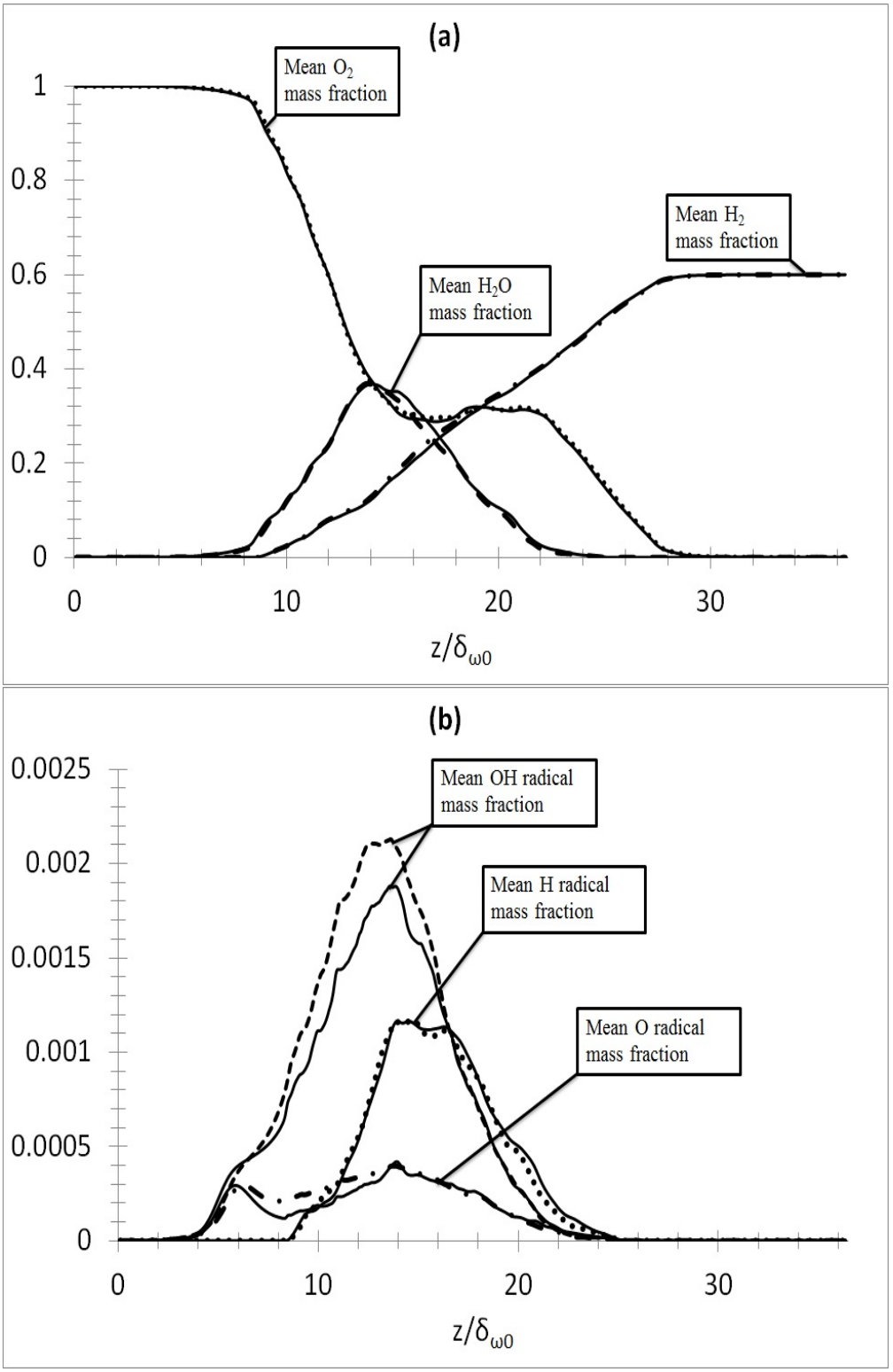

FIGURE 5.13: Mean scalar mass fraction across the mixing layer for both cases at $tU_{ref}/\delta_{\omega_0}$=160. (a) (———) for $\overline{Y_{H_2}}$, $\overline{Y_{O_2}}$ and $\overline{Y_{H_2O}}$ in case 1L, (– · – ·) for $\overline{Y_{H_2}}$, (· · · ·) for $\overline{Y_{O_2}}$ and (– – –) for $\overline{Y_{H_2O}}$ in case 2L; (b) (———) for $\overline{Y_O}$, $\overline{Y_H}$ and $\overline{Y_{OH}}$ in case 1L, (– · – ·) for $\overline{Y_O}$, (· · · ·) for $\overline{Y_H}$ and (– – –) for $\overline{Y_{OH}}$ in case 2L.

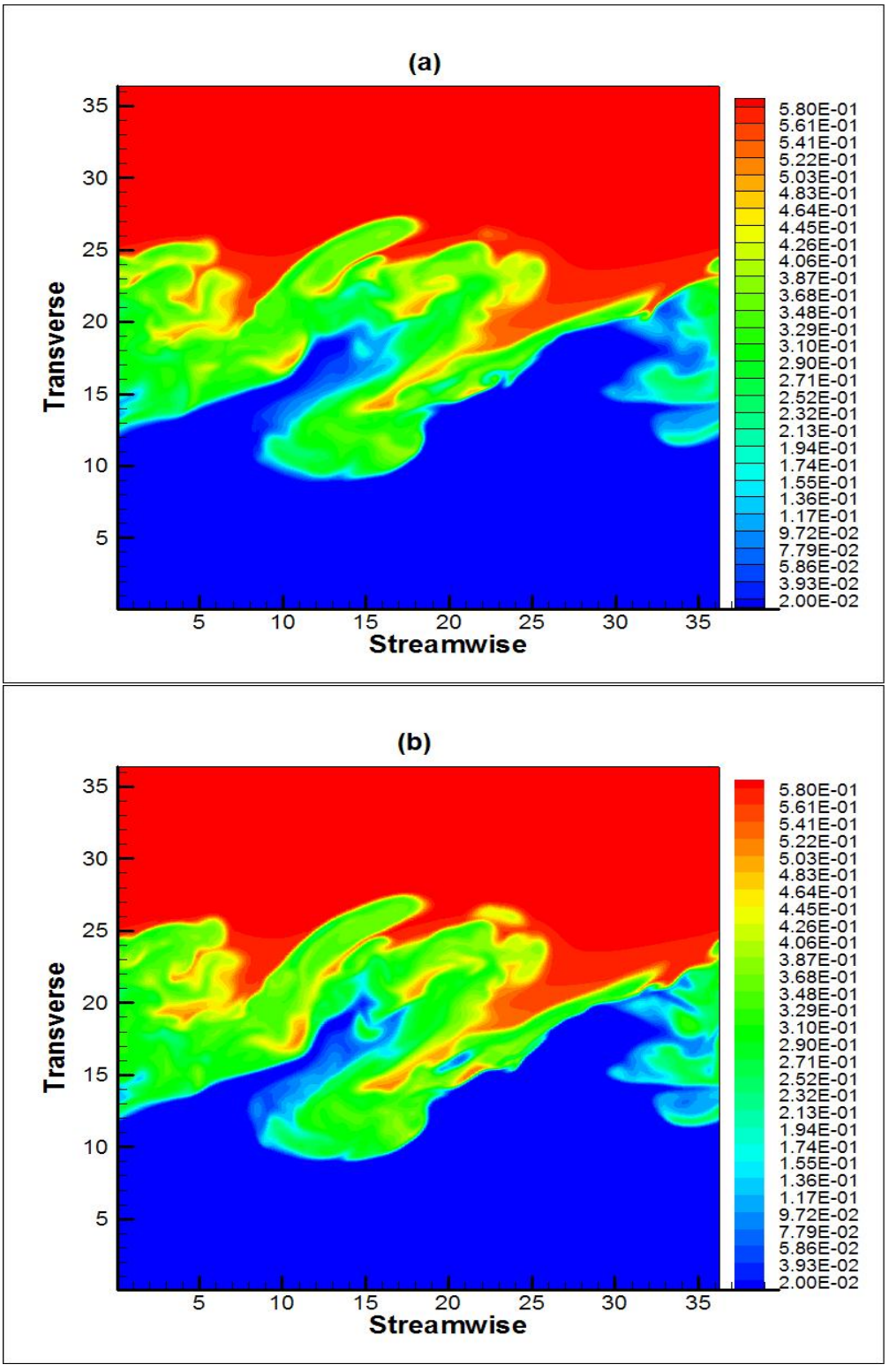

FIGURE 5.14: Snapshots of H_2 mass fraction in the middle plane. (a) case 1L, (b) case 2L.

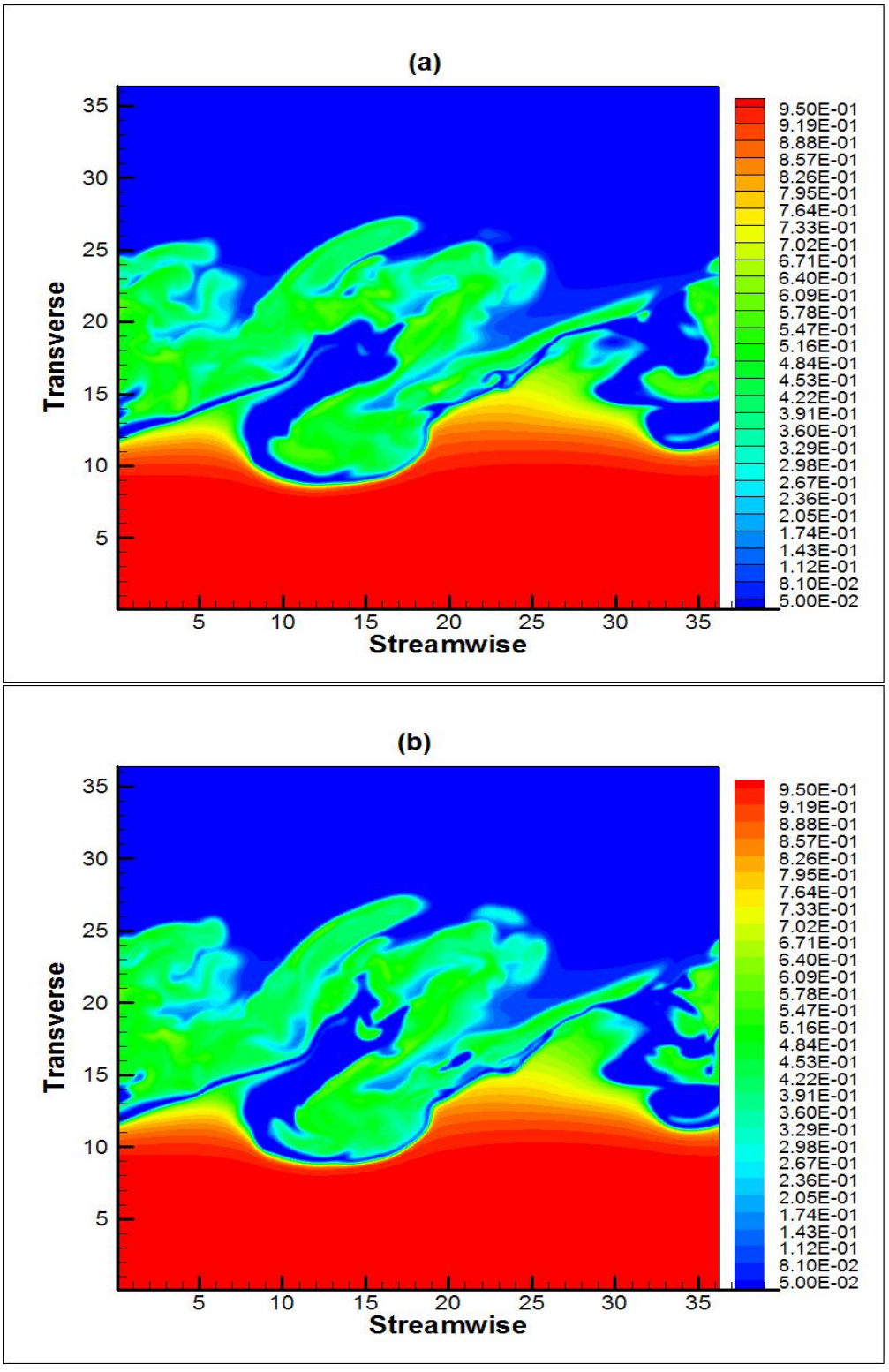

FIGURE 5.15: Snapshots of O_2 mass fraction in the middle plane. (a) case 1L, (b) case 2L.

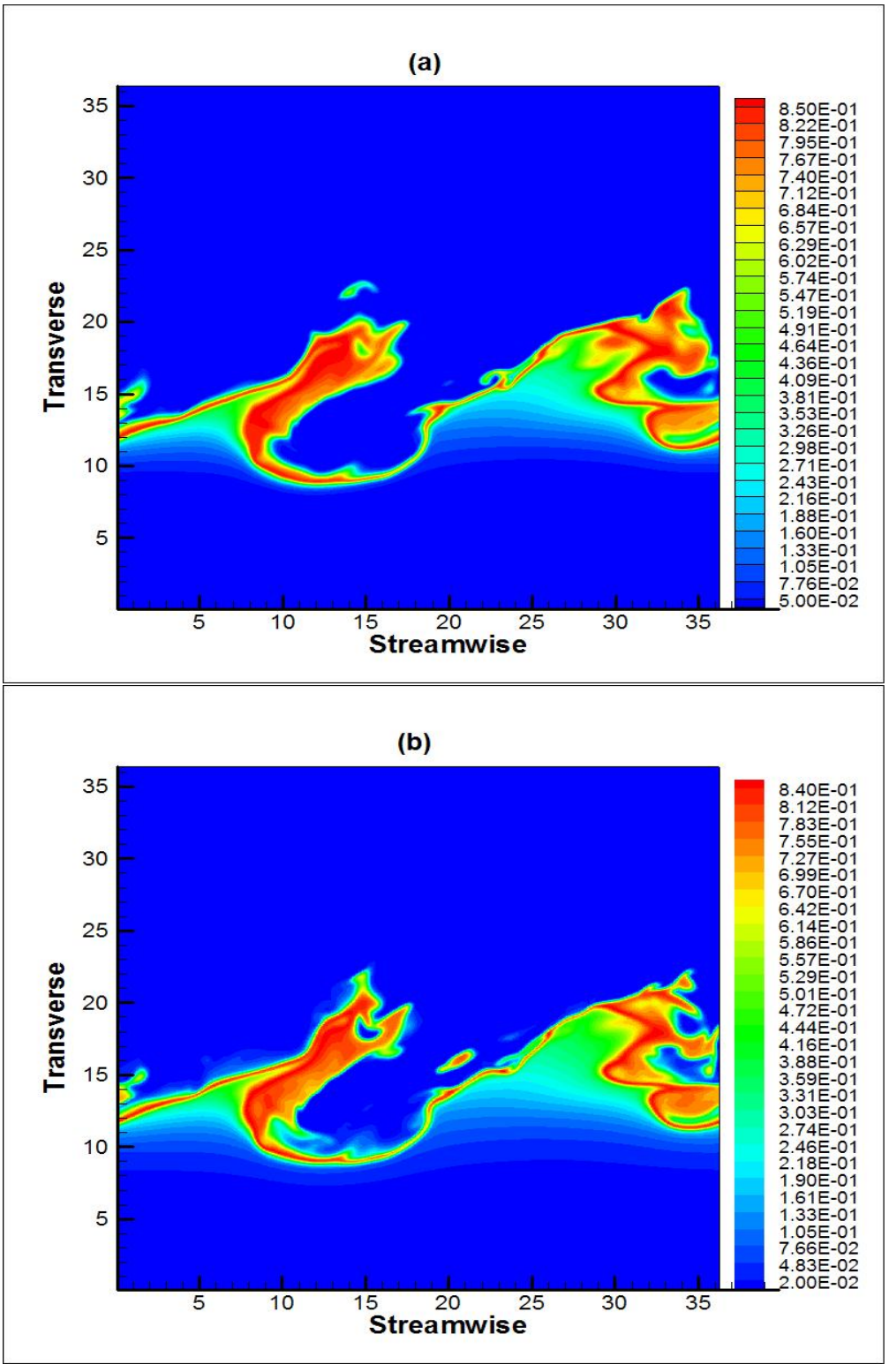

FIGURE 5.16: Snapshots of H_2O mass fraction in the middle plane. (a) case 1L, (b) case 2L.

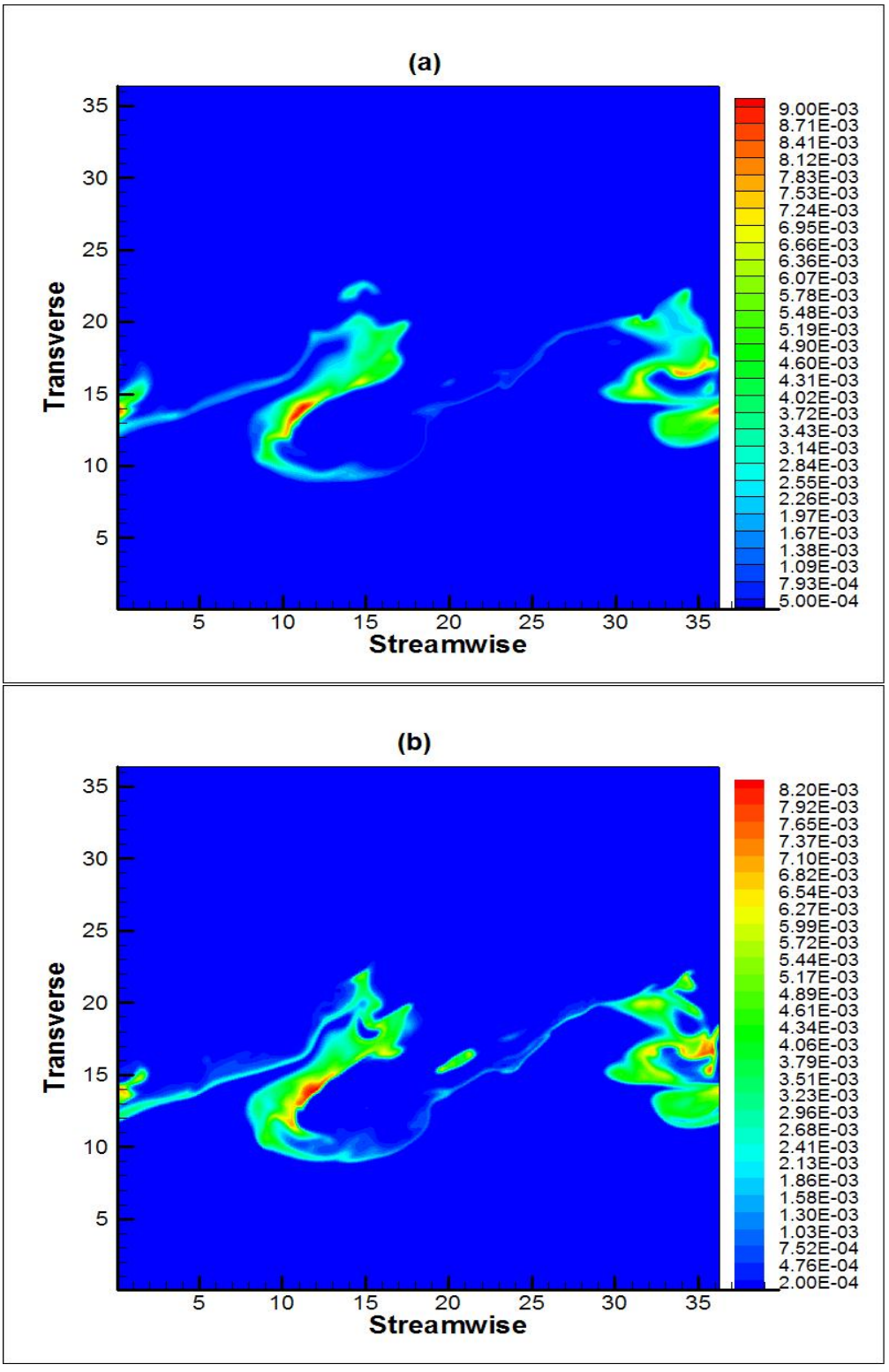

FIGURE 5.17: Snapshots of H mass fraction in the middle plane. (a) case 1L, (b) case 2L.

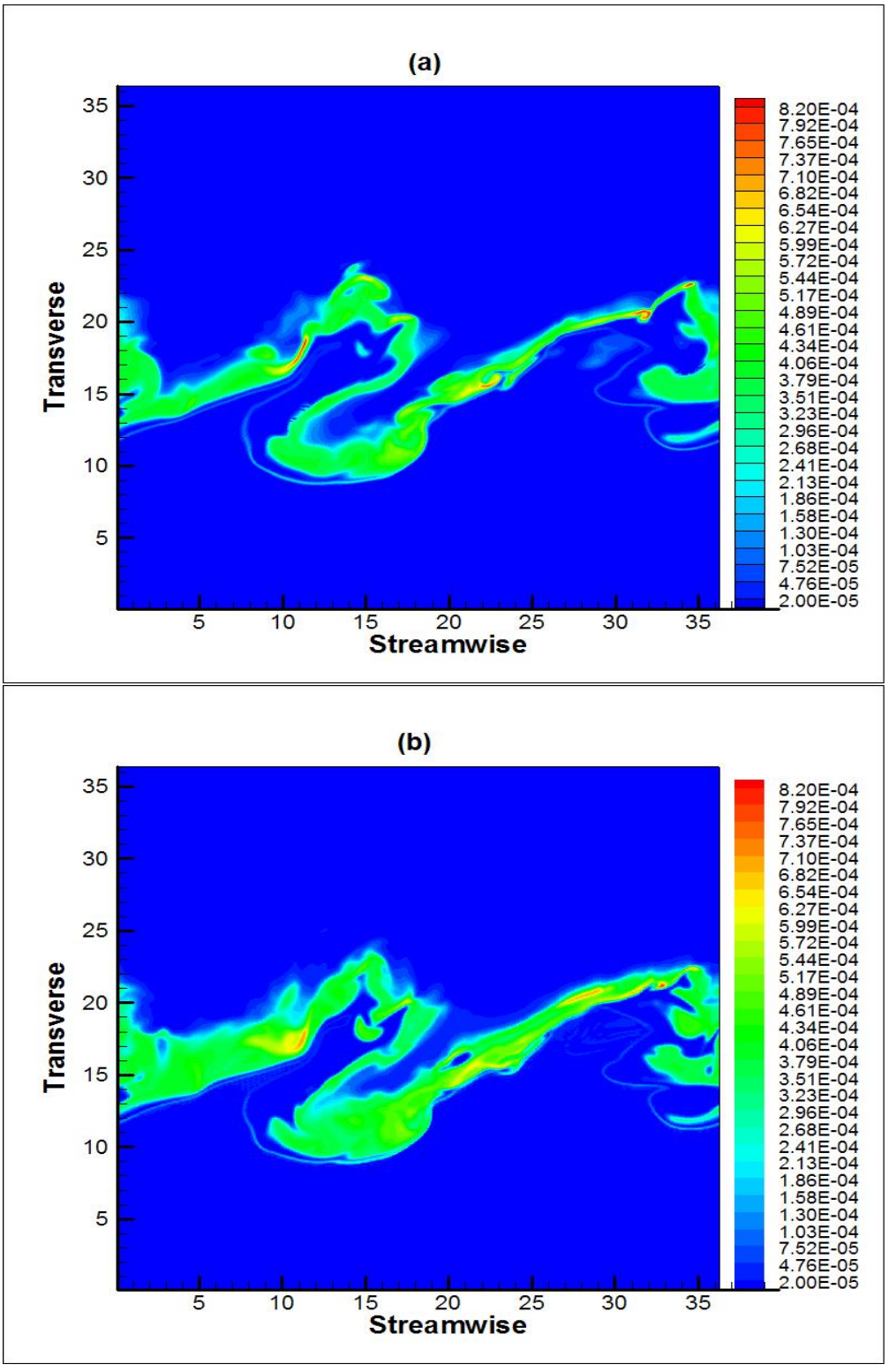

FIGURE 5.18: Snapshots of HO_2 mass fraction in the middle plane. (a) case 1L, (b) case 2L.

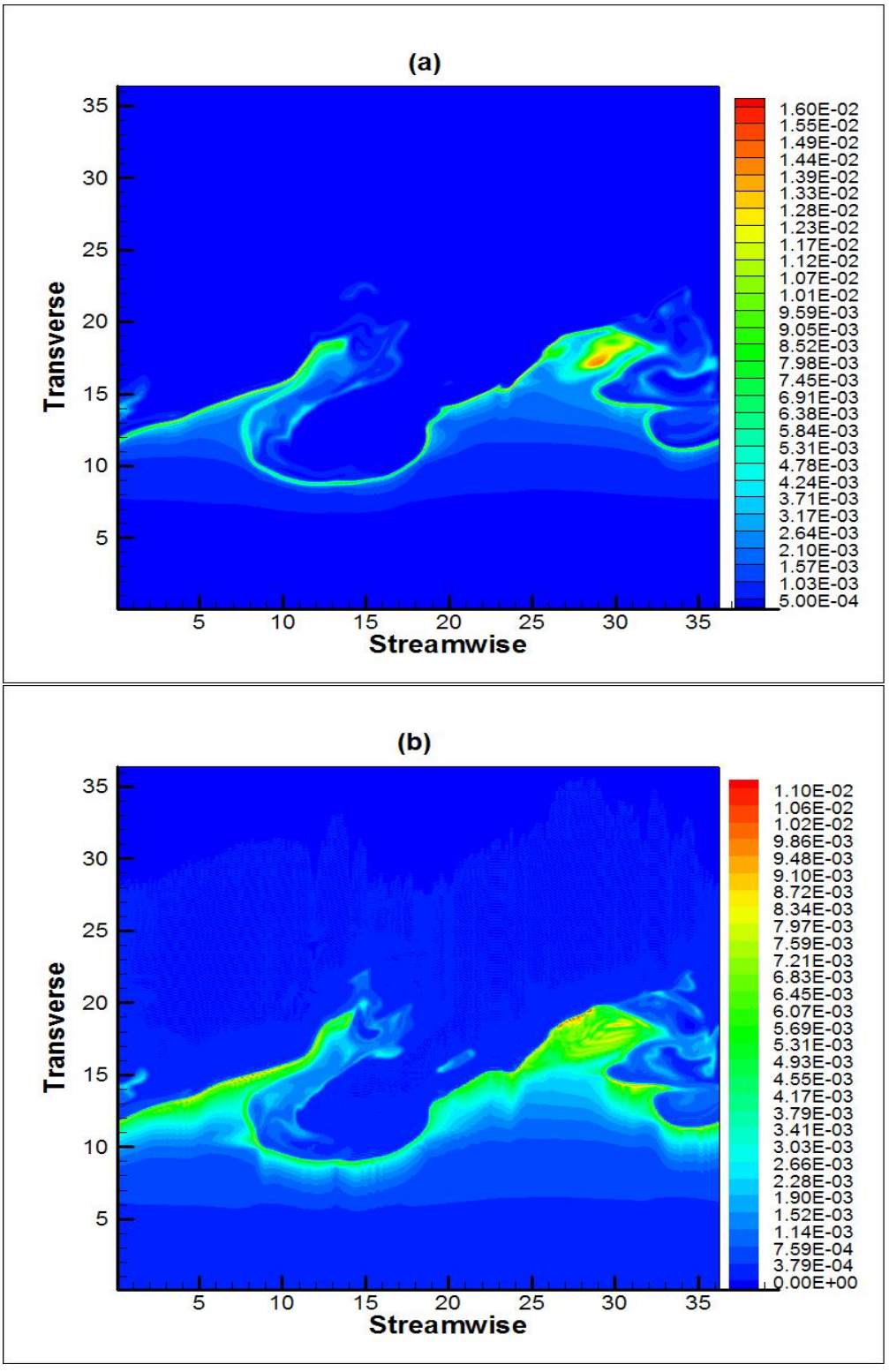

FIGURE 5.19: Snapshots of OH mass fraction in the middle plane. (a) case 1L, (b) case 2L.

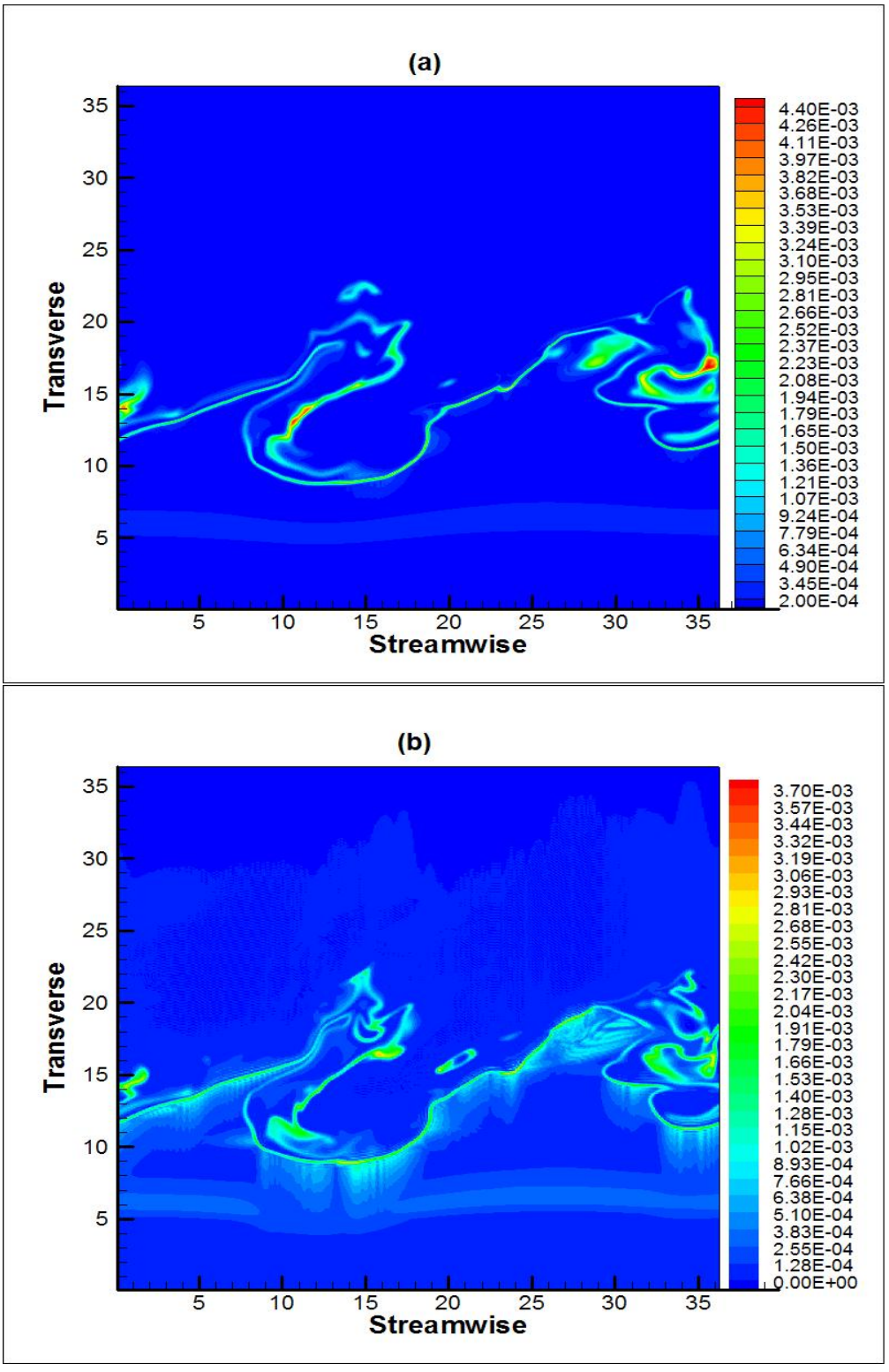

FIGURE 5.20: Snapshots of O mass fraction in the middle plane. (a) case 1L, (b) case 2L.

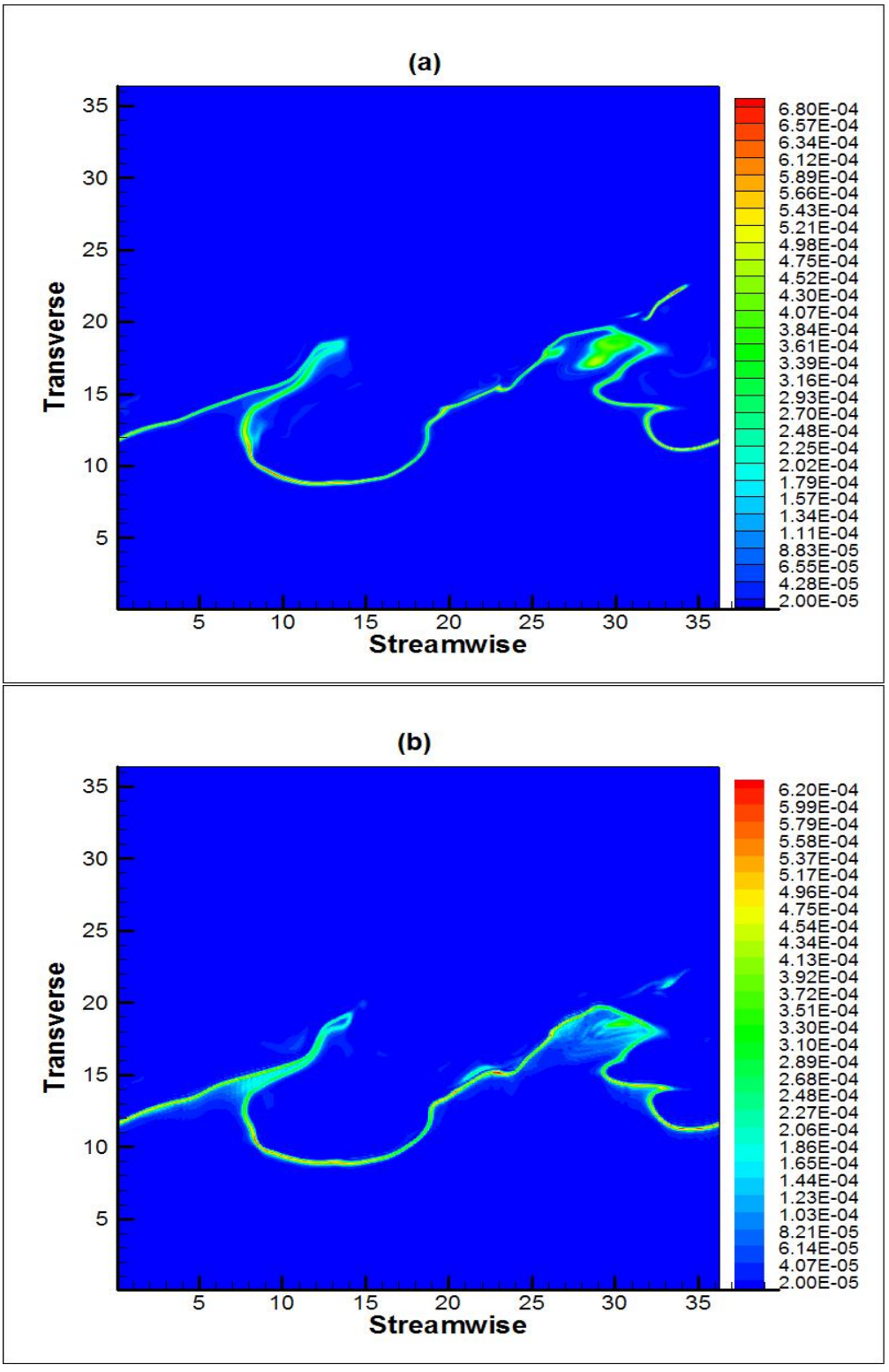

FIGURE 5.21: Snapshots of H_2O_2 mass fraction in the middle plane. (a) case 1L, (b) case 2L.

plot. The lower plot shows the species reaction rate at $tU_{ref}/\delta_{\omega_0}$=150.5, when the net rate of production or consumption of the species reaches its maximum. The lower plot, illustrated this value at the end of the simulation at $tU_{ref}/\delta_{\omega_0}$=160. In figure 5.22 it is shown that the hydrogen and oxygen molecules are continuously consumed as their reaction rates are negative throughout the simulation time. At time $tU_{ref}/\delta_{\omega_0}$=150.5 when concentrations are much higher, the rate of consumption is also higher until at the end of the simulation when this rate dramatically is dropped. This is consistent with the integrated values showed earlier in figure 5.10. For the products(figures 5.23 to 5.25), all the contours shown in the lower part of each plot have positive values at earlier stage after combustion is started i.e. at time $tU_{ref}/\delta_{\omega_0}$=150.5. This is due to the fact that all the species are being produced at the earlier stages and the rate of the reactions which cause this, move forward with a higher rate compared to backward reaction which consume these species. At later stages which is shown in here as $tU_{ref}/\delta_{\omega_0}$=160, contours take positive and negative values that means that there is a balance between the forward reactions and the backward reactions and hence, species are simultaneously produced and consumed within the reaction zone.

5.2 Scalar variance transport in a reactive multi-species mixing layers

A budget analysis for the scalar variance transport has been done. Mass fraction of the H_2, O_2 and H_2O molecules as well as H, O and OH radicals for the case 1L are selected to be analysed. Since the mass fraction of the HO_2 and H_2O_2 species is the smallest amongst other radicals, they have not been selected for this purpose. Data are plotted at the time when species maximum reaction rate occurs($tU_{ref}/\delta_{\omega_0}$=150.5) and at the end of the simulation ($tU_{ref}/\delta_{\omega_0}$=160).

Scalar variance of the selected species are shown in figure 5.26. In plot(a), variance of the molecules have been shown. At earlier stages of the reaction process the variance of the main reactants are smaller than those at the later time. For the H_2O this is due to the fact that at earlier stages after reaction, total mass fraction of H_2O is small compared to H_2 or O_2 and hence, its variance is still small. At later stages, as Y_{H_2O} increases, the mass fraction fluctuations increases accordingly that causes increase in variance. For radicals, however, the trend is not the same as for the molecules i.e. the variance does not necessarily increases with time. While hydrogen radical (H) shows an increase in the variance quantity from almost zero to a value greater than zero(a very small value, though), oxygen radical (O) shows a decrease from values above 3e+5(non-dimensional) to values almost equal to zero or very close to zero. The same story for OH radical which shows the maximum change from variance above 6e+5 to variance below 1e+5.

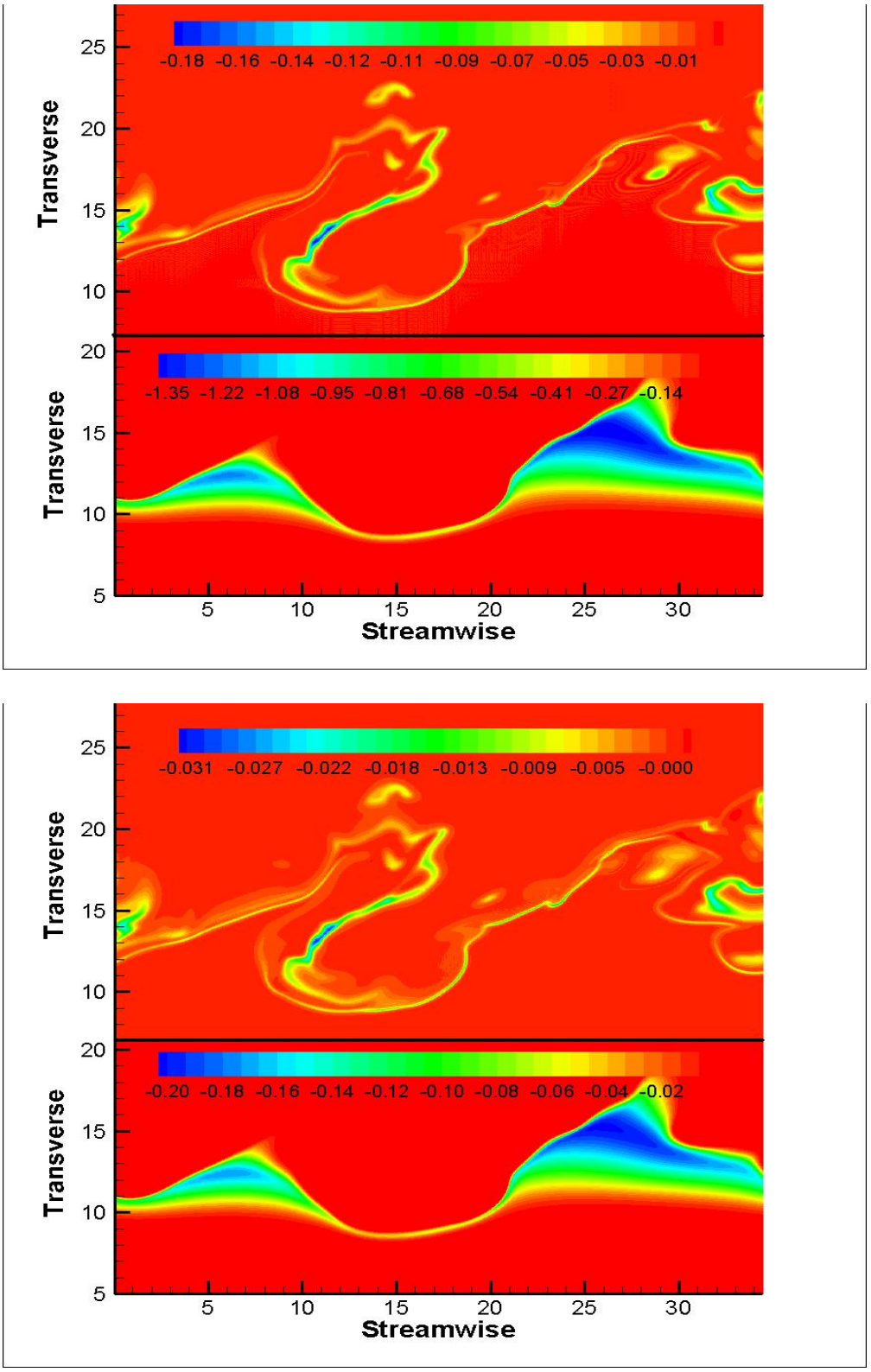

FIGURE 5.22: Snapshots of reaction rate for the species O_2 and H_2 in the middle plane for case 1L. Upper figure shows $\dot{\omega}_{O_2}$ and lower figure shows $\dot{\omega}_{H_2}$. Each figure has been split into a lower part which shows the rate at $tU_{ref}/\delta_{\omega_0}$=150.5 and an upper plot that shows the rate at $tU_{ref}/\delta_{\omega_0}$=160. Values are non-dimensional and are multiplied by $W_n * t_{ref}/\rho_{ref}$ in which W_n is the molecular weight of the species. Molecule of oxygen is consumed at a much higher rate than molecule of hydrogen.

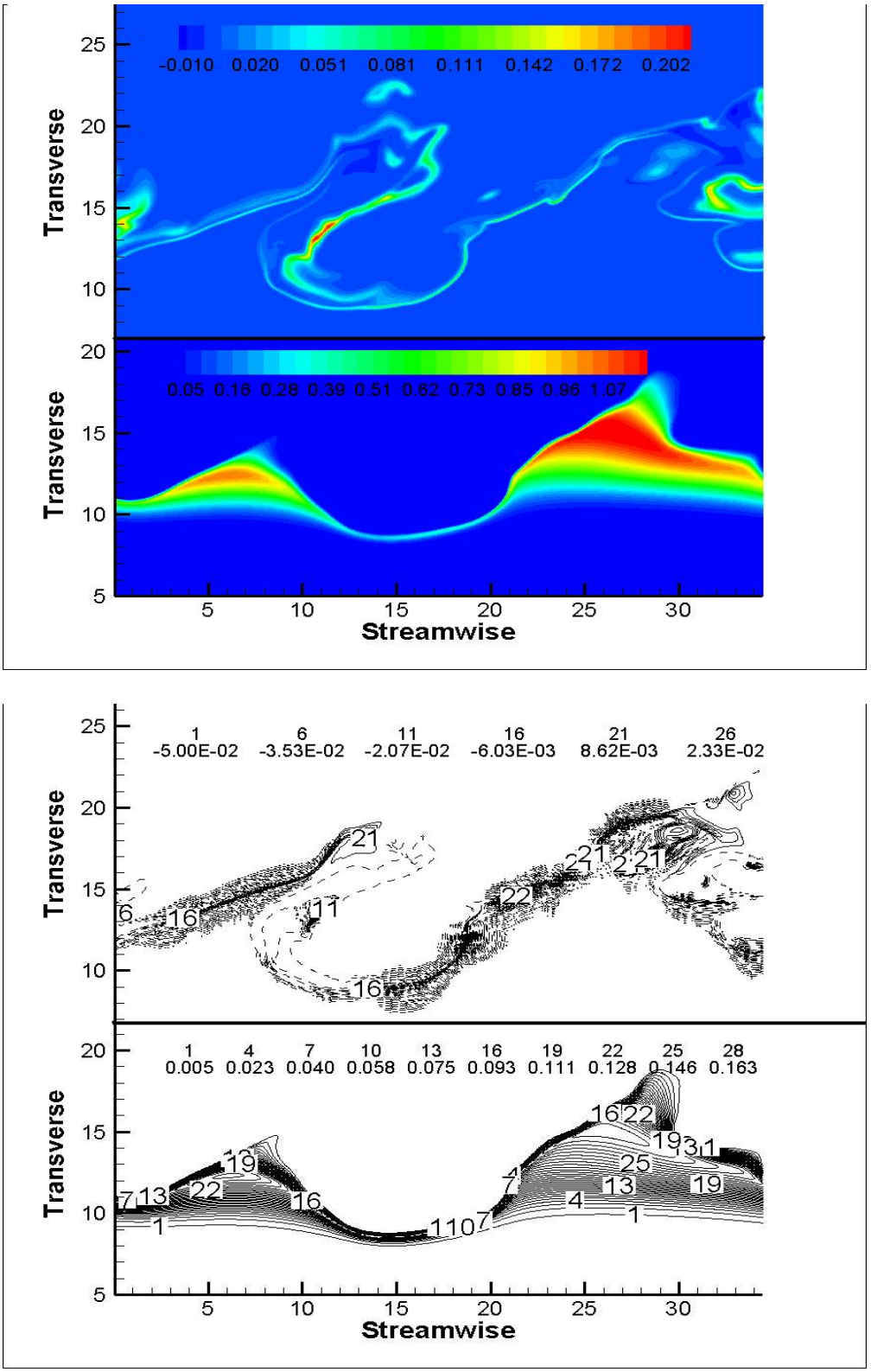

FIGURE 5.23: Snapshots of reaction rate for the species H_2O and OH in the middle plane for case 1L. Upper figure shows $\dot{\omega}_{H_2O}$ and lower figure shows $\dot{\omega}_{OH}$. Each figure has been split into a lower part which shows the rate at $tU_{ref}/\delta_{\omega_0}$=150.5 and an upper plot that shows the rate at $tU_{ref}/\delta_{\omega_0}$=160. Values are non-dimensional and are multiplied by $W_n * t_{ref}/\rho_{ref}$ in which W_n is the molecular weight of the species. For the black and white figure, dashed lines show negative contours which means the species is consumed.

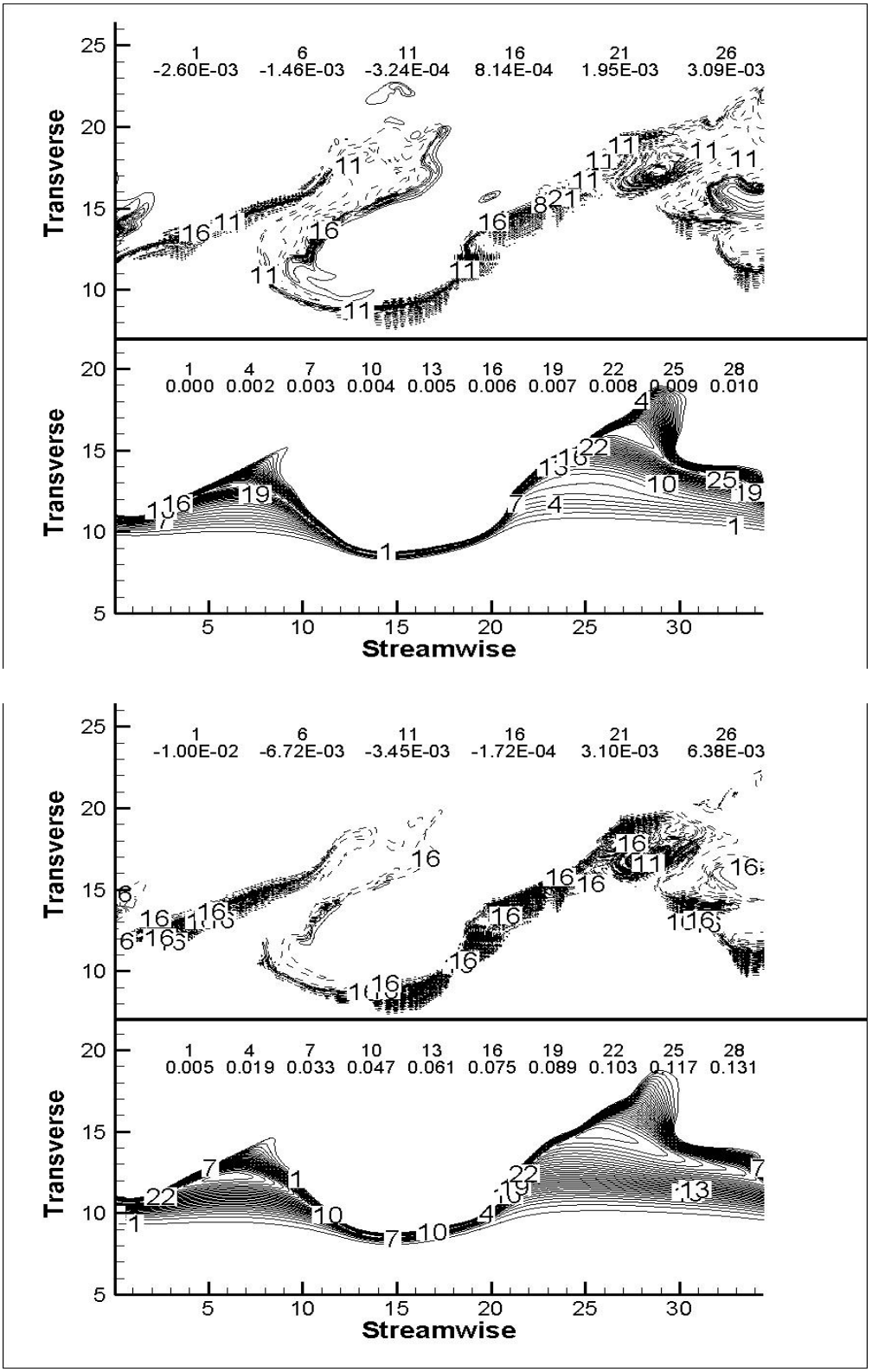

FIGURE 5.24: Snapshots of reaction rate for the species H and O in the middle plane for case 1L. Upper figure shows $\dot{\omega}_H$ and lower figure shows $\dot{\omega}_O$. Each figure has been split into a lower part which shows the rate at $tU_{ref}/\delta_{\omega_0}$=150.5 and an upper plot that shows the rate at $tU_{ref}/\delta_{\omega_0}$=160. Values are non-dimensional and are multiplied by $W_n * t_{ref}/\rho_{ref}$ in which W_n is the molecular weight of the species.

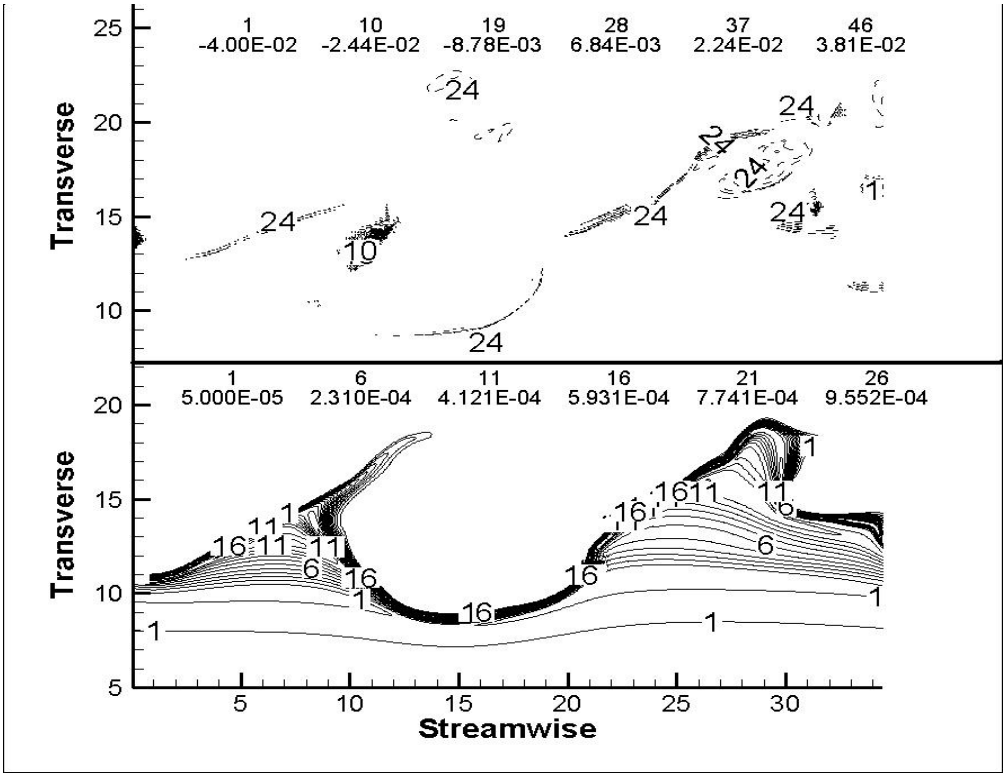

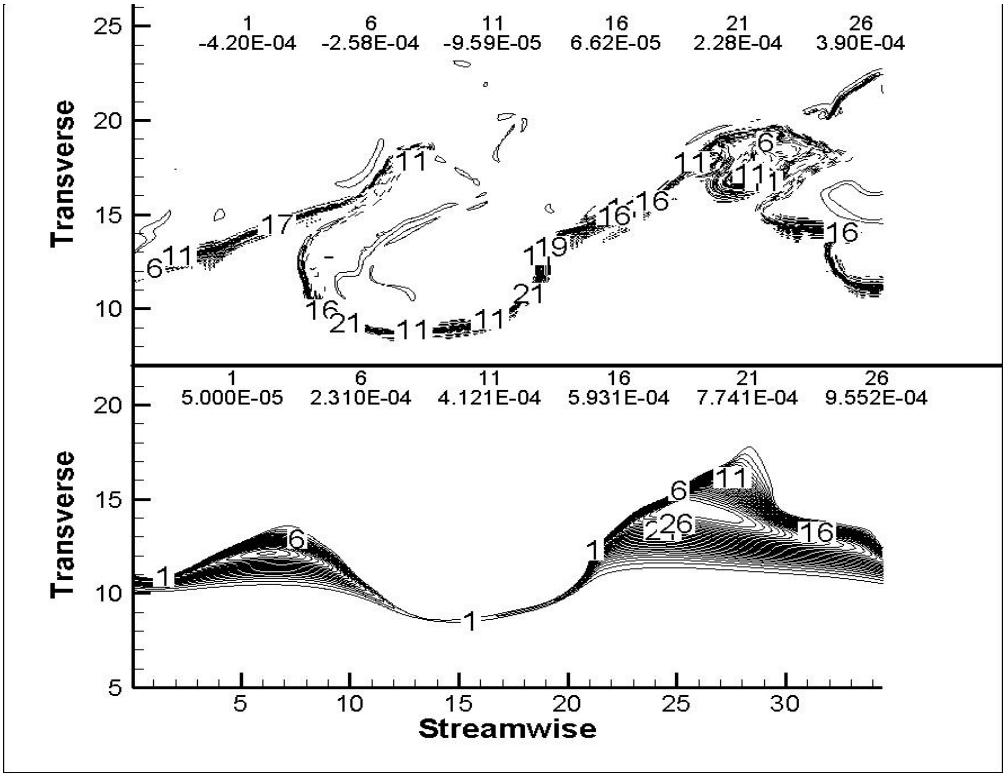

FIGURE 5.25: Snapshots of reaction rate for the species HO_2 and H_2O_2 in the middle plane for case 1L. Upper figure shows $\dot{\omega}_{HO_2}$ and lower figure shows $\dot{\omega}_{H_2O_2}$. Each figure has been split into a lower part which shows the rate at $tU_{ref}/\delta_{\omega_0}$=150.5 and an upper plot that shows the rate at $tU_{ref}/\delta_{\omega_0}$=160. Values are non-dimensional and are multiplied by $W_n * t_{ref}/\rho_{ref}$ in which W_n is the molecular weight of the species.

Budget analysis has been performed for the non-conservative terms(whose integrals are not summed up to zero so not acting as redistributive terms; similar to the case in figure 4.19). Therefore, scalar production/destruction term(Π_{var}), scalar dissipation rate(χ) and the scalar mass fraction-reaction correlation(Ω_{var}). Figure 5.27 shows the production/destruction term for 6 species mentioned above. In agreement with variance of H_2 and O_2, these two species show a positive value for the production term and also an increase in the value with time(plot (a)). However, for H_2O at t_{ND}=160, there is a negative part in the graph which shows a destruction rather than production. This is in the lower side of the mixing layer(oxygen side). As for the radicals, O and OH show the extrema for the production or destruction at t_{ND}=150.5 in accordance with their value for the variance showed in figure 5.26. Π_{var_H} is considerably smaller than two other radicals. It should be noted that the production of the radicals is three order of magnitude smaller than the molecules. This is also the case for their variance quantity shown in figure 5.26 with the variance of H_2, O_2 and H_2O in the order of O(-1) and O(-2) whereas the variance of radicals H, O and OH is in the order of O(-5).

Scalar dissipation rate is shown in figure 5.28 for the six species considered in this section. In plot(a), dissipation rate of the molecules (H_2, O_2 and H_2O) are shown for t_{ND}=150.5 and t_{ND}=160. During development of the mixing layer, species mixing level(molecular diffusion) increases with time and as a result, magnitude[2] of the scalar dissipation rate increases accordingly. Figure 5.28(b) shows the scalar dissipation rate for the three radicals mentioned earlier(H, O and OH). In contrast to their production rate showed in figure 5.27(b), radicals dissipation rate increases as the reaction proceeds. Similar to the molecules, the level of the mixing and entrainment with the flow is also increases for the radicals. The exception is only for O atom that shows a drop in scalar dissipation rate.

The last terms which is assessed in the scalar variance transport equation is the scalar mass fraction-reaction rate correlation term. The variations of this quantity for the 6 species of interest are shown in figure 5.29. Plot(a) is for the molecules and plot(b) shows this terms for the radicals. Since this terms is a linear correlation between the scalar mass fraction fluctuations and the net rate of the scalar production or consumption, all the quantities show a drop at later stages after reaction starts due to drop in the reaction rate value. This can be understood by comparing the values at t_{ND}=150.5 and the values at t_{ND}=160. Some of the quantities are overlapping lines which are located along the z axis because of their small magnitude. Molecule of oxygen in plot(a) shows a negative value and this is because of the fact that the mass fraction fluctuations of oxygen molecule varies in the opposite direction compared with the hydrogen molecule.

[2] Here, the scalar dissipation term is shown with the negative sign appears in the scalar variance equation. The magnitude of this value is of interest which is a measure for the mixing of the scalars at the molecular level(micro-mixing).

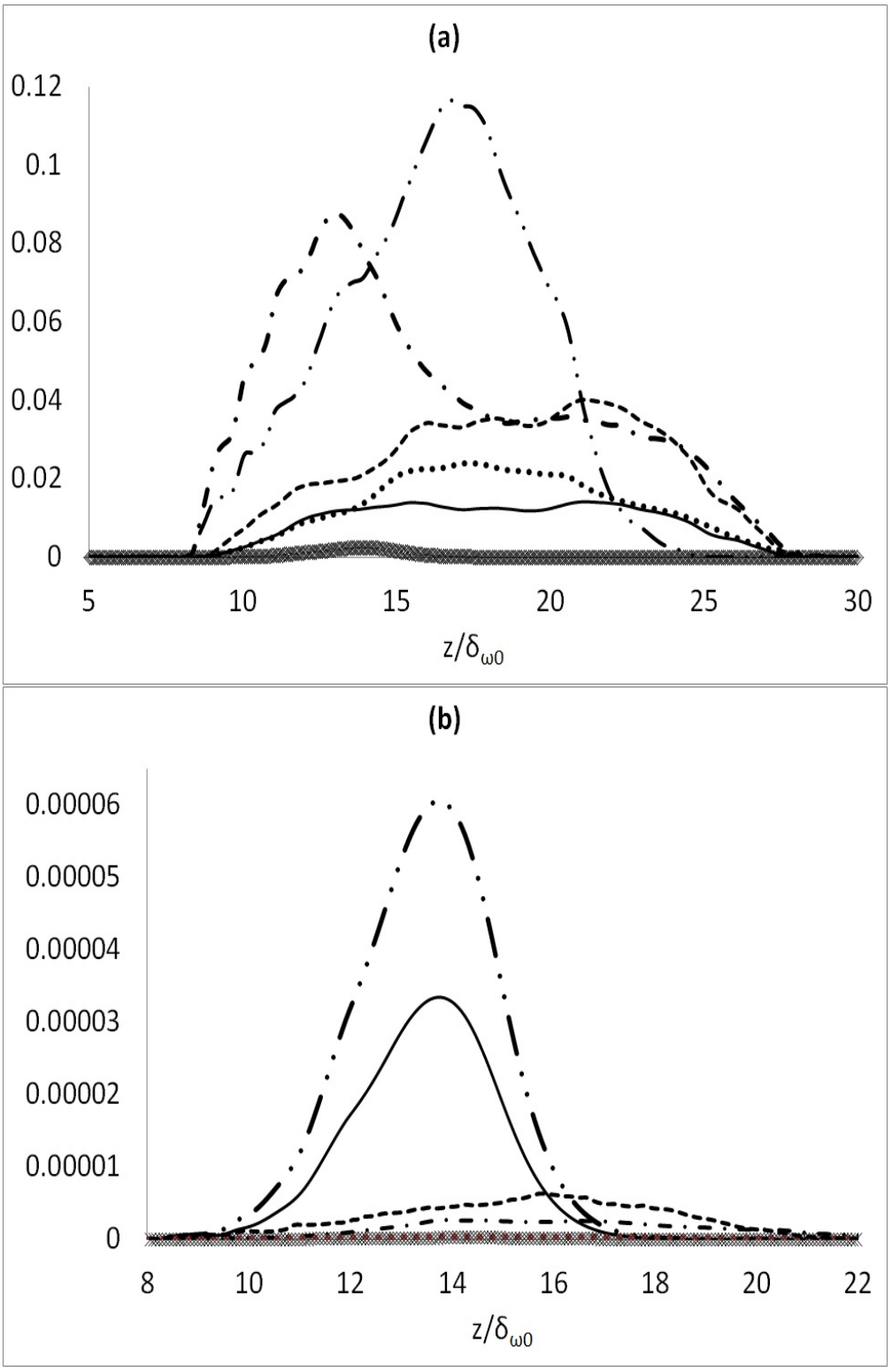

FIGURE 5.26: (a) Variance of the H_2, O_2 and H_2O mass fraction for case 1L: (———) $\widetilde{Y''_{H_2}Y''_{H_2}}$ at t_{ND}=150.5, ($\cdots$) $\widetilde{Y''_{H_2}Y''_{H_2}}$ at t_{ND}=160, (– – –) $\widetilde{Y''_{O_2}Y''_{O_2}}$ at t_{ND}=150.5, (– · – ·) $\widetilde{Y''_{O_2}Y''_{O_2}}$ at t_{ND}=160, (◊) $\widetilde{Y''_{H_2O}Y''_{H_2O}}$ at t_{ND}=150.5, (– · · –) $\widetilde{Y''_{H_2O}Y''_{H_2O}}$ at t_{ND}=160. (b) Variance of the H, O and OH mass fraction for case 1L: (×) $\widetilde{Y''_HY''_H}$ at t_{ND}=150.5, (– · – ·) $\widetilde{Y''_HY''_H}$ at t_{ND}=160, (———) $\widetilde{Y''_OY''_O}$ at t_{ND}=150.5, ($\cdots$) $\widetilde{Y''_OY''_O}$ at t_{ND}=160, (– · · –) $\widetilde{Y''_{OH}Y''_{OH}}$ at t_{ND}=150.5, (– – –) $\widetilde{Y''_{OH}Y''_{OH}}$ at t_{ND}=160.

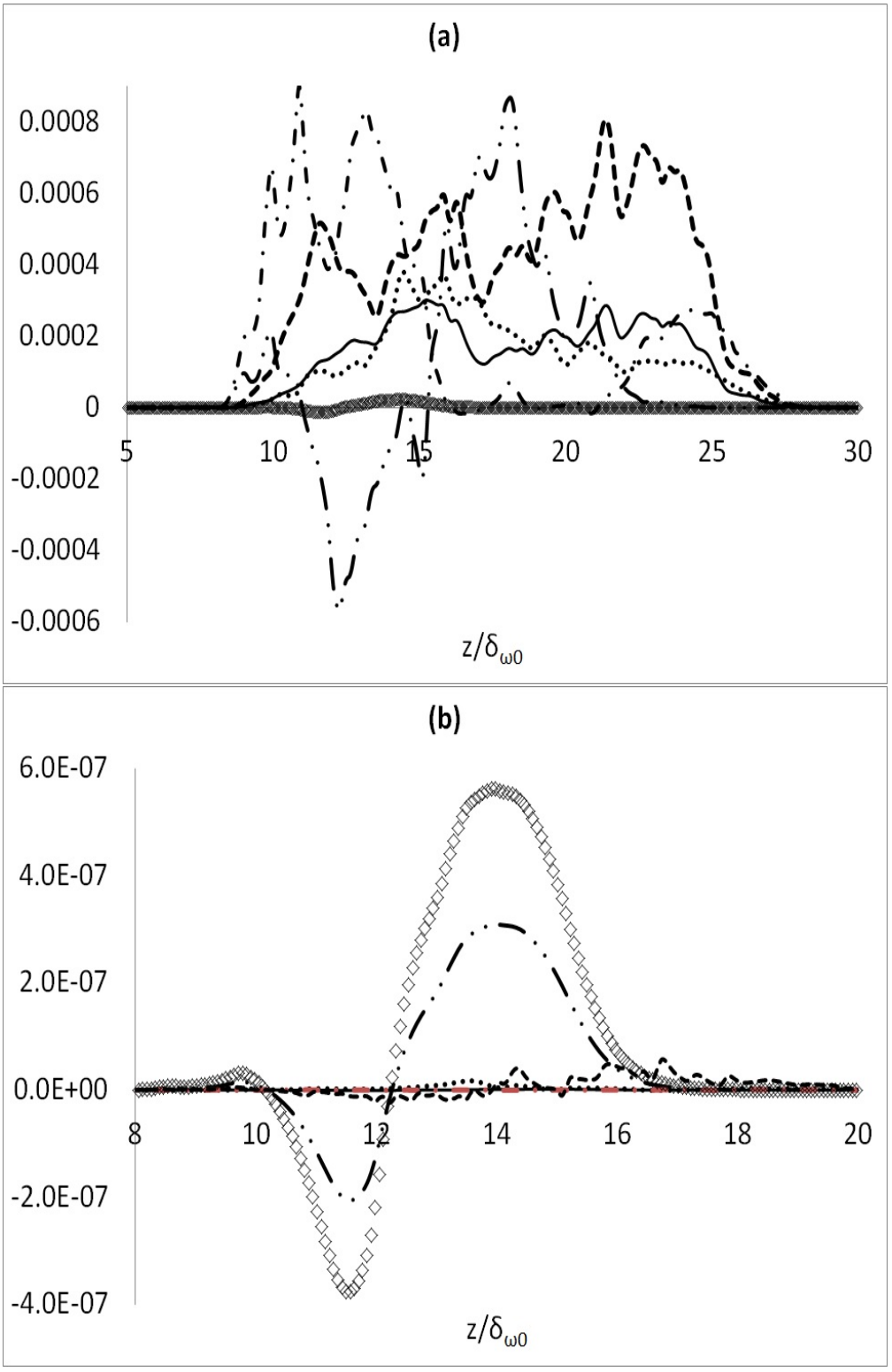

FIGURE 5.27: Scalar variance budget analysis. (a) Production/Destruction term for H_2, O_2 and H_2O mass fraction for case 1L: (———) $\Pi_{var_{H_2}}$ at t_{ND}=150.5, (· · ·) $\Pi_{var_{H_2}}$ at t_{ND}=160, (– – –) $\Pi_{var_{O_2}}$ at t_{ND}=150.5, (– · – ·) $\Pi_{var_{O_2}}$ at t_{ND}=160, (◊) $\Pi_{var_{H_2O}}$ at t_{ND}=150.5, (– · · –) $\Pi_{var_{H_2O}}$ at t_{ND}=160. (b) Production/Destruction term for H, O and OH mass fraction for case 1L: (———) Π_{var_H}=150.5, (· · ·) Π_{var_H} at t_{ND}=160, (– · · –) Π_{var_O} at t_{ND}=150.5, (– · – ·) Π_{var_O} at t_{ND}=160, (◊) $\Pi_{var_{OH}}$ at t_{ND}=150.5, (– – –) $\Pi_{var_{OH}}$ at t_{ND}=160.

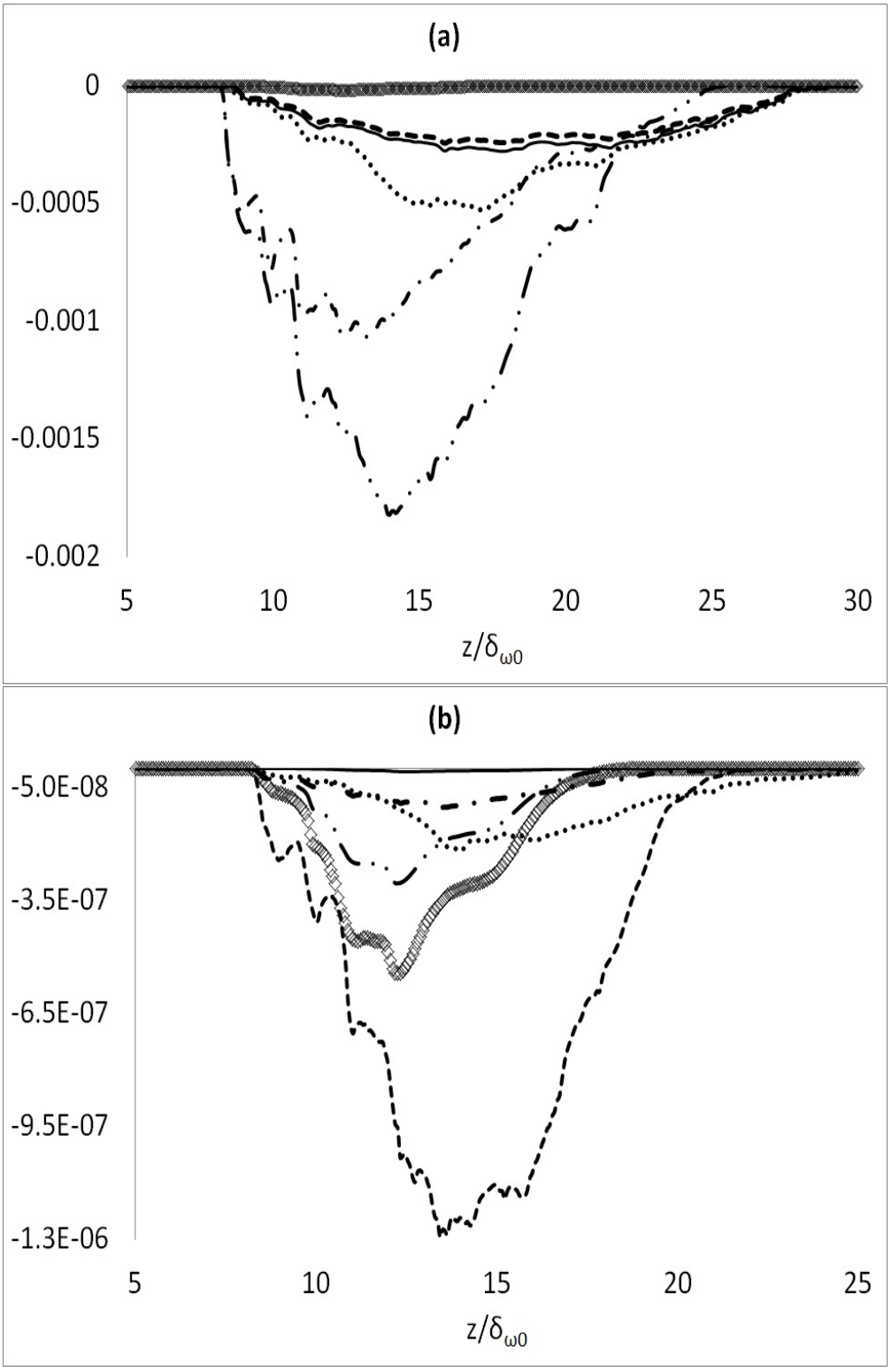

FIGURE 5.28: Scalar variance budget analysis. (a) Dissipation term for H_2, O_2 and H_2O mass fraction for case 1L: (———) χ_{H_2} at t_{ND}=150.5, ($\cdots$) χ_{H_2} at t_{ND}=160, ($-\ -\ -$) χ_{O_2} at t_{ND}=150.5, ($-\cdot-\cdot$) χ_{O_2} at t_{ND}=160, ($\Diamond$) χ_{H_2O} at t_{ND}=150.5, ($-\cdots-$) χ_{H_2O} at t_{ND}=160. (b) Dissipation term for H, O and OH mass fraction for case 1L: (———) χ_H=150.5, ($\cdots$) χ_H at t_{ND}=160, ($-\cdots-$) χ_O at t_{ND}=150.5, ($-\cdot-\cdot$) χ_O at t_{ND}=160, ($\Diamond$) χ_{OH} at t_{ND}=150.5, ($-\ -\ -$) χ_{OH} at t_{ND}=160.

Reaction rate of both species are negative as they are consumed throughout the reaction process as showed earlier.

Spectra of the mass fraction fluctuations also shown in figures 5.30 to 5.33. This shows the scalar energy variation from larger scales to smaller scales in the turbulent field. Spectra of H_2, O_2 and H_2O are shown in figure 5.30 and figure 5.31. Data for figure 5.30 are for two different x-y planes, one at $z = L_z/3$ and the other one at $z = L_z/2$. Mass fraction fluctuations at $z = 2L_z/3$ are also shown in figure 5.31. Spectra are shown at t_{ND}=150.5 and t_{ND}=160. In plot(a), it is shown that the energy of hydrogen molecules extends to smaller values compared to that of the O_2 and H_2O. Also at t_{ND}=150.5 when there is not much H_2O formed, the larger scales in the spectrum of the mass fraction fluctuations are less energetic compared to the t_{ND}=160 when the mass fraction of H_2O is considerably increased. This is in agreement with the variance of H_2O which was shown earlier in the figure 5.26 where the H_2O variance increases when mass fraction of the molecule increases. The same scenario for plot(b) but with even lower energy level for H_2O at t_{ND}=150.5 as the majority of this product is formed in the reaction fronts located in the lower stream(this was shown earlier in the reaction rate contour of H_2O in figure 5.23). Spectra of H_2O shown in figure 5.31(c) at t_{ND}=150 has the minimum value amongst two other plots since the plane from which the fluctuations are extracted for considerations is above the location where maximum interaction between two stream occurs and therefore, the mass fraction of the H_2O is minimum and so are the fluctuations. Spectra of H_2 and O_2 are close to each other with $E_{O_2}(\alpha)$ always above $E_{H_2}(\alpha)$ irrespective of the plane they are considered at.

Spectra of radical mass fraction are shown in figure 5.32 (at planes $z = L_z/3$ and $z = L_z/2$) and figure 5.33 (at plane $z = 2L_z/3$). In plot (a) and (b) and at t_{ND}=150.5, it is observed that the OH spectrum has the highest amount of energy at larger scales followed by the O radical and then H radical. This is also the case at later stages during the reaction i.e. t_{ND}=160 expect very few locations where O radical show more energy for larger scales. In plot(c) in figure 5.33 which is located in the hydrogen stream, hydrogen radical has the highest scalar energy at larger scales at both times i.e. t_{ND}=150.5 and t_{ND}=160. For the OH at t_{ND}=150.5, there is also some energy pile-up observed due to the smaller scales of this particular species could not completely be resolved by the mesh used in the simulations. This shows that the energy cascade from larger scales to lower scales for OH does not follow the Kolmogorov's theory and the energy in the smallest scales has not dissipated fully by the viscosity.

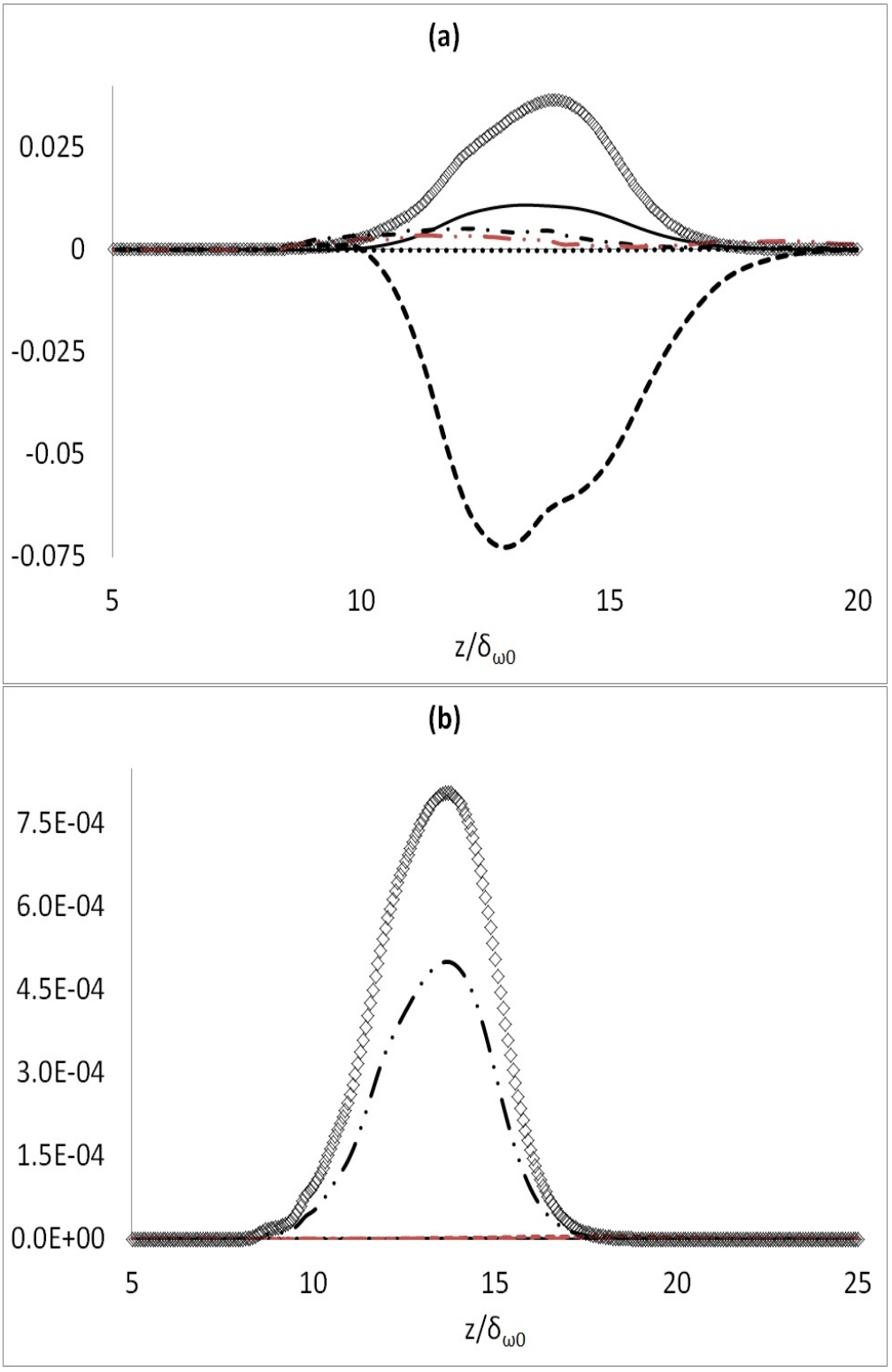

FIGURE 5.29: Scalar variance budget analysis. (a) Reaction-mass fraction correlation term for H_2, O_2 and H_2O for case 1L: (———) $\Omega_{var_{H_2}}$ at t_{ND}=150.5, ($\cdots$) $\Omega_{var_{H_2}}$ at t_{ND}=160, ($-\ -\ -$) $\Omega_{var_{O_2}}$ at t_{ND}=150.5, ($-\cdot-\cdot$) $\Omega_{var_{O_2}}$ at t_{ND}=160, ($\Diamond$) $\Omega_{var_{H_2O}}$ at t_{ND}=150.5, ($-\cdot\cdot-$) $\Omega_{var_{H_2O}}$ at t_{ND}=160. (b) Reaction-mass fraction correlation term for H, O and OH for case 1L: (———) Ω_{var_H}=150.5, ($\cdots$) Ω_{var_H} at t_{ND}=160, ($-\cdot\cdot-$) Ω_{var_O} at t_{ND}=150.5, ($-\cdot-\cdot$) Ω_{var_O} at t_{ND}=160, ($\Diamond$) $\Omega_{var_{OH}}$ at t_{ND}=150.5, ($-\ -\ -$) $\Omega_{var_{OH}}$ at t_{ND}=160.

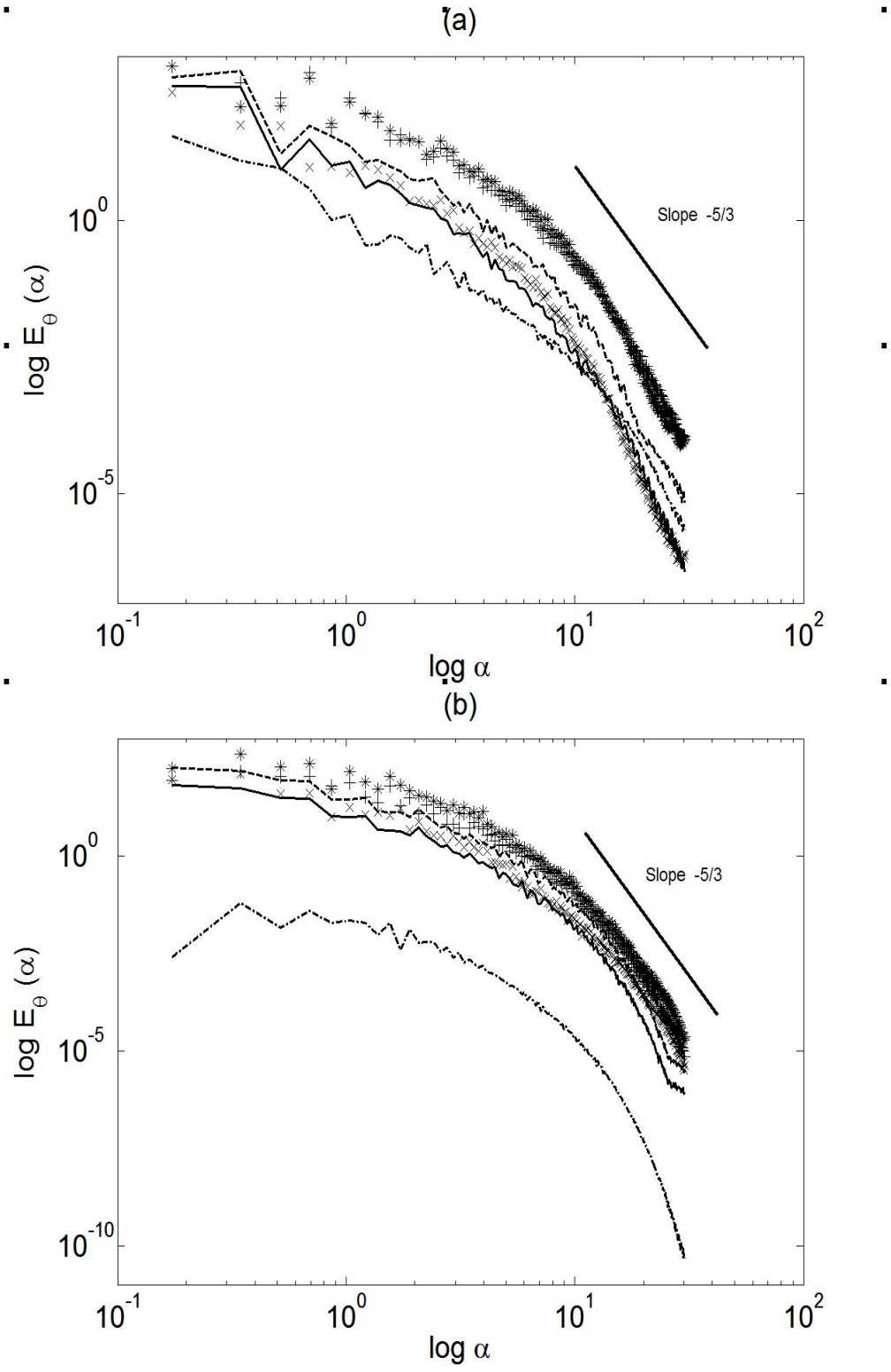

FIGURE 5.30: Species(molecules) mass fraction spectra at three different planes across the mixing layer for case 1L: (a) at $z = L_z/3$, (b) at $z = L_z/2$, and (c) at $z = 2L_z/3$ continues in figure 5.31. (———) $\log E_{H_2}(\alpha)$ at t_{ND}=150.5, (− − −) $\log E_{O_2}(\alpha)$ at t_{ND}=150.5, (− · − ·) $\log E_{H_2O}(\alpha)$ at t_{ND}=150.5, (×) $\log E_{H_2}(\alpha)$ at t_{ND}=160, (+) $\log E_{O_2}(\alpha)$ at t_{ND}=160, (∗) $\log E_{H_2O}(\alpha)$ at t_{ND}=160.

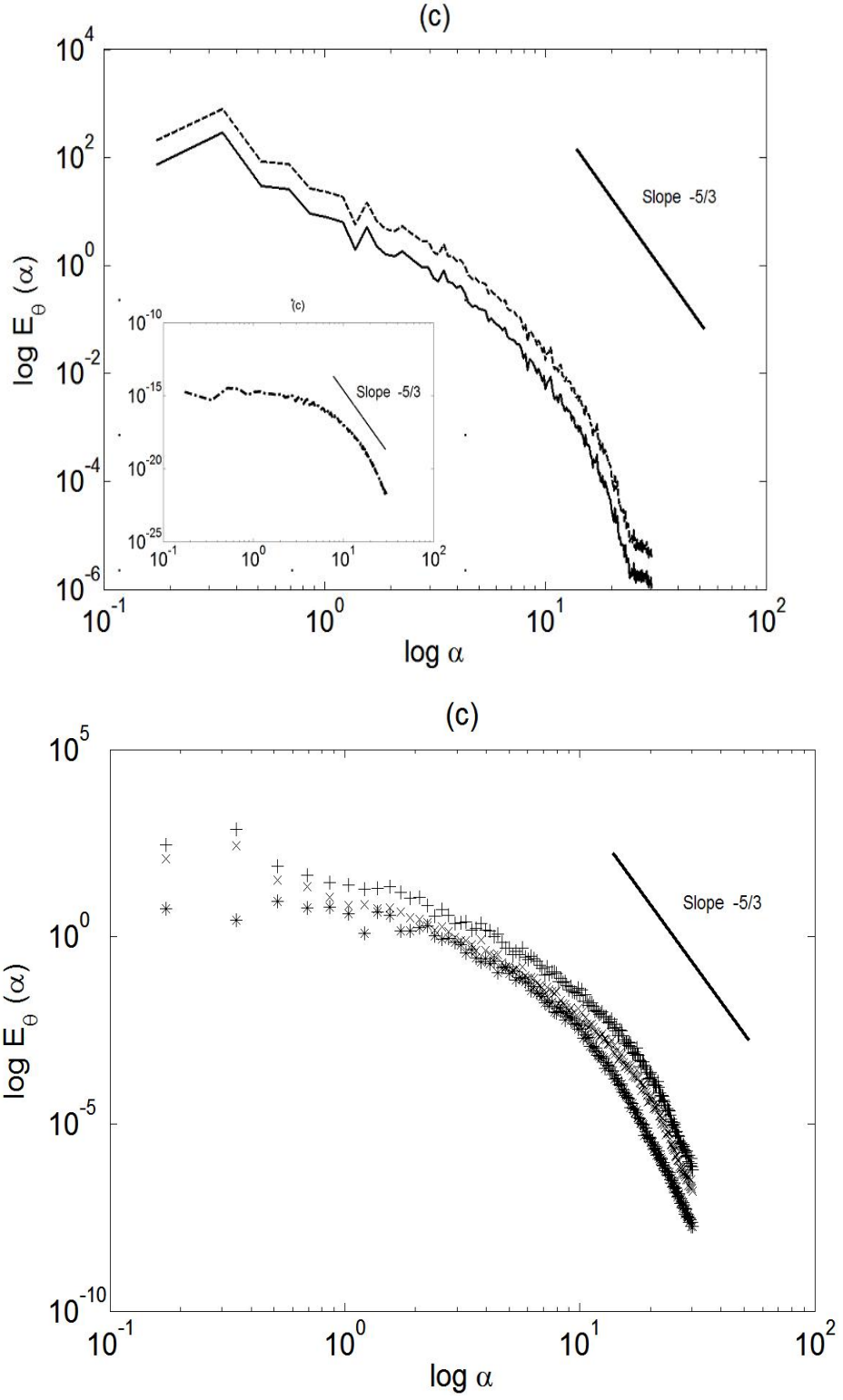

FIGURE 5.31: Continued from figure 5.30: Species(molecules) mass fraction spectra across the mixing layer for case 1L at (c) $z = 2L_z/3$. (———) $\log E_{H_2}(\alpha)$ at t_{ND}=150.5, (– – –) $\log E_{O_2}(\alpha)$ at t_{ND}=150.5, (– · – ·) $\log E_{H_2O}(\alpha)$ at t_{ND}=150.5, (×) $\log E_{H_2}(\alpha)$ at t_{ND}=160, (+) $\log E_{O_2}(\alpha)$ at t_{ND}=160, (∗) $\log E_{H_2O}(\alpha)$ at t_{ND}=160.

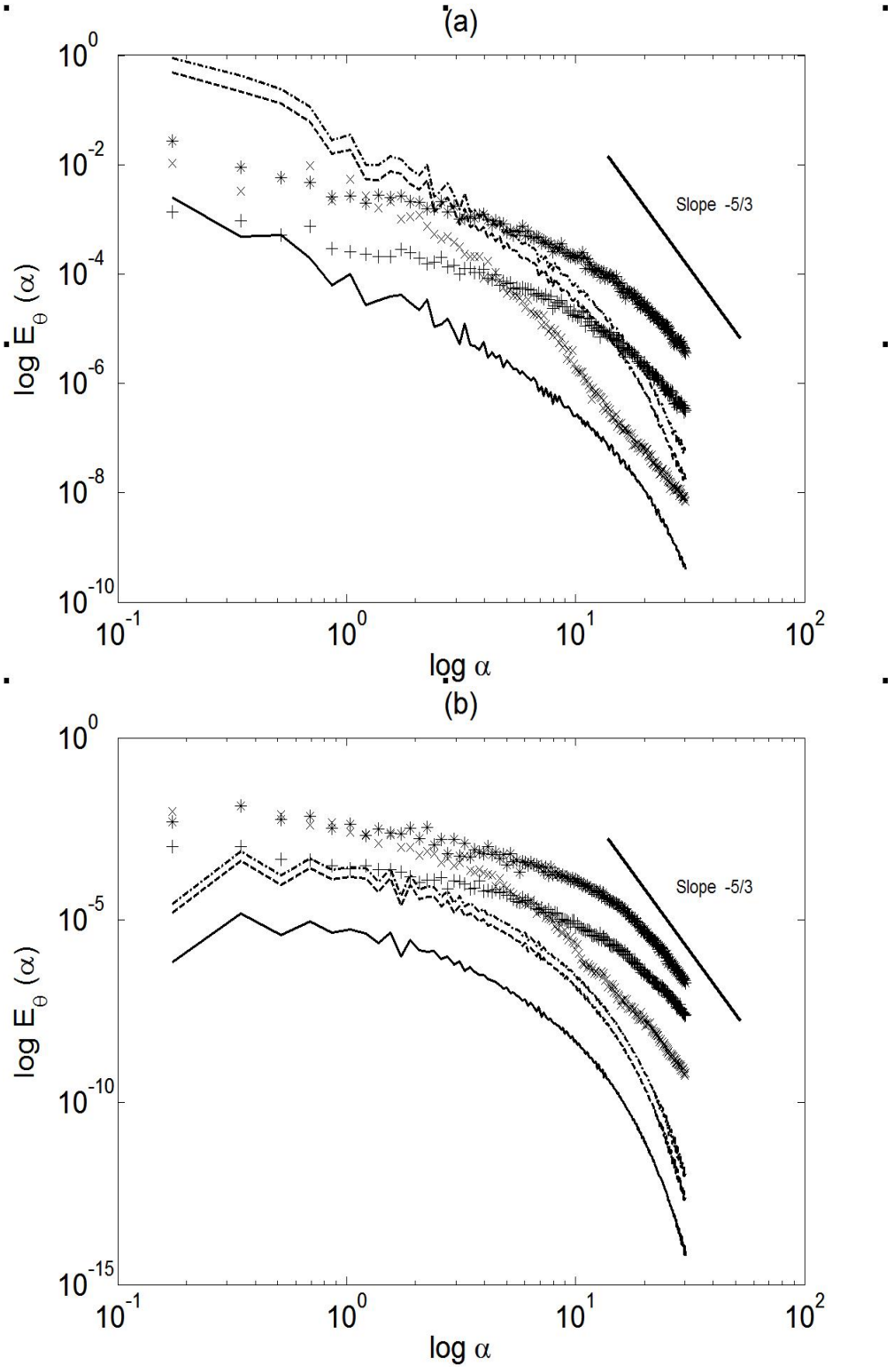

FIGURE 5.32: Species(radicals) mass fraction spectra at three different planes across the mixing layer for case 1L: (a) at $z = L_z/3$, (b) at $z = L_z/2$, and (c) at $z = 2L_z/3$ continues in figure 5.33. (———) $\log E_H(\alpha)$ at t_{ND}=150.5, (– – –) $\log E_O(\alpha)$ at t_{ND}=150.5, (– · – ·) $\log E_{OH}(\alpha)$ at t_{ND}=150.5, (×) $\log E_H(\alpha)$ at t_{ND}=160, (+) $\log E_O(\alpha)$ at t_{ND}=160, (∗) $\log E_{OH}(\alpha)$ at t_{ND}=160.

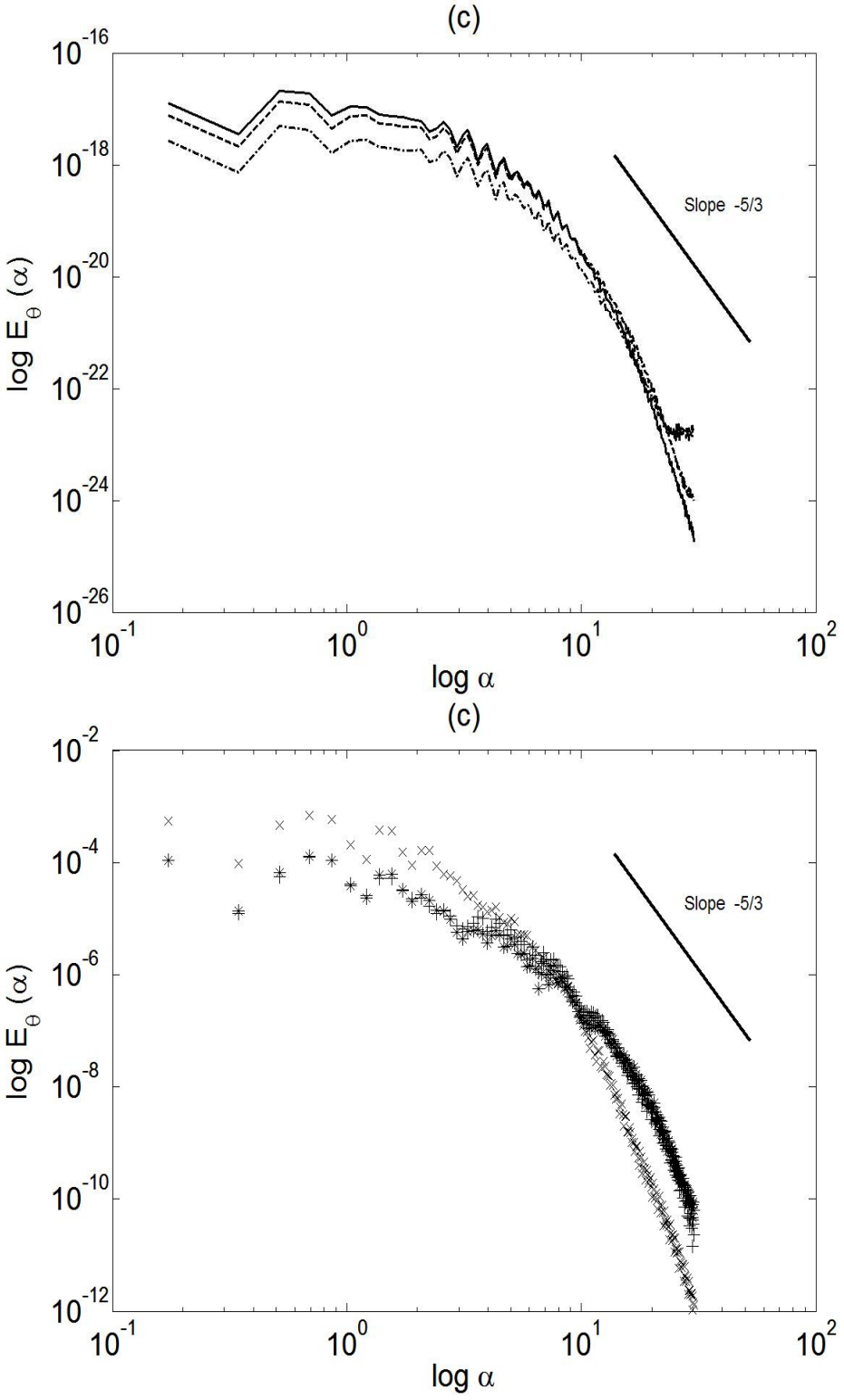

FIGURE 5.33: Continued from figure 5.32: Species(radicals) mass fraction spectra across the mixing layer for case 1L at (c) $z = 2L_z/3$. (———) $\log E_H(\alpha)$ at t_{ND}=150.5, (– – –) $\log E_O(\alpha)$ at t_{ND}=150.5, (– · – ·) $\log E_{OH}(\alpha)$ at t_{ND}=150.5, (×) $\log E_H(\alpha)$ at t_{ND}=160, (+) $\log E_O(\alpha)$ at t_{ND}=160, (∗) $\log E_{OH}(\alpha)$ at t_{ND}=160.

5.3 Turbulent scalar flux in a reactive multi-species mixing layers

Turbulent scalar flux for a multi-component mixture has not been addressed a lot in the literatures. In addition, the majority of the research works have focused on the passive scalars. Therefore, in this work it is aimed to do a study on the active scalars exist in a multi-species mixture. In order to do that, a budget analysis for the turbulent flux of different species undergoing a finite-rate chemical mechanism has been done. Similar to what expressed in chapter 4, it is started to illustrate the mean scalar gradient first, and compare their trend with the trace of the turbulent scalar flux in order to locate the counter-gradient or gradient transport across the mixing layer. Analysis has been done for the molecules and radicals separately. Three radicals which has higher mass fraction have been chosen for this purpose. These radicals are the ones which were studied in previous section i.e. H, O and OH.

Figures 5.34 and 5.35 show the mean mass fraction gradient across the mixing layer (transverse direction) for the molecules of H_2, O_2 and H_2O and the three radicals mentioned earlier. For the main reactants, the gradients move in the opposite direction; while hydrogen shows a positive gradient, oxygen has got a negative gradient and this is due to the type of the problem that has been set-up in this work i.e. non-premixed reactants. Main product(H_2O) however, shows a positive part followed by a negative gradient. Moreover, it shows more fluctuations with larger magnitude for the mean mass fraction gradient at later stages after reaction(t_{ND}=160) compared to the earlier periods after the reaction. This shows an increase in the level of mixing which results in a larger gradient for the mass fraction across the domain. As for the radicals, it is observed that the peak values for mass fraction gradient(and obviously the mass fraction itself) happens at earlier stages after the start of the reaction. This is in contrast with what was observed for the molecules in figure 5.34. Radicals mass fraction gradient at t_{ND}=150.5 when the reaction rates are maximum, are larger with an order of magnitude compared to their values at t_{ND}=160. This proves that unstable nature of the radicals as intermediate combustion products since they tend to be converted to more stable molecules such as H_2O whose mass fraction gradient increases with time in a reactive environment.

As stated before, gradient transport occurs when the turbulent flux of a scalar(active scalar which is species mass fraction in this study), moves in the opposite direction as the scalar mass fraction gradient whereas counter-gradient transport is called to a phenomenon when the turbulent flux and the scalar mean mass fraction gradient move in the same direction i.e. their changes along the desired direction is either positive or negative.

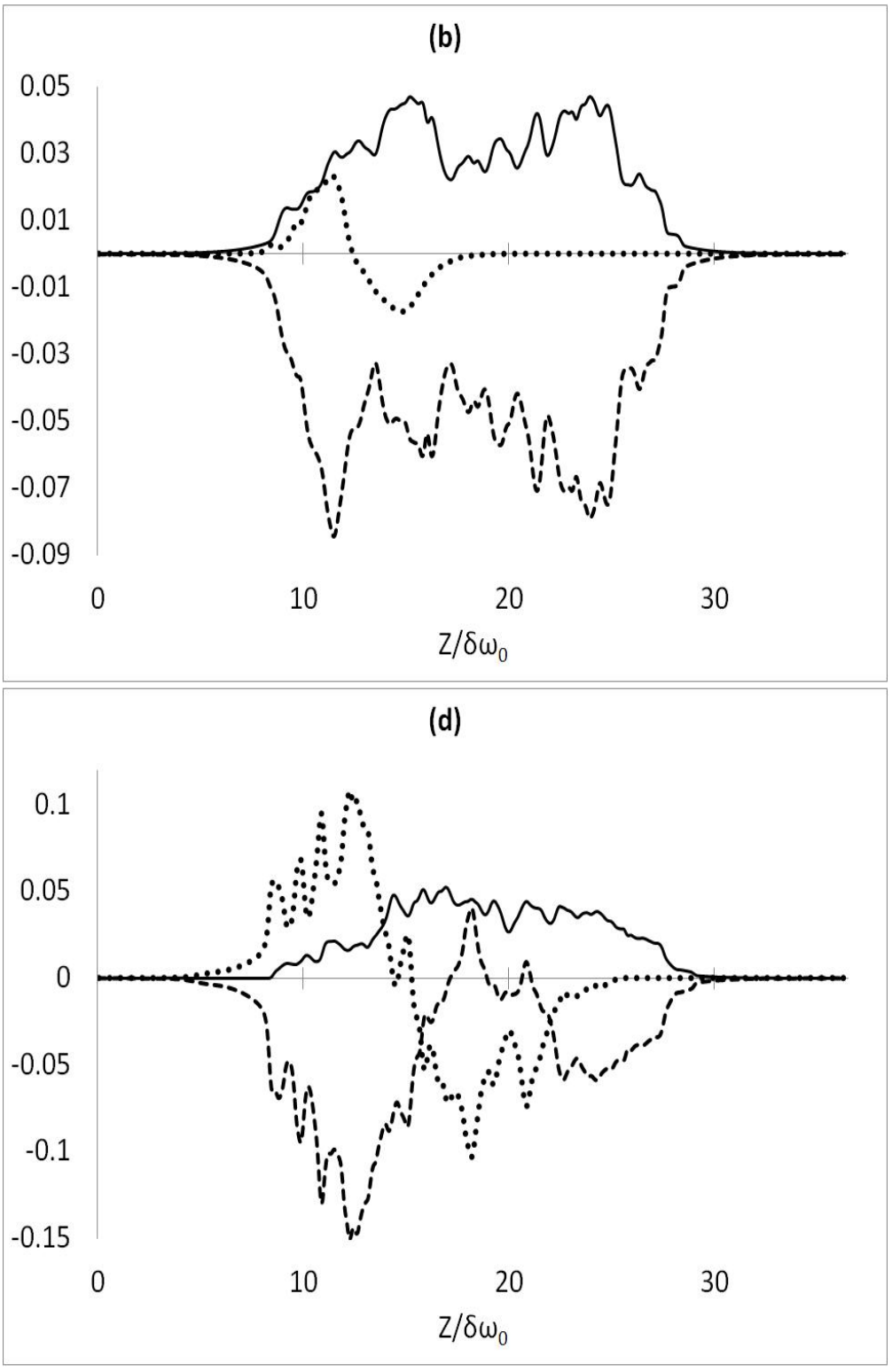

FIGURE 5.34: Mean scalar mass fraction gradient for Y_{H_2}, Y_{O_2}, an Y_{H_2O} against mixing layer transverse direction (z/δ_{ω_0}): (a) at t_{ND}=150.5, (b) at t_{ND}=160. (———) $\partial\widetilde{Y_{H_2}}/\partial z$, (– – –) $\partial\widetilde{Y_{O_2}}/\partial z$, ($\cdots$) $\partial\widetilde{Y_{H_2O}}/\partial z$.

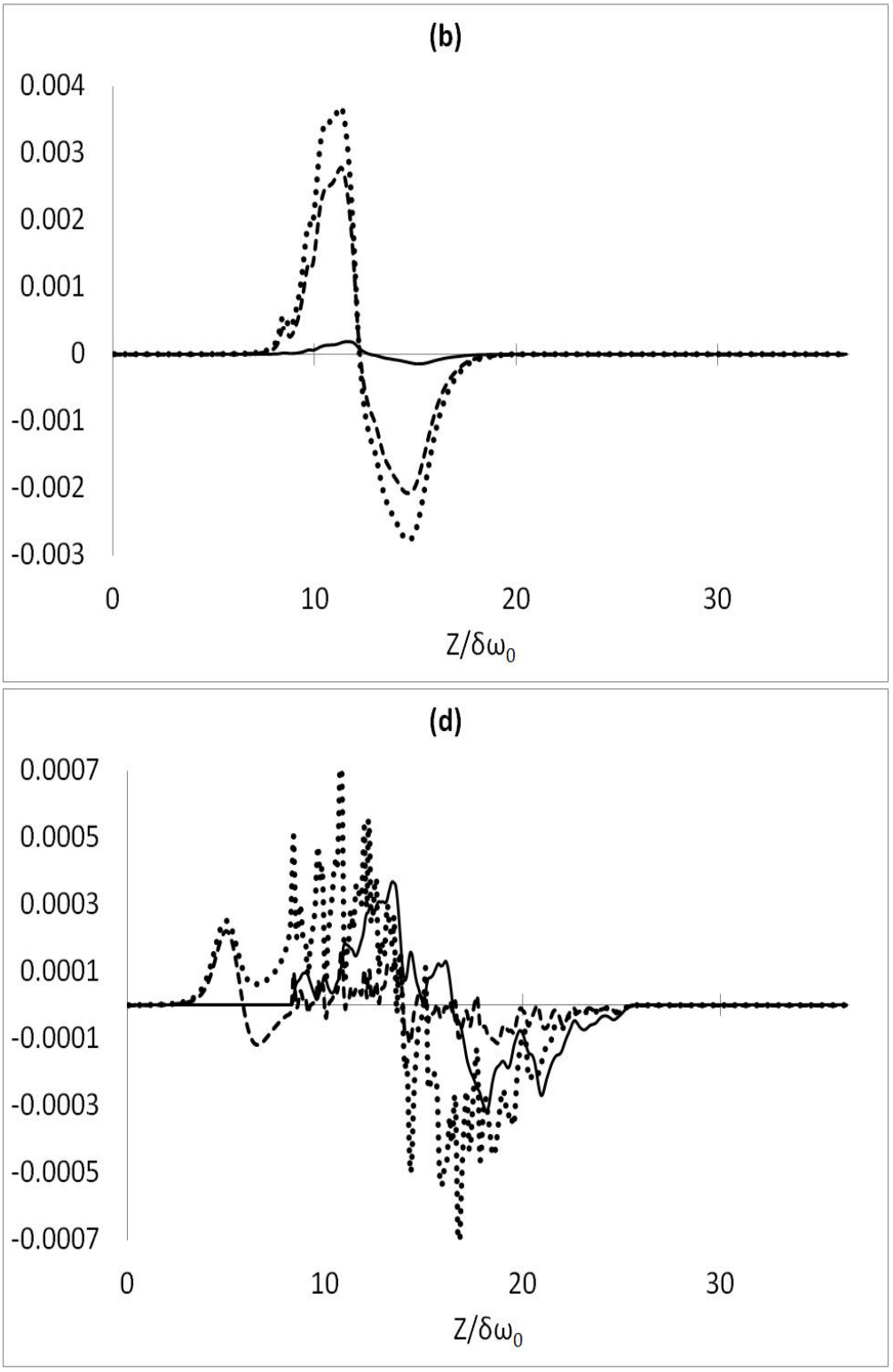

FIGURE 5.35: Mean scalar mass fraction gradient for Y_H, Y_O, and Y_{OH} against mixing layer transverse direction(z/δ_{ω_0}): (a) at t_{ND}=150.5, (b) at t_{ND}=160. (———) $\partial\widetilde{Y_H}/\partial z$, (– – –) $\partial\widetilde{Y_O}/\partial z$, ($\cdots$) $\partial\widetilde{Y_{OH}}/\partial z$.

This has been shown in figure 5.36 for the molecules and in figure 5.37 for the radicals. Figure 5.36(a) shows that at t_{ND}=150.5 which is the early stage after start of the reaction, only the product H_2O shows counter-gradient transport(CGT)[3]whereas the main reactants follow the natural rule exist for mass transfer that is transfer from higher concentration to the lower concentration. Even H_2O shows CGT at very limited locations across the domain. The large peak at lower side of the mixing layer is because of the fact that there are two consecutive points, one with positive value and one with negative value. So a sharp change in the direction of the changes causes such trend which shows the occurrence of the CGT at only a small region across the domain. At t_{ND}=160, oxygen molecule also shows CGT whereas hydrogen always follow the normal gradient transport principle. Figure 5.37 shows that the radicals(H, O and OH) have CGT at locations across the mixing layer at both times selected for this purpose i.e. t_{ND}=150.5 and t_{ND}=160. The extrema of the variations is almost constant which means that the ratio of the turbulent scalar flux to its mean mass fraction gradient does not change much as time proceeds. However, at earlier stage after reaction, there are only a few points across the domain exist with CGT phenomenon observed in them whereas at t_{ND}=160, number of such points have been increased especially for O and OH radicals. Radical H shows CGT at very few points across the domain and such disparity can only be due to fluctuations in the turbulent filed rather than a clear physical behaviour. In contrast, O and OH radicals show counter-gradient transport at wider region across the domain.

5.3.1 Budget analysis

Among the terms exist in the turbulent scalar flux transport equation, it was shown in chapter 4 that the pressure terms and production terms have the net effect on the gradient or counter-gradient transport together with reaction-velocity correlation whereas the rest act as redistributive terms and although they affect the GT or CGT in local context, but if they are integrated over time, their net effect will be negligible. In this part, a budget analysis for non-distributive(or non-conservative) terms will be presented in two section: One for H_2, O_2 and H_2O molecules and the other one for H, O and OH radicals. The terms are nominated as follows: Production terms as Π_I and Π_{II}, Mean pressure gradient term as Φ and fluctuating pressure gradient as Ψ, and finally, reaction rate-fluctuating velocity correlation as Ω. Results are presented at two different times: t_{ND}=150.5 when the reaction rates are at their extremum values and at time t_{ND}=160 which is the end of the current simulation. As previously stated, all the quantities

[3]Quantities are normalised by their corresponding mean mass fraction gradient so that a positive trend shows that $\overline{\rho\theta'' u_j''}$ and $\partial\widetilde{\theta}/\partial z$ move in the same direction.

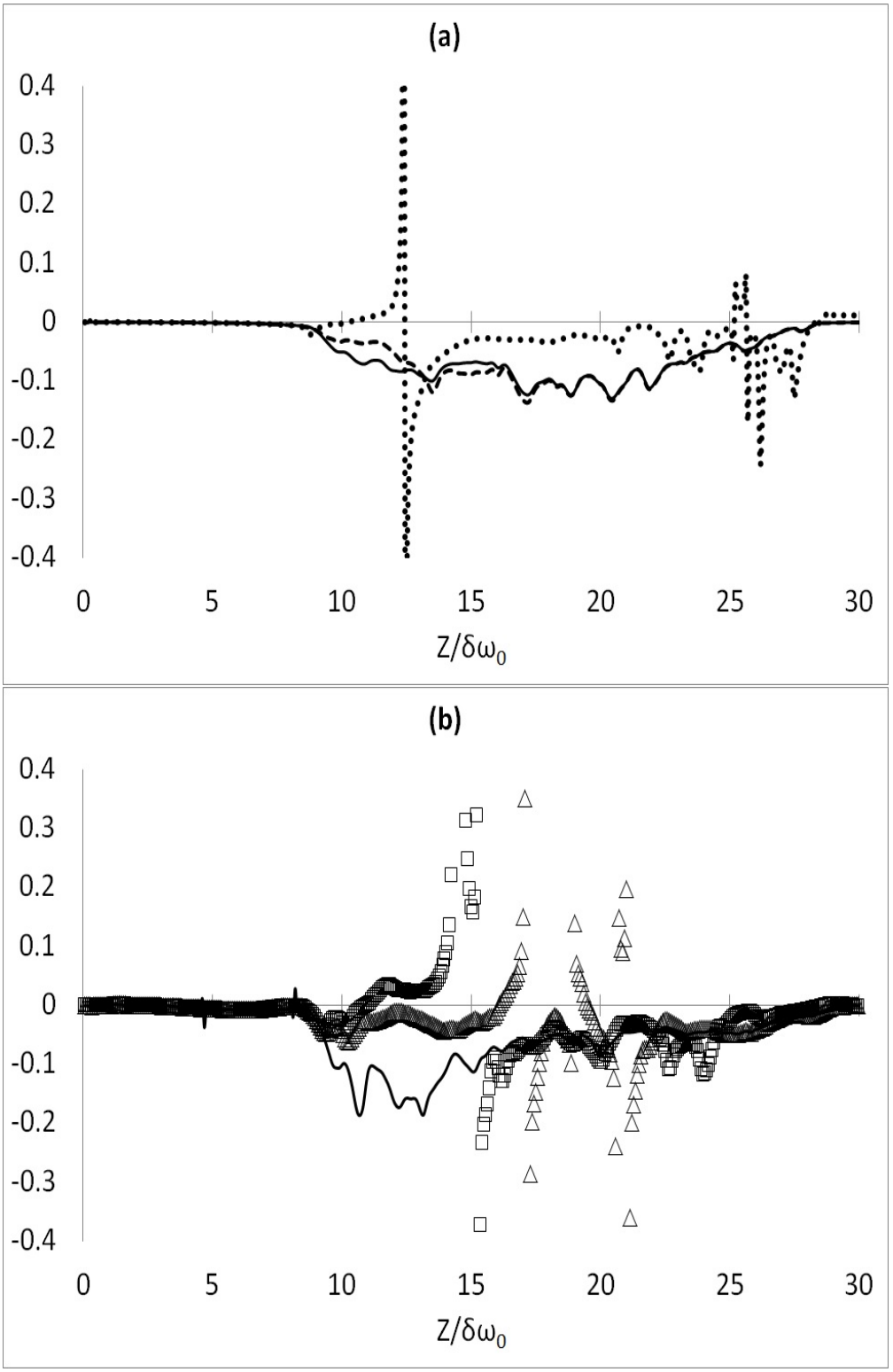

FIGURE 5.36: Turbulent scalar flux($\overline{\rho\theta'' u_j''}$) for H_2, O_2 and H_2O in transverse direction at: (a) t_{ND}=150.5 and (b) t_{ND}=160. (———) $\overline{\rho Y_{H_2}'' w''}$, (– – – and △) $\overline{\rho Y_{O_2}'' w''}$, (· · · · and □) $\overline{\rho Y_{H_2O}'' w''}$. Each quantity is normalised by its corresponding mean scalar gradient in transverse direction($\partial\widetilde{Y_n}/\partial z$).

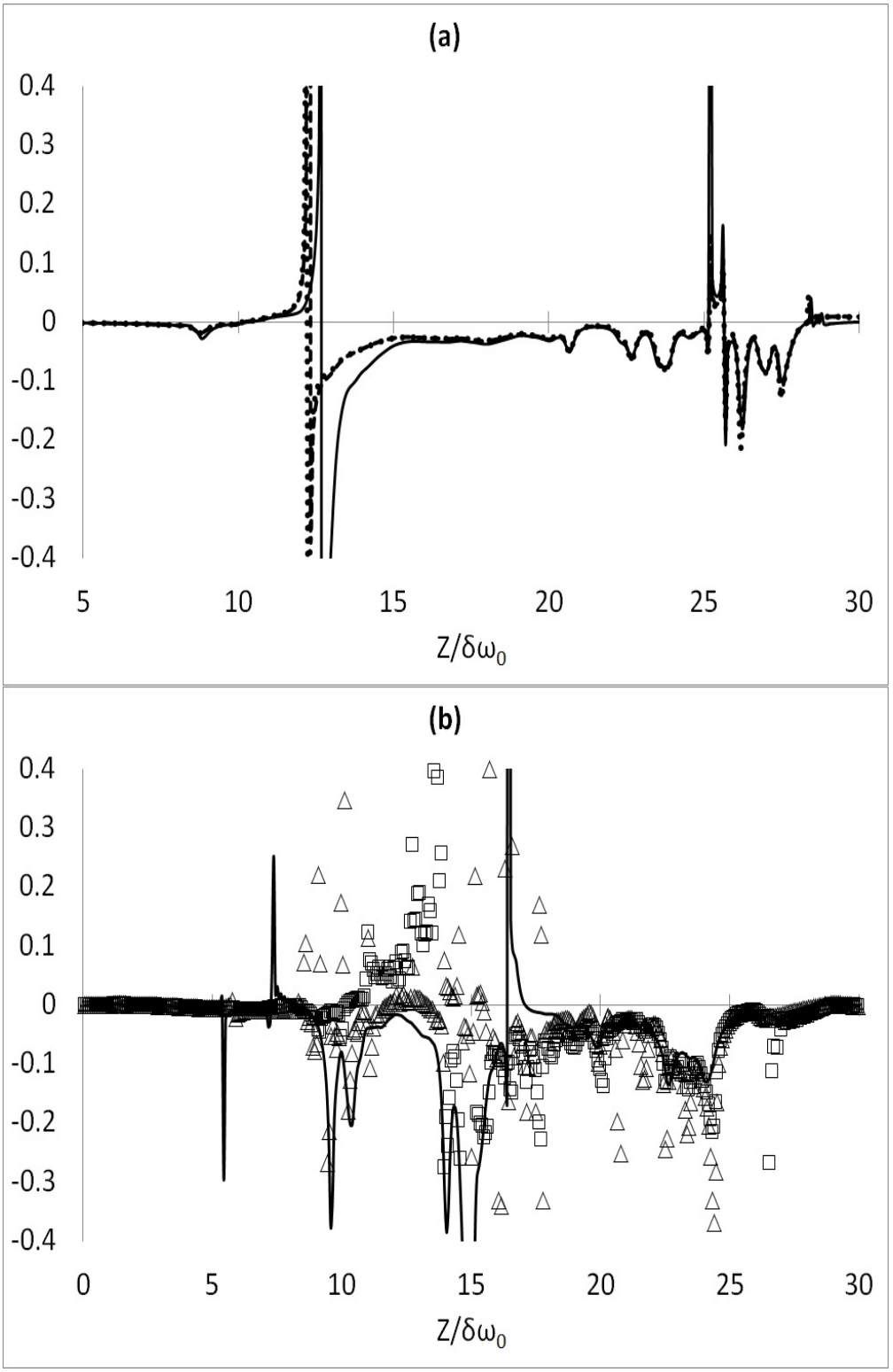

FIGURE 5.37: Turbulent scalar flux($\overline{\rho\theta'' u_j''}$) for H, O and OH in transverse direction at: (a) t_{ND}=150.5 and (b) t_{ND}=160. (———) $\overline{\rho Y_H'' w''}$, (– – – and △) $\overline{\rho Y_O'' w''}$, (· · · · and □) $\overline{\rho Y_{OH}'' w''}$. Each quantity is normalised by its corresponding mean scalar gradient in transverse direction($\partial\widetilde{Y_n}/\partial z$).

are normalised by their corresponding mean scalar gradient so that any positive trace represents counter-gradient transport and vice versa.

5.3.1.1 Molecules gradient or counter-gradient transport

Figure 5.38 shows the mean pressure gradient term. Plot (a) is the case when the reaction rates are maximum. It is observed that both hydrogen and oxygen have counter-gradient transport; however, at later stages all the three species show CGT but in a different location due to evolution of the mixing layer. Fluctuating pressure gradient shows an behaviour opposite to the mean value as it causes CGT but at the location about which the mean pressure gradient had shown GT. Also, as a result of mixing layer development and generation of smaller scales, both fluctuating pressure term as well as mean pressure term show more variations at t_{ND}=160. It is also observed that the magnitude of the fluctuating pressure term is almost two times larger than the magnitude of the mean pressure term and hence, it plays a more important role in shifting an overall trend toward occurrence of CGT or GT. Production by mean velocity gradient(Π_I) and production by mean scaler gradient (Π_{II}) have been presented in figures 5.40 and 5.41, respectively.Similar to what stated for the pressure terms, it can be observed that Π_{I_n} at time t_{ND}=160 is an order of magnitude larger than the corresponding value at t_{ND}=150.5. Π_{II_n} has not been normalised by the mean scalar gradient as the outcome will be the fluctuating velocity flux which is not relevant to the subject covered in this section. Therefore, the variation of Π_{II_n} will be a scaled version of the mean scalar gradient which was shown earlier in figure 5.34 with H_2O showing CGT at t_{ND}=150.5 and t_{ND}=160 whereas O_2 shows CGT only at later stages of the reaction process and H_2 shows GT during the process. Reaction-fluctuating velocity correlation term has also been plotted in figure 5.42(a,b). It is seen that while at earlier stages reaction term for oxygen has CGT across the mixing layer in the lower stream side, H_2 molecule only has GT. At final stage in the simulations, i.e. t_{ND}=160, both scalars show CGT at different locations but the trend of these changes for both species are always in the opposite direction. H_2O as the main product of reaction has counter-gradient behaviour only over a limited region across the mixing layer at both times. Due to reduction of the reaction rate value with time, the magnitude of this term experiences a drop in the magnitude from t_{ND}=150.5 to t_{ND}=160 for all species.

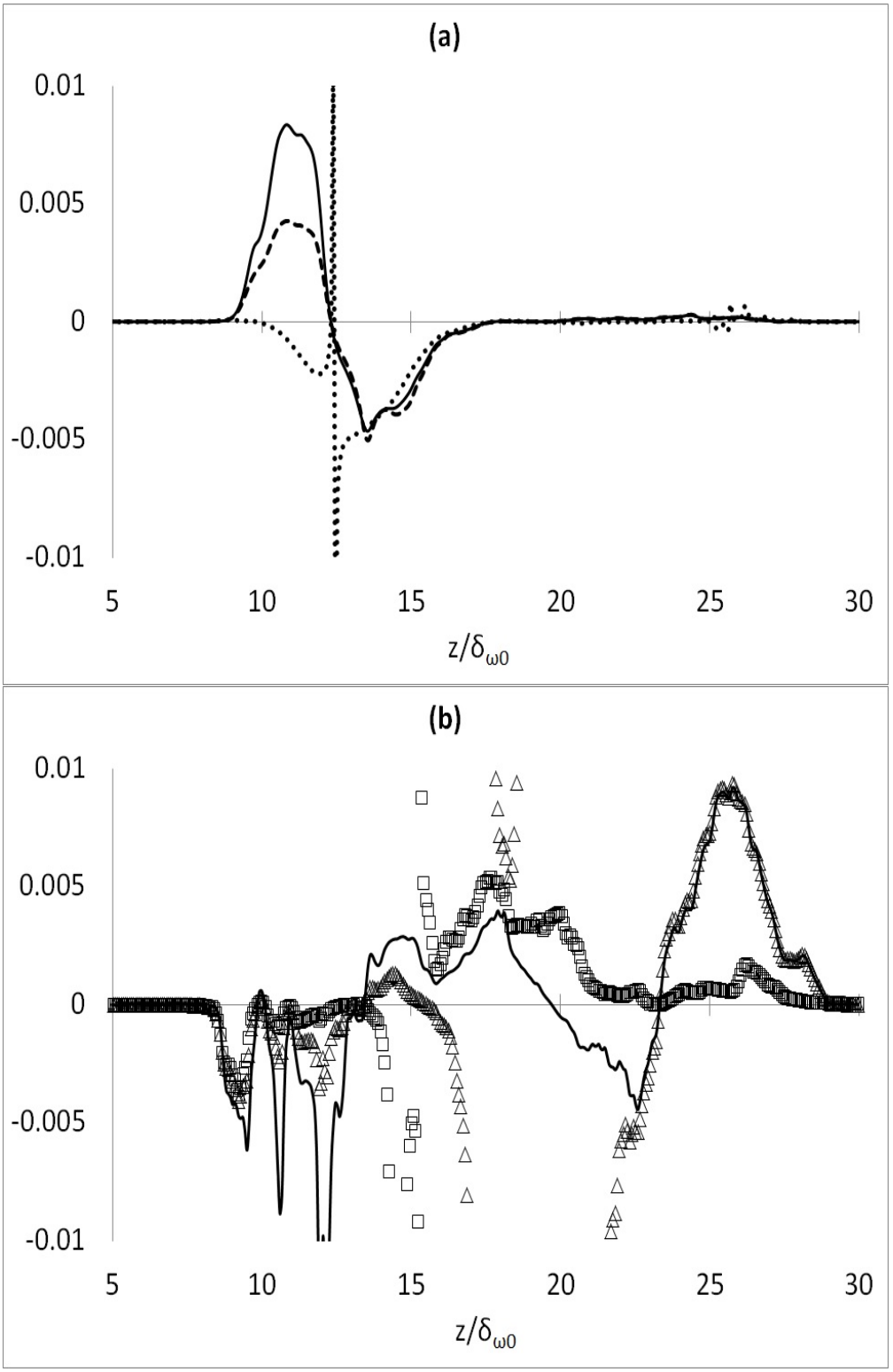

FIGURE 5.38: Mean pressure gradient term(Φ) for H_2, O_2 and H_2O in transverse direction at: (a) t_{ND}=150.5 and (b) t_{ND}=160. (———) Φ_{H_2}, (– – – and △) Φ_{O_2}, ($\cdots$ and □) Φ_{H_2O}. Each quantity is normalised by its corresponding mean scalar gradient in transverse direction($\partial\widetilde{Y_n}/\partial z$).

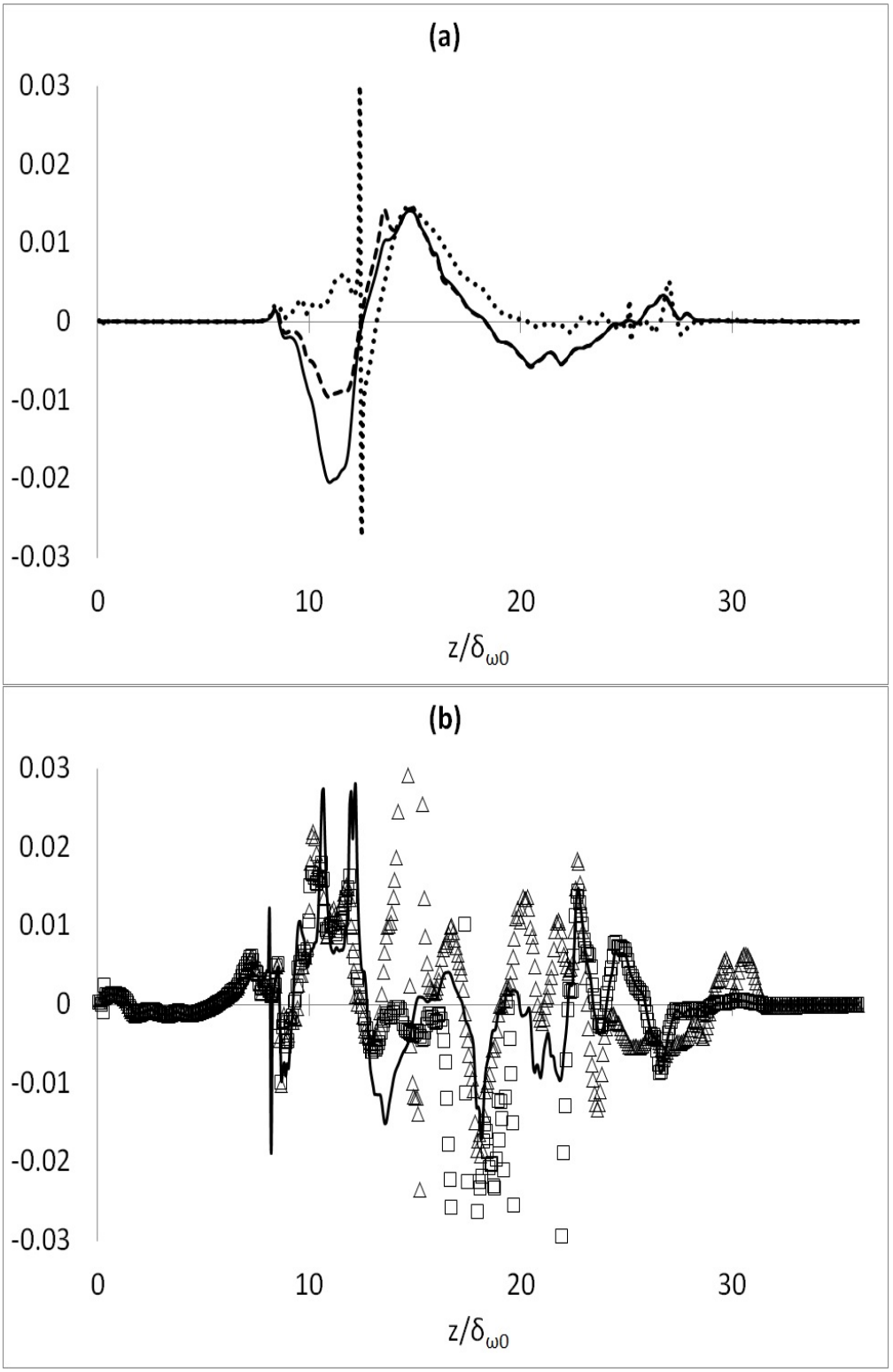

FIGURE 5.39: Fluctuating pressure gradient term(Ψ) for H_2, O_2 and H_2O in transverse direction at: (a) t_{ND}=150.5 and (b) t_{ND}=160. (———) Ψ_{H_2}, (– – – and △) Ψ_{O_2}, ($\cdots$ and □) Ψ_{H_2O}. Each quantity is normalised by its corresponding mean scalar gradient in transverse direction($\partial\widetilde{Y_n}/\partial z$).

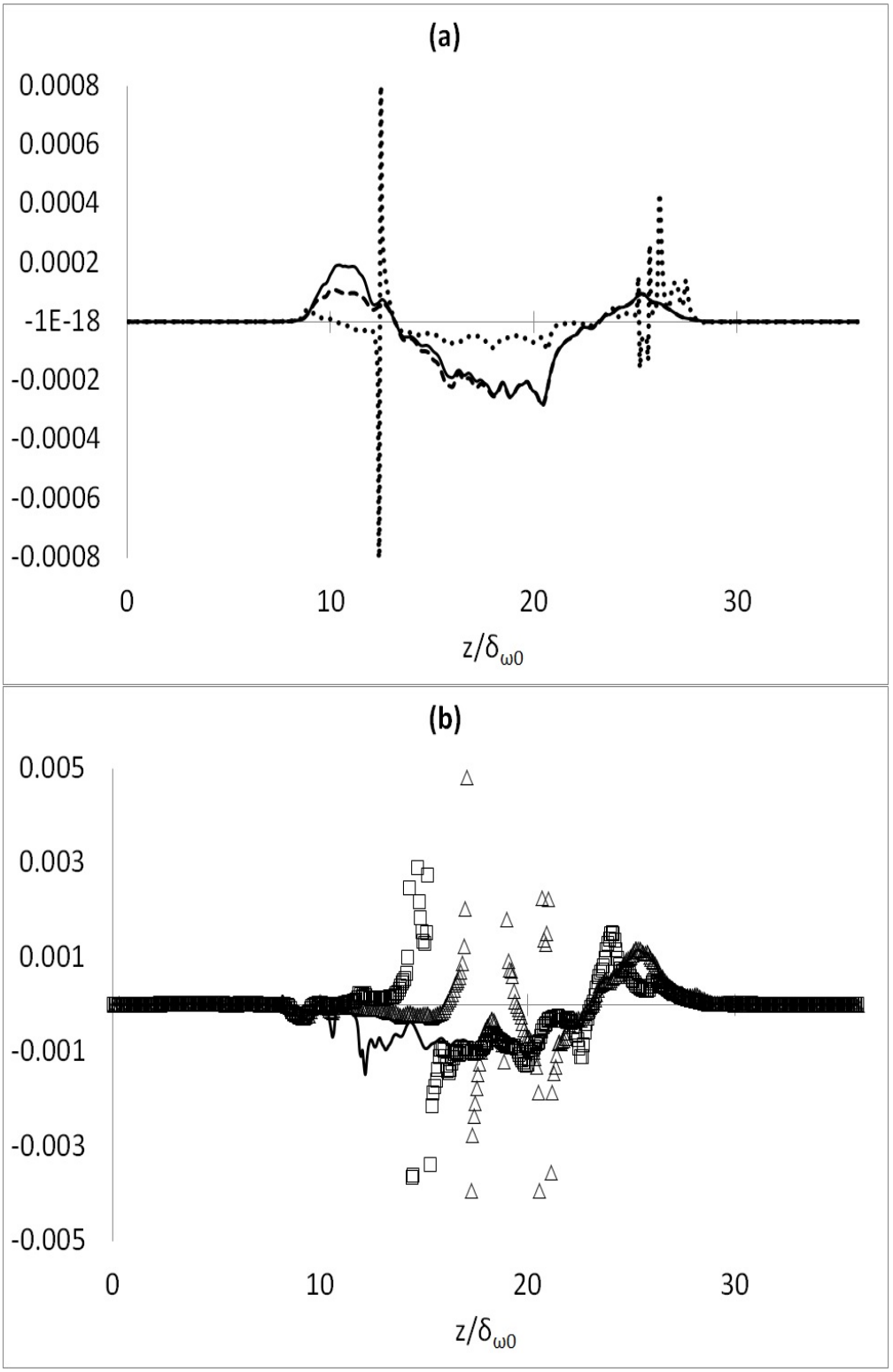

FIGURE 5.40: Production by mean velocity gradient term(Π_I) for H_2, O_2 and H_2O in transverse direction at: (a) t_{ND}=150.5 and (b) t_{ND}=160. (———) $\Pi_{I_{H_2}}$, (– – – and △) $\Pi_{I_{O_2}}$, (· · · · and □) $\Pi_{I_{H_2O}}$. To show the effects of the mean scalar gradient, Π_{I_n} has not been normalised.

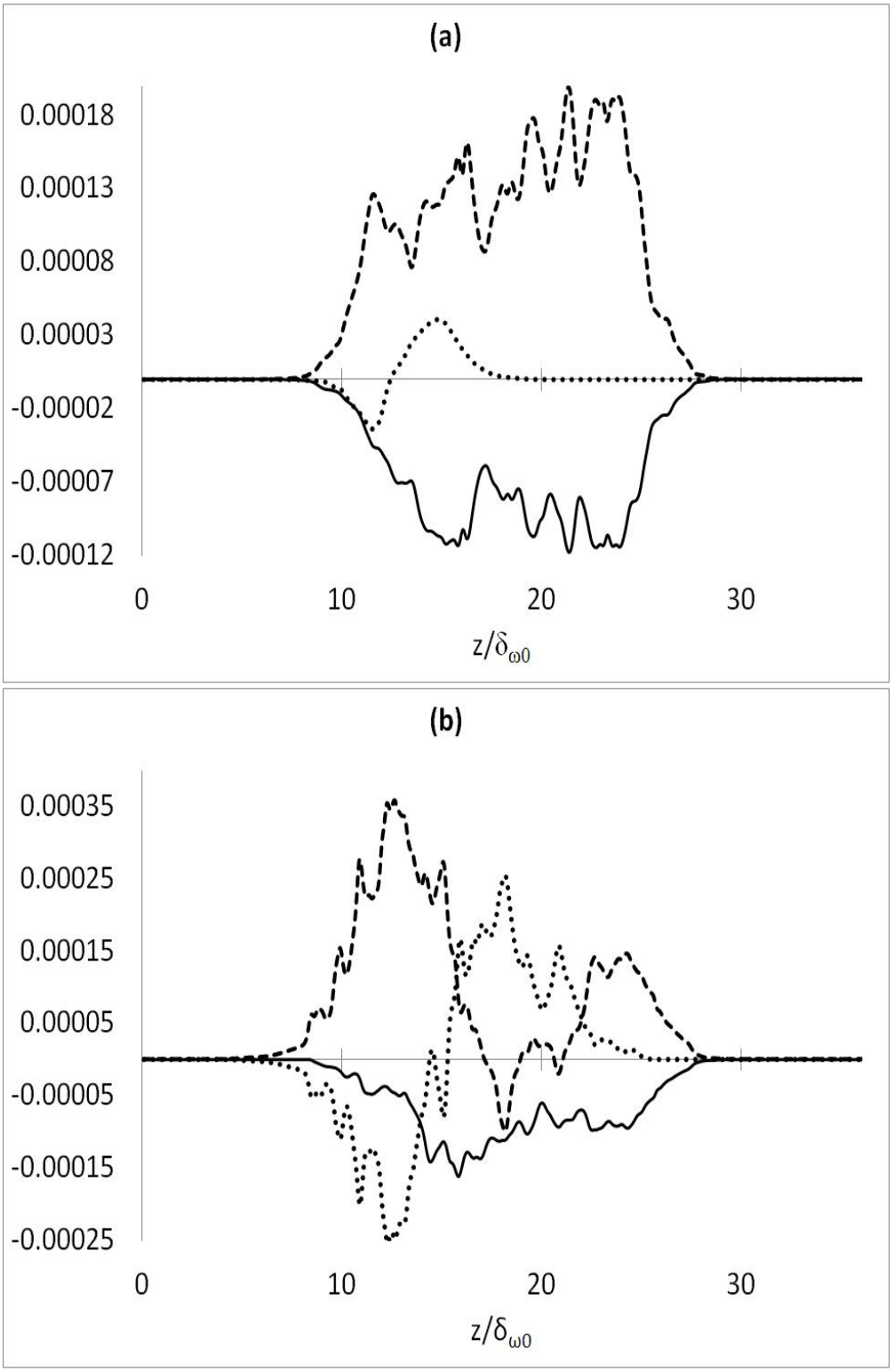

FIGURE 5.41: Production by mean scalar gradient term(Π_{II}) for H_2, O_2 and H_2O in transverse direction at: (a) t_{ND}=150.5 and (b) t_{ND}=160. (———) $\Pi_{II_{H_2}}$, (– – –) $\Pi_{II_{O_2}}$, ($\cdots$) $\Pi_{II_{H_2O}}$ - overlapping lines. To show the effects of the mean scalar gradient, Π_{II_n} has not been normalised.

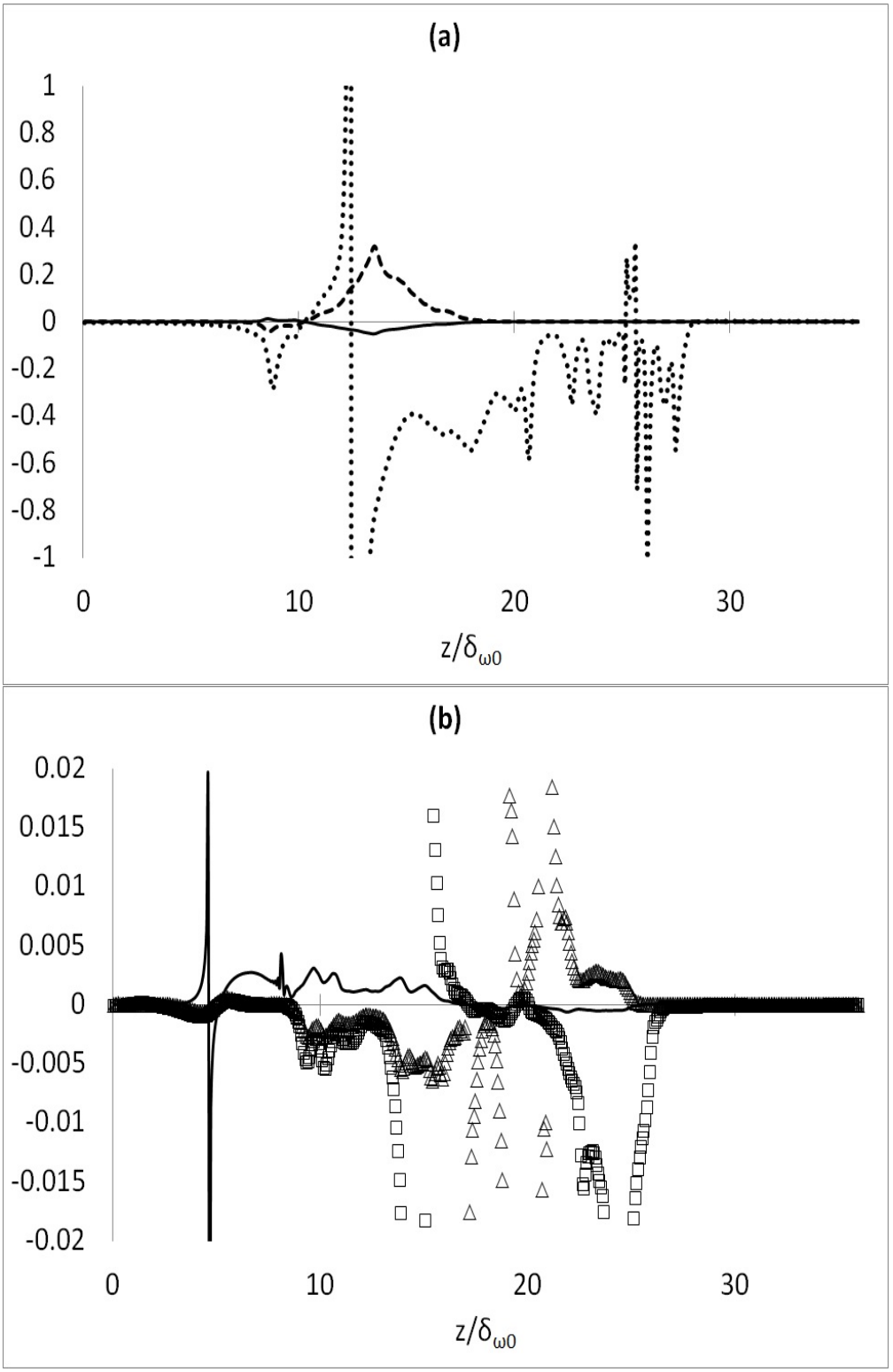

FIGURE 5.42: Reaction-fluctuating velocity correlation term(Ω) for H_2, O_2 and H_2O in transverse direction at: (a) t_{ND}=150.5 and (b) t_{ND}=160. (———) Ω_{H_2}, (– – – and △) Ω_{O_2}, ($\cdots$ and □) Ω_{H_2O}. Each quantity is normalised by its corresponding mean scalar gradient in transverse direction($\partial\widetilde{Y_n}/\partial z$).

5.3.1.2 Radicals gradient or counter-gradient transport

Following the same procedure presented for the molecules, budget analysis for the non-conservative terms in radicals scalar flux have also been studied. Mean pressure gradient term at t_{ND}=150.5 and t_{ND}=160 have been shown in figure 5.43. In plot(a), apart from a narrow region which shows CGT, all the radical species have GT across the mixing layer. At t_{ND}=160, however, CGT is observed at more locations although it is highly localised and unlike the trends for the molecules observed in previous section, CGT for radicals is limited to a few peaks rather than covering a region across the domain. Comparing mean pressure gradient for the radicals to its counterparts for molecules presented in previous section, it can be seen that the former is larger by a factor of about 5. The fluctuating pressure gradient for the radicals is presented in figure 5.44. It is observed that this term is larger than the mean pressure gradient by a factor of 4 to 5. In addition, comparing the fluctuating pressure gradient of radicals with molecules presented in previous section, it can be seen that the radicals have much larger fluctuations. As these terms are all normalised by the corresponding scalar mean mass fraction gradient, it can be concluded that in a mixture of different species, contribution of the radicals to shift the mixture toward the state of showing counter-gradient or gradient transport is more than the molecules. Production terms, however, are in the same order between radicals and molecules. Production by mean velocity gradient as well as production by mean scalar gradient for the radicals are shown in figures 5.45 and 5.46, respectively. Similar to the scenario explained for the molecules, Π_{I_n} at t_{ND}=150.5 shows CGT at lesser locations across the domain compared to later stages at t_{ND}=160. Also Π_{II_n} follows the same trend as in mean scalar gradient presented in figure 5.35 for radicals. Despite having pressure terms larger than pressure terms showed for the molecules, production terms of the radicals is smaller than that of the molecules. This originates from having smaller mass fraction in comparison with molecules and hence, having smaller mass fraction gradient and fluctuations than molecules. Reaction-fluctuating velocity correlation for radicals has been plotted in figure 5.47. At earlier phase of reaction, this quantity for the radicals is in the order of the corresponding term for the molecules(figure 5.42(a)). At t_{ND}=160, Ω_n for radicals is much larger than that of the molecules. This shows while the main reactants are being consumed and their rate of production or consumption has dramatically decreases, radicals still have got much higher reaction rate compared to the molecules although for the radicals, this rate is also decreasing monotonically with time.

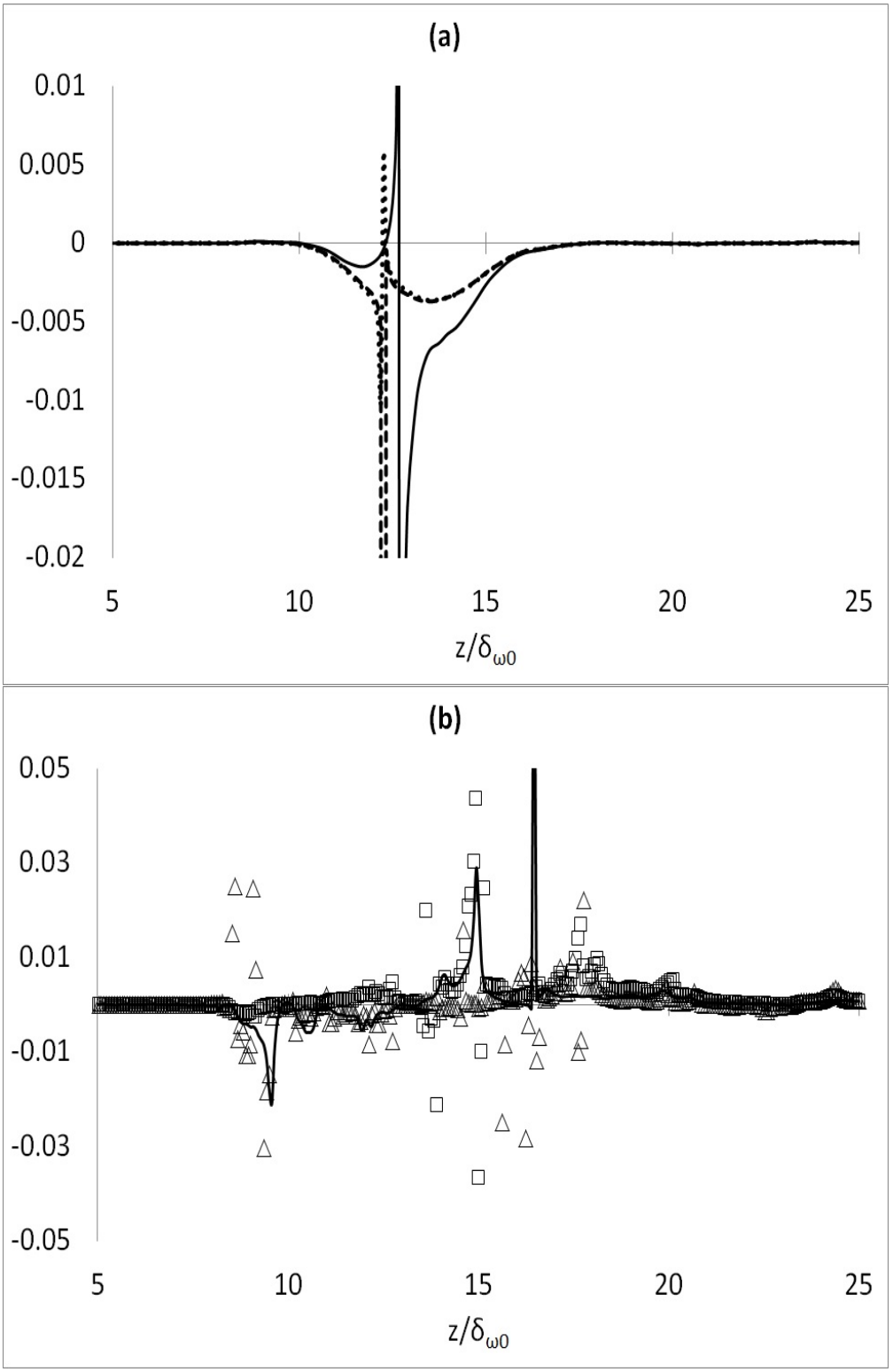

FIGURE 5.43: Mean pressure gradient term(Φ) for H, O and OH in transverse direction at: (a) t_{ND}=150.5 and (b) t_{ND}=160. (———) Φ_H, (– – – and △) Φ_O, ($\cdots$ and □) Φ_{OH}. Each quantity is normalised by its corresponding mean scalar gradient in transverse direction($\partial\widetilde{Y_n}/\partial z$).

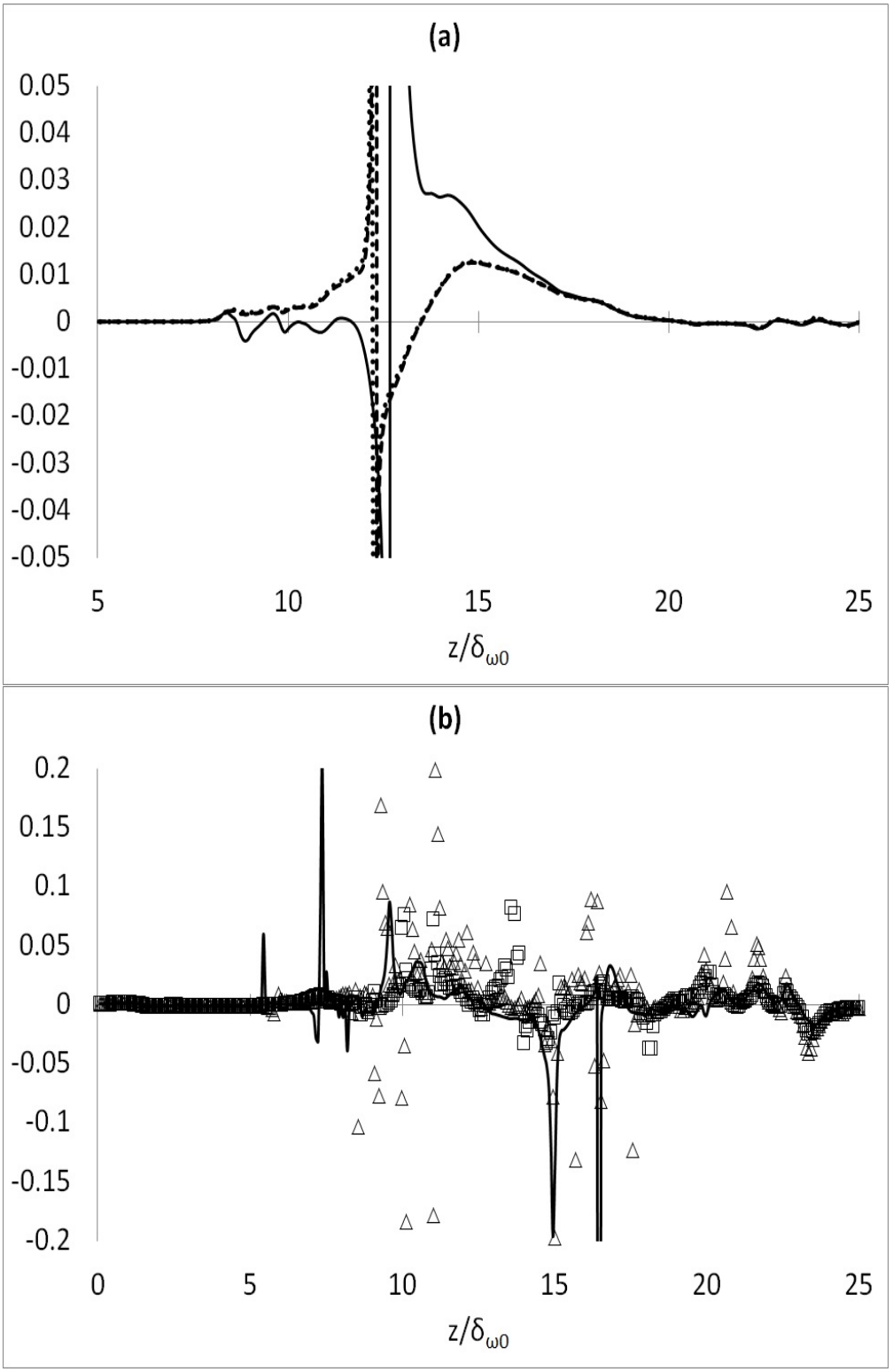

FIGURE 5.44: Fluctuating pressure gradient term(Ψ) for H, O and OH in transverse direction at: (a) t_{ND}=150.5 and (b) t_{ND}=160. (———) Ψ_H, (– – – and △) Ψ_O, ($\cdots$ and □) Ψ_{OH}. Each quantity is normalised by its corresponding mean scalar gradient in transverse direction($\partial\widetilde{Y_n}/\partial z$).

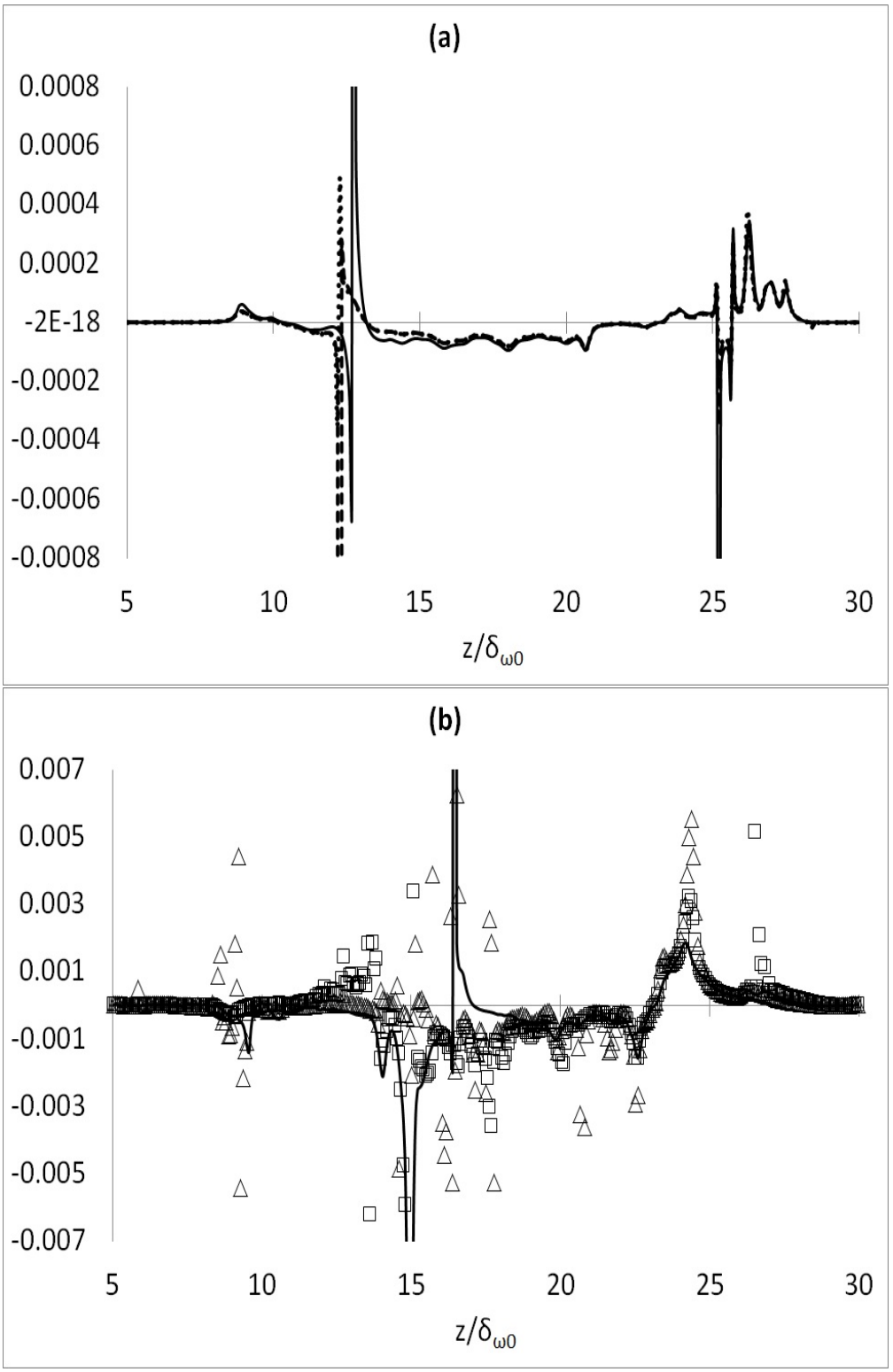

FIGURE 5.45: Production by mean velocity gradient term(Π_I) for H, O and OH in transverse direction at: (a) t_{ND}=150.5 and (b) t_{ND}=160. (———) Π_{I_H}, (– – – and △) Π_{I_O}, (· · · · and □) $\Pi_{I_{OH}}$. To show the effects of the mean scalar gradient, Π_{I_n} has not been normalised.

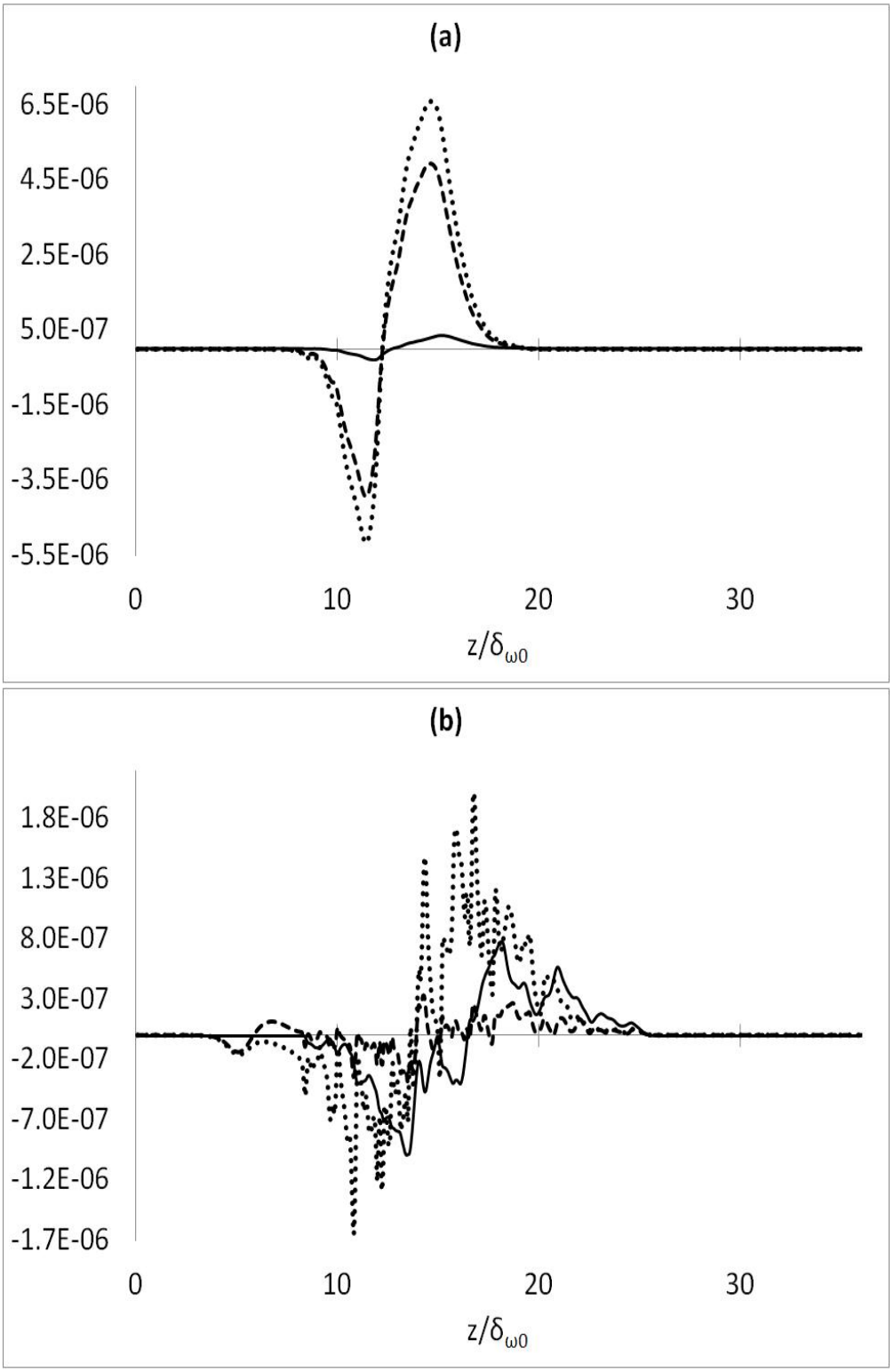

FIGURE 5.46: Production by mean scalar gradient term(Π_{II}) for H, O and OH in transverse direction at: (a) t_{ND}=150.5 and (b) t_{ND}=160. (———) Π_{II_H}, (– – –) Π_{II_O}, ($\cdot\cdot\cdot$) $\Pi_{II_{OH}}$ - overlapping lines. To show the effects of the mean scalar gradient, Π_{II_n} has not been normalised.

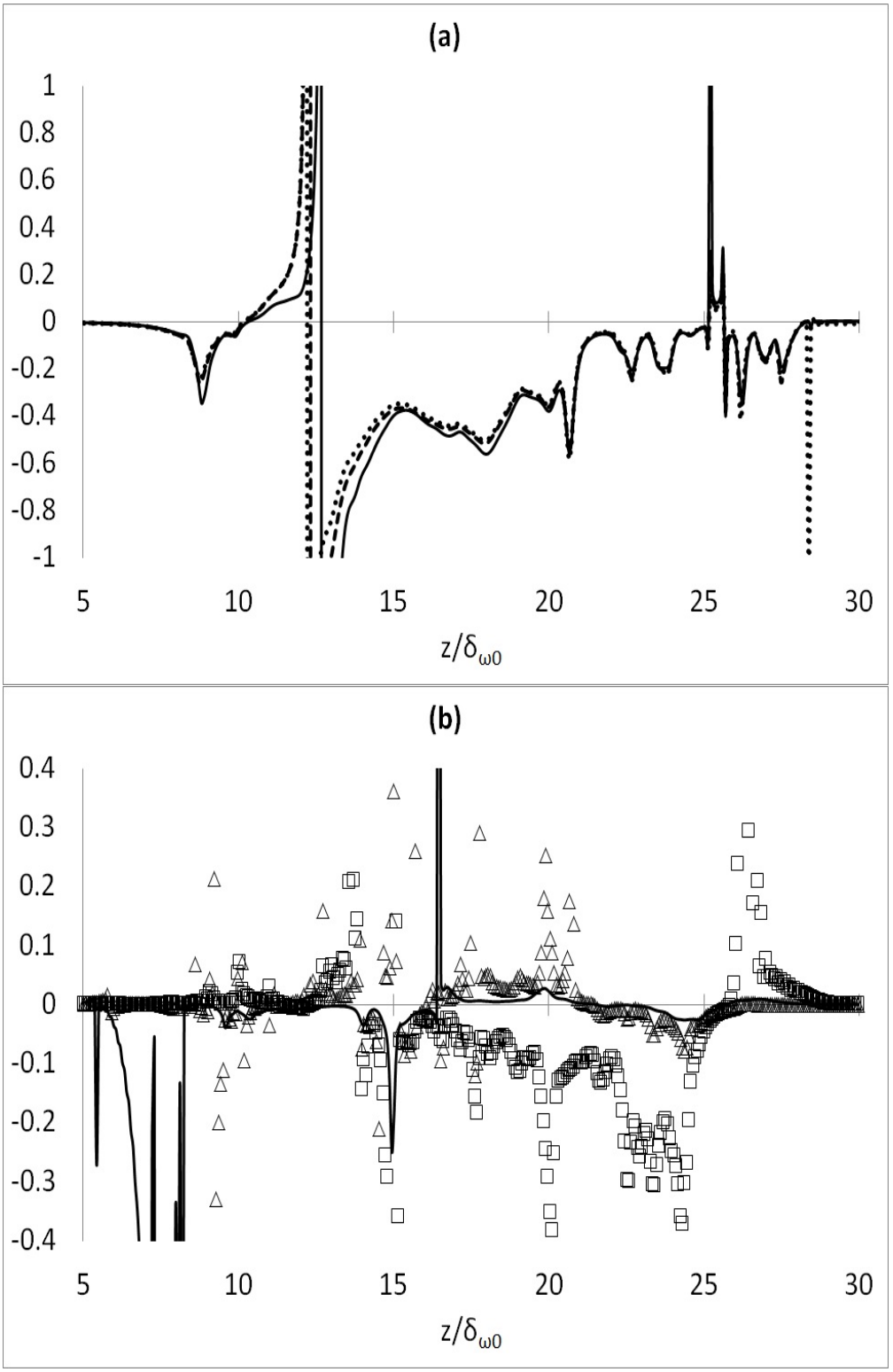

FIGURE 5.47: Reaction-fluctuating velocity correlation term(Ω) for H, O and OH in transverse direction at: (a) t_{ND}=150.5 and (b) t_{ND}=160. (———) Ω_H, (– – – and △) Ω_O, ($\cdot\cdot\cdot$ and □) Ω_{OH}. Each quantity is normalised by its corresponding mean scalar gradient in transverse direction($\partial\widetilde{Y_n}/\partial z$).

5.4 Quantification of differential diffusion in a reactive multi-species mixing layers

Based on the expression used in chapter 4(equation 4.7), DD in reactive case has been calculated to highlight the effects of each species on the differential diffusion in a mixture. Figure 5.48 shows this quantity for all nine species at t_{ND}=150.5. Molecules of H_2, O_2 and H_2O are shown in plot(a); H, O and OH radicals are presented in plot (b); and finally, the contribution of HO_2 and H_2O2 are shown in plot (c). The term DD is also plotted in all three plots in order to help in quantifying the contribution of individual species. In all three plots i.e. (a),(b) and (c), contribution of the products are almost zero because it is only the early period after start of the reaction and the mass fraction of such species is considerably smaller than that of the main reactants(H_2 and O_2). Therefore, the difference between κ_{H_2} and κ_{O_2} is the value of the DD. Only hydrogen radical shows contribution toward DD which has as shown in plot(b). At t_{ND}=160, the mass fraction of the products has been increased and therefore, it is expected that their contribution is also increased accordingly. However, there is only hydrogen radical which shows some degree of contribution with the values greater than the values shown in figure 5.48(b). Other radicals still do not show any evidence of contribution toward DD. Another point worths noting is that the extent of the variations of κ_n for the H_2 or O_2 increases with time. Initially it was only the lower part of the domain that was affected by such species fluctuations contributing toward DD whereas at t_{ND}=160, the oscillations of the κ_n has been extended toward the upper part of the computational domain in hydrogen side. Figure 5.50 is an illustration of the radical contribution into the DD which has been isolated from the effects of the molecules. Their value is at least, an order of magnitude smaller than the molecules contribution toward DD. Plot(a) shows the κ_n for radical at t_{ND}=150.5 and plot(b), shows the same but at t_{ND}=160. As seen in these two plots, κ_H and κ_O have the most contribution amongst other scalars. Also, their contribution has spread throughout the mixing layer with time. This is also a sign of the species diffusion into all parts of the domain and the progress of this phenomenon with time. In addition, as mass fraction of hydrogen oxygen radicals increases due to the reactions, their contribution in differential diffusion quantity also increases.

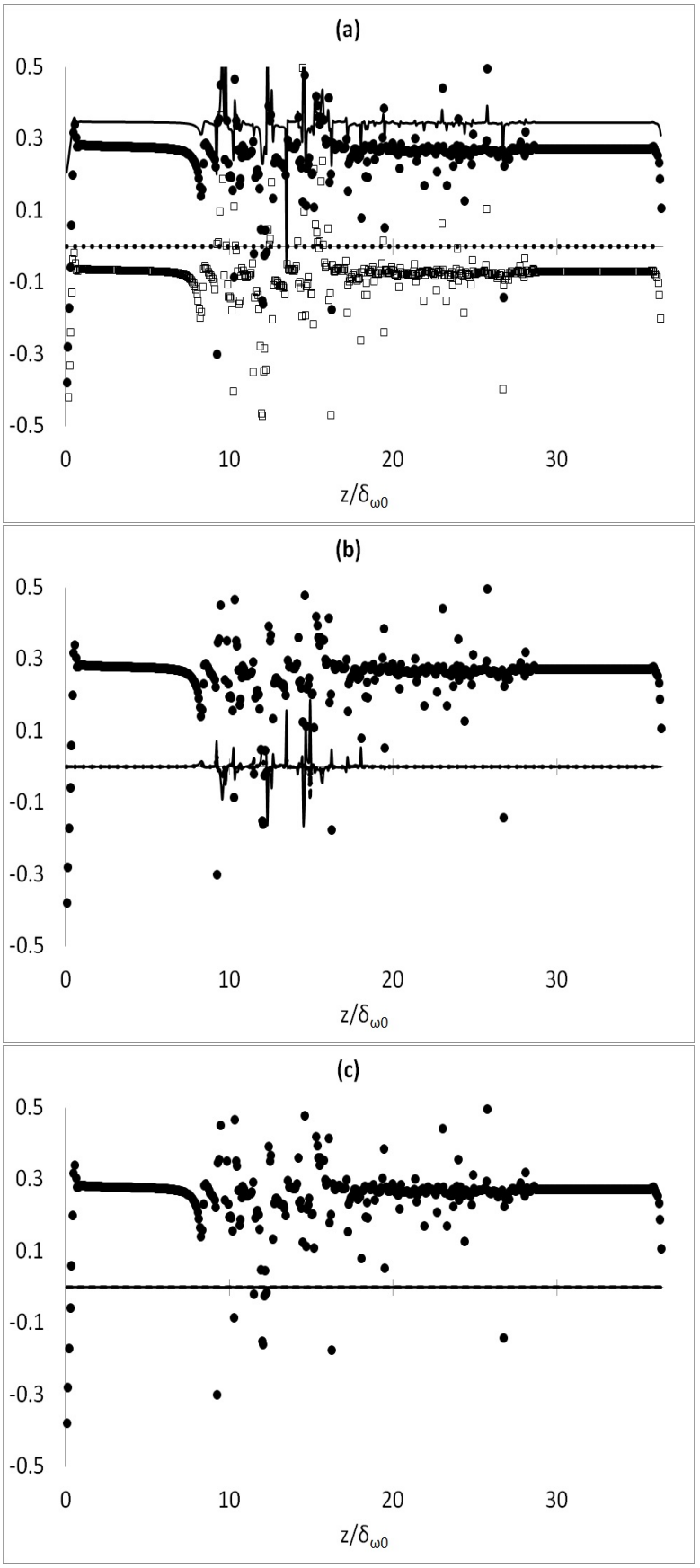

FIGURE 5.48: Differential diffusion(DD) and species contribution to DD at t_{ND}=150.5 in transverse direction. (a): (•) DD, (———) κ_{H_2}, (□) κ_{O_2}, (· · · ·) κ_{H_2O}. (b): (•) DD, (———) κ_H, (– – –) κ_O, (· · · ·) κ_{OH}. (c): (•) DD, (———) κ_{HO_2}, (– – –) $\kappa_{H_2O_2}$. Overlapping lines for radicals.

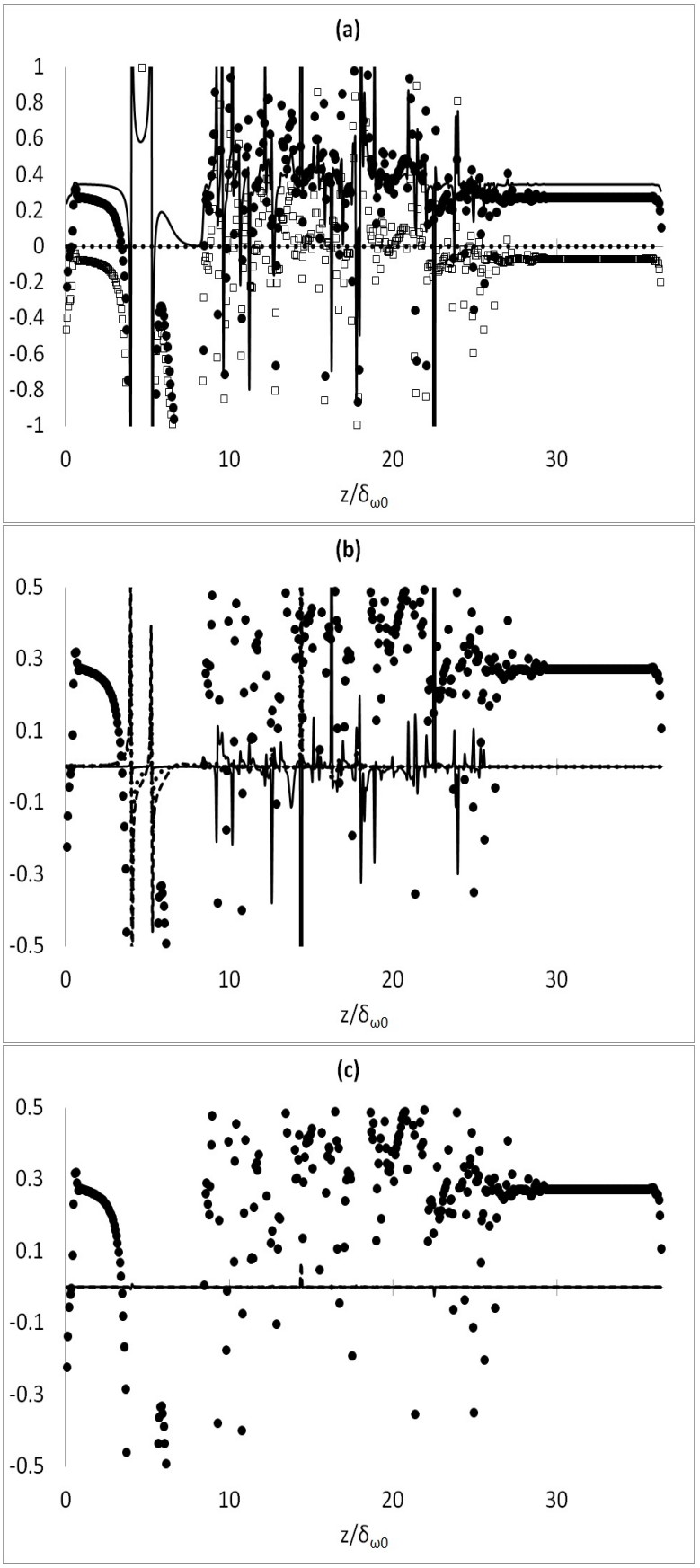

FIGURE 5.49: Differential diffusion(DD) and species contribution to DD at t_{ND}=160 in transverse direction. (a): (•) DD, (———) κ_{H_2}, (□) κ_{O_2}, (· · · ·) κ_{H_2O}. (b): (•) DD, (———) κ_H, (– – –) κ_O, (· · · ·) κ_{OH}. (c): (•) DD, (———) κ_{HO_2}, (– – –) $\kappa_{H_2O_2}$. Overlapping lines for radicals.

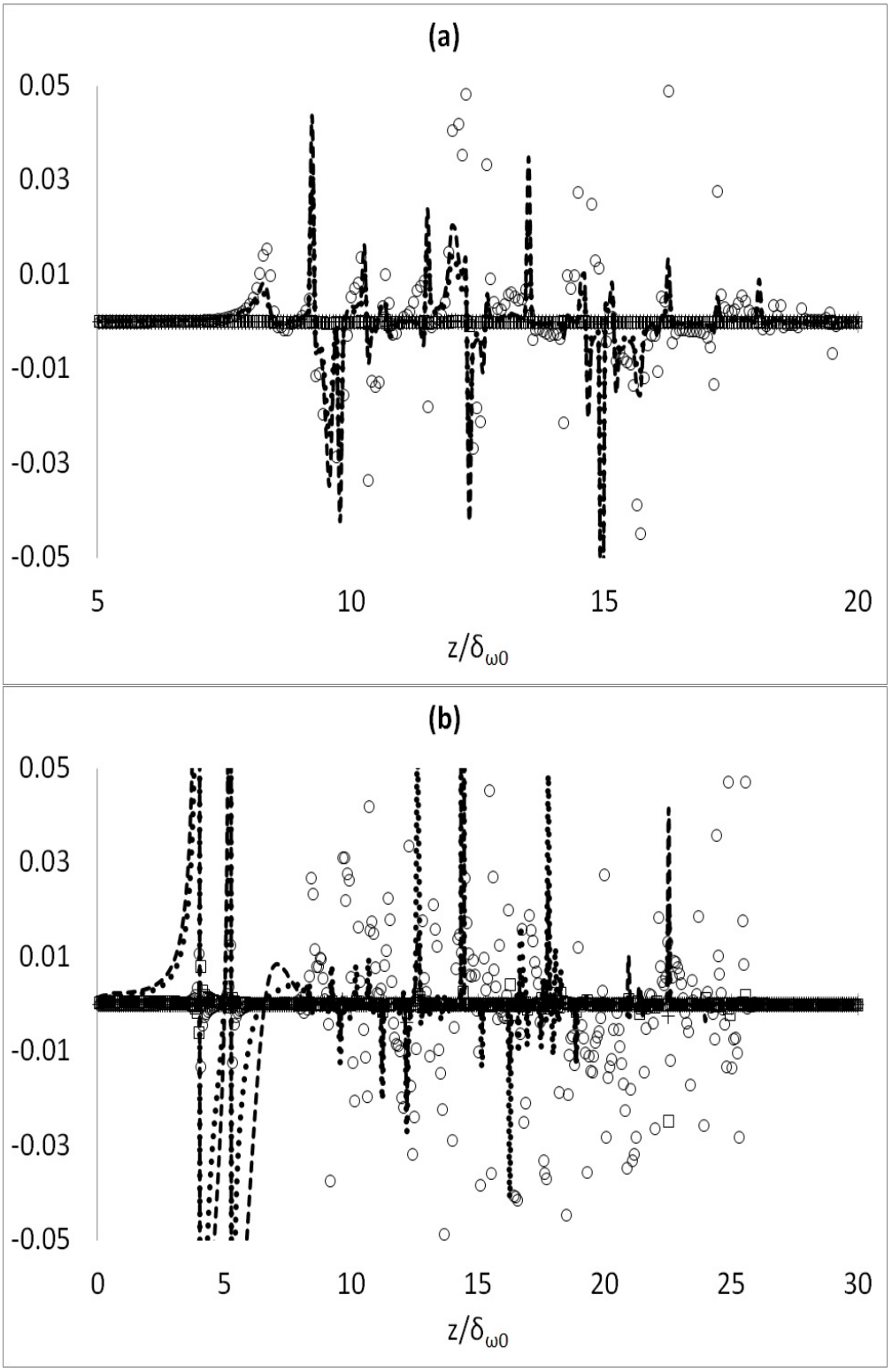

FIGURE 5.50: Comparison of species(radicals) contribution to DD at (a) t_{ND}=150.5 and (b) t_{ND}=160 in transverse direction. ($\circ$) κ_H, ($-\ -\ -$) κ_O, ($\cdot\cdot\cdot$) κ_{OH}, ($\square$) κ_{HO_2} and ($+$) $\kappa_{H_2O_2}$. Overlapping lines for HO_2 and H_2O_2 at both times.

5.5 Summary and Conclusions

Three-dimensional direct numerical simulation has been performed for diluted hydrogen and oxygen streams within the context of a temporally evolving shear layer. The initially non-premixed shear layer start to entrain until a finite-rate reaction mechanism is started which results in a multicomponent mixture. Five series of simulations have been performed. Three of them, comprises a smaller geometry. Setting up a small geometry was only because of the fact that for a new code under development, many tests are required to make sure all the equations have been implemented correctly and all parts of the code works fine and also the code returns resonable output. Considering loads of the trial and error which have to be done before a piece of programme becomes ready, it makes sense to do DNS on a smaller domain with a lesser number of grids in order to save time and reduce the elementary costs. Simulations are done for two cases by considering constant but different values for the species Lewis number for one case and unity Lewis number for the other case. To check the grid independency of, the third was set up according to the first case but with four times more grid points. Mixing layer development and mixture composition were tested. The results showed that the change in the species Lewis number will not affect the flow development and vortex structure. Although there are some differences in the maximum and minimum values, but the overall trend of the time rate of change of momentum thickness, vorticity thickness and spanwise or streamwise vorticity extrema are very close or at some stages overlapped between all cases. Vorticity contours also show a similar pattern which proves a very close stage of flow entrainment even after reaction. Species mass fraction were extracted at two different times during the simulation and it was shown that before reaction, the scalar distribution for all the cases is the same among the cases. however, reaction makes changes to the scalar field. The case with unity Lewis number under-predicts mass fraction distribution for some species and over-predicts for some other in comparison with the cases with real species Lewis number. The two cases with real Lewis number but different number of grid points, the changes are the same to be a proof for the grid independency of the simulations.

Simulations continued by setting up two other cases with larger geometry to help us have a better picture of the vorticity field and the species contours. One case with 86 million grids and real values for species Lewis number and one case, with 24 million grids and unity Lewis number were set up. Setting up a series of simulation with higher number of grid points shows the scalability of the numerical code and also having two different grid system and also larger domain size, will be a further proof for the simulations to be grid independent plus their reliability under different conditions. Analysis first started by looking at the evolution of the vorticity and momentum thickness as well as spanwise and streamwise vorticity extrema. Vorticity contours and snapshots of species

mass fraction also show the flow development and the extent to which Lewis number can affect the scalar field. Focus of the study for this part is one the transport equations for scalar flux and scalar variance. Despite the strategy taken in chapter 4 in comparing the results of binary-species mixing layer under different species diffusivity, the focus in this chapter has been on the scalars behaviour in the context of a multi-species mixing layer undergoing a finite-rate reaction mechanism (rather than an one-step global mechanism employed in chapter 4). To observe the interaction of the turbulent field and a multi-component scalar field, scalar variance as well as turbulent scalar flux transport equations have chosen to be analysed for individual species. In each transport equation, only those terms were selected whose integrals over a time period are not negligible or even identical to zero. Moreover, the results were presented for those species which have higher mass fraction value; these species were H_2, O_2 and H_2O molecules as well as H, O and OH radicals. DNS data were analysed at two different times: at the time when the reaction rates reach their extremum values(either positive which means the species is generated or negative which means the species is consumed) and at the time when simulations were ended(during which the flow and vorticity structure have been developed completely).

For the scalar variance production/destruction term, scalar dissipation term and also reaction-mass fraction correlation have been presented. It was shown that variance of the molecules increases with time whereas the radicals behave differently. While H radicals show a slight increase in the variance, the variance of the other two decreases which can be as a result of very low concentration of these species in the domain and the variations of the terms exist in the transport equation for which a budget analysis has been performed. While production/destruction term of the molecules show a lot of fluctuations due to turbulent field(i.e. at some locations they have positive values(production) whereas at some locations they have negative values(destruction)), radicals show a reduction in this term which is a sign for destruction rather than production. In contrast, their dissipation rate increases with time and so do the molecules. Higher dissipation rate will be the result of scalar mixing in the flow at molecular level which is affected by molecular and turbulent diffusion. That's why the variance of the radicals experience reduction over time. The correlation between the species reaction rate and mass fraction fluctuations shows a reduction over time since the reaction rate of each individual species reduces with time. Therefore, it can be seen that the scalar dissipation term will be a key component in transport of the scalar variance which is a measure of the scalar energy.

Budget analysis for turbulent scalar flux has been performed, too. It was shown that for the mean and fluctuating pressure gradient have opposite effects on the occurrence of CGT. Where the mean pressure promote CGT(GT), fluctuating pressure term inhibit CGT(GT). This was observed for molecules and radicals. Also, it was shown that the

gradient of pressure terms for radicals is greater than those for molecules. Such difference is originated from the higher level of fluctuations for the mass fraction of the radicals compared to the molecules which shows the unstable condition of the radicals versus more stable condition of the molecules under turbulent conditions. However, pressure terms for radicals are highly localised with sharp variations around a narrow region across the domain in comparison with those for molecules. This is also a result of highly fluctuating nature of these radicals. As for the production terms, in contrary with the relation between the pressure terms for radicals and molecules, it is observed that although the production by mean velocity gradients are of the same order for radicals and molecules, production due to mean scalar gradient for the molecules are much larger that that of the radicals. Therefore, it can be concluded that although for the molecules both pressure terms and production terms contribute toward the gradient or counter-gradient transport, for the radicals, this is the pressure term(out of which fluctuating part is more prominent) which makes the most contribution in the CGT or GT of such species rather than the production terms. Correlation between the reaction rate and fluctuating velocity component for the radicals as well as the molecules are of the same order of importance at early stages of the combustion. However, at later stages in the reactive flow, this term for the molecules will drop an order of magnitude as their rte of production or consumption considerably decreases but for the radicals, it is still play as important role as it has at earlier times but with a lesser degree. This shows that the radicals are still being produced or consumed at a rate whose contribution in CGT or GT can still be considered as important.

Chapter 6

Future work

There is no end for the objectives sought in DNS studies of turbulent flows. In this thesis, it was tried to highlight the effects of species Lewis number on the turbulent flow. Also, multi-species simulations showed the behaviour of individual scalars in mixing layer context. The 3D code which has been developed for this purpose considers differential diffusion and mixture properties in order to solve the system of compressible multi-species Navier-Stokes equations. The first step in improvement of this task is to incorporate a more complex diffusion coefficient formulation based on the binary-diffusion coefficient for the interacting species rather than using a constant Lewis number which is indeed, not supposed to be constant in a reactive flow.

In addition, other chemistry mechanisms worth to be incorporated especially those which take into consideration the effects of Nitrogen molecule in order to study the NOx formation under different conditions. Also, mechanisms which contain hydrocarbon mixed with hydrogen will provide an interesting database for analysis of such complex reaction mechanisms which has potential to be used extensively in practical applications. However, performing such tasks are far more difficult than the hydrogen-oxygen chemistry since there will be too many time scales induced by the wide spectra of the reactions and individual species.

Other tasks which can be performed, is to use DNS data from a multi-step multi-species reaction mechanism to validate the combustion models such as CMC, PDF and FGM models. These models are widely being used but there are still gaps which are needed to be filled. DNS with realistic chemistry and species transport mechanisms, i.e. real species diffusivity together with finite rate reactions whose rates are affected by the temperature, pressure and species concentration, would become a benchmark for these models to be assessed under conditions of premixed or non-premixed combustion.

Appendix A

Boundary Treatment Formulation

As explained in section 2.4, treatment of boundaries in this work is based on dealing with characteristic waves travelling in and out of the computational domain. In this appendix, the method by which these waves are computed and treated, are explained and corresponding equations have been derived. The boundary condition formulation has been obtained for a three-dimensional equations containing a scalar. The derivation has been accomplished for only one direction (x-direction in here is assumed to be non-reflecting boundary) as other directions can simply be done similar to this direction. For two or multi-species calculations, dimension of matrices increase with the number of species which are involved in the process.
Let's consider the governing equations in conservation form as follows:

$$\frac{\partial Q}{\partial t} + \frac{\partial F}{\partial x} = R.H.S \tag{A.1}$$

where Q is the solution vector, F is the flux vector and $R.H.S$ is the flux terms in other directions as well as source terms which have no derivatives in respect of any directions:

$$Q = \begin{bmatrix} \rho \\ \rho u \\ \rho v \\ \rho w \\ E_T \\ \rho Y_f \end{bmatrix} \qquad F = \begin{bmatrix} \rho u \\ \rho u^2 + p \\ \rho uv \\ \rho uw \\ (E_T + p)u \\ \rho u Y_f \end{bmatrix} \tag{A.2}$$

Defining vector of primitive variables U as follows:

$$U = \begin{bmatrix} \rho \\ u \\ v \\ w \\ d \\ Y_f \end{bmatrix} \tag{A.3}$$

with $d = p\rho^{-\gamma}$, so the total energy, E_T can be written as:

$$E_T = \frac{p}{\gamma - 1} + \frac{1}{2}\rho(u^2 + v^2 + w^2) = \frac{d\rho^{\gamma}}{\gamma - 1} + \frac{1}{2}\rho(u^2 + v^2 + w^2) \tag{A.4}$$

Rearranging governing equations in terms of primitive variables will result in:

$$\frac{\partial Q}{\partial U}\frac{\partial U}{\partial t} + \frac{\partial F}{\partial U}\frac{\partial U}{\partial x} = R.H.S \tag{A.5}$$

or:

$$\frac{\partial U}{\partial t} + \frac{\partial U}{\partial Q}\frac{\partial F}{\partial U}\frac{\partial U}{\partial x} = \frac{\partial U}{\partial Q}R.H.S \tag{A.6}$$

Let $A = \frac{\partial U}{\partial Q}\frac{\partial F}{\partial U}$ and $R = \frac{\partial Q}{\partial U}$, so the equation(A.6) can be written as follows:

$$\frac{\partial U}{\partial t} + A\frac{\partial U}{\partial x} = A.(R.H.S) \tag{A.7}$$

where $A = R^{-1}\frac{\partial F}{\partial U}$. The eigenvalues of A will give the characteristic waves. To form matrix A, following derivations need to be done:

$$R = \frac{\partial Q}{\partial U}\begin{bmatrix} 1 & 0 & 0 & 0 & 0 & 0 \\ u & \rho & 0 & 0 & 0 & 0 \\ v & 0 & \rho & 0 & 0 & 0 \\ w & 0 & 0 & \rho & 0 & 0 \\ k & \rho u & \rho v & \rho w & \frac{\rho^{\gamma}}{\gamma - 1} & 0 \\ Y_f & 0 & 0 & 0 & 0 & \rho \end{bmatrix} \tag{A.8}$$

$$\frac{\partial F}{\partial U} = \begin{bmatrix} u & \rho & 0 & 0 & 0 & 0 \\ u^2 + d\gamma\rho^{\gamma-1} & 2\rho u & 0 & 0 & \rho^{\gamma} & 0 \\ uv & \rho v & \rho u & 0 & 0 & 0 \\ uw & \rho w & 0 & \rho u & 0 & 0 \\ m & n & \rho uv & \rho uw & \frac{\gamma\rho^{\gamma}u}{\gamma - 1} & 0 \\ uY_f & \rho Y_f & 0 & 0 & 0 & \rho u \end{bmatrix} \tag{A.9}$$

with $k = \frac{\partial E_T}{\partial \rho} = \frac{\gamma d \rho^\gamma}{\gamma - 1} + \frac{1}{2}(u^2+v^2+w^2)$, $m = \frac{\partial (E_T+p)u}{\partial \rho} = \left[\frac{\gamma^2 d \rho^{\gamma-1}}{\gamma-1} + \frac{1}{2}(u^2+v^2+w^2)\right] u$, and $n = \frac{\partial (E_T+p)u}{\partial u} = \frac{\gamma d \rho^\gamma}{\gamma-1} + \frac{\rho}{2}(3u^2+v^2+w^2)$.
Inverse of matrix R is then need to be calculated. R^{-1} will become:

$$R^{-1} = \begin{bmatrix} 1 & 0 & 0 & 0 & 0 & 0 \\ \frac{-u}{\rho} & \frac{1}{\rho} & 0 & 0 & 0 & 0 \\ \frac{-v}{\rho} & 0 & \frac{1}{\rho} & 0 & 0 & 0 \\ \frac{-w}{\rho} & 0 & 0 & \frac{1}{\rho} & 0 & 0 \\ g & -\frac{\gamma-1}{\rho^\gamma}u & -\frac{\gamma-1}{\rho^\gamma}v & -\frac{\gamma-1}{\rho^\gamma}w & \frac{\gamma-1}{\rho^\gamma} & 0 \\ -\frac{Y_f}{\rho} & 0 & 0 & 0 & 0 & \frac{1}{\rho} \end{bmatrix} \tag{A.10}$$

in which $g = \frac{\gamma-1}{\rho^\gamma}\left[-\frac{\gamma d \rho^{\gamma-1}}{\gamma-1} + \frac{1}{2}(u^2+v^2+w^2)\right]$. Matrix A is then takes the form of[1]:

$$A = R^{-1}\frac{\partial F}{\partial U} = \begin{bmatrix} u & \rho & 0 & 0 & 0 & 0 \\ d\gamma\rho^{\gamma-2} & u & 0 & 0 & \rho^{\gamma-1} & 0 \\ 0 & 0 & u & 0 & 0 & 0 \\ 0 & 0 & 0 & u & 0 & 0 \\ 0 & 0 & 0 & 0 & u & 0 \\ 0 & 0 & 0 & 0 & 0 & u \end{bmatrix} = \begin{bmatrix} u & \rho & 0 & 0 & 0 & 0 \\ \frac{c^2}{\rho} & u & 0 & 0 & \rho^{\gamma-1} & 0 \\ 0 & 0 & u & 0 & 0 & 0 \\ 0 & 0 & 0 & u & 0 & 0 \\ 0 & 0 & 0 & 0 & u & 0 \\ 0 & 0 & 0 & 0 & 0 & u \end{bmatrix} \tag{A.11}$$

To find the eigenvalues of A, λ_i, which are velocities of characteristic waves, matrix $[A - \lambda I]$ must be generated in which I is the unit matrix. Setting determinant of $[A - \lambda I]$ to zero, eigenvalues are computed as follows:

$$\lambda_1 = u - c \qquad \lambda_2 = \lambda_3 = \lambda_4 = u \qquad \lambda_5 = u + c \qquad \lambda_6 = u \tag{A.12}$$

Hence right eigenvectors of A may be written:

$$r1 = \begin{bmatrix} \frac{1}{2c^2} \\ -\frac{1}{2\rho c} \\ 0 \\ 0 \\ 0 \\ 0 \end{bmatrix} \quad r2 = \begin{bmatrix} 0 \\ 0 \\ 1 \\ 0 \\ 0 \\ 0 \end{bmatrix} \quad r3 = \begin{bmatrix} -\frac{1}{c^2} \\ 0 \\ 0 \\ 0 \\ \rho^{-\gamma} \\ 0 \end{bmatrix} \quad r4 = \begin{bmatrix} 0 \\ 0 \\ 0 \\ 1 \\ 0 \\ 0 \end{bmatrix} \quad r5 = \begin{bmatrix} \frac{1}{2c^2} \\ \frac{1}{2\rho c} \\ 0 \\ 0 \\ 0 \\ 0 \end{bmatrix} \quad r6 = \begin{bmatrix} 0 \\ 0 \\ 0 \\ 0 \\ 0 \\ 1 \end{bmatrix} \tag{A.13}$$

A diagonalizing similarity transformation need to be generated for A so that $TAT^{-1} = \Lambda$, and therefore $A = T^{-1}\Lambda T$. So, matrix T^{-1} to be formed so that its columns are right

[1] $d\gamma\rho^{\gamma-2} = \frac{d\gamma\rho^\gamma}{\rho^2} = \frac{\gamma p}{\rho^2} = \frac{c^2}{\rho}$. Note that for multi-species calculations, species mass fractions must also be considered as pressure will become: $p = \frac{\rho T}{\gamma M_a^2}(\sum_{n=1}^{N_s} \frac{Y_n}{W_n})$; so they affect the pressure and according to relation above, the speed of sound.

eigenvectors of A:

$$T^{-1} = \begin{bmatrix} \frac{1}{2c^2} & 0 & -\frac{1}{c^2} & 0 & \frac{1}{2c^2} & 0 \\ -\frac{1}{2\rho c} & 0 & 0 & 0 & \frac{1}{2\rho c} & 0 \\ 0 & 1 & 0 & 0 & 0 & 0 \\ 0 & 0 & 0 & 1 & 0 & 0 \\ 0 & 0 & \rho^{-\gamma} & 0 & 0 & 0 \\ 0 & 0 & 0 & 0 & 0 & 1 \end{bmatrix} \tag{A.14}$$

and consequently matrices T and Λ will become:

$$T = \begin{bmatrix} c^2 & -\rho c & 0 & 0 & \rho^{\gamma} & 0 \\ 0 & 0 & 1 & 0 & 0 & 0 \\ 0 & 0 & 0 & 0 & \rho^{\gamma} & 0 \\ 0 & 0 & 0 & 1 & 0 & 0 \\ c^2 & \rho c & 0 & 0 & \rho^{\gamma} & 0 \\ 0 & 0 & 0 & 0 & 0 & 1 \end{bmatrix} \qquad \Lambda = \begin{bmatrix} u-c & 0 & 0 & 0 & 0 & 0 \\ 0 & u & 0 & 0 & 0 & 0 \\ 0 & 0 & u & 0 & 0 & 0 \\ 0 & 0 & 0 & u & 0 & 0 \\ 0 & 0 & 0 & 0 & u+c & 0 \\ 0 & 0 & 0 & 0 & 0 & u \end{bmatrix} \tag{A.15}$$

Now to find a formulation for characteristic waves amplitudes, equation(A.6) is multiplied by $R = \frac{\partial Q}{\partial U}$ to generate the original conservation form of the governing equations. So equation(A.6) can be written in the form of:

$$\frac{\partial Q}{\partial t} + \frac{\partial Q}{\partial U}\frac{\partial U}{\partial Q}\frac{\partial F}{\partial U}\frac{\partial U}{\partial x} = R.H.S \tag{A.16}$$

Rewriting the flux term(second term) of equation(A.16) results in:

$$\frac{\partial F}{\partial x} = RA\frac{\partial U}{\partial x} \tag{A.17}$$

Pressure is more easily found computationally than the the quantity d in term $\frac{\partial U}{\partial x}$; therefore by decomposition of term $\frac{\partial U}{\partial x}$ into two terms and replacing A with $T^{-1}\Lambda T$, equation (A.17) is converted to the form:

$$\frac{\partial F}{\partial x} = RT^{-1}\Lambda TM\frac{\partial V}{\partial x} \tag{A.18}$$

in which:

$$V = \begin{bmatrix} \rho \\ u \\ v \\ w \\ p \\ Y_f \end{bmatrix} \qquad M = \frac{\partial U}{\partial V} = \begin{bmatrix} 1 & 0 & 0 & 0 & 0 & 0 \\ 0 & 1 & 0 & 0 & 0 & 0 \\ 0 & 0 & 1 & 0 & 0 & 0 \\ 0 & 0 & 0 & 1 & 0 & 0 \\ -\gamma p\rho^{-(\gamma+1)} & 0 & 0 & 0 & \rho^{-\gamma} & 0 \\ 0 & 0 & 0 & 0 & 0 & 1 \end{bmatrix} \tag{A.19}$$

The outcome of multiplication of the last four terms in equation (A.18) will be the amplitude of characteristic waves that is the aim of this section [2]:

$$\Lambda.T.M.\frac{\partial V}{\partial x} = \begin{bmatrix} (u-c)(\frac{\partial p}{\partial x} - \rho c\frac{\partial u}{\partial x}) \\ u\frac{\partial v}{\partial x} \\ u(\frac{\partial p}{\partial x} - c^2\frac{\partial \rho}{\partial x}) \\ u\frac{\partial w}{\partial x} \\ (u+c)(\frac{\partial p}{\partial x} + \rho c\frac{\partial u}{\partial x}) \\ u\frac{\partial Y_f}{\partial x} \end{bmatrix} = \begin{bmatrix} \ell_1 \\ \ell_3 \\ -\ell_2 \\ \ell_4 \\ \ell_5 \\ \ell_6 \end{bmatrix} \tag{A.20}$$

which have been appeared in section(2.4). Evaluation on these wave amplitudes to be done in here, where a wave is coming into the domain (e.g. at the upper boundary, a negative value for ℓ_i's represents an incoming wave), it is zeroed whereas outgoing waves at the boundaries, just leave the computational domain without any modification.
For multi-component system of equations considering the mixture properties, the reader is referred to the detailed description published by Pakdee and Mahalingam[75].

[2] Arrangement of ℓ_i's in matrix are in accordance with the computer code used in this work. One can set the ℓ_i's in their numerical order but corresponding rows in matrices of other variables (i.e. T^{-1} and R) must also be arranged accordingly.

Appendix B

Expansion of the governing equations

B.1 Expanded form of the governing equations used in chapter 2

Expanded version of governing equations in three directions will get the form of:

$$\frac{\partial \rho}{\partial t} = -\frac{\partial(\rho u)}{\partial x} - \frac{\partial(\rho v)}{\partial y} - \frac{\partial(\rho w)}{\partial z} \tag{B.1}$$

$$\frac{\partial(\rho u)}{\partial t} = -\frac{\partial(\rho uu + p - \tau_{xx})}{\partial x} - \frac{\partial(\rho uv - \tau_{xy})}{\partial y} - \frac{\partial(\rho uw - \tau_{xz})}{\partial z} \tag{B.2}$$

$$\frac{\partial(\rho v)}{\partial t} = -\frac{\partial(\rho uv - \tau_{yx})}{\partial x} - \frac{\partial(\rho vv + p - \tau_{yy})}{\partial y} - \frac{\partial(\rho vw - \tau_{yz})}{\partial z} \tag{B.3}$$

$$\frac{\partial(\rho w)}{\partial t} = -\frac{\partial(\rho uw - \tau_{zx})}{\partial x} - \frac{\partial(\rho vw - \tau_{zy})}{\partial y} - \frac{\partial(\rho ww + p - \tau_{zz})}{\partial z} \tag{B.4}$$

$$\begin{aligned} \frac{\partial E_T}{\partial t} = &-\frac{\partial[(E_T + p)u]}{\partial x} - \frac{\partial q_x}{\partial x} + \frac{\partial(u\tau_{xx} + v\tau_{xy} + w\tau_{xz})}{\partial x} \\ &-\frac{\partial[(E_T + p)v]}{\partial y} - \frac{\partial q_y}{\partial y} + \frac{\partial(u\tau_{yx} + v\tau_{yy} + w\tau_{yz})}{\partial y} \\ &-\frac{\partial[(E_T + p)w]}{\partial z} - \frac{\partial q_z}{\partial z} + \frac{\partial(u\tau_{zx} + v\tau_{zy} + w\tau_{zz})}{\partial z} \\ &+ \sum_{n=1}^{N_s} \Delta h^o_{f_n} \omega_n \end{aligned} \tag{B.5}$$

with the total energy, stress terms and the heat flux terms as follows:

$$E_T = \rho(e + \frac{1}{2}uu + \frac{1}{2}vv + \frac{1}{2}ww), \tag{B.6}$$

$$\tau_{xx} = \frac{\mu}{Re}\left(\frac{2}{3}(2\frac{\partial u}{\partial x} - \frac{\partial v}{\partial y} - \frac{\partial w}{\partial z})\right), \tag{B.7}$$

$$\tau_{yy} = \frac{\mu}{Re}\left(\frac{2}{3}(2\frac{\partial v}{\partial y} - \frac{\partial u}{\partial x} - \frac{\partial w}{\partial z})\right), \tag{B.8}$$

$$\tau_{zz} = \frac{\mu}{Re}\left(\frac{2}{3}(2\frac{\partial w}{\partial z} - \frac{\partial v}{\partial y} - \frac{\partial u}{\partial x})\right), \tag{B.9}$$

$$\tau_{xy} = \tau_{yx} = \frac{\mu}{Re}\left(\frac{\partial u}{\partial y} + \frac{\partial v}{\partial x}\right), \tag{B.10}$$

$$\tau_{xz} = \tau_{zx} = \frac{\mu}{Re}\left(\frac{\partial u}{\partial z} + \frac{\partial w}{\partial x}\right), \tag{B.11}$$

$$\tau_{yz} = \tau_{zy} = \frac{\mu}{Re}\left(\frac{\partial v}{\partial z} + \frac{\partial w}{\partial y}\right), \tag{B.12}$$

$$q_x = \frac{-\mu}{(\gamma-1)Ma^2PrRe}\frac{\partial T}{\partial x}, \tag{B.13}$$

$$q_y = \frac{-\mu}{(\gamma-1)Ma^2PrRe}\frac{\partial T}{\partial y}, \tag{B.14}$$

$$q_z = \frac{-\mu}{(\gamma-1)Ma^2PrRe}\frac{\partial T}{\partial z} \tag{B.15}$$

Non-dimensional species transport equation in three coordinate directions will be:

$$\begin{aligned}\frac{\partial(\rho Y_n)}{\partial t} = &-\frac{\partial}{\partial x}(\rho Y_n u - \frac{1}{Re}\frac{1}{Sc_n}\mu\frac{\partial Y_n}{\partial x}) - \frac{\partial}{\partial y}(\rho Y_n v - \frac{1}{Re}\frac{1}{Sc_n}\mu\frac{\partial Y_n}{\partial y})\\ &-\frac{\partial}{\partial z}(\rho Y_n w - \frac{1}{Re}\frac{1}{Sc_n}\mu\frac{\partial Y_n}{\partial z}) + \dot{\omega_n}\end{aligned} \tag{B.16}$$

B.2 Expanded form of the governing equations used in chapter 3

Only expansion of the energy equation and the species transport equation are chosen to be shown in here as continuity and momentum equations are the same for binary- or multi-species mixture. Shear stress terms exist in the energy equation are repeated for consistency.

$$\begin{aligned}\frac{\partial E_T}{\partial t} = &-\frac{\partial[(E_T+p)u]}{\partial x} - \frac{\partial q_x}{\partial x} + \frac{\partial(u\tau_{xx} + v\tau_{xy} + w\tau_{xz})}{\partial x}\\ &-\frac{\partial[(E_T+p)v]}{\partial y} - \frac{\partial q_y}{\partial y} + \frac{\partial(u\tau_{yx} + v\tau_{yy} + w\tau_{yz})}{\partial y}\\ &-\frac{\partial[(E_T+p)w]}{\partial z} - \frac{\partial q_z}{\partial z} + \frac{\partial(u\tau_{zx} + v\tau_{zy} + w\tau_{zz})}{\partial z}\end{aligned} \tag{B.17}$$

in which:

$$\tau_{xx} = \frac{\mu}{Re}\left(\frac{2}{3}(2\frac{\partial u}{\partial x} - \frac{\partial v}{\partial y} - \frac{\partial w}{\partial z})\right), \tag{B.18}$$

$$\tau_{yy} = \frac{\mu}{Re}\left(\frac{2}{3}(2\frac{\partial v}{\partial y} - \frac{\partial u}{\partial x} - \frac{\partial w}{\partial z})\right), \tag{B.19}$$

$$\tau_{zz} = \frac{\mu}{Re}\left(\frac{2}{3}(2\frac{\partial w}{\partial z} - \frac{\partial v}{\partial y} - \frac{\partial u}{\partial x})\right), \tag{B.20}$$

$$\tau_{xy} = \tau_{yx} = \frac{\mu}{Re}\left(\frac{\partial u}{\partial y} + \frac{\partial v}{\partial x}\right), \tag{B.21}$$

$$\tau_{xz} = \tau_{zx} = \frac{\mu}{Re}\left(\frac{\partial u}{\partial z} + \frac{\partial w}{\partial x}\right), \tag{B.22}$$

$$\tau_{yz} = \tau_{zy} = \frac{\mu}{Re}\left(\frac{\partial v}{\partial z} + \frac{\partial w}{\partial y}\right), \tag{B.23}$$

$$\begin{aligned} q_x = \frac{-\mu}{Re}\frac{C_{p_{mix}}}{pr}\frac{\partial T}{\partial x} + \sum_{n=1}^{N_s} h_n(-\frac{\mu}{Re}\frac{1}{Sc_n}\frac{1}{W_{mix}}\frac{\partial}{\partial x}(Y_n W_{mix}) \\ + \sum_{\beta=1}^{N_s}\frac{\mu}{Re}\frac{1}{Sc_n}\frac{Y_n}{W_{mix}}\frac{\partial}{\partial x}(Y_\beta W_{mix})) \end{aligned} \tag{B.24}$$

$$\begin{aligned} q_y = \frac{-\mu}{Re}\frac{C_{p_{mix}}}{pr}\frac{\partial T}{\partial y} + \sum_{n=1}^{N_s} h_n(-\frac{\mu}{Re}\frac{1}{Sc_n}\frac{1}{W_{mix}}\frac{\partial}{\partial y}(Y_n W_{mix}) \\ + \sum_{\beta=1}^{N_s}\frac{\mu}{Re}\frac{1}{Sc_n}\frac{Y_n}{W_{mix}}\frac{\partial}{\partial y}(Y_\beta W_{mix})) \end{aligned} \tag{B.25}$$

$$\begin{aligned} q_z = \frac{-\mu}{Re}\frac{C_{p_{mix}}}{pr}\frac{\partial T}{\partial z} + \sum_{n=1}^{N_s} h_n(-\frac{\mu}{Re}\frac{1}{Sc_n}\frac{1}{W_{mix}}\frac{\partial}{\partial z}(Y_n W_{mix}) \\ + \sum_{\beta=1}^{N_s}\frac{\mu}{Re}\frac{1}{Sc_n}\frac{Y_n}{W_{mix}}\frac{\partial}{\partial z}(Y_\beta W_{mix})) \end{aligned} \tag{B.26}$$

all in non-dimensional form.

Non-dimensional species transport equation in three coordinate directions will be:

$$\begin{aligned}
\frac{\partial(\rho Y_n)}{\partial t} &= -\frac{\partial}{\partial x}(\rho Y_n u) - \frac{\partial}{\partial y}(\rho Y_n v) - \frac{\partial}{\partial z}(\rho Y_n w) \\
&+\frac{\partial}{\partial x}(\rho D_n \frac{\partial Y_n}{\partial x}) + \frac{\partial}{\partial y}(\rho D_n \frac{\partial Y_n}{\partial y}) + \frac{\partial}{\partial z}(\rho D_n \frac{\partial Y_n}{\partial z}) \\
&+\frac{\partial}{\partial x}[\rho Y_n(\frac{1}{W_{mix}}\frac{\partial W_{mix}}{\partial x}(D_n - \sum_\beta D_\beta Y_\beta) - \sum_\beta D_\beta \frac{\partial Y_\beta}{\partial x})] \\
&+\frac{\partial}{\partial y}[\rho Y_n(\frac{1}{W_{mix}}\frac{\partial W_{mix}}{\partial y}(D_n - \sum_\beta D_\beta Y_\beta) - \sum_\beta D_\beta \frac{\partial Y_\beta}{\partial y})] \\
&+\frac{\partial}{\partial z}[\rho Y_n(\frac{1}{W_{mix}}\frac{\partial W_{mix}}{\partial z}(D_n - \sum_\beta D_\beta Y_\beta) - \sum_\beta D_\beta \frac{\partial Y_\beta}{\partial z})] \\
&+\dot{\omega_n}
\end{aligned} \tag{B.27}$$

Perfect gas law in non-dimensional form takes the form of:

$$p = \frac{\rho R_u T}{W_{mix}} \tag{B.28}$$

Dimensional species enthalpy and heat capacity in constant pressure will be:

$$h_n(T) = \Delta h^0_{f_n} + \int_{T_0}^{T_1} C_{p_n}(T)dT, \qquad C_{p_n}(T)/R_u = a_1 + a_2 T + a_3 T^2 + a_4 T^3 + a_5 T^4 \tag{B.29}$$

with two series of different values for coefficients $a1 \sim a5$. Series 1 from $T = 300K$ to $T = 1000K$, and series 2 for $T \geq 1000K$. Species enthalpies as well as C_{p_n} are then need to be non-dimensionalised before they are used in the energy equation.

Reference which was used in order to obtain these data is "CHEMKIN database" on "Gas-phase data format, Thermophysics Resource, Sandia National Laboratory" which was available online (URL: http://www.sandia.gov/HiTempThermo/). JANAF Thermochemical Tables can also be used for this purpose.

Appendix C

Progression milestone

Below is a summary of the efforts made to develop the 3D Navier-Stokes equations capable of simulating multi-species mixture with a complex chemistry. Although the code development was not started from the scratch, the changes had started to be made on a code which was only performing calculation for binary scalars with equal molecular weight(generally unity in non-dimensional context) and Schmidt numbers equal to one. The steps taken to reach to the final stage have been started with incorporating real molecular properties (i.e. molecular weight and Lewis number) and taken into account the effects of differential diffusion by adding the diffusion correction velocity to the species transport equation. The one-step global chemistry mechanism that was already included in the code, was not altered at this stage for the sake of studying the turbulent flow field under such circumstances.DNS results with this code were presented in chapter 4.

Code development continued by incorporating a system of 9 species undergoing a finite-rate chemistry mechanism with 37 elementary reaction steps, 18 of which perform shuffle reactions between hydrogen and oxygen. The new code was tested in several ways under different geometry size and grid point numbers to make sure the equations have been incorporated correctly and the results are reliable for the purposes that may be sought in the future. Results from DNS of multi-component multi-step mixing layer were presented in chapter 5.

For the post-processing part, a great deal of programming have been performed to fulfill the requirements sought from this study although results from some of the subroutines in the post-processing part have not been presented in this work. such as calculations for strain rate tensor or even elements of Reynolds stress tensor. Moreover, conditional averages for scalar mass fraction and mixture fraction PDF have been computed as well but these still needed to be evaluated more before being used.

During development of the multi-species code, setting the correct formulation for the

Chapter No.	Case No.	No. of (MPI) processes	CPU hours
Chapter 4	Case 1	352	8900
Chapter 4	Case 2	352	9500
Chapter 4	Case 3	352	16440
Chapter 5	Case 1	176	20740
Chapter 5	Case 2	176	28440
Chapter 5	Case 1-HR	352	37620
Chapter 5	Case 1L	528	43850
Chapter 5	Case 2L	352	56100

TABLE C.1: CPU hours spent for each case presented in this work

boundary condition was very tricky and cumbersome. Around 14 different ways tried to tackle the problems exist before obtaining a correct set-up for non-reflecting boundary conditions required for a multi-species mixture. Also for the Reynolds number considered in chapter 4, the flow did not perform transition to turbulence and therefore, a higher Reynolds number was applied for multi-species simulations presented in chapter 5. The time spent on these trial and error has not been counted toward the total CPU hours spent for the simulations, though. For the final results presented in this work, a sum of 221500 CPU hours has been used on HECToR (UK national computing service) as listed in detail in table C.1 [1] .

[1]For case 2L in chapter 5, simulation was continued until t_{ND}=199.

Bibliography

[1] Smooke M.D. and Giovangigli V. Formulation of the premixed and nonpremixed test problems. *Lecture notes in physics: Reduced kinetic mechanisms and asymptotic approximations for methane-air flames. Springer-Verlag*, 384:1–28, 1991.

[2] Pope S.B. Turbulent flows. *Cambridge University Press*, First published 2000; Reprinted with corrections 2001,2003.

[3] Moin P. and Mahesh K. Direct numerical simulation: A tool in turbulence research. *Annual Review of Fluid Mechanics*, 30:539–578, 1998.

[4] Mahle I., Sesterhenn J., and Friedrich R. Large eddy simulation of turbulent reacting shear layers including finite-rate chemistry and detailed diffusion processes. *Flow, Turbulence and Combustion*, 80(1):81–105, 2008.

[5] Knaus R. and Pantano C. On the effect of heat release in turbulence spectra of non-premixed reacting shear layers. *Journal of Fluid Mechanics*, 626:67–109, 2009.

[6] Okong'o N., Harstad K., and Bellan J. Direct numerical simulations of O_2/H_2 temporal mixing layers under supercritical conditions. *AIAA Journal*, 40:914–926, 2002.

[7] Luo K.H. and Bray K.N.C. Combustion-induced pressure effects in supersonic diffusion flames. *Twenty-Seventh Symposium (International) on Combustion, The Combustion Institute*, pages 2165–2171, 1998.

[8] Kim J. and Kim J.S. Modelling of lifted turbulent diffusion flames in a channel mixing layer by the flame hole dynamics. *Combustion Theory and Modelling*, 10 (1):21–37, 2006.

[9] Im H.G., Chen J.H., and Law C.K. Ignition of hydrogen-air mixing layer in turbulent flows. *Twenty-Seventh Symposium (International) on Combustion, The Combustion Institute*, pages 1047–1056, 1998.

[10] Rogers M.M. and Moser R.D. The three-dimensional evolution of a plane mixing layer: the kelvin-helmholtz rollup. *Journal of Fluid Mechanics*, 243:183–226, 1992.

[11] Moser R.D. and Rogers M.M. the three-dimensional evolution of a plane mixing layer: pairing and transition to turbulence. *Journal of Fluid Mechanics*, 247: 275–320, 1993.

[12] Dexun F., Yanwen M., and Linbo Z. Direct numerical simulation of transition and turbulence in compressible mixing layer. *Science in China(Series A)*, 43(4): 421–429, 2000.

[13] Lele S.K. Direct numerical simulation of compressible free shear flows. *Report N89-22827, Center for Turbulence Research, Annual Research Briefs*, pages 79–98, 1988. Also published as AIAA paper AIAA-89-0374.

[14] Steinberger C.J. Mixing and non-equilibrium chemical reaction in a compressible mixing layers. *NASA Contractor Report 187084, NASA Lewis Research Center*, 1991.

[15] Luo K.H. Combustion effects on turbulence in a partially premixed supersonic diffusion flame. *Combustion and Flame*, 119:417–435, 1999.

[16] Xia J. and Luo K.H. Direct numerical simulation of diluted combustion by evaporating droplets. *Proceedings of the combustion institute*, 32:2267–2274, 2009.

[17] Xia J. and Luo K.H. Direct numerical simulation of inert droplet effects on scalar dissipation rate in turbulent reacting and non-reacting shear layers. *Flow Turbulence and Combustion*, 84:397–422, 2010.

[18] Echekki T. and Chen J. H. Direct numerical simulation of autoignition in non-homogeneous hydrogen-air mixtures. *Combustion and flame*, 134(3):169–191, 2003.

[19] Xu B. P. and Wen J. X. Numerical study of spontaneous ignition in pressurized hydrogen release through a length of tube with local contraction. *International Journal of Hydrogen Energy*, 37(22):17571–17579, 2012.

[20] Mastorakos E. Ignition of turbulent non-premixed flames. *Progress in Energy and Combustion Science*, 35(1):57–97, 2009.

[21] Doom J. and Mahesh K. Direct numerical simulation of auto-ignition of a hydrogen vortex ring reacting with hot air. *Combustion and Flame*, 156(4):813–825, 2009.

[22] Owston R. and Abraham J. Flame propagation in stratified hydrogenair mixtures-spark placement effects. *International Journal of Hydrogen Energy*, 34(15):6532–6544, 2009.

[23] Lu T., Yoo C.S., Chen J.H., and Law C.K. Analysis of a turbulent lifted hydrogen/air jet flame from direct numerical simulation with computational singular perturbation. *46th AIAA Aerospace Science Meeting and Exhibit*, 7-10 January 2008, Reno, Nevada.

[24] Pantano C., Sarkar S., and Williams F.A. Mixing of a conserved scalar in a turbulent reacting shear layer. *Journal of Fluid Mechanics*, 481:299, 2003.

[25] Pantano C. and Sarkar S. A study of compressibility effects in the high-speed turbulent shear layer using direct simulation. *Journal of Fluid Mechanics*, 451: 329–371, 2002.

[26] Mason A. and Rutland C.J. Turbulent transport in spatially developing reacting shear layers. *Proceedings of the combustion institute*, 28:505–513, 2000.

[27] Mahle I., Foysi H., Sarkar S., and Friedrich R. On the turbulence structure in inert and reacting compressible mixing layers. *Journal of Fluid Mechanics*, 593: 171–180, 2007.

[28] Mathew J., Mahle I., and Friedrich R. Effects of compressibility and heat release on entrainment processes in mixing layers. *Journal of Turbulence*, 9(14):1–12, 2008.

[29] Vreman A.W., Sandham N.D., and Luo K.H. Compressible mixing layer growth rate and turbulence characteristics. *Journal of Fluid Mechanics*, 320:235–258, 1996.

[30] Swaminathan N. and Bray K.N.C. Effect of dilatation on scalar dissipation in turbulent premixed flames. *Combustion and Flame*, 143:549–565, 2005.

[31] Pitsch H., Chen M., and Peters N. Unsteady flamelet modeling of turbulent hydrogen-air diffusion flames. *Twenty-Seventh Symposium (International) on Combustion, The Combustion Institute*, 27(1):1057–1064, 1998.

[32] Pitsch H. Unsteady flamelet modeling of differential diffusion in turbulent jet diffusion flames. *Combustion and Flame*, 123(3):358–374, 2000.

[33] Pitsch H. and Peters N. A consistent flamelet formulation for non-premixed combustion considering differential diffusion effects. *Combustion and Flame*, 114:26–40, 1998.

[34] Ranga Dinesh K.K.J., Jiang X., and van Oijen J.A. Analysis of impinging wall effects on hydrogen non-premixed flame. *Combustion Science and Technology*, 184 (9):1244–1268, 2012.

[35] Ranga Dinesh K.K.J., Kirkpatrick M.P., and Odedra A. Computational fluid dynamics modelling toward clean combustion. *Computational Thermal Sciences*, 4(1):49–65, 2012.

[36] Ranga Dinesh K.K.J., Jiang X., van Oijen J.A., Bastiaans R.J.M., and de Goey L.P.H. Hydrogen-enriched nonpremixed jet flames: Effects of preferential diffusion. *International Journal of Hydrogen Energy*, 38(11):4848–4863, 2013.

[37] Ranga Dinesh K.K.J., Jiang X., and van Oijen J.A. Hydrogen-enriched non-premixed jet flames: Compositional structures with near-wall effects. *International Journal of Hydrogen Energy*, 38(12):5150–5164, 2013.

[38] Bilger R.W. Turbulent diffusion flames. *Annual Review of Fluid Mechanics*, 21: 101–135, 1989.

[39] Chakraborty N. and Cant R.S. Effects of lewis number on turbulent scalar transport and its modelling in turbulent premixed flames. *Combustion and Flame*, 156: 1427–1444, 2009.

[40] Poinsot T.J. and Lele S.K. Boundary conditions for direct simulations of compressible viscous flows. *Journal of computational physics*, 101(1):104–129, 1992.

[41] Sandham N.D. and Reynolds W.C. A numerical investigation of the compressible mixing layer. *Report No. TF-45, Thermosciences Divisions, Department of Mechanical Engineering, Stanford University, Stanford, CA.*, pages 46–47, 1989.

[42] Thompson K.W. Time-dependent boundary conditions for hyperbolic systems, ii. *Journal of computational physics*, 89(2):439–461, 1990.

[43] Lele S.K. Compact finite difference schemes with spectral-like resolution. *Journal of computational physics*, 103(1):16–42, 1992.

[44] Wray A.A. Very low storage time-advancement schemes. *Internal Report, NASA Ames Research Center, Moffett Field, CA.*, 1986.

[45] Rogers M.M. and Moser R.D. Mixing transition and the cascade to small scales in a plane mixing layer. *Physics of fluids:A*, 3(5):1128–1134, 1991.

[46] Saxena P. and Williams F. A. Testing a small detailed chemical-kinetic mechanism for the combustion of hydrogen and carbon monoxide. *Combustion and Flame*, 145:316–323, 2006.

[47] Li J., Zhao Z., Kazakov A., and Dryer F.L. An updated comprehensive kinetic model of hydrogen combustion. *International Journal of Chemical Kinetics*, 36 (10):566–575, 2004.

[48] Ströhle J. and Myhrvold T. An evaluation of detailed reaction mechanisms for hydrogen combustion under gas turbine conditions. *International Journal of Hydrogen Energy*, 32:125–135, 2007.

[49] Mauss F., Peters N., Rogg B., Williams F.A. in: N.Peters, and B.Rogg(Eds.). Reduced kinetic mechanisms for applications in combustion systems. *Springer-Verlag Berlin Heidelberg*, pages 29–43, 1993.

[50] Williams F. A. Detailed and reduced chemistry for hydrogen autoignition. *Journal of Loss Prevention in the process industries*, 21:131–135, 2008.

[51] Grinstein F.F. and Kailasanath K. Chemical energy release and dynamics of transitional, reactive shear flows. *Physics of Fluids:A*, 4(10), 1992.

[52] Fernández Galisteo D., Sánchez A. L., Linán A., and Williams F. A. One-step reduced kinetics for lean hydrogen-air deflagration. *Combustion and flame*, 156 (5):985–996, 2009.

[53] Wang C., Wen J., Lu S., and Guo J. Single-step chemistry model and transport coefficient model for hydrogen combustion. *Science China Technological Sciences*, 55(8):2163–2168, 2012.

[54] Hirsh R.S.J. Higher-order accurate difference solutions of fluid mechanics problems by a compact differencing technique. *Journal of computational physics*, 19(1):90–109, 1975.

[55] Adam Y.J. Highly accurate compact implicit methods and boundary-conditions. *Journal of computational physics*, 24(1):10–22, 1977.

[56] Miller R.S. and Bellan J. Direct numerical of a confined three-dimensional gas mixing layer with one evaporating hydrocarbon-droplet-laden stream. *Journal of Fluid Mechanics*, 384:293–338, 1999.

[57] Thompson K.W. Time-dependent boundary conditions for hyperbolic systems. *Journal of computational physics*, 68(2):1–24, 1987.

[58] Polifke W., Wall C., and Moin P. Partially reflecting and non-reflecting boundary conditions for simulation of compressible viscous flow. *Journal of computational physics*, 213:437–449, 2006.

[59] Rudy D.H. and Strikwerda J.C. A nonreflecting outflow boundary condition for subsonic navier-stokes calculations. *Journal of computational physics*, 36(1):55–70, 1980.

[60] Prosser R. Improved boundary conditions for the direct numerical simulation of turbulent subsonic flows. i. inviscid flows. *Journal of computational physics*, 207: 736–768, 2005.

[61] HEDSTROM G.W. Nonreflecting boundary conditions for nonlinear hyperbolic systems. *Journal of computational physics*, 30(2):222–237, 1979.

[62] Lodato G., Domingo P., and Vervisch L. Three-dimensional boundary conditions for direct and large-eddy simulation of compressible viscous flows. *Journal of computational physics*, 227:5105–5143, 2008.

[63] Prosser R. Towards improved boundary conditions for the dns and les of turbulent subsonic flows. *Journal of computational physics*, 222:469–474, 2007.

[64] Lodato G., Ham F., and Pitsch H. *Annual research briefs 2010, Centre for turbulence research.*

[65] Fosso A., Deniau H., Lamarque N., and Poinsot T. Comparison of outflow boundary conditions for subsonic aeroacoustic simulations. *International journal for numerical methods in fluids*, 68:1207–1233, 2012.

[66] Gustafsson B. and Sundström A. Incompletely parabolic problems in fluid dynamics. *SIAM Journal of Applied Mathematics*, 35(2):343, 1978.

[67] Colonius T. Modeling artificial boundary conditions for compressible flow. *Annual Review of Fluid Mechanics*, 36:315–345, 2004.

[68] Stahl G. and Warnatz J. Numerical investigation of time-dependent properties and extinction of strained methane- and propane- air flamelets. *Combustion and Flame*, 85:285–299, 1991.

[69] Baum M., Poinsot T.J., Haworth D.C., and Darabiha N. Direct numerical simulation of $h_2/o_2/n_2$ flames with complex chemistry in two-dimensional turbulent flows. *Journal of fluid mechanics*, 281:1–32, 1994.

[70] Gopalakrishnan V. and Abraham J. Effects of multicomponent diffusion on predicted ignition characteristics of an n-heptane diffusion flame. *Combustion and Flame*, 136:557–566, 2004.

[71] Tabejamaat S., Ju Y., and Niioka T. Numerical simulation of secondary combustion of hydrogen injected from preburner into supersonic airflow. *AIAA Journal*, 35(9), 1997.

[72] Baum M., Poinsot T.J., and Thevenin D. Accurate boundary conditions for multicomponent reactive flows. *Journal of computational physics*, 116:247–261, 1994.

[73] Moureau V., Lartigue G., Sommerer Y., Angelberger C., Colin O., and Poinsot T. Numerical methods for unsteady compressible multi-component reacting flows on fixed and moving grids. *Journal of Computational Physics*, 202:710–736, 2005.

[74] Okong'o N. and Bellan J. Consistent boundary conditions for multicomponent real gas mixtures based on characteristic waves. *Journal of Computational Physics*, 176:330–344, 2002.

[75] Pakdee W. and Mahalingam S. An accurate method to implement boundary conditions for reacting flows based on characteristic wave analysis. *Combustion theory and Modelling*, 7:705–729, 2003.

[76] Sutherland J.C. and Kennedy C.A. Improved boundary conditions for viscous, reacting, compressible flows. *Journal of computational physics*, 191:502–524, 2003.

[77] Dutt P. Stable boundary conditions and difference schemes for navier-stokes equations. *SIAM Journal on Numerical Analysis*, 25(2):245–267, 1988.

[78] Poinsot T. and Veynante D. Theoretical and numerical combustion. *R T Edwards; 2nd edition*, 2005.

[79] Okong'o N and Bellan J. Turbulence and fluid-front area production in binary-species, supercritical, transitional mixing layers. *Physics of Fluids*, 16(5):1467–1492, 2004.

[80] Bellan J. Theory, modeling and analysis of turbulent supercritical mixing. *Combustion Science and Technology*, 178:253–281, 2006.

[81] Masi E., Bellan J., Harstad K., and Okong'o N. Multi-species turbulent mixing under supercritical-pressure conditions: modeling, direct numerical simulation and analysis revealing species spinodal decomposition. *Journal of Fluid Mechanics*, 721:578–626, 2013.

[82] Schlichting H. and Gersten K. Boundary layer theory. *Springer-Verlag; 8th edition*, 2000; Corrected printing 2003.

[83] Hadjadj A., Yee H.C., and Sjogreen B. *Annual research briefs 2010, Centre for turbulence research.*

[84] Rogers M.M. and Moser R.D. Direct simualtion of a self-similar turbulent mixing layer. *Physics of fluids*, 6(2):903–923, 1994.

[85] Balaras E., Piomelli U., and Wallace J.M. Self-similar states in turbulent mixing layers. *Journal of Fluid Mechanics*, 446:1–24, 2001.

[86] Zhuang F.G. and Li J.C.(Editors). New trends in fluid mechanics research. *Proceedings of the fifth international conference on fluid mechanics(Shanghai, 2007). Springer*, 2008.

[87] Danaila I., Dusek J., and Anselmet F. Coherent structures in a round, spatially evolving, unforced, homogeneous jet at low Reynolds numbers. *Physics of Fluids*, 9(11):3323–3342, 1997.

[88] Y. Na and P. Moin. Direct numerical simulation of a separated turbulent boundary layer. *Journal of Fluid Mechanics*, 374:379–405, 1998.

[89] Kim J., Moin P., and Moser R. Turbulence statistics in fully developed channel flow at low reynolds number. *Journal of Fluid Mechanics*, 177:133–166, 1987.

[90] Chakraborty N. and Swaminathan N. Effects of lewis number on scalar variance transport in premixed flames. *Flow Turbulence and Combustion*, 87:261–292, 2011.

[91] Malkeson S.P. and Chakraborty N. The modeling of fuel mass fraction variance transport in turbulent stratified flames: A direct numerical simulation study. *Numerical Heat Transfer, Part A*, 58:187–206, 2010.

[92] Denev A.J., Fröhlich J., Bockhorn H., Schwertfirm F., Manhart M. in: I. Lirkov, S. MArgenov, and J. Waániewski(Eds.). Dns and les of scalar transport in a turbulent plane channel flow at low reynolds number. *Springer-Verlag Berlin Heidelberg*, pages 251–258, 2008.

[93] Cao S. and Echekki T. Autoignition in nonhomogeneous mixtures: Conditional statistics and implications for modeling. *Combustion and Flame*, 151:120–141, 2007.

[94] Juneja A. and Pope S.B. A dns study of turbulent mixing of two passive scalars. *Physics of Fluids*, 8(8):2161–2184, 1996.

[95] Livescu D. and Madina C.K. Compressibility effects on the scalar mixing in reacting homogeneous turbulence. *IUTAM Symposium on turbulent Mixing and Combustion*, 70:125–135, 2002.

[96] Kaul C.M., Raman V., Knudsen E., Richardson E.S., and Chen J.H. Large eddy simulation of a lifted ethylene flame using a dynamic nonequilibrium model for subfilter scalar variance and dissipation rate. *Proceedings of the combustion institute*, 34:1289–1297, 2013.

[97] Burton G.C. Large-eddy simulation of passive-scalar mixing using multifractal subgrid-scale modeling. *Center for Turbulence Research, Annual Research Briefs*, pages 211–222, 2005.

[98] Tabet F., Sarh B., and Gökalp I. Turbulent non-premixed hydrogen-air flame structure in the pressure range of 1-10 atm. *International Journal of Hydrogen Energy*, 36:15838–15850, 2011.

[99] Ristorcelli J.R. Passive scalar mixing: Analytic study of time scale ratio, variance, and mix rate. *Physics of Fluids*, 18:075101–1–075101–17, 2006.

[100] Vedula P., Yeung P.K., and Fox R.O. Dynamics of scalar dissipation in isotropic turbulence: a numerical and modelling study. *Journal of Fluid Mechanics*, 433: 29–60, 2001.

[101] Johansson A.V. and Wikström P.M. Dns and modelling of passive scalar transport in turbulent channel flow with a focus on scalar dissipation rate modelling. *Flow Turbulence and Combustion*, 63:223–245, 1999.

[102] Knudsen E., Richardson E.S., Doran E.M., Pitsch H., and Chen J.H. Modeling scalar dissipation and scalar variance in large eddy simulation: Algebraic and transport equation closures. *Physics of Fluids*, 24:055103–1–055103–24, 2012.

[103] Jaberi F.A., Miller R.S., Mashayek F., and Givi P. Differential diffusion in binary scalar mixing and reaction. *Combustion and Flame*, 109:561–577, 1997.

[104] Yeung P.K. and Pope S.B. Differential diffusion of passive scalars in isotropic turbulence. *Physics of Fluids:A*, 5(10):2467–2478, 1993.

[105] Veynante D., Trouve A., Bray K.N.C., and Mantel T. Gradient and counter-gradient scalar transport in turbulent premixed flames. *Journal of Fluid Mechanics*, 332:263–293, 1997.

[106] Bailly P., Champion M., and Garreton D. Counter-gradient diffusion in a confined turbulent premixed flame. *Physics of Fluids*, 9(3):766–775, 1997.

[107] Malkeson S.P. and Chakraborty N. *Combustion Science and Technology.*

[108] Lipatnikov A.N. and Sabelnikov V.A. Transition from countergradient to gradient scalar transport in developing premixed turbulent flames. *Flow, Turbulence and Combustion*, 90:401–418, 2013.

[109] Zimont V.L. and Biagioli F. Gradient, counter-gradient transport and their transition in turbulent premixed flames. *Combustion Theory and Modelling*, 6(1): 79–101, 2002.

[110] Chakraborty N. and Cant R.S. Effects of lewis number on scalar transport in turbulent premixed flames. *Physics of Fluids*, 21:035110–1 – 035110–11, 2009.

[111] Swaminathan N., Bilger R.W., and Cuenot B. Relationship between turbulent scalar flux and conditional dilatation in premixed flames with complex chemistry. *Combustion and Flame*, 126:1764–1779, 2001.

[112] Yoshizawa A., Fujiwara H., Abe H., and Matsuo Y. Mechanisms of countergradient diffusion in turbulent combustion. *Physics of Fluids*, 21(1):015107–1 – 015107–18, 2009.

[113] Richardson E.S., Chakraborty N., and Mastorakos E. Analysis of direct numerical simulations of ignition fronts in turbulent non-premixed flames in the context of conditional moment closure. *Proceedings of the combustion institute*, 31:1683–1690, 2007.

[114] Luo K.H. On local countergradient diffusion in turbulent diffusion flames. *Twenty-Eighth Symposium (International) on Combustion, The Combustion Institute*, 28: 489–495, 2000.

[115] Shepherd I.G., Moss J.B., and Bray K.N.C. Turbulent transport in a confined premixed flame. *Nineteenth Symposium (International) on Combustion, The Combustion Institute*, 19(1):423–431, 1982.

[116] Linan A. The structure of diffusion flames. *In Fluid Dynamical Aspects of Combustion Theory. Ed. by Onfori, M. and Tesev, A. Longman Scientific and Technical*, pages 11–29, 1991.

[117] Linan A., Orlandi R., Verzicco R., and Higuera F.J. Effects of non-unity lewis number in diffusion flames. *Center for Turbulence Research, Proceedings of the Summer Program*, pages 5–18, 1994.

[118] Cuenot B. and Poinsot T. Asymptotic and numerical study of diffusion flames with variable lewis number and finite rate chemistry. *Combustion and Flame*, 104: 111–137, 1996.

[119] Veynante D. and Vervisch L. Turbulent combustion modeling. *Progress in Energy and Combustion Science*, 28:193–266, 2002.

[120] Sutherland J.C., Smith P.J., and Chen J.H. Quantification of differential diffusion in nonpremixed systems. *Combustion Theory and Modelling*, 9(2):365–383, 2005.

[121] Kronenburg A. and Bilger R.W. Modelling of differential diffusion effects in non-premixed nonreacting turbulent flow. *Physics of Fluids*, 9(5):1435–1447, 1997.

[122] Zheng X.L., Yuan J., and Law C.K. Nonpremixed ignition of H_2/air in a mixing layer with a vortex. *Proceedings of the combustion institute*, 30:415–421, 2004.